TECHNISCHE UNIVERSITÄT MÜNCHEN
Fakultät für Elektrotechnik und Informationstechnik
Lehrstuhl für Nanoelektronik

Nanomaterials for hybrid organic-inorganic optoelectronic devices processed from solution

Marius T. Loch

Vollständiger Abdruck der von der Fakultät für Elektrotechnik und Informationstechnik der Technischen Universität München zur Erlangung des akademischen Grades eines

Doktor-Ingenieurs
(Dr.-Ing.)

genehmigten Dissertation.

Vorsitzender: Prof. Dr. Gerhard Kramer
Prüfer der Dissertation: 1. Prof. Dr. Paolo Lugli
2. Prof. Dr. Marc Tornow

Die Dissertation wurde am 03.07.2018 bei der Technischen Universität München eingereicht und durch die Fakultät für Elektrotechnik und Informationstechnik am 28.11.2018 angenommen.

Abstract

Inorganic nanomaterials can combine the advantages that are typical for organic semiconductors, especially the fabrication by simple solution processes, and the high performance associated with inorganic semiconductors. In this work, we investigate the integration of such nanomaterials into solution processed, hybrid organic-inorganic thin film solar cells and light emitting diodes (LEDs). In particular, we use quantum dots (QDs) made from silicon as active material in those devices and metal nanowires made from silver and copper for transparent electrodes.

The silicon nanocrystals (SiNC) used in this work have a diameter of 3.1 nm and are functionalized with different surface groups. While bulk silicon has an indirect band gap and does not emit light, at this size SiNC exhibit luminescence that can be used in quantum dot LEDs (QLEDs). We build functional devices that emit bright red light, clearly visible under ambient lighting. The device performance was improved by the addition of ZnO and PolyTPD hole- and electron-blocking layers.

We investigated the impact of different surface functionalization methods and different surface groups. SiNC that are functionalized with organolithium reagents result in better LEDs than functionalization by the more common hydrosilylation method. Concerning the surface groups, we achieve better results with short alkyl chains compared to longer ones and could see no improvement by replacing the alkyl chain with a π-conjugated phenyl group.

In SiNC:P3HT bulk heterojunction solar cells addition of hexyl-thiophene functionalized SiNC improved the performance over P3HT reference devices. We identified an optimal mixing ratio of SiNC:P3HT = 1:1 and showed the positive effect of a short annealing treatment. Due to the band gap widening caused by the quantum confinement in small SiNC, an Al electrode showed quenching of the open circuit voltage. This could be overcome with a low work function Ca electrode. A fully optimized device reached a V_{OC} of 0.9 V and a power conversion efficiency (PCE) of 0.03 %, which is far behind devices that use unfunctionalized SiNC.

The transparent electrode in most organic optoelectronic devices is made from sputter-coated indium tin oxide (ITO). We investigated spray coated films of silver (AgNW) or copper nanowires (CuNW) as a solution-processable alternative. The spray parameters of the films were optimized to find an optimal balance between transparency and conductivity. AgNW films were planarized with a thin ZnO interlayer and implemented as bottom electrode into P3HT:PCBM solar cells. The haziness inherent to nanowire networks further increases light absorption inside the solar cell. Accordingly, the resulting devices reach a power conversion efficiency (PCE) of up to 3.2 %, surpassing the ITO reference by 0.6 percentage points.

CuNW are too rough to serve as bottom electrode. A pre-depostion acid treatment of CuNW in solution allows to deposit well performing films without the need for any post treatment that would harm sensitive underlying polymer layers. This way CuNW films could be used as transparent top electrode. We present different proof-of-concept applications in organic solar cells and LEDs as well as in perovskite solar cells.

Zusammenfassung

Anorganische Nanomaterialien verbinden die hohe Leistungsfähigkeit hochkristalliner, anorganischer Halbleiter mit den positiven Eigenschaften, die üblicherweise organischen Materialien vorbehalten sind - insbesondere die Möglichkeit sie in Flüssigkeit zu verarbeiten. In dieser Arbeit untersuchen wir die Integration solcher Nanomaterialien in hybride organisch-anorganische Dünnfilmsolarzellen und –leuchtdioden (LEDs), die aus Flüssigkeit prozessiert werden. Dabei verwenden wir Quantenpunkte (QDs) aus Silizium als aktives Material und Silber- oder Kupfernanodrähten für leitfähige, transparente Elektroden.

Die verwendeten Siliziumnanokristalle (SiNC) haben einen Durchmesser von 3.1 nm und wurden mit verschiedenen Oberflächengruppen funktionalisiert. Während makroskopisches Silizium auf Grund seines indirekten Bandübergangs kein Licht emittiert, weisen Siliziumnanopartikel Lumineszenz auf, die man in Quantenpunktleuchtdioden (QLEDs) nutzen kann. Wir präsentieren funktionsfähige LEDs, die helles, rotes Lichts ausstrahlen und bei normaler Raumbeleuchtung gut sichtbar sind. Die Leistungsfähigkeit der LEDs konnte durch zusätzliche Elektronen- und Löchersperrschichten aus ZnO und PolyTPD deutlich gesteigert werden.

Wir haben den Einfluss verschiedener Funktionalisierungsmethoden und verschiedener Oberflächengruppen auf die Leistung der LEDs untersucht. Die Funktionalisierung mit Organolithiumreagenzien liefert deutlich bessere LEDs als die üblicherweise verwendete Hydrosilylierung. Bezüglich der unterschiedlichen Oberflächengruppen konnten wir feststellen, dass längere Alkylketten schlechtere Ergebnisse liefern als kürzere. Außerdem konnten wir durch die Verwendung einer π-konjugierten Phenylgruppe keinen Vorteil gegenüber einer einfachen Hexylkette erkennen.

Wenn wir SiNC funktionalisiert mit Hexylthiophen in SiNC:P3HT bulk heterojunction Solarzellen verwenden, werden die Bauteile deutlich besser verglichen mit einer Referenzsolarzelle nur aus P3HT. Wir konnten ein optimales Mischungsverhältnis von SiNC:P3HT = 1:1 finden und zeigen, dass ein kurzes Ausheizen die Zellen verbessert. Auf Grund der Bandlückenvergrößerung bei sehr kleinen Nanopartikeln drückt die Austrittsarbeit der Al Elektrode die Leerlaufspannung ab. Dieser Effekt konnte mit einer Ca Elektrode überwunden werden. Eine optimierte Solarzelle mit $V_{OC} = 0.9$ V liefert einen Wirkungsgrad von 0.03 % und liegt damit weit darunter, was in der Literatur mit unfunktionalisierten SiNC erreicht werden kann.

Die transparente Elektrode in organischen, optoelektronischen Bauteile besteht üblicherweise aus gesputtertem Indiumzinnoxid (ITO). Hier untersuchen wir gesprühte Filme aus Silber- (AgNW) oder Kupfernanodrähten (CuNW) als lösungsprozessierbare Alternative. Die Sprühparameter wurden optimiert, um einen idealen Ausgleich zwischen Leitfähigkeit und Transparenz zu finden. AgNW-Filme wurde mit einer dünnen ZnO-Schicht planarisiert und dann als untere Elektrode in P3HT:PCBM Solarzellen verwendet. Durch die Lichtstreuung an den Nanodrähten wird die Absorption in der Solarzelle erhöht. Dementsprechend weisen die Bauteile mit AgNW-Elektrode einen höheren Wirkungsgrad auf als die mit ITO-Elektrode (3.2 vs 2.6 %).

CuNW-Filme sind zu rau, um sie als untere Elektrode in solch dünnen Bauteilen zu verwenden. Aber eine Säurebehandlung, während die CuNW noch in Lösung sind, führt zu leitfähigen Filmen, die keine weiter Nachbehandlung benötigen. Dadurch können die CuNW-Filme als obere Elektrode auf den empfindlichen Polymerschichten verwendet werden, die sonst unter den üblichen Nachbehandlung leiden würden. Wir präsentieren verschiedene Proof of Concept Anwendungen auf organischen Solarzellen und Leuchtdioden sowie auf Perowskitsolarzellen.

Contents

1 Introduction

Organic conjugated polymers and inorganic nanoparticles similarly combine electronic properties of semiconductors with chemical and mechanical benefits of plastics. As such they can selectively conduct charges and absorb or emit light while at the same time their properties can be tuned during synthesis, they can be synthesized in and processed from solution and form mechanically robust and flexible thin films [1]. Both groups of materials can be combined into a new class of organic-inorganic hybrid devices that enjoy all the advantages of printed electronics like reduced cost, new design possibilities and increased sustainability.

Processing from solution (i.e. from liquid state) promises to massively decrease the cost of manufacturing: firstly, fixed cost are reduced as printing equipment is simpler and cheaper than conventional semiconductor fabrication equipment (e.g., epitaxy and diffusion furnaces, ion implanters, wafer steppers, lithography masks). Secondly, variable cost decrease when source materials and devices can be produced in large-scale solution processes and without the need for energy intensive high temperature and vacuum steps. Thirdly, flexible electronics can be processed on foil, which enables large area, roll-to-roll processing and can vastly increase manufacturing throughput compared to wafer-based batch processing. Maybe in the future we will print electronics like newspapers. The most prominent applications for such roll-to-roll printed electronics are optoelectronic devices that cover large areas: light emitting devices in displays and lighting (OLEDs) and light absorbing ones in solar cells (OSC, also OPV) and photo detectors (OPD). But there also is a large variety of other applications like organic thin film transistors (OTFT) and all kinds of sensors.

Apart from the cost advantages, there is the possibility to build flexible and even stretchable devices that can be transparent and very light. This opens up many new applications ("soft electronics") not accessible for conventional electronics. A popular topic are wearable electronics that are so thin, flexible and light that they can be integrated into clothes or even directly on skin. For example on skin oxygen sensing can be implemented by combining OLEDs and OPDs together with a larger organic display [2]. Other on-skin examples are muscle contraction sensors [3] or tactile sensing for robot skin [4]. There is a large variety of flexible, stretchable, foldable and rollable displays and touchscreen that can be transparent or have integrated OTFTs display drivers [5]. Printed electronics can also be integrated on paper [6], lightweight solar cells can be used airborne on balloons [7] and flexible OPDs can be implanted into the eye to replace a damaged retina [8].

Printed electronics can also contribute to a more ecologically sustainable future. Organic materials are obtained from synthesis instead of mining and are potentially biodegradable and recyclable. The low cost of OPV can contribute to an increased use of renewable solar energy and the low energy consumption during fabrication leads to a very low energy payback time (EPBT). EPBT is the time it takes for a given technology to earn back the energy invested in its making. While mature crystalline silicon solar cells have an EPBT in the range of 1-2 years, projected EPBT for organic solar cells is as low as a few days [9].

Also OLEDs can contribute to a more sustainable future. Contrary to the common transmissive liquid crystal displays (LCDs) that are based on selectively shading pixels covering a back light, OLEDs are self emitting. This does not only result in amazing contrast ratios and very thin displays, but also in more energy efficient light generation. In lighting applications, efficient OLEDs can replace incredibly wasteful light bulbs, mercury-containing fluorescent tube lamp or expensive inorganic LEDs. Additionally, they generate attractive diffuse light and emit over large areas, which will help to drive their adoption.

1.1 Scope

When it comes to inorganic nanomaterials the most popular active materials are quantum dots based on Cd or Pb [10–13]. In this work we investigate silicon nanocrystals (SiNC) as an environmentally benign alternative in printed optoelectronic devices.

We use them as sole emitter in LEDs together with organic and inorganic blocking layers. Referring to the emissive material such devices are often described as quantum-dot LEDs (QLEDs). For solar cells we combine SiNC with a polymer into an organic-inorganic hybrid solar cell.

In addition to SiNC we use metal nanowires from either silver (AgNW) or copper (CuNW). They are not used as active material, but for transparent, conductive electrodes in solar cells and LEDs.

1.2 Outline

This thesis is structured as follows:
Chapter 2 gives an overview of the underlying physical processes involved in hybrid electronics, i.e. organic semiconductors and inorganic nanomaterials. A brief introduction on organic optoelectronic devices will be will be extended further in the respective chapters on OLEDs and OSCs.

Chapter 3 addresses the experimental methods used in this work. The first part of the chapter covers the sample design and fabrication, followed by a description of the employed materials, including the fabrication of functionalized SiNC. Finally, characterization methods relevant for all chapters are introduced, whereas more specific characterization methods for LEDs and solar cells are covered in Chapter 4 and Chapter 5 respectively.

Chapter 4 deals with QLEDs based on SiNC. Working principle, LED characterization and State of the Art are discussed before the experimental results are presented. Here, we investigate the influence of different functionalization methods and different surface groups on the performance of SiNC-LEDs.

Chapter 5 is about hybrid solar cells that combine functionalized SiNC and polymer P3HT in the active layer. After introducing the working principle of excitonic heterojunction solar cells and their characterization, the State of the Art is presented. We then compare different device optimization methods and SiNC surface groups regarding their influence on solar cell performance.

Chapter 6 switches from silicon nanoparticles in the active layer to metal nanowires in transparent electrodes. Spray coated films of either silver or copper nanowires are optimized. Then networks of AgNW are introduced as bottom electrode and of CuNW as top electrode into different devices.

Chapter 7 eventually summarizes the results of this work.

2 Hybrid electronics

2.1 Organic semiconductors

The whole field of solution-processable electronics was started with the discovery of organic semiconductors. Organic materials are commonly referred to as plastics and are based on mostly carbon and hydrogen atoms together with a few heteroatoms such as sulfur, oxygen, and nitrogen. While these materials are usually perceived as insulators, they can also exhibit conducting and semiconducting behavior. The earliest reports of fluorescence and photoelectric properties of organic solids go back to the beginning of the twentieth century [14–17]. Actual electroluminescence was then shown for the first time in 1953 by Bernanose et al. [18], followed by some breakthrough work in 1963 by Martin Pope [19] and in 1965 by W. Helfrich and W. Schneider [20]. Their work however, was based on molecular crystals with a minimum thickness of at least several micrometers, which requires very high operating voltages of around 100 V. Feasible, low-voltage operation only became possible when thin film devices (in the order of 100 nm) made from small molecules or polymers were introduced. Important early works were published from C. Tang and S. VanSlyke in 1987 [21] and from Burroughes et al. in 1990 [22].

A notable milestone for the field was the work Shirakawa et al. in 1977 that showed how polyacetylene can be doped to achieve very high conductivity [23]. For this work Heeger, MacDiarmid and Shirakawa were later awarded with the 2000 Nobel Prize in Chemistry for the “discovery and development of conductive polymers” [24].

Inorganic semiconductors like silicon form crystals based on strong covalent bonds. Organic molecules on the other hand are bound by much weaker Van-der-Waals forces. Due to this weak molecular interaction, the optical and electrical properties of the organic semiconductor are primarily determined by the properties of the single molecules. The weak binding also leads to flexibility, light weight and low sublimation temperatures. However, it also results in crystals of low order and thus severely limits charge carrier mobility, which is often several orders of magnitude below that of inorganic semiconductors.

There are two groups of organic semiconductors distinguished by their size: small molecules and conjugated polymers. While small molecules only consist of a few atoms, polymers are long chains of repeating sub-units called monomers. Those monomers can

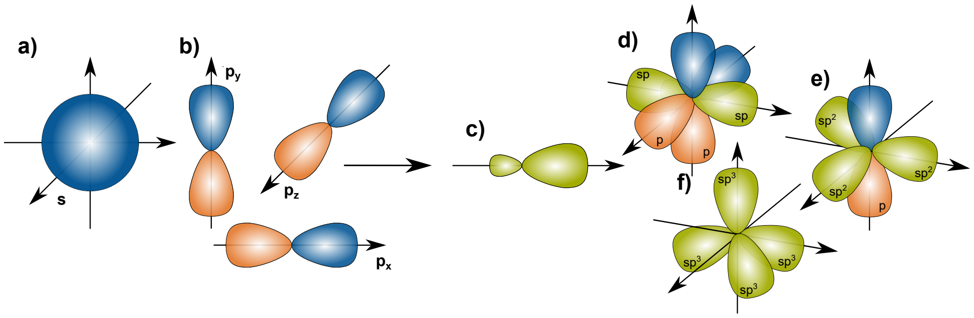

Figure 2.1: *Hybridization of atomic orbitals of carbon: a) unhybridized* s*- and b)* p*-orbitals and c) a single hybridized orbital with barbell shape. d)*sp*-hybridization, e)* sp^2*-hybridization and f)* sp^3*-hybridization. The smaller bell of the hybridized orbitals is omitted for clarity (adapted from ref. [25]).*

be identical over the whole chain (homopolymers) or alternating (copolymers). Typically polymers used in organic electronics have chains that consist of 100 - 400 monomers [1]. This size difference between small molecules and polymers leads to a lot of different properties, most notably their solubility in liquids and hence their processability. Small molecules are usually not well soluble, but more thermally stable and therefore generally deposited by thermal evaporation. Evaporation is done under high vacuum and results in high quality films with low risk of contamination. This makes this material group ideal for fundamental research on the properties of organic semiconductors.

However, evaporation is not a low-cost, high-throughput process due to the required vacuum and high temperatures; therefore a lot of the advantages associated with solution-processability do not apply to small molecules. Polymers on the other hand are generally well soluble (or can be tuned by appropriate side chains to be soluble) and therefore can be deposited with a large variety of low cost fabrication methods e.g., spin and spray coating, doctor blading and inkjet-, screen or gravure printing. Such techniques allow lower temperatures, do not require vacuum and can be implemented into roll-to-roll lines. Furthermore, soluble polymers lend themselves to blending with other materials which is important for bulk heterojunction solar cells (see section 5.1).

However, the underlying principle that gives rise to their semiconducting characteristics is the same for both material groups: a conjugated bonding structure (alternating single and double bonds) of carbon atoms and the formation of molecular orbitals, leading to a band-like structure similar to inorganic semiconductors. The following sections will explain this phenomenon in more detail.

2.1.1 Hybridization in conjugated polymers

Organic materials consist of mostly carbon atoms. Carbon is an element from the fourth main group of the periodic system with four valence electrons and the electron configuration $1s^2 2s^2 2p_x^1 2p_y^1$. However, this configuration is only valid for single carbon atoms; when bonding to other carbon atoms and forming larger molecules, other energetic configurations become favorable. There emerges a phenomenon called *hybridization*: s- and p-orbitals combine into hybrid orbitals energetically between the s- and p-level, which allows binding in an energetically lower configuration. This corresponds to the energy release associated with bonding of the valence electrons. There are three different hybrid orbitals possible depending on how many of the three possible p-orbital are involved in the hybridization with the $2s$-orbital: one p-orbital combines into two sp-orbitals (leaving two $2p$-orbitals), two combine into three sp^2-orbitals (leaving one p-orbital) and three into four sp^3-orbitals.

The shape of these orbitals can be obtained by solving Schrödinger's equation for the respective electrons to receive their wave function Ψ and probability density $|\Psi|^2$ [26]. The resulting orbital shapes are depicted in Fig. 2.1 a) and b) s-orbitals form a sphere and p-orbitals a symmetrical dumb bell; the hybrid orbitals form asymmetrical dumb bells as in Fig. 2.1 c). In all three cases of hybridization the hybrid orbitals spatially arrange for maximal distance to each other to minimize repulsion and the p-orbitals will arrange accordingly as shown in 2.1 d) - f): The four sp^3-orbitals form a tetrahedral with an angle of 109.5° between each orbital. The three sp^2-orbitals orbitals arrange in a plain with 120° between them and the single p-orbital perpendicular to this plain. sp-orbitals will have 180° between them and the two $2p$-orbitals perpendicular to them.

2.1.2 Molecular Orbitals

Conjugated polymers consist of a backbone chain of carbon atoms with alternating double and single bonds. Accordingly, every carbon atom forms three bonds and is therefore sp^2-hybridized. In this case the sp^2-orbitals of neighboring atoms strongly overlap and form a so-called σ-bond as seen in Fig. 2.2 a) and b). This strong bond holds the molecule together and provides it with stability. The neighboring p_z-orbitals lie perpendicular to the sp^2-plain and only overlap partially; therefore, they form a weaker so-called π-bond. This weak bonding allows the involved electrons to easily move between the atoms and thus across the molecule; therefore, these electrons are described as delocalized over the molecule. This delocalization is the origin of (semi)conducting behavior in organic materials.

One approach to explain this behavior is molecular orbital (MO) theory. It describes how in a molecule overlapping *atomic* orbitals form *molecular* orbitals. Overlapping sp^2-orbitals will form σ-orbitals, overlapping p_z-orbitals form π-orbitals. Calculating the

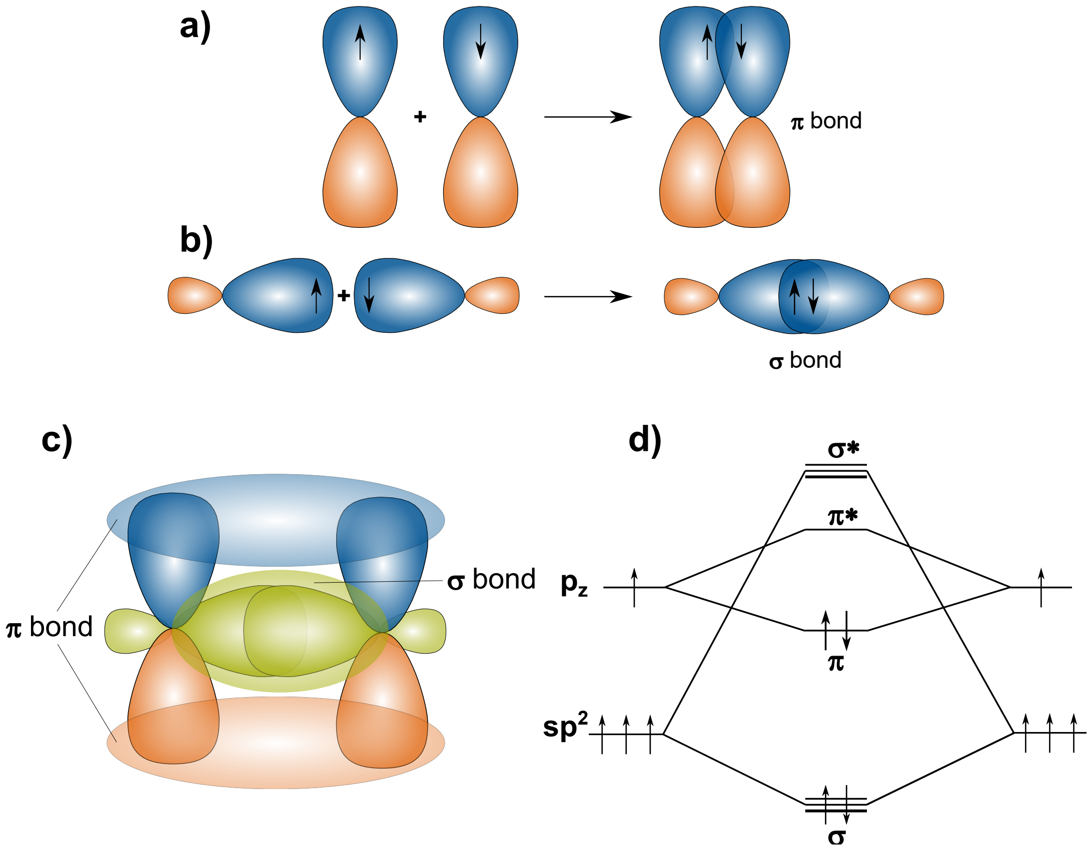

Figure 2.2: *Formation of molecular orbitals: a) partially overlapping atomic p-orbitals form π-bonds, b) strongly overlapping hybrid orbitals form much stronger σ-bonds. c) Energetic structure of ethylene with a carbon-carbon double bond consisting of a σ- and a π-bond (adapted from ref. [25]) and d) exemplary molecular orbital diagram.*

energies of those molecular orbitals is not trivial and quickly becomes more complicated for larger molecules due to the many interactions between all the moving electrons and nuclei. There are several different approaches to calculate molecular orbitals, e.g., the valence-bond (VB) method, intermediate neglect of differential overlap (INDO), and density functional theory (DFT). A very common approach is to calculate the molecular orbitals by linear combination of the atomic orbitals, the LCAO-:method. Typically certain approximations are evoked to keep the computational complexity down; e.g., the Born–Oppenheimer approximation assumes that nuclei can be considered static compared to much smaller and faster electrons.

The linear combinations can result in constructive or destructive overlapping of the atomic orbitals. Constructive overlapping results in *bonding* molecular orbitals π and σ, destructive overlapping in *anti-bonding* π^* and σ^* orbitals. The anti-bonding orbitals are higher in energy, forming an energetic landscape as illustrated in the molecular orbital diagram in Fig. 2.2 d). In an unexcited molecule – following the Aufbau principle - the lower energy bonding orbitals will be occupied first, leaving the anti-bonding orbitals vacant. Therefore the highest bonding orbital is referred to as *highest occupied molecular orbital* (HOMO) and the lowest anti-bonding orbital as *lowest unoccupied molecular orbital* (LOMO). When identical molecules are connected, their identical molecular orbitals should add up at the same energy levels. This, however, is not possible due to Pauli's exclusion principle: no two electrons can have the same energetic configuration within one molecule. Therefore the molecular orbitals of the connected molecules split up into slightly different levels. Since polymers consist of long chains of identical molecules, their molecular orbitals will split up into many different, closely packed states until a band-like energetic structure can be assumed. As such we can compare organic semiconductors with conventional ones, whereby the HOMO corresponds to the valence band, the LUMO to the conduction band and the energy difference between HOMO and LUMO to the band gap E_g. This band gap then gives rise to all the optical phenomena that make organic semiconductors interesting for optoelectronic applications.

2.1.3 Charge transport

Charge transport in organic semiconductors is a complex topic. There are several different models (e.g., band transport, polaronic transport, disorder-based transport) for different regimes (e.g., low carrier density, high carrier density, space charge limited, trap charge limited, doped semiconductors, strong coupling), but there is no satisfying theory describing all aspects of the charge transport in organic semiconductors. A detailed discussion of this topic is out of the focus of this work and can be found in chapter 1 of the book of Bässler and Köhler [27]. In the following some key aspects will be discussed.

The band like transport described in the previous section is very simplified as it only holds true for perfect, defect-free molecular crystals. However, in reality solution-processed devices are made from amorphous polymer films, which consist of many weakly-bound molecules and have many chemical and structural defects. While inorganic semiconductors form covalent bonds, organic molecules form much weaker van-der-Waals bonds. Accordingly, electronic wavefunctions are less delocalized among neighboring molecules than within a single molecule. Therefore, two cases of charge transport have to be considered: *intra-molecular* transport within a single molecule and *inter-molecular* transport between different molecules. Due to the weak bonding, charges moving between molecules face potential barriers, which they have to overcome by a phonon-assisted tunneling mechanism called *hopping*. This process is significantly less efficient than band-transport and the main reason organic materials have slower charge transport than inorganic materials.

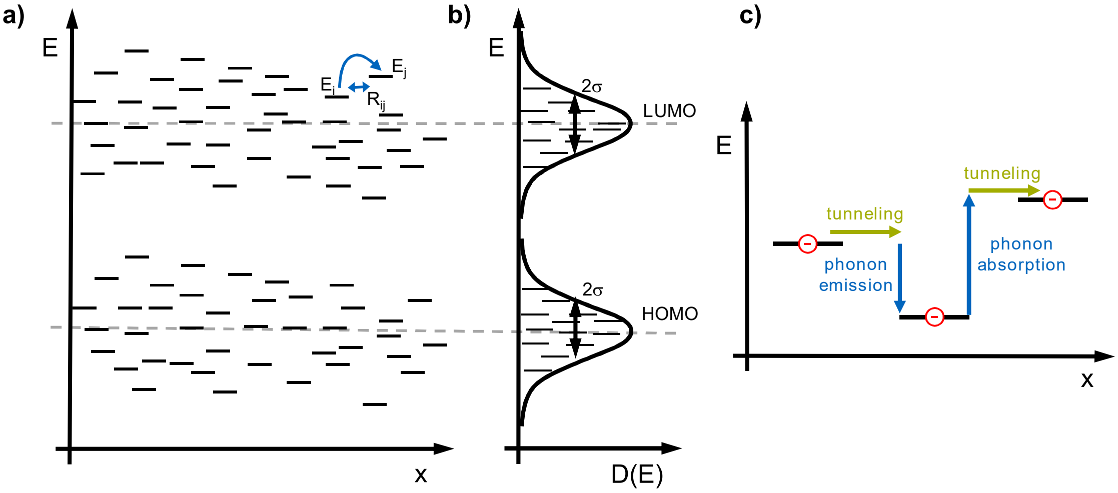

Figure 2.3: *Charge transport in organic semiconductors: a) hopping between localized states, b) Gaussian distribution of localized states in the HOMO and LUMO and c) upwards and downwards hopping as phonon-assisted tunneling.*

For the intra-molecular transport charge carriers are often considered delocalized and able to move freely through the overlapping π-orbitals, which is referred to as a (conjugated) π-system. However, this simplified model does not consider defects that often occur in polymer chains (e.g., chain twists and kinks or chemical impurities). These defects disturb the π-system and present potential barriers, which also have to be overcome by hopping. Actual band like transport only applies to very short, undisturbed chain segments and therefore the overall charge transport in organic polymer films is dominated by hopping between localized charges. This process was famously described as *impurity conduction* by Miller and Abrahams in 1960 [28], which was later extended to the variable range hopping theory by N.F. Mott [29, 30]. In the Miller-Abrahams equation the transition or hopping rate ω_{ij} between two localized states i and j with spatial distance R_{ij} differentiates for hopping upwards or downwards as:

$$\omega_{ij} = \nu_0 \exp(-2\alpha R_{ij}) \begin{cases} \exp\left(-\frac{E_j - E_i}{k_B T}\right) & \text{for } E_j - E_i \geq 0 \text{ (uphop)} \\ 1 & \text{for } E_j - E_i \leq 0 \text{ (downhop)} \end{cases} \tag{2.1}$$

Where ν_0 is the maximum hopping rate (attempt-to-escape frequency), α is the inverse localization radius (a quantity for the wavefunction overlap of the involved electrons and thus related to the tunneling probability). The first exponential term represents the probability of the charge to tunnel from state i to state j. If the energy of the target state is lower ($E_j < E_i$) tunneling can occur without additional energy and excess energy can be thermalized by emission of a phonon (this is assumed to always be possible). The process is illustrated in Fig. 2.3 c). If the energy of the target state is higher ($E_j > E_i$), additional energy is necessary to reach this higher energy before tunneling can occur. This is covered by the second exponential term of the equation, where phonons provide a thermal energy k_BT. Hence, contrary to inorganic materials, in organic semiconductors charge transport increases with temperature. The equation can be extended by an additional term in case of an external field. As an applied field can lower the energetic difference $E_j - E_i$ hopping can already happen at lower temperatures and charge transfer is enhanced.

A popular approach to eventually calculate carrier mobility and diffusion is a parametric model based on monte carlo simulation introduced in 1993 by H. Bässler [31] called *Gaussian disorder model* (GDM, also known as Bässler model). It uses Miller-Abrahams hopping and extends the model by using a Gaussian distribution of localized states to describe the density of states (DOS) in HOMO and LUMO:

$$D(E) = \frac{N}{\sigma\sqrt{2\pi}} \exp\left(-\frac{E^2}{2\sigma^2}\right), \tag{2.2}$$

With N the density of localized states, E the energy measured relative to the center of the DOS distribution and σ the width of the distribution (also ”disorder parameter” as it describes the disorder in material – the less ordered, the higher σ). The assumption of a Gaussian distributed density of states is experimentally supported e.g., by absorption and fluorescence spectra of organic semiconductors which often yield a Gaussian profile.

Another phenomenon that has to be considered is that charge transport involves ionic molecular states. An additional charge on a molecule has an influence on the geometry and electronic configuration of the molecule and it polarizes surrounding molecules. This combination of charge carrier and polarization of the environment is describe as a quasi particle called *polaron*. This limitation is eliminated when using Marcus-type hopping rates, so that polaronic effects are included.

2.2 Nanomaterials

Nano materials are commonly defined as materials where at least one spatial dimension of a single unit of the material is below 100 nm in size. This can be nano sheets (one dimension), tubes and wires (two dimensions) and particles (all three dimensions). At this size nanomaterials typically show properties different to their macroscopic bulk counter parts. Suddenly the properties of these materials depend on their size and not only on their elemental composition. This can be optical properties, conductivity, magnetic behavior, chemical reactivity or melting temperature as some examples. This is what makes nanomaterials so exciting as they offer access to a completely new class of materials.

There are two factors at play that are causing this change of properties: free energy variation (surface effects) and quantum confinement. All nanomaterials have a very **high surface-area-to-volume ratio** and therefore a large fraction of the involved atoms are surface atoms. In any material, the surface atoms make a proportional contribution to the total free energy. While this is mostly negligible in bulk materials as only a very small fraction of the atoms is at the surface, this is a major factor in nanomaterials; most of their surface atomic bonds are unsaturated, and there is a large energy related to the surface. The free energy variation is the major reason for variations of thermodynamic properties. The resulting size-dependent melting point depression of nanoparticles is well observed for many materials; gold nanoparticles for examples have been reported to show very significant melting point depression once their diameter drops below 10 nm, with depression of up to about 500 °C compared to bulk gold [32].

The **quantum confinement** effect only becomes relevant in very small particles, which are then called quantum dots (QDs). Often the terms nanoparticle (NP) or nanocrystal (NC) are also used to describe particles affected by quantum confinement effects. Quantum dots typically have a diameter between 1 to 10 nm and only consist of few 100 to 10 000 atoms. In this size range the particles are so small that their electron wavefunctions are confined by the particle's spatial boundaries and have to adjust to the particle size. This has two implications: the energetic landscape becomes a) quantized and b) tunable by the particle size. This tunability makes quantum dots especially interesting for optoelectronic applications. PbSe particles e.g., have been show with tunable optical peaks ranging between 0.56 eV (2.2 µm) and 1.1 eV (1.1 µm) by changing the particle size from 9.5 to 2.6 nm [33].

The first discovery of this quantum size effect is attributed to the Russian scientist Alexey I. Ekimov in his study on CuCl crystals in 1981 [34]. In 1984 he published a similar study on CdS [35]. Similar work was done around the same time by Louis E. Brus at AT&T Bell Laboratories in the USA [36, 37]. At the time quantum dots were a niche subject in solid state physics as they were fabricated by expensive and sophisticated methods like molecular epitaxy or chemical vapor deposition (CVD) and were usually embedded in a glass matrix. A big shift started when in 1986 Brus for the first time used a liquid-phase approach to fabricate nanoparticles from II-VI compound semiconductors [38]. This lead to some breakthrough work by Murray, Norris and Bawendi in 1993 [39], where they describe the solution-based synthesis of monodisperse nanocrystals, which then enabled more systematic and detailed studies of the quantum size effect. The interdisciplinary and widespread field of **colloidal quantum dots** was born. These colloidal quantum dots are functionalized with surfactant molecules to saturate surface states and prevent agglomeration. This way they are freestanding and can be colloidally dispersed (due to the small size of the quantum dots the dispersion are often simply referred to as solution). As such all advantages of solution-processing apply and colloidal quantum dots can easily be integrated into the existing fabrication processes of organic electronics.

Silicon nanocrystals

The most widely studied material systems for QDs are based upon II-VI (e.g., CdSe, CdS and CdTe), III-V (e.g., InP, InAs, GaAs) and IV-VI (e.g., PbS and PbSe) compound materials. They are the pioneering materials of the quantum dot research field, have been thoroughly investigated and demonstrated succesfully in many applications such as sensing [40–42], fluorescent bio labels [43–46], quantum computing [47–49] and many optoelectronic devices such as solar cells [11, 12, 33, 50], LEDs [10, 13, 51–53] and lasers [54–56].

Major disadvantages are that they are based either on toxic heavy metals like lead, cadmium and arsenic and/or on increasingly rare elements like indium and selenium [57–60]. The use of such toxic materials in consumer products is becomimg increasingly regulated and all the mentioned heavy meals are on the World Health Organization's list of *Ten chemicals of major public health concern* [61]. And in the European Union, the Restriction of Hazardous Substances (RoHS) Directive sets a maximum permitted concentrations for many hazardous materials, e.g., lead is limited to 0.1 wt.-% and cadmium to 0.01 wt.-% in any homogeneous material employed for a product (not just the finished product in total). [62]

Silicon as alternative is highly abundant, non-toxic (even in nanoparticle form [63–65]) and bio compatible [66, 67]. While bulk silicon has an indirect band gap and thus generally does not emit light, nanoparticles with diameter below the Bohr radius of bulk silicon ($\sim$ 5 nm) show strong luminescence due to quantum confinement [68–70] and high quantum yields of up to 75 % [71, 72].

Similarly to the compound quantum dots, SiNC have first been discovered in a solid state matrix (often described as *porous silicon*) before moving to freestanding, colloidal nanocrystals. The first report of nanostructured silicion exhibiting photoluminescence was in 1990 by Canham [73]. Since then many prototype applications based on SiNC have been shown: different sensors [74–78], bio-markers [79–83] and batteries [84–86] and of many optoelectronic devices that will be the topic of this thesis, solar cells [87–95] and LEDs [96–104].

A drawback of silicon is the lack of core-shell particles. A lot of the compound semiconductor based quantum dots utilize a core–shell structure where the core material is covered with a lattice-matching wide-band-gap material that confines charges within the core, isolates them from dangling surface states and increases the probability of radiative recombination [51, 52, 105, 106]. To date, there are no methods for preparing Si-NCs with similar structures [107]. Therefore, SiNCs are functionalized directly with organic ligands and this functionalization has a larger influence on the particle properties compared to compound particles.

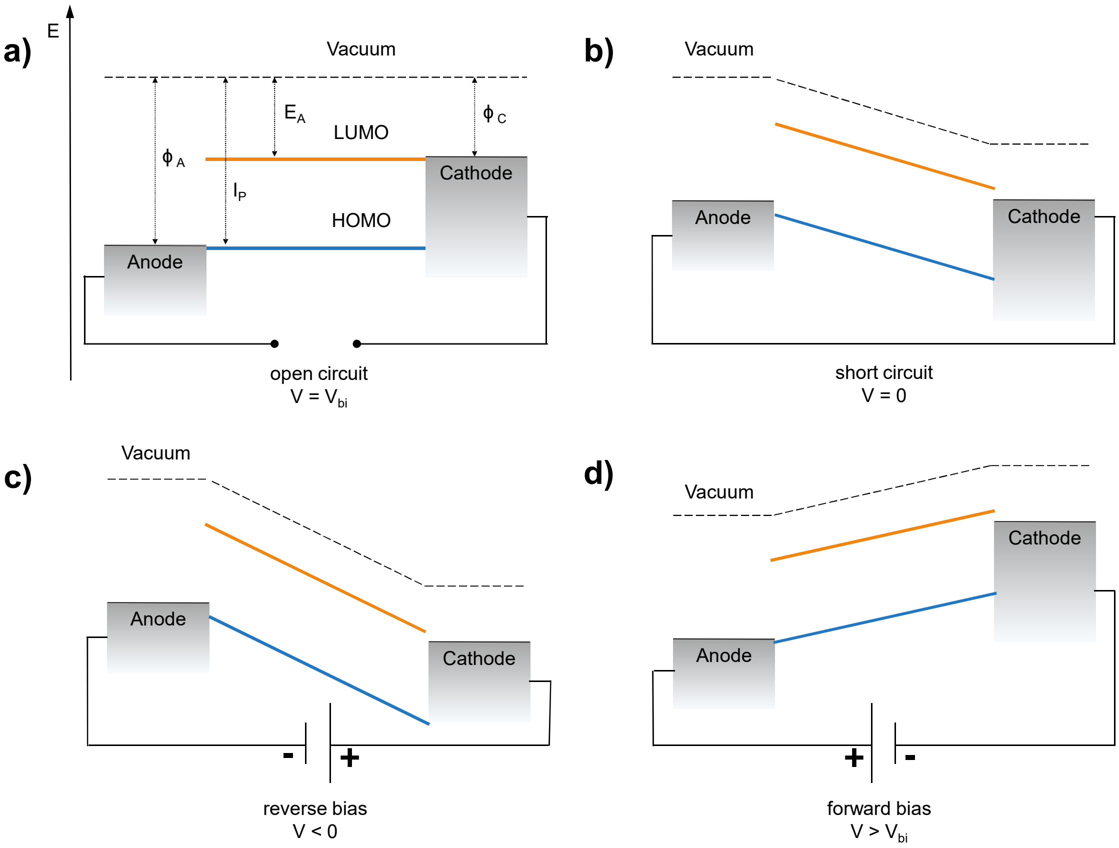

Figure 2.4: *Operating modes of an organic diode according to the metal-insulator-metal model: a) open circuit condition, b) short-circuit condition, c) reverse bias and d) forward bias.*

2.3 Optoelectronic devices

Optoelectronic devices convert light into current as in solar cells and photodetectors or current into light e.g., light emitting diodes and lasers. All these devices can also be made from semiconducting polymers and/or nanoparticles. This work only deals with solar cells and light emitting diodes. Both devices - OSCs and OLEDs - are based on a diode architecture and therefore have many similarities. While the basic working principle of organic devices is the same as of their inorganic counter parts - rectifying, asymmetric behavior with selective materials for electrons and holes - there are some differences. While inorganic semiconductors get their asymmetry through p- and n-type doping and are based on diffusion currents, organic devices typically employ metals with different work functions or other additional interlayers for charge selectivity and due to the low intrinsic charge carriers they rely on charge injection and drift currents.

The simplest organic diode consists of an organic semiconductor between two metal electrodes with different work functions. A simplistic, but useful model to understand the rectifying behavior and the operating modes of an organic diode is the **metal-insulator-metal (MIM) model**. Due to the low intrinsic charge carrier density and low charge mobilities in organic materials (and assuming non-ohmic contact between metal and semiconductor) the organic material can be considered as dielectric and such a device is conceptually close to a parallel plate capacitor - hence the MIM model. The according energy band diagrams are depicted in Fig. 2.4.

In the **open circuit** case, when the two metal electrodes are not connected, the energy levels of the device align as represented in Fig. 2.4 a). HOMO and LUMO are simplified from a Gaussian distribution (see section 2.1.3) to a more convenient straight line. The arrows indicate the energies necessary to remove an electron from the electrodes (work functions of the anode Φ_A and and the cathode Φ_C), the HOMO (ionization potential I_P) and the LUMO (electron affinity E_A). Since in this case none of the bands are tilted, it is also described as flat band condition. The vacuum levels of all materials are aligned, there is no potential drop over the organic layer and accordingly no charge transport occurs. The applied voltage is called the open circuit voltage V_{OC} and corresponds to the potential difference between the two electrode work functions.

The device is in **short circuit** condition, when the two electrodes are connected through an external circuit and no voltage is applied. Electrons flow from the anode to the cathode until the Fermi levels of two electrodes are aligned as in Fig. 2.4 b). The resulting potential difference falls off evenly across the organic layer, manifesting is a displacement of the vacuum levels and a tilting of the HOMO and LUMO levels. This potential difference corresponds to the difference of the work functions of the electrodes and is referred to as built-in potential V_{bi}:

$$V_{bi} = \frac{1}{e}(\Phi_A - \Phi_C). \tag{2.3}$$

In an ideal diode V_{bi} is equal to the open circuit voltage V_{OC}). In this condition there is no current flow, as any injected charges will immediately flow back to their respective electrodes. However, if charges are generated in the organic layer e.g., by illumination, they will drift in this electric field to the respective contacts and can be extracted. This extraction of charges utilizing the built-in potential without applying an external voltage is optimal for diodes used as solar cells.

Under **reverse bias** when a positive, external voltage is applied to the cathode, this voltage adds to the built-in potential and the tilting of the HOMO and LUMO levels will become even steeper (Fig. 2.4 c)). In an ideal device still no current would flow as the resulting field acts against charge injection. In real devices however, a small parasitic dark current will flow due to device defects like pin holes in the organic layer. Due to the increased field, photo-generated charges will be extracted more efficiently than in the short circuit condition; therefore this operation mode is used for photo detectors.

Under **forward bias** (positive voltage at the anode) is applied, the HOMO and LUMO levels tilt in the other direction. When they are tilted beyond flat band condition (Fig. 2.4 d)), charge carriers can efficiently be injected from the electrodes into the organic layer. Here electrons and holes can recombine radiatively, so a diode in this operating mode constitutes a light emitting diode (LED).

3 Experimental methods and materials

3.1 Device design

Both basic optoelectronic devices - solar cells and LEDs - will be presented in this work. The two devices in principle have the same buildup, with some adjustments to the used materials and interlayers, but are operated in different regimes. A typical device consists of a stack of several thin films between 10 - 200 nm, deposited on one another.

Basis is an active (light absorbing or emitting) material sandwiched between two metal electrodes. The electrodes need to have different work functions to create the charge selective asymmetry of a diode. Holes are injected or extracted at the high work function (HWF) electrode (anode), electrons at the low work function (LWF) electrode (cathode). Additionally, at least one of the electrodes needs to be transparent to let light enter or leave the device. Depending on the application the second electrode can be opaque or transparent: if it is also transparent the whole device can be semi-transparent, which is attractive for certain applications like in windows or see-through displays. On the other hand if the second electrode is opaque, it is usually reflective. This typically improves device performance as the reflected light would be lost otherwise. In a solar cell the optimal thickness of the absorbing layer is usually not thick enough to absorb all light entering the device and some light would leave the device on the backside unabsorbed; a reflective electrode sends the light back through the devices and thus doubles the optical path length for absorption. In an LED it is the same: the generated light is emitted in all directions and half of the light would leave the device through the back of the device (which is often covered by electronics), but front emission is almost doubled if the light is reflected at the back. Therefore see-through devices typically have lower performance than devices with one reflective electrode.

This barebone metal-semiconductor-metal device is usually extended by additional charge-selective interlayers on each side. These interlayers block one kind of charge while transporting the other well, therefore they are referred to as hole blocking or electron transport layer (HBL/ETL) on the one side and electron blocking or hole transport layer (EBL/HTL) on the other side. The blocking and transport layers can also be separated or extended into several ones, especially in LEDs. The interlayers can also have additional functionality like planarization or work functions adjustments of the underlying layer.

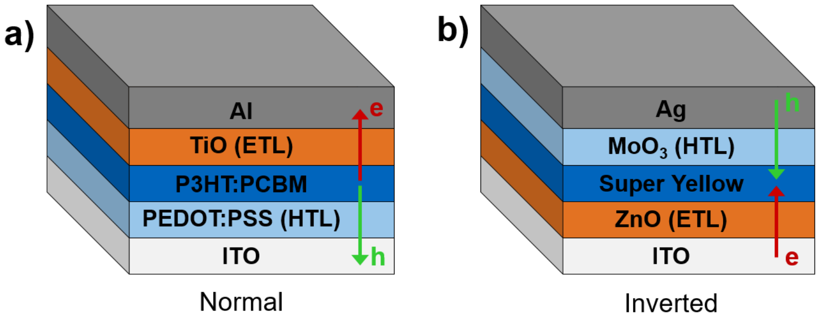

Figure 3.1: *Normal and inverted device architectures: a) a typical solar cell design with normal architecture: holes are extracted at the bottom, electrons at the top. b) An OLED design with inverted architecture; here anode and cathode are the other way around: electrons are injected form the bottom, holes from the top. The ZnO ETL makes it possible to extract electrons at the bottom despite the high WF of ITO.*

3.1.1 Device architecture

Historically most devices are based on a glass substrate covered with ITO, the go-to material for transparent electrodes with a relatively high work function of around 4.7 eV, and build on top of that. Therefore the device architecture with anode at the bottom and cathode at the top is referred to as *normal* (also regular or non-inverted). The inverse structure with cathode at the bottom and anode at the top is called *inverted* accordingly. As such the there are two typical, generic device stacks:
HWF anode / HTL / active layer / ETL / LWF cathode (normal),
LWF cathode / ETL / active layer / HTL / HWL anode (inverted).
Examples of the two architectures are shown in Fig. 3.1.

3.1.2 Sample layout

The sample layout used in this work is illustrated in Fig. 3.2 and features six devices per substrate, each with an active area of 9 mm². Basis is a commercially available glass substrate (25 mm x 25 mm x 1.1 mm) that is covered with two pre-structured stripes of ITO (3 mm wide), which are connected at the end to form an O-ring (Fig. 3.2 a)). On top of the ITO all solution processable layers are deposited by spin coating. As such, they cover the whole substrate, which means all devices on one sample will have the same configuration as they cannot be covered separately. The top electrode consists of six separate, evaporated metal stripes (3 mm x 10 mm) that can be seen in Fig. 3.2 b). The active area of each diode is then defined by the overlap of top and bottom electrode (3 mm x 3 mm) as illustrated in Fig. 3.2 c). This is due to the fact that typical organic semiconductors have low charge carrier mobilities and diffusion length, just enough

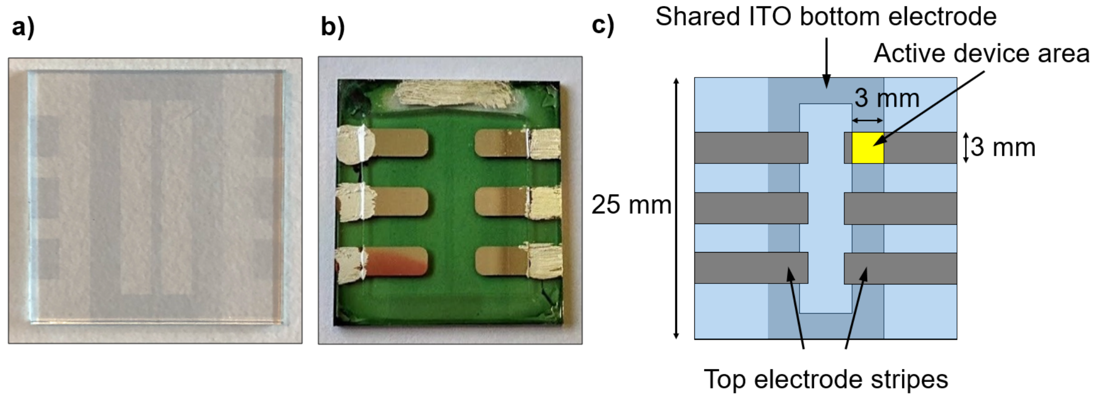

Figure 3.2: *Device layout: a) glass substrate with pre-structured ITO-stripes, b) a finished device with six top electrodes, encapsulation and silver paste on all contacts and c) a schematic of the device layout showing the active device area at the electrode overlap.*

to travel horizontally through a device with thickness in the order of around 100 nm. There is no lateral movement beyond this roughly 100 nm, therefore charges outside of the electrode overlap can not be extracted (solar cell) or charges injected into the device will not recombine outside of it. This phenomenon allows to share the bottom electrode between all six devices, which simplifies the layout. This can be easily verified, when working with light emitting devices. However, great care has to be taken - especially with solar cells, where the active area cannot be easily inspected by eye - when interlayers with higher conductivity (e.g., some PEDOT:PSS variants) are used, as this can enlarge the active area (an example is shown in Fig. 6.12). The electrodes are situated as such that the active device area is positioned towards the middle of the sample. As spin coated films can have some unwanted edge effects the highest film uniformity is in the middle of the sample. This layout also leaves enough room to encapsulate the active area and still have access to the electrodes.

3.2 Fabrication

One great promise of solution-processable hybrid devices is their easy fabrication. One hurdle to this is that a lot organic materials and nanoparticles are prone to oxidation or sensitive to humidity. Therefore these materials have to be stored and processed in inert atmosphere, until the device is encapsulated. For this work a nitrogen-filled MBraun glovebox was used, which filters any hydrogen and oxygen introduced to its atmosphere and typically keeps their levels below 0.1 ppm. Non-metallic layers were deposited with a spin coater, metallic layers with an evaporation chamber (Univex 350 evaporation system by Oerlikon Leybold Vacuum GmbH), which both were also inside the glove box. This allows to do all fabrication steps without exposure to ambient atmosphere. In chapter 6 devices were prepared with spray coated nanowire electrodes, the relevant fabrication details are describe there.

A typical fabrication process consists of the following steps:

1. Cleaning of the substrates
2. Spin coating and subsequent annealing of all solution-based layers (inside glovebox)
3. Deposition of the top electrode by thermal evaporation (inside glovebox)
4. Encapsulation (inside glovebox)

These steps will be explained in more detail in the following.

Substrate preparation

The fabrication process starts with a chemical cleaning of the ITO-covered glass substrates to make sure they are free from any grease, dust particles and chemical residuals. The substrates are put in three successive ultrasonic bathes for a few minutes each: first in lab detergent, followed by acetone and isopropanol (IPA). Subsequently they are rinsed with deionized water and dried with a nitrogen gun .

After the wet cleaning follows treatment with oxygen plasma. This so-called plasma activation increases the surface energy and thus the wettabiliy of the glass. This is especially relevant for water-based solutions that would not spread well on glass. Since very often the first layer to cover the ITO/glass is the water-soluable PEDOT:PSS, the plasma treatment is important to enable layer deposition and improve film uniformity. It has also been shown, that an oxygen plasma treatment of ITO can increase the ITO work function which is typically desirable to better match the HOMO level of the following layer [108]. In this work a Femto plasma asher by Diener electronics was used. Typical process parameters are gas pressure of 0.3 mbar, generator power of 50 % ($\sim$ 165 W) and process time of 2 min.

Spin-coating

Spin-coating is a simple and well understood deposition technique for thin uniform films, which is widely used in industrial application, e.g., for photoresist layers in lithography processes. Layer thicknesses ranging from few nm to a few µm can be obtained with very high reproducabiliy.

The process is illustrated in Fig. 3.3. For this coating technique the substrate is fixed on a rotating disk called chuck by air suction. The solution (often called ink) is dispensed

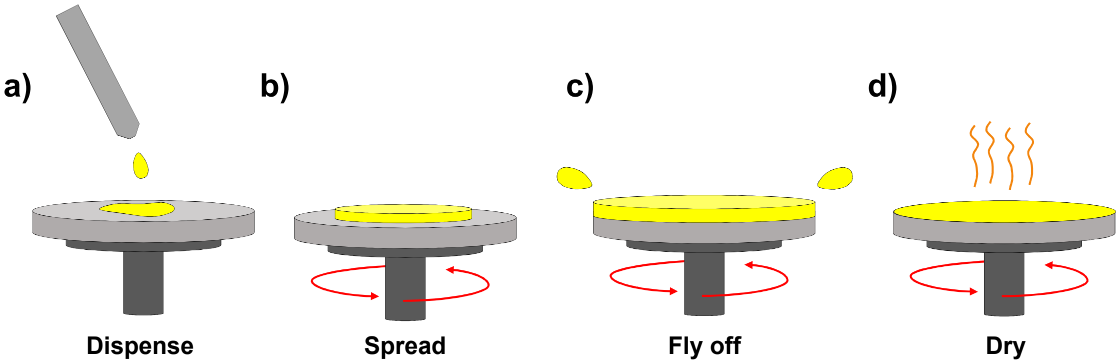

Figure 3.3: *The spin coating phases: a) the ink is dispensed on the substrate, b) the rotation spreads the material over the substrate, c) excess material is flying of, the amount depending on the rotation speed and d) the solvents in the film dry, leaving the final, solid film.*

on the substrate with a pipette or a syringe (Fig. 3.3 a)). Depending on the wettability of the surface and the viscosity of the solvent, a drop in the middle of the substrate is sufficient; under non-optimal conditions it is advisable to cover the whole substrate with solution. After the solvent deposition the chuck is rotated at high speed and the resulting centrifugal forces spread the material across the substrate (Fig. 3.3 b)). Firstly a lot of the material is flung of the sample (Fig. 3.3 c)); then the wet layer is drying under the air flow of the rotation until the final dry layer remains (Fig. 3.3 d)).

The final film thickness is determined by the spinning parameters (rotational speed, acceleration, rotation time) and the solution properties (viscosity, density, drying rate). Typically, the rotation time is set as such, that it is just long enough to give a dry film. For many organic semiconductors the film drying can have a major influence on the film morphology and thus on performance, therefore this process should be considered carefully. Many materials profit from a slower drying due to crystallization and self-assembly processes that happen during drying. The drying time depends foremost on the volatility of the solvent and the loading with solids, but also the rotation speed. Therefore solvent choice can be very critical for certain polymers. Water, Ethanol and IPA solutions only need about 30 s to dry, a highly concentrated DCB solution can need up to 90 s and more. Also the fume exhaust plays a critical role as during drying the spin coater atmosphere can saturate with solvent and slow down the drying process. Therefore, spin coater ventilation should always be considered when working inside the glove box as the ventilation holes can be covered up.

For a given the solution the film thickness is primarily set by the rotation speed: faster spinning results in thinner layers. The films thickness is proportional to the inverse square root of the rotational speed ω: $t \propto 1/\sqrt{\omega}$ as shown in Fig. 3.4. This results in large differences in thickness at low rotation speeds and diminishing influence on the film thickness at high rotation speeds [109]. Generally faster spinning results in

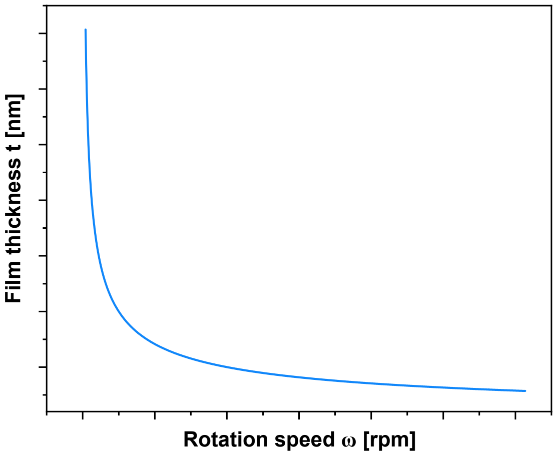

Figure 3.4: *The film thickness of spin coated films follows a* $1/\sqrt{\omega}$ *relation, which means large differences at low rotation speeds and diminishing changes for high ones.*

more homogeneous films, so if possible speeds below 1000 revolutions per minute (rpm) should be avoided.

Spin coating is very susceptible to contamination on the substrate as they will shadow the radial material flow creating typical defects of uncovered streaks called *comets*. Therefore the thorough cleaning described above and the use of well dissolved solutions is critical. Difficult solutions should be filtered before use, sometimes even twice. RC (regenerated cellulose) filters are used for aqueous solutions, PTFE (Polytetrafluoroethylene) ones for organic solvents.

After spin coating typically follows an annealing step, where the film is heated on a hotplate for about 10 minutes. This has two parts: firstly this makes sure there is no residual solvent left inside the film. Secondly for some materials this heating step can have crucial influence on the film morphology and as such should be taken in careful consideration.

Spin coating also does have some disadvantages: about 90% of the deposited material is thrown of the sample and thus wasted. There are some edge effects, that lead to film non-uniformities on the substrate edges. Unlike many spaying and printing techniques, spin coating cannot be structured and will always cover the whole substrate surface. And finally, spin coating is not really scalable, as it is not suitable for larger substrates and as a batch process it is not roll-to-roll compatible. However, despite its limitations it is still a very convenient methods to get very high quality thin films and thus the most widely employed deposition technique for lab-scale research in organic electronics. A good introduction to the topic can be found on the Ossila website [110].

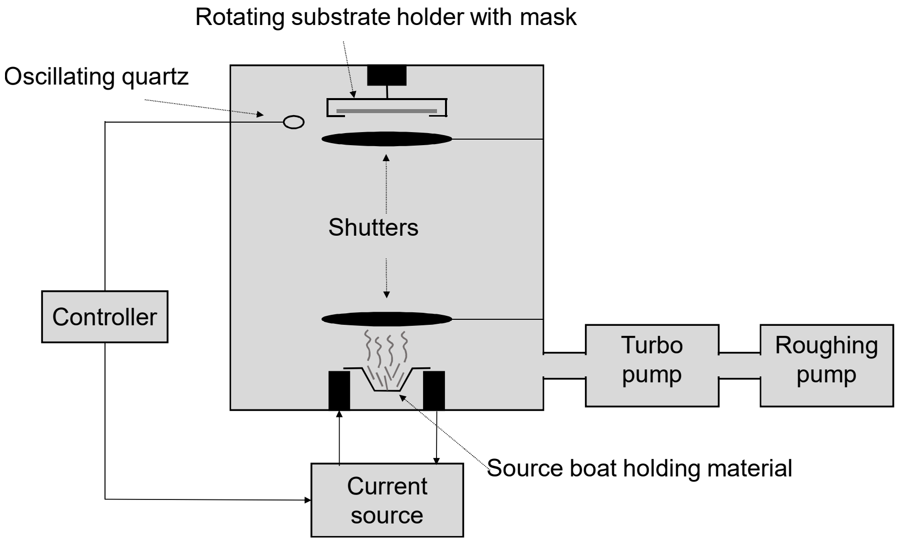

Figure 3.5: *Schematic of PVD system for resistive thermal evaporation. A high current heats up the boat and evaporates the material it holds. The metal vapor then rises and condenses at the substrates, which is held by a shadow mask. An oscillating quartz crystal monitors the deposition rate and film thickness. Mechanical shutters control start and end of the deposition. A high vacuum prevents contamination and scattering of the evaporated material.*

Resistive thermal evaporation

The thin metal films used for the electrodes are deposited by resistive thermal evaporation (RTE). The working principle is depicted in Fig. 3.5. RTE is a physical vapour deposition (PVD) technique using a high current to heat a so called boat, a container holding the material for deposition. The boat is usually made from tungsten or molybdenum, which both have very high melting points. RTE is one of the most common methods to deposit metal layers and offers very high resolution for thickness control (< 1 nm) and deposition rate (< 1 Å/s). Thickness and deposition rate are monitored with a quartz crystal that changes its eigenfrequency when covered with evaporated material.

To ensure the evaporated particles can move freely to the samples without scattering and avoid contamination, the process is done under high vacuum ($p < 10^{-5}$ mbar). This constitues one of the main disadvantages of this method as vacuum euipment is expensive and preparing the vacuum takes a lot of time. Also due to the the vacuum this process is inherently a batch process, not compatabile with roll-to-roll farbication.

The samples are positioned facedown above the boat, where the metal vapour condenses on their surface. To counter act inhomogeneities in the process, the substrate is rotated during the whole time.

To define the electrode structure, the samples are put into a metallic shadow mask, which

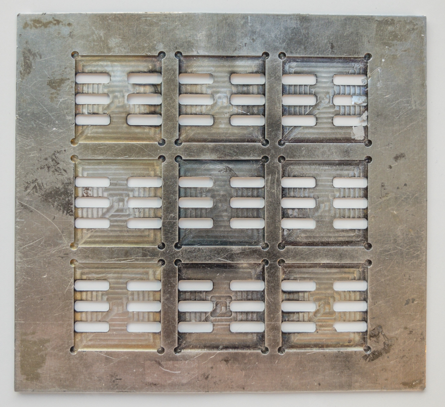

Figure 3.6: *Shadow mask used for the evaporated top electrodes. Each sample is covered with six fingers, which have a width of 3 mm.*

only leaves the desired areas free. The six finger structure used in this work was shown in Fig. 3.2, the corresponding mask (Fig. 3.6) can take up to nine samples at a time.

Since the metal layer is deposited right on top of the active organic layer, this is a critical step. Therefore the deposition rates are kept low in the beginning of the process, so that the impinging metal atoms have limited kinetic energy. Typically the first 20 nm deposited are evaporated very slow, since those metal particles come in direct contact with the organic layer; rates between 0.1 and 0.5 Å/s are used. Once a continuous metal layer is evaporated the rate can be increased to values between 1 and 5 Å/s.

In this work an Univex 350 evaporation system with two boats (Oerlikon Leybold Vacuum GmbH, Switzerland) was used.

Encapsulation

After the evaporation the devices are fully functional. However, to protect the organic materials from the oxygen and water in our atmosphere, a protective encapsulation is applied. This is especially important for LEDs as they are driven at high power input, get hot and react more easily. It also protects particles from particles and scratching. A thin microscope cover glass (18 mm × 18 mm × 0.1 mm) is glued on top of the device with a two component epoxy adhesive. After application it is cured by a heat treatment at 80 °C for 10 min. The glass is positioned as such that the active material of all diodes are covered, but the electrodes are left open to contact.

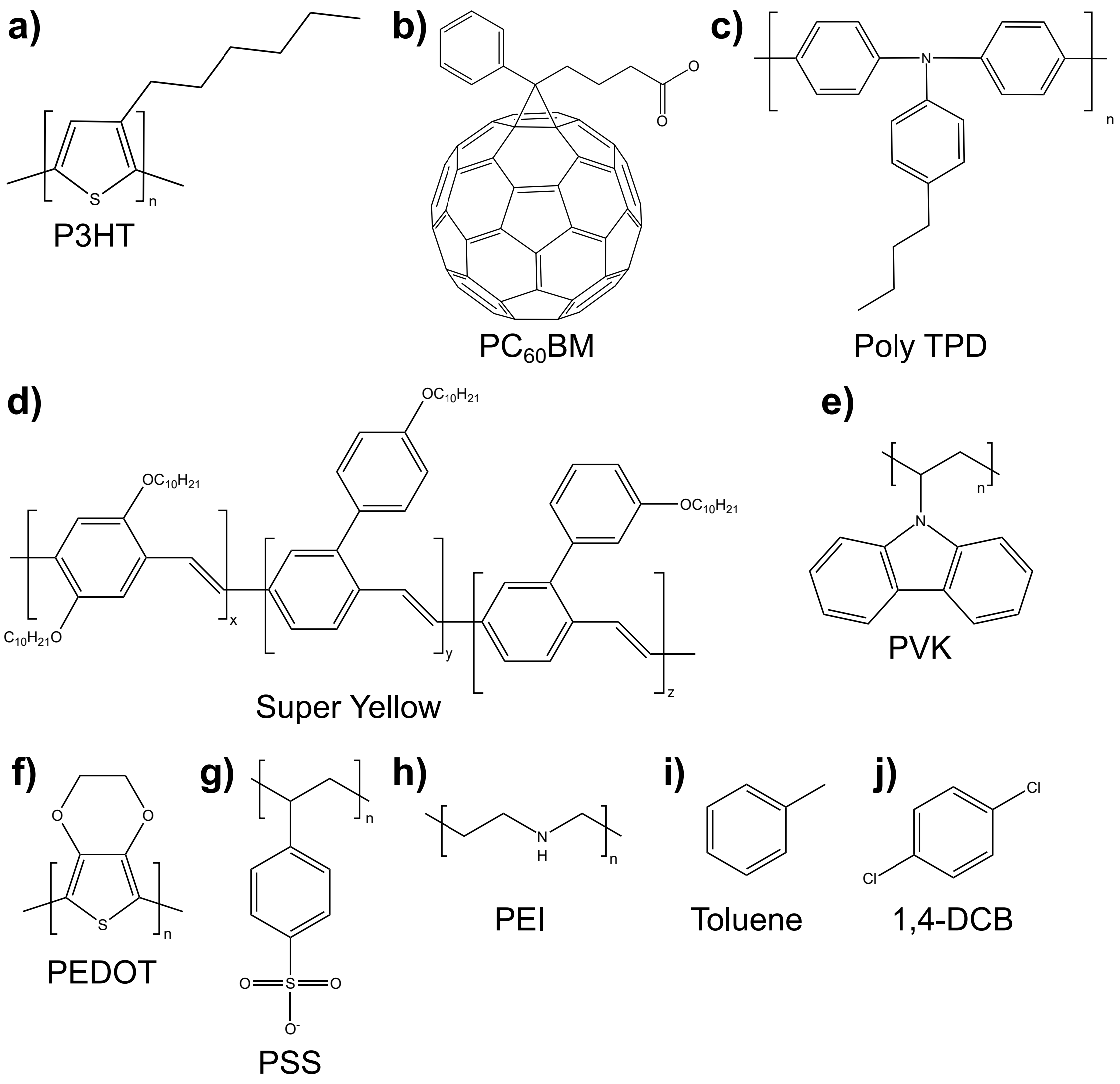

Figure 3.7: *Structural formulas of organic materials used in this work.*

3.3 Materials

This section gives an overview of the materials used in this work. We firstly introduce the materials used exclusively in SCs or LEDs, then the interlayers that can be found in both. The structural formulas of all these materials shown in Fig. 3.7. It follows a more detailed introduction on SiNCs.

3.3.1 Light absorbing materials

Organic solar cells use two active materials in a heterojunction for light absorption and exciton dissociation (explained in more detail in sec. 5.1). Such materials need to combine good absorption properties in the wavelength range between about 400 and 900 nm, where the sun has strong emission (see below in Fig. 5.4), and the energetic properties for good charge separation. In particular, electron donor (p-type) and electron acceptor (n-type) with high carrier mobility fro the respective charge type are required. The most studied material combination to date is the model system of poly(3-hexylthiophene-2,5-diyl) (P3HT) as donor and [6,6]-phenyl-C_{61}-butyric acid methyl ester (PCBM) as acceptor. While nowadays there is a variety of higher performing material systems, we stick to P3HT:PCBM to save costs and be able to compare results to the vast existing body of work covering this system.

Poly[3-hexylthiophene-2,5-diyl] (P3HT)

P3HT is a π-conjugated polymer used as electron donator. Its LUMO level lies between -3.0 and -2.9 eV, the HOMO level between -5.0 and -4.8 eV. It is therefore used as hole conductor and with a band gap E_G around 2.0 eV it absorbs light in the visible range.

Polythiophenes emerge from the polymerization of thiophene, a sulfur heterocycle. These heterocycles can be functionalized with a variety of functional groups; in the case of P3HT a hexyl group is added group as side chain of the thiophene ring to render it soluble in common organic solvents (Fig. 3.7 a)). During polymerization these hexyl chains can arrange regularly alternating on head and tail side of the heterocycle (regioregular) or irregularly (regiorandom). Regioregular P3HT has a flatter structure and forms crystals of higher order than regiorandom P3HT, which results in significantly higher carrier mobility [111]. For this work high purity P3HT (# 4002-EE) was provided by Rieke Metals. It is specified with a molecular weight between 50 000 and 70 000 and a regioregularity between 91 and 94 %.

[6,6]-phenyl-C_{61}-butyric acid methyl ester (PCBM)

The Buckminster-fullerene C_{60} consists of 60 carbon atoms, arranged as 12 pentagons and 20 hexagons in the form of a hollow sphere resembling a ball. Similar to polythiophenes C_{60} by itself does not dissolve well in most common organic solvents and is therefore functionalized with a methyl-ester-group resulting in the soluble fullerene derivate PCBM (Fig. 3.7 b)). The PCBM LUMO level lies at -4.0 eV and the HOMO level at -6.1 eV and is used as electron conductor. PCBM only absorbs in the UV-range and thus contributes very little to the total light absorption in solar cells. However, a C_{60} molecule can absorb up to six electrons, which makes it an outstanding electron acceptor. The

PCBM for this work was provided by Solenne B.V. with a molecular weight of 910.9 g/mol and a purity of 99.5 %.

3.3.2 Light emitting materials

Super Yellow

Super Yellow (SY) - also known as PDY-132 - is a commercial polymer specifically engineered for application in organic electronics, highly luminescent, emitting yellow-green light. It is a poly[p-phenylene vinylene] (PPV) based copolymer made from three different monomers in a ratio x:y:z = 1:12:12 as shown in Fig. 3.7 d). SY is quite undemanding, dissolves very quickly in toluene, needs no post-treatments and shines very brightly in a simple device stack, without the need for additional interlayers. The SY used in this work was provided as a complimentary sample by Merck (formerly Covion).

Poly[N,N'-bis-4-butylphenyl-N,N'-bisphenyl]benzidine (PolyTPD)

PolyTPD is a blue emitting conjugated polymer from the group of poly[triarylamines] as shown in Fig. 3.7 c). It is not a particular effective emitter and mostly used as transport layer. In that case, the blue emission is more of an unwanted side effect. PolyTPD has its LUMO level at -2.4 eV and the HOMO level at -5.5 eV. The deep HOMO level in combination with a hole mobility of $\mu_\mathrm{h} = 2.1 \times 10^{-3}$ cm^2/Vs [112] are ideal for hole injection LEDs, especially into QDs that typically have deep valence bands [113]. The low LUMO energy also makes it a good electron blocker for example in perovskite solar cells [114]. PolyTPD easily dissolves in common organic solvents, we typically used 5 mg/ml in DCB. The PolyTPD used in this work was provided by Solaris Chem Inc. (Canada) with a typical molecular weight of $M_\mathrm{w} = 80 - 150$ kDa.

Poly[9-vinylcarbazole] (PVK)

PVK has properties similar to PolyTPD. It is also a blue emitting, conjugated polymer that is not so much used for its luminescence but its interesting energy levels. With a LUMO level at -2.2 eV and the HOMO level at -5.8 eV, it has even better hole injection and electron blocking properties, but with a lower hole mobility of $\mu_\mathrm{h} = 2.5 \times 10^{-6}$ cm^2/Vs [115]. It is most famous for its use a host material for organometallic complex in Phosphorescent OLEDS (PHOLEDS), but has also been used for blocking layers in perovskite solar cells [116] and QLEDs [117]. The PVK used in this work was was purchased from Sigma-Aldrich with an average molecular weight of M_w ~1100 kDa and was typically prepared with 1 wt.-% in DCB.

3.3.3 Interlayers

Poly[3,4-ethylenedioxythiophene]:poly[styrenesulfonate] (PEDOT:PSS)

PEDOT:PSS is one of the most successful and most commonly used conductive polymers. It is an acqueous dispersion of the two ionomers PEDOT and PSS (shown in Fig. 3.7 f) and g)). PEDOT is a conjugated polymer that provides charge transport, while PSS is used use as charge balancing counter ion and provides water solubility (it actually forms a stable microdispersion/gel). In thin layers it is highly transparent, which is important for optoelectronic applications. PEDOT:PSS has a HOMO level between -4.8 and -5.2 eV and at around -2.3 EV. The HOMO level can form an ohmic contact with ITO and the low LUMO provides electron blocking properties. PEDOT:PSS can be either a p-type semiconductor used as hole transport layer or can be highly conductive and serve as transparent electrode (thicker films can reach up to 1000 S/cm). This behavior can be tuned by the PSS contents (therefore often loosely referred to as dopant), where a lower amount of PSS leads to higher conductivities, but also to decreased solubility and processability [118]. For highest conductivity any excess PSS has to be washed out with an post deposition treatments [119].

In this work we used three different PEDOT:PSS fomulations from the Clevios line provided by Heraeus. The Al 4083 formulation is the go to material for blocking layers and has a very low conductivity due to a PEDOT:PSS ratio of 1:6. The HTL Solar formulation is also used for blocking layers and is tuned for deposition on top of hydrophobic interface. It is typically used for spin coating on top of P3HT:PCBM, where it gives much better wetting than the Al 4083 variant. The PEDOT:PSS ratio of 1:2.5 results in higher conductivity and solar cells with HTL solar should be characterized with a shadow mask. The PH 1000 formulation is optimized for highly conductive layers and has a PEDOT:PSS ratio of 1:2.5. To further increase the conductivity, 5 wt.-% of either ethylene glycol (EG) or dimethyl sulfoxide (DMSO) is added to the water based solution. If necessary, all formulations can be diluted with isopropanol (IPA) to reach thinner film thickness and improve the wetting properties.

Poly[ethylenimin] (PEI)

PEI is a non-conjugated polymer and as such a large band-gap insulator. It is therefore not considered as blocking or transfer layer, but as a surface modifier and has to be applied in ultrathin layers not thicker than 10 nm. In 2012 Zhou et al. could show that such a thin layer could universally lower the work function of a large variety of underlying materials by about 1 eV [120]. This effect is based on the induction of a permanent dipole at the conductor surface. As such PEI is a very useful tool to enable new device architectures based on existing materials. Particularly interesting is the possibility to lower the work function of ITO, which is the most commonly used bottom electrode. This turns it from an anode into a cathode and lead to a lot of new studies on inverted devices [121–124] . PEI can be processed in air and was dissolved in either ethanol or methanol. To reach the necessary low layer thickness it was typically used in a concentration of 0.1 wt.-%. Since PEI is very viscous exact preparation of such a low concentration can be difficult, which can be alleviated by the use of a 1 wt-% stock solution that can be further diluted as necessary. Alternatively the less viscous PEIE (poly[ethylenimine] ethoxylated) variant can be used.

3.3.4 Metal oxides

Metal oxides with wide band gap have become an attractive alternative to organic blocking layers. Being oxides they are immune to oxidization and thus show very good stability. Furthermore, they are highly transparent. can often be processed from solution and ss inorganic crystals, they can feature high charge mobility. Commonly used oxides for hole transport are nickel (NiO), molybdenum (MoO_3), vanadium (V_2O_5) and tungsten (WO_3), for electron transport there are titanium (TiO_2) and zinc (ZnO) [125–127].

In this work we used ZnO and MoO_3. ZnO were used as colloidal nanoparticles that can be spin coated. There are two different formulations: ZnO NP in IPA (5.6 % w/v) provided by infinityPV (Denmark) and al-doped ZnO (AZO) NP in IPA (2.5 wt.-%) provided by Nanograde (Switzerland) and bought from Sigma-Aldrich. Both have comparable properties and can be further diluted with IPA depending on the required film thickness. They were routinely annealing at 140 °C, but it not necessary for proper functionality of the layer. Elemental MoO_3 powder was bought from Sigma-Aldrich and evaporated in a PVD process.

Another important metal oxide is indium tin oxide (ITO). In consists of indium oxide (In_2O_3) doped with about 10 % tin oxide (SnO_2). It then becomes conductive and is therefore not used as blocking layer, but as highly transparent electrode. ITO is the most widely used transparent conductive electrode (TCO) material in research as well as industrial applications. Generally, ITO is not solution processable and is deposited by sputter coating with a post annealing at around 400 °C. The ITO used in this work was bought prestructured on glass substrates (see Fig. 3.2) from Xinyan Technology (Hongkong). The films have typical sheet resistance of 16 Ω/sq. and a transparency of 90 % at 550 nm (see Fig. 6.4).

3.3.5 Silicon Nanocrystals

There are several characteristics of semiconductor nanoparticles that have influence on their optical and electronic properties such as size, size distribution, shape, crystal structure and surface chemistry. All of these are influenced by the way the particles are prepared. An ideal fabrication method should address all of these characteristics while also producing substantial quantities from readily available, low cost, non-hazardous materials [128].

Overview

There is a variety of **synthesis** techniques with different advantages and disadvantages, which can broadly be divided in three categories [66]: firstly, fully solution-based, bottom-up approaches, which are based on self-assembly of precursor materials. Common methods for this appraoch are based on reducing silane precursors [129] or silicon Zintl salts [130]. Being solution based, they can typically be done with fundamental chemical lab equipment, scale quite well and yield good amount of products. However, not all particles sizes can be produced with these methods and they often show wide size distributions. So far only blue emitting particles have been produced, often with limited quantum yield, probably due to chemical nitrogen and oxygen impurities from the solution process [131].

Secondly, more physical, top-down approaches that break down bulk silicon into small nanoscale pieces. Widely used examples for this approach are etching of bulk silicon [132, 133] and breaking down silicon-rich oxides, typically SiNC grown inside a SiO_x matrix [134, 135]. Top-down approaches generally give better control over the particle size and smaller size distributions, but employ harsh processing conditions and do not scale very well, giving only small amount of products.

Thirdly, there is silane precursor decomposition by plasma or heat. Different methods are the preparation in supercritical fluids [136] as well as by plasma [71, 137] or laser pyrolysis [138, 139]. These methods provide good control over particle size and can deliver particles with high quantum yield, but often require very high temperatures and expensive, specialized equipment. For a more in-depth treatment of the different synthesis methods, there are several good overviews in the literature [66, 128, 140].

The particle synthesis is followed by **surface modification**. Functional organic groups (ligands) are grafted onto the particles surface to render the particles stable in solution and prevent surface oxidization. This process is called surface functionalization. It can also be referred to as surface passivation, to emphasize the saturation of surface states. For SiNC this is especially critical since on the one hand silicon very readily reacts with oxygen in the presence of air or water (synthesis has to be done under inert atmosphere) and SiO is electrically insulating.Additionally the SiNC surface has a strong impact to their luminescence properties and performance [141]. This is different for compound semiconductor QDs with core-shell design, where the shell materials already protects the core's surface. The SiNC surface can be functionalized with ligands,

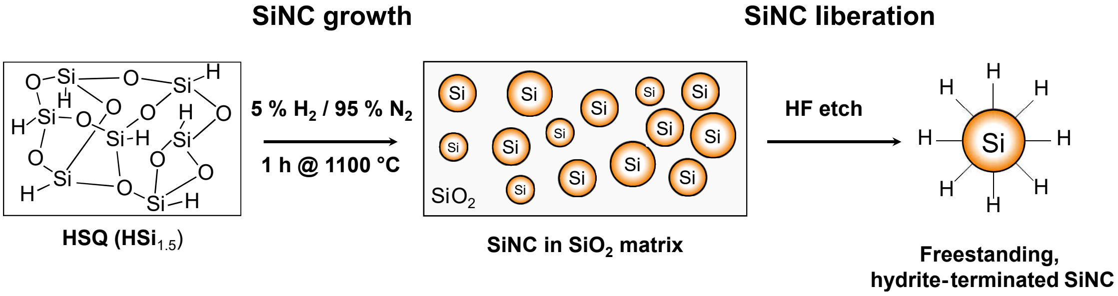

Figure 3.8: *SiNC synthesis by thermolysis of hydrogen silsesquioxane (HSQ). Heating the HSQ under reducing atmosphere leads to SiNC growth within a* SiO_2*-matrix. By etching the* SiO_2 *with HF acid, the SiNC are liberated from the matrix and free-standing, hydrite-terminated SiNC remain (adopted from ref. [143]).*

whose different size and electronic properties can impact particle and film formation properties [101]. But also different functionalization routes (using the same ligands) can influence performance due to different bonding mechanisms, surface coverage and chain length (ligand oligomerization). Probably the most common functionalization method is hydrosilylation of hydrite-terminated SiNC. A ligand with a double or triple bond forms a covalent Si-C bond through addition reaction with the Si-H surface group [141]. The hydrosilylation can be induced by many different initiators, e.g., thermally, by UV irradiation, radical initiators or Lewis acids. For an overview of the different functionalization routes refer to the literature [107, 142, 143].

Fabrication

All SiNC used in this work were provided by Arzu Angı from Bernhard Rieger's WACKER-Chair of Macromolecular Chemistry as part of the Alberta/Technical University of Munich International Graduate School for Hybrid Functional Materials (ATUMS) collaboration network.

The SiNC were **synthesized** via thermolysis of hydrogen silsesquioxane (HSQ), a method introduced by Veinot et al. in 2006 [134] and thoroughly reviewed in 2017 [143]. The process is illustrated in Fig. 3.8. HSQ is a commercially available silicon rich oxide (SRO) in the form of $HSiO_{1.5}$. It is derived from a sol-gel process and commonly used as an electron-beam resist or as spin-on dielectric. Since it only contains Si, O and H there is minimal possibility of introducing impurities. The white powder is heated in a quartz tube furnace under reducing atmosphere of 5 % H and 95 % N_2 or Ar. The Si atoms subsequently diffuse and cluster, which yields SiNC embedded in a SiO_2 matrix. The SiNC size is conveniently tuned by the maximum processing temperature and/or time. 1100 °C results in a diameter of about 3 nm. In a second high temperature step the particles can be grown larger to sizes between 6 nm (1200 °C) and 9 nm (1300 °C). After

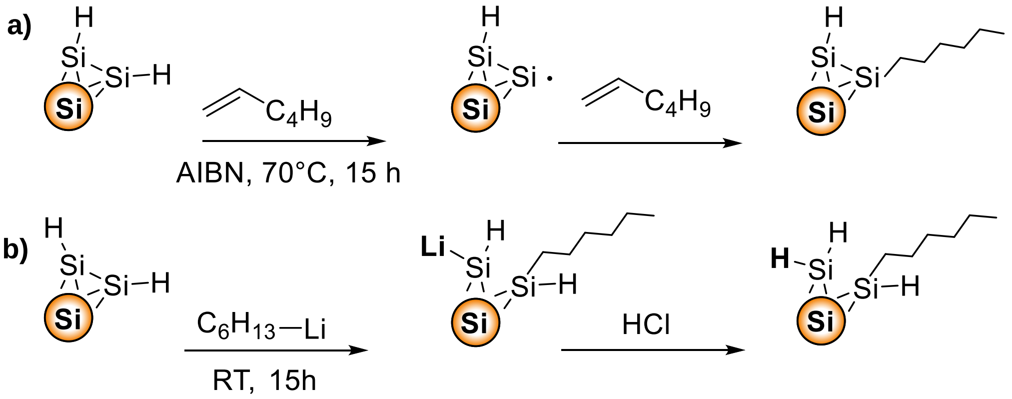

Figure 3.9: *SiNC surface functionalization with hexyl groups by a) hydrosilylation (initiated by radical initiator AIBN) and b) use of organolithium reagents (adapted from ref. [144] with permission from The Royal Society of Chemistry.).*

this heating process the white powder turns brown. In the next step the particles are liberated from their SiO_2 matrix by etching with hydrofluoric acid (HF) solution that preferentially etches away the SiO_2. Finally, the free-standing, hydrate-terminated SiNC are extracted into an organic solvent and isolated by centrifugation.

After the synthesis follows the **surface functionalization**. The particles in this work have been functionalized by two different methods. Either by *hydrosilylation (HS)* reaction, the most commonly used method for functionalization of hydride-terminated SiNC, or the relatively new method of using *organolithium reagents (OLR)*. The two mechanisms are illustrated in Fig. 3.9. For both methods SiNC solution together with the desired ligands and possible initators are stirred together under argon atmosphere for 15 h. HS can be induced by different methods, the simplest being heating the solution at around 150 °C [145]. This method was used for functionalization with dodecene. However, not all surface groups can stand such elevated temperatures and for functionalization with hexyl chains hydrosilylation was initiaded via the radical initiator azobisisobutyronitrile (AIBN) which allows lower temperatures of 75 °C [146].

The use of organolithium reagents is based on a mechanism in which surface Si–Si bonds cleave due to an attack of the organolithium reagent, yielding Si-R bonds and neighboring Si–Li surface species. After an additional acid workup, the Si–Li groups are quenched to yield surface Si–H species [147]. The organilithium reaction can be done at room temperature and allows to bind aryl- or alkinyl-groups directly to the SiNCs surface, which is not possible with HS. Such groups with conjugated π-systems offer the possibility of improved charge transfer from or to the SiNC [147]. The influence of the two functionalization methods on the SiNC surface and the corresponding impact on the device performance is investigated in Chapter 4.5.3. Eventually, the particles are purified by several centrifugation and decanting steps and a final filtration with a PTFE filter.

3.4 Characterization techniques

3.4.1 Profilometer

Film thicknesses in this work were measured with Dektak XT stylus profilometer by Bruker (USA). A stylus porfilometer is physically moving a probing stylus along the surface and uses a feedback loop to maintain a constant force. From the necessary corrections of this feedback loop the surface height along the scan line can be computed. To measure a films thickness it spin coated on a separate glass substrate and scratched with a scalpel; the scalpel should be kept flat (use whole blade, not just the tip) and not be tilted vertically. Applying too much force will scratch the underlying substrate (even glass), too little force does not give a clean cut. Then the profilometer stylus can scan across the scratch and the thickness can be extracted from the resulting profile. Adjacent to the scratch there can be some material overthrow that should not be used to determine the profile height; therefore, the profile should have a length of at least 80 – 100 µm. Data leveling was used to compensate for tilt of the sample.

3.4.2 Atomic force microscopy (AFM)

Atomic force microscopy (AFM) uses a cantilever with a tip that is scanned over the sample surface and produces a three dimensional image of the surface topography. The cantilever is excited at its resonant frequency and oscillates close to the sample surface at a fixed amplitude. During the scan, a variety of (atomic) forces interact with the tip and in turn change its oscillating amplitude. A feedback loop compensates for this change by constantly controlling the tip-to-sample distance and the required corrections are computed into surface height information.

The cantilever is made from high purity silicon and the tip has a radius of 7 nm. Typical resonance frequencies lie in the range between 10 kHz and 1 MHz. To detect the oscillation of the cantilever, its movement is traced by a laser beam deflected from the cantilever back side onto a photo detector. Due to this measurement principle AFM does not require conductive samples, an advantage of electron beam based microscopy. AFM provides a vertical resolution in the nanometer range and z-resolution below 1 nm and can scan areas of several μm^2. The AFM images presented in this work were taken with a Jeol JSPM-5200 in tapping mode and processed with the Gwyddion software.

3.4.3 Scanning electron microscopy (SEM)

Scanning electron microscopy (SEM) is based on a beam of accelerated electrons scanning over the surface of a sample. Those primary electrons (PE) are emitted from a tungsten filament and accelerated by electric potentials in the kV-regime. When they hit the sample, their interaction with the surface material leads to the emission of secondary electrons (SE). Those SE are accelerated towards a detector, which then can construct an image of the surface.

Resolution of optical microscopy is limited by the Abbe diffraction limit which is directly proportional to the wavelength of the light source used for illumination: $d_{\mathrm{Abbe}} \sim \lambda/2$. For visible light this results in a diffraction limit in the order of 200 - 300 nm. Electrons have a wavelength in the order of 10 pm and therefore SEM greatly surpasses the resolution of optical microscopes. SEM is limited by other factors such as spherical aberration and reaches resolutions around 1 nm. However, it is limited to conductive samples, as non-conductive ones will charge up under the electron impact and then distort the incoming beam. This limitation can be overcome by sputter coating a thin metal layer, typically a few nm of Au, on top of the non-conductive sample.

In this work, we used a field emission scanning electron microscope (FESEM), the NVision 40 by Carl Zeiss (Germany). The extractor voltage was a constant 5 kV for all measurements. For both devices, an acceleration voltage of 0.5 to 2 kV was used for non conductive and polymer samples, whereas a voltage of 5 to 7 kV was used for conductive specimen. The aperture size for both devices was 30 µm and the working distance at around 7 mm.

3.4.4 Sheet resistance measurement

Sheet resistance is used to compare the electrical resistance of thin films independent of their size. It is measured with the van der Pauw method using a four-point probe head with separated sourcing and sensing pairs. Compared to a two-probe measurement this method allows to remove contact and wiring resistances from the measurement, which can be in the same order of magnitude as the resistance in such thin films and would therefore severely distort the measurement. For this work we used a probe head from Jandel and a Keysight B2901A source measuring unit (SMU).

3.4.5 Transmission spectroscopy (UV-VIS)

UV-Vis spectroscopy is used to investigate the light transmission of a film at different wavelength.

In this work we used a broadband xenon lamp (Ushio 150W) as white light source. The white light is then passed through a chopper wheel that modulates the light at a set chopping frequency. It is then spectrally dispersed by a monochromator (Oriel Cornerstone 260 1/4 m by Newport (USA)). Such a so-called Czerny-Turner monochromator collimates incoming light with a curved mirror onto a diffraction grating. Here it undergoes a wavelength-dependent deflection onto another mirror, which focusses the dispersed light onto the output slit. This monochromatic light is used to shine through the sample onto a detector, which are put into a dark box to avoid interference from ambient lighting. As a reference measurement, the photoresponse of the silicon detector (DET-L-SIUV-R-C by Newport) is measured with a blank glass substrate. The resulting photocurrent is converted into a voltage signal and amplified by a lock-in amplifier that operates at the chopping frequency (Merlin Digital Lock-in Radiometry System). With a band gap of $E_{\mathrm{Si}} = 1.12\,\mathrm{eV}$ the silicon detector can detect light between 300 and 1100 nm, exceeding most polymers' absorption range. After the reference measurement, the blank glass is replaced with the actual sample and the detectors response is compared to the reference measurement. The response ratio $R_{\mathrm{sample}}/R_{\mathrm{ref}}$ then reveals how much light the sample absorbed at a given wavelength. The whole setup is controlled via the TracQ software by Newport that is also used for data acquisition and processing.

For a more intuitive presentation of the data, we often prefer to show absorption curves instead of transmission curves. They are calculated as $A = 100\,\%$ - T, which does not take in consideration potential reflection losses (due to $T = A$ - R) and therefore cannot be presented with absolute values, but are given in arbitrary units.

The setup can also be used to measure the external quantum efficiency (EQE) of a solar cell as described in Chapter 5.2. For this, instead of comparing the response of one detector to different samples, we compare the response of two detectors to the same light input. First the irradiance of the generated light is calibrated with the reference diode, which has a known responsitvity. After this calibration, the silicon detector is replaced by the solar cell under test, carefully making sure it is positioned at the same distance and height as the detector. Now input power and flux of the light are known for each wavelength and can be compared to the generated photo current to calculate the EQE. Since the reference detector has a larger area than the solar cells ($1\,\mathrm{cm}^2$ vs. $9\,\mathrm{mm}^2$) the resulting EQE value has to be scaled by the area ratio $A_{\mathrm{SC}}/A_{\mathrm{Ref}} = 100/9 = 11.1$ to compensate for that mismatch.

4 Silicon nanocrystal light emitting devices

In this chapter we use surface functionalized SiNC as light emitter in hybrid QLEDs (SiNC-LEDs). We investigated the impact of different surface functionalization methods and different surface groups on the LED performance. After a brief motivation, the working principle and the characterization of LEDs are described. It follows a summary of the current state of the art, before we present and discuss our experimental results, which are then briefly summarized in the conclusion.

4.1 Motivation

It is a longstanding dream of the semiconductor industry to use their core material - silicon - for optical applications and integrate optical data transmission with existing data storage and processing devices all in one silicon-based process. Unfortunately, silicon has an indirect band gap and as such constitutes a very poor light emitter. At the nano scale however, when Si particles become smaller than the Bohr radius of bulk silicon (5 nm), such SiNC develop a quasi-direct band gap and show strong luminescence. Especially colloidal SiNC that can be processed from solution are interesting candidates for application in LEDs. Such QLEDs bring with them all the advantages of OLEDs like thin, light and flexible devices, that can be processed on large areas and with simple printing methods. At the same time they can possibly overcome efficiency hurdles of OLEDs as inorganic nanoparticles are not bound to the spin statistics that limit OLED efficiency to 25 % (only singlet states can be converted into photons). Furthermore, the optical and electronic properties of colloidal SiNC can be tuned by particle size and surface treatment and functionalization. Silicon's abundance and low toxicity are particularly appealing in comparison to II–VI and IV–VI quantum dots based on Cd or Pb (e.g., CdSe, PbS) commonly employed in opto-electronic devices.

4.2 Working principle

QLEDs work very similar to OLEDs, they just use a different emitter layer. The basic device structure consist of an anode, the emitting QD layer and a cathode. This structure

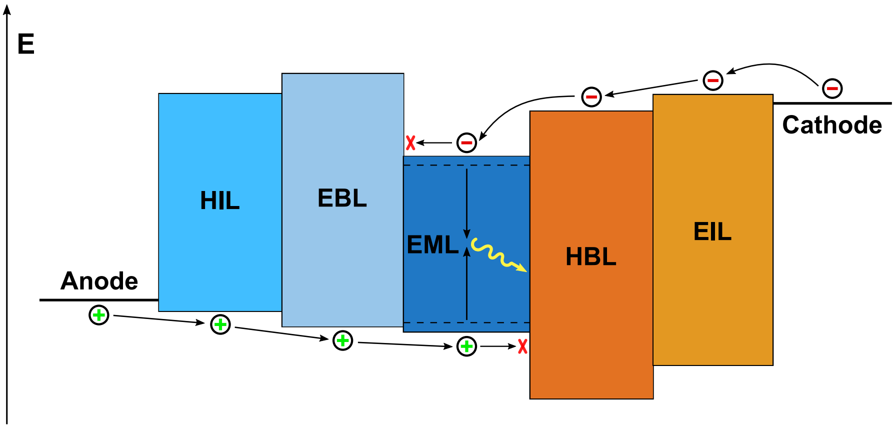

Figure 4.1: *Working principle of QLEDs. Injection layers lower the potential barrier between electrode and emitting material. Blocking layers confine charges within the emitting layer (EML), which reduces leakage currents and increases the chance for radiative recombination. Under forward bias holes are injected at the anode and travel through the hole injection layer (HIL) and the electron blocking layer (EBL) into the EML. Electrons are injected from the cathode and travel through an electron injection layer (EIL) and a hole blocking layer (HBL) until they are injected into the EML. In the EML the opposite charges form an exciton, which eventually can recombine radiatively.*

can be extended with additional interlayers for charge injection and blocking, sometimes summarized as charge transport layers (CTLs).

Injection layers are there to lower the potential barrier between electrode and emissive layer (EML). A hole injection layer (HIL) should then have a HOMO/VB level between the work function of the anode and the VB of the emitting QDs. The injection barrier between anode and EML is then lowered by the potential difference of the anode work function and the HIL HOMO level.

The blocking layers' task is to confine charges into the EML. This prevents leakage currents and increases the chance for radiative recombination. Electron blocking layers (EBLs) should have a high LUMO/CB level that lies above the CB of the emitter material and a HOMO/VB level that fits to the neighboring layers; hole blocking layers (HBL) accordingly should have a low HOMO/VB level underneath the VB of the emitter. All interlayers should have high mobilities for their respective charges to avoid unnecessary voltage drops.

OLEDs based on evaporated small molecules can be designed with very elaborate stacks with more than ten different functional layers. This way an energetic cascade can minimize the potential barriers at every interface and the charge balance can be carefully tuned to assure electrons and holes are injected at the same rate. In solution-processed QLEDs it is very difficult to deposited so many layers on top of another. Therefore, here injection and blocking layers are often consolidated into one.

Based on those interlayers, QLEDs are sometimes categorized into four different groups, enumerated after their historic introduction: type I QLEDs only have one polymer CTL at the bottom, type II have organic top and bottom CTLs enabled by using evaporated small molecules. Type III uses inorganic CTLs and type IV combines an organic CTL at the bottom with a inorganic one at the top. Type IV hybrid devices recently have gathered the most attention and so far show the highest efficiency values [10].

The working mechanism of QLEDs then goes as follows: under forward bias electrons and holes are injected at anode and cathodes into the charge transport layers, the charges travel through the transport layer until they are injected into the emitting QDs, where they form excitons and eventually recombination under the emission of a photon.

4.3 LED characterization

An LED converts current into light. To assess their performance we need to measure the electrical input and the resulting optical output. The electrical characterization is relatively straight forward. An LED is driven in forward bias and shows the typical diode behavior of a low saturation current until the threshold or turn-on voltage is reached and current starts to rise exponentially. In this regime a lot charge carriers are injected into the device that can be converted into light. For the I-V-characterization the device under test is connected to a SourceMeter (Keithley 2602A) and a voltage sweep is applied. For every applied voltage, the current through the device is measured, typically in the voltage range from 0 to between 10 and 15 V. At some point the device becomes too hot and breaks down. This depends on the internal resistance of the diode and the associated power input and varies with device architecture. Therefore this breakdown point should be determined for the first device of a certain sample/architecture and following devices should only be measured in a safe range. From the I-V-characterization resistance, turn-on voltage and power consumption can be extracted.

Photometric luminance measurement

For the optical characterization we have to consider that the light from LEDs used for lighting or display applications undergo human perception through our eyes. The human eye can only perceive electromagnetic waves with wavelengths in the range from 380 to 700 nm, thus called visible light. Furthermore, the eye is not equally sensitive to all wavelength and the perceived brightness depends on the color of the light. The spectral response of the eye is described by the luminous efficiency function depicted in Fig. 4.2. This function is standardized by the International Commission on Illumination (abbr. CIE, French for Commission Internationale de l'Éclairage). The eye has two different kinds

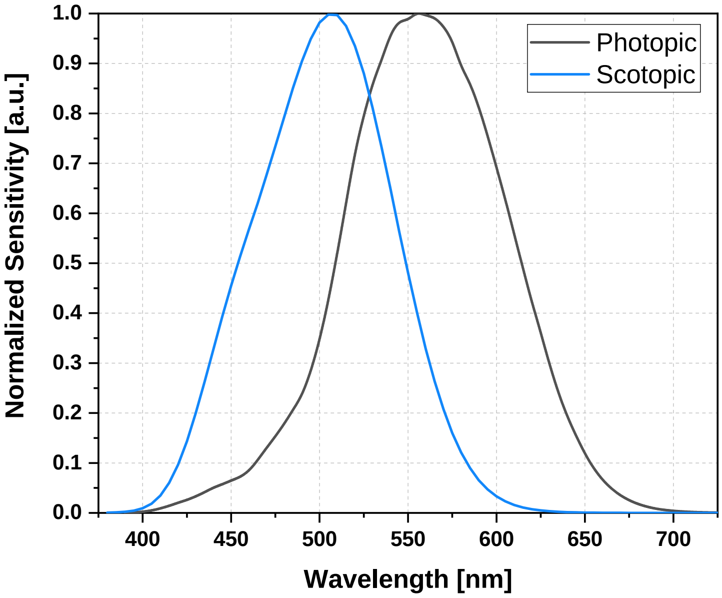

Figure 4.2: *The luminous efficiency function describes the sensitivity of the human eye at different wavelengths. There is $V(\lambda)$ for day light vision (photopic) and $V'(\lambda)$ for low light vision (scotopic). In day light the highest sensitvity is in the green while there is a sharp decline for blue and red light [148].*

of photoreceptors, so called cones for high light levels and rods for low light levels. Therefore, there are two curves: $V(\lambda)$ for day light (photopic) vision and $V'(\lambda)$ for low light (scotopic) vision. As can be seen, day light vision has a peak in the green at 555 nm and there is a sharp sensitivity decline towards red and blue light. Night vision is shifted about 50 nm to the blue. For lighting technology optical values are mostly given in *photometric* units, which correspond to the common *radiometric* units but applied with the photopic luminous efficiency function. As such interpretation or conversion of photometric units requires spectral information in addition to the absolute power value. Table 4.1 shows an overview of common radiometric units and their photometric counterparts. They represent flux Φ, flux per unit area E, flux per unit solid angle I and flux per unit area per unit solid angle L. Radiometric quantities are denoted with index e for energetic, photometric quantities with v for visual The most important characteristic for planar emitters like OLEDs is the luminance L_v as it correlates the most to how humans perceive the brightness of luminous areas. In this work the luminance was measured with the *MAVO-SPOT 2* luminance meter from Gossen (Fig. 4.3 a)). It contains a silicon photodiode in combination with a filter system emulating the luminous efficiency function. The sample is held by a clamp on an optical table and the luminance meter is put on a tripod so that the optical axis is orthogonal to the sample surface and at a distance of 34 cm above the sample (Fig. 4.3 b)). This is the closest possible distance and requires the use of screw on close-up lens. Since the measurement circle is

Table 4.1: *Overview of radiometric and photometric units that characterize light intensity. While radiometric units describe absolute radiant energy, their photometric equivalents describe brightness as perceived by the human eye. The shown units represent power, power per unit area, power per unit solid angle and power per unit area per unit solid angle.*

Radiometric		
Symbol	Quantity	Unit
Φ_e	Radiant flux	W
E_e	Irradiance	$\mathrm{W/m^2}$
I_e	Radiant intensity	$\mathrm{W/sr}$
L_e	Radiance	$\mathrm{W/m^2 \cdot sr}$
Photometric		
Φ_v	Luminous flux	Lumen (lm) = $\mathrm{cd \cdot sr}$
E_v	Illuminance	Lux (lx) = $\mathrm{cd \cdot sr/m^2}$
I_v	Luminous intensity	Candela (cd) = $\mathrm{lm/sr}$
L_v	Luminance	Nit (nt) = $\mathrm{cd/m^2}$

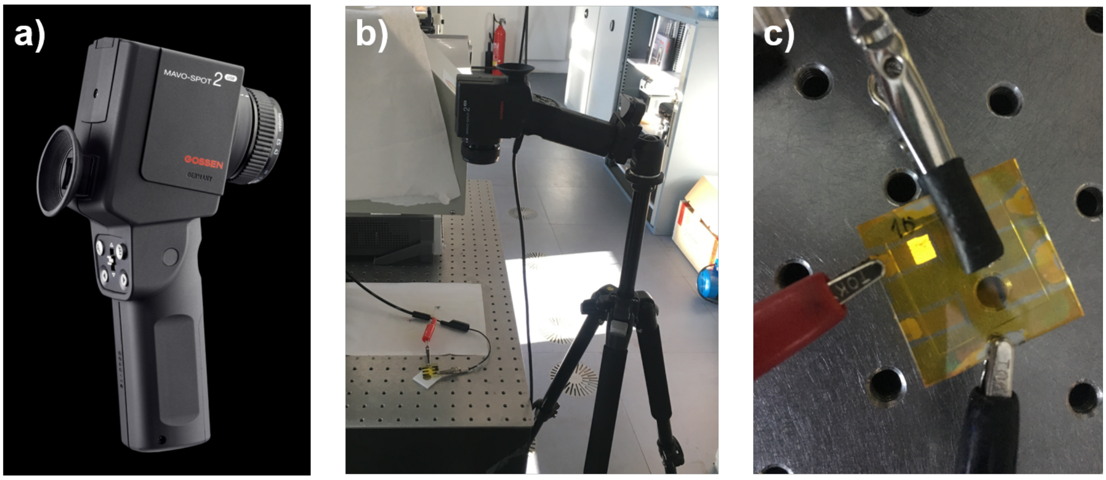

Figure 4.3: *LED measurement setup: a) MAVO-SPOT 2 luminance meter (© 2018 GOSSEN Foto- und Lichtmesstechnik GmbH [149]), b) lab setup with luminance meter on a tripod positioned 34 cm above the sample and c) LED held by clamp during measurement.*

about the same size as the measured devices, the setup has to be aligned very carefully. The luminance meter is connected to a computer via USB and remotely controlled by a LabView program, which also controls the Keithley SMU (source measure unit). Then luminance measurements are taken during the I-V-measurement. Since the luminance measurements are relatively slow, 0.5 V steps are applied instead of finer steps. The typical measured ambience luminance for in our lab lies around 70 cd/m^2, therefore devices that are not significantly brighter than this were characterized in a dark room.

External quantum efficiency

Apart from the absolute brightness we want to know about the efficiency of LEDs. There are several different efficiency values that can be considered. The ratio of luminous flux and input power gives the *power efficiency* in lm/W and a common performance parameter for LEDs. While the luminous flux encompasses all the light generated by the devices for some purposes only the light emitted into a certain direction is relevant. For this the derivative of the luminous flux with respect to solid angle - the luminous intensity in cd - is considered. Divided by the input current we get the *current efficiency* in cd/A. Since this value only considers the current and no voltage, the resistance of the device caused by e.g., injection barriers, are not considered.

When working with photometric units green LEDs will always have higher deficiencies than red or blue ones. In the red at 700 nm the luminous efficiency function has a value of $V(700\,\text{nm}) = 0.004$, in the blue at 450 nm $V(400\,\text{nm}) = 0.065$. So if a red, a blue and a green (555 nm) LED (monochromatic) generate the same radiant flux from the same power, the green one will seem 250 times brighter than red one and 15 times brighter than the blue one with correspond higher power efficiency. To actually assess how well a device converts current into light we turn to the quantum efficiency, which then allows to compare devices emitting at different wavelength. Quantum efficiency for LEDs is defined as the ratio of injected electrons over the emitted photons. This can be separated in internal quantum efficiency (IQE), which takes into consideration all generated photons inside the emitting layer, and external quantum efficiency (EQE), which only counts photons actually leaving the device taking in consideration different loss mechanisms like re-absorption by blocking layers or the electrode and different reflections inside the device. IQE is difficult to measure and EQE the more relevant parameter in real life applications and therefore more commonly used. The number of injected electrons can easily extracted by dividing the current through the device I by the electron charge e. To get the number of emitted photons one needs to know the radiant flux (and photon energy i.e. wavelength) and thus measure all light leaving the device, which is emitting in 180 °. For this the device has to be put in an integrating (Ulbricht) sphere with highly reflective surface, which evenly distributes the emitted light over the sphere's surface. Then the light is extracted and measured through a little opening via

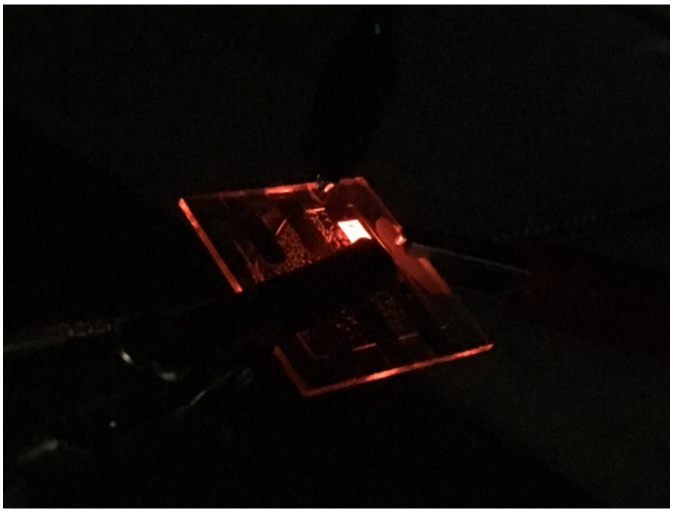

Figure 4.4: *LED sample with light coming out of the edges of the glass substrate. Some light from the LED is emitted under an angle below the critical angle for total inner reflection; this light is then trapped inside the glass, waveguided to the edges and lost for forward emission.*

a fiber connected to a spectrometer. The measured value can then be multiplied with the ratio of the sphere's surface area and the the surface area of the opening. However, since this ratio typically has a value around 1000, the measured signal becomes strongly attenuated. This makes measurements of LEDs with limited light output difficult and places high demand on the employed spectrometer requiring a very low noise floor. Therefore in this work EQE was estimated from the luminance measurements.

EQE calculation

1. We measure **Luminance** L_v [cd/m^2].
2. By multiplication with area A [m^2] we receive the **Luminous intensity** $I_\mathbf{v}$ [cd] = [lm/sr]:
$$I_\text{v} = A \times L_\text{v} \tag{4.1}$$
3. To receive the whole **Luminous flux** $\Phi_\mathbf{v}$ [lm] emitted by the OLED, we need to integrate the luminous intensity over the the solid angle that the device is emitting into, in this case a 180 ° semi-circle. For this we need to know the flux distribution over the solid angle. However, OLEDs are generally assumed to be lambertian emitters with constant flux in all directions. Due to this the integral comes down to a multiplication with π. This neglects that some light is emitted under an angle below the critical angle for total internal reflection and thus is trapped in the glass

substrate (Fig. 4.4), but greatly simplifies the calculation.

$$
\begin{aligned}
\Phi_{\mathrm{v}} &= \int_{0}^{\pi} I_{\mathrm{v}} \, \mathrm{d}\Omega \\
&= \pi \times I_{\mathrm{v}} \\
&= \pi \times A \times L_{\mathrm{v}}
\end{aligned}
\tag{4.2}
$$

4. To now get the **radiant flux** $\Phi_{\mathbf{e}}$ [W] we need to move from photometric to radiometic units. The relationship between radiant and luminous flux is defined with help of the (photopic) luminous efficiency function V(λ) and the conversion factor K_{m} = 683 lm/W:

$$
\Phi_{\mathrm{v}}(\lambda) = K_{\mathrm{m}} \int_{380\,nm}^{780\,nm} \Phi_{\mathrm{e},\lambda}(\lambda) V(\lambda) \, \mathrm{d}\lambda \tag{4.3}
$$

In a second simplification we now assume a narrow emission spectrum for our LEDs and asign all of flux to the (weighted) average wavelength. This way the integral is reduced to a single product and we can solve for Φ_{e}:

$$
\begin{aligned}
\Phi_{\mathrm{e}} &= \frac{1}{K_{\mathrm{m}}} \frac{\Phi_{\mathrm{v}}}{V(\lambda_{\mathrm{average}})} \\
&= \frac{\pi \times A \times L_{\mathrm{v}}}{K_{\mathrm{m}} \times V(\lambda_{\mathrm{average}})}
\end{aligned}
\tag{4.4}
$$

5. The photon energy E_{ph} can be computed from E_{ph} = hc/$\lambda_{\mathrm{average}}$ and everything is in place to calculate the **external quantum efficiency** [%]:

$$
\begin{aligned}
\mathrm{EQE} &= \frac{\#\mathrm{photons}_{\mathrm{out}}}{\#\mathrm{electrons}_{\mathrm{in}}} \\
&= \frac{\text{radiant flux/photon energy}}{\text{injected current/elementary charge}} \\
&= \frac{\Phi_{\mathrm{e}}/E_{\mathrm{ph}}}{I_{\mathrm{in}}/\mathrm{e}} = \frac{\Phi_{\mathrm{e}} \times \mathrm{e}}{I_{\mathrm{in}} \times E_{\mathrm{ph}}} \\
&= \frac{\pi \times A \times L_{\mathrm{v}} \times \mathrm{e} \times \lambda_{\mathrm{average}}}{K_{\mathrm{m}} \times V(\lambda_{peak}) \times I_{\mathrm{in}} \times \mathrm{hc}}
\end{aligned}
\tag{4.5}
$$

This way we can calculate the EQE from a luminance measurement and a spectral measurement. However, we have to keep in mind that the assumed simplifications bring in some insecurities. Furthermore, the conversion from photometric to radiometric is highly sensitive to the chosen wavelength and a few nm difference can already make a large difference in EQE. Depending on the output of the LED and the employed spectrometer, the measurements can be noisy and introduce further inaccuracies. As such the calculated EQE should be treated more like a rough approximation for comparing LEDs with different colors and not as accurate absolute value. It is important to note that EQE in the literature is often derived by several different ways, which are not necessarily completely comparable or accurate.

Spectral characterization

The spectral output of the LEDs fabricated in this work has been characterized with either the Thorlabs CCS200 or the AVANTES AvaSpec-ULS2048x64 TEC-USB2 spectrometer (spectroradiometer). Both are so-called Czerny-Turner spectrometers with a CCD sensor. The light is fed into the device with an optical fiber, where it is then split up into its spectral components: incoming light is entering through the entrance slit, collimated with a curved mirror onto a diffraction grating. Here it undergoes a wavelength-dependent deflection onto another mirror which focusses the light onto the CCD detector. The light is spread across an array of photodiodes, which can detect all wavelength components simultaneously without scanning. The CS200 features a 20 µm entrance slit, the AvaSpec a 100 µm slit. While a larger slit reduces the spectral resolution it also allows more light in and thus boosts the signal reducing noise. Furthermore, the AVANTES spectrometer features a back thinned sensor and is actively cooled, further reducing noise and enabling longer integration times.

4.4 State of the art

While colloidal SiNCs have been been studied very extensively, LEDs based on such SiNCs as emitter are still a niche. Firstly reported in 2010, there have been a lot of improvements since [96–104, 150–154]. A good overview of the topic can be found from Zhao et al. [155].

The first SiNC-LED was reported by Cheng et al. [96]. They use particles made from nonthermal plasma with diameter 5 nm and functionalized with 1-Dodecyl by hydrosilylation. Their device reached a peak EQE of 0.6 %. In their follow-up work one year later, they presented an optimized device featuring a much increased EQE with a peak value of 8.6 %. This very high efficiency is still a standing record today. However, these high efficiency values pertain only in an operating range where the device emitts in the non-visible infrared spectrum. Only at higher current densities does the wavelength of the emitted light shift into the visible region and the EQE falls below 1 %. However, in their work they touch on a lot of important themes that will also be investigated in other works in the following years: SiNC size, thickness of the emitting layer and the influence of different interlayers.

SiNC size

In Cheng's work they compare SiNCs with diameter of 3 and 5 nm. While optical and electrical perfomance are comparable, emission color changes significantly: at 100 mA/cm^2 3nm-SiNC-LEDs have their emission peak around 730 nm, 5 nm-SiNC-LEDs around 810 nm. Such a reduction in the emission wavelength is in agreement with the band gap widening associated with quantum confinement in smaller particles as a larger band gap results in a higher photon energy and thus lower photon wavelength.

As similar effect is observed in the work of Puzzo et al. from the group of Prof. Ozin [99]. They use SiNC with diameter of 3.0 and 3.2 nm synthesized from thermolysis of hydrogen silsesquioxane (HSQ) and functionalized with 1-decene by hydrosilylation. The reduction of the diameter from 3.0 to 3.2 nm shifted the emission peak from 685 to 645 nm. However, they do not present performance of devices with larger particles. Their optimized devices with 3.0 nm SiNC reach a peak EQE of 0.7 % which drops below 0.1 % for higher current densities.

An extensive study on the influence of the particles size was conducted by Maier-Flaig et al. in the group of Prof. Lemmer [150]. They use SiNC with diameter of 1.3, 1.6 and 1.8 nm synthesized from thermolysis of hydrogen silsesquioxane (HSQ) and functionalized with allylbenzene by hydrosilylation. Like in the previous reports the smaller particles exhibit lower emission wavelength, which are the same for photoluminescence (PL) and for electroluminescence (EL): 680 nm (1.8 nm), 650 nm (1.6 nm) and 625 nm (1.3 nm). While the J-V-behavior barely changes, luminance and EQE decrease with the particle size. The 1.6nm-SiNC perform slightly worse than the 1.8nm-SiNC and 1.3nm-SiNC perform drastically worse. The autors attribute this to decreased quantum yield (QY) of smaller particles [156] and less favorable band alignment with adjacent blocking layers. Optimized devices with 1.8nm-SiNC could reach a peak EQE of 1.1 %. In addition, they could show that size-separation of SiNC leads to improved lifetimes of the devices and much less sensitivity of the emission wavelength to the applied voltage.

Architecture and impact of interlayers

As described in section 4.2 transport and blocking layers play an important role in the design of OLEDs, easing energetic transitions and confining charges in the emissive layer.

Different electron and hole transport layers (ETL and HTL) have been investigated for SiNC-LEDs. In Cheng's first work they used MEH-PPV [1] for the HTL and bathocuproine (BCP) for the ETL [96]. While these materials proved to be sub-optimal, the work revealed a common problem with certain HTL materials: MEH-PPV is itself a light emitting polymer. As such they report an unwanted light contribution polluting the red light emitted from the SiNC when the SiNC layer is too thin or at increasing current densities. From 10 mA/cm^2 and up there is significant MEH-PPV contribution in the LED spectrum of their thickest device with increasing controbution for thinner layers.

A similar issue was observed by Gosh et al. [103]. However, in their work they try to use this effect to their advantage and use the blue emitting PolyTPD as HTL to mix the emission of PolyTPD and SiNC into white light. They used SiNC with diameter of 2.1 nm synthesized from thermolysis of triethoxysilane (TED) and functionalized with 1-octadecene by hydrosilylation. While a device with a 50 nm thick layer of SiNC would show now sign of PolyTPD emission, 20 nm showed some traces and 10 nm resulted in roughly equal contribution from SiNC and PolyTPD and thus white light emission. This however only holds true at low driving voltages as for higher ones PolyTPD emission increases more then SiNC emission and shift the color more towards the blue. A white emitting device with ZnO ETL and 10 nm SiNC layer thickness exhibited an estimated EQE of 0.035%.

The work of Puzzo compares PEDOT:PSS and PVK as HTL materials in combiantion with TBPi[2] as ETL material [99]. The device based on PVK would turn on at much higher voltages (∼22 vs ∼10 V). While PEDOT:PSS is declared as superior hole transporter, unfortunately the the PVK layer is twice as thick as the PEDOT:PSS layer, making a direct comparison difficult. However, the device with PVK interlayer is much brighter and more current efficient at the same time, increasing the peak luminance from to 0.3 cd/cm^2 at 400 mA/cm^{2}to 60 cd/cm^2 at 200 mA/cm^2. They attribute this to three different factors: exciton energy transfer from PVK to the SiNC is the primary contribution to EL; efficient exciton energy transfer from the SiNC to the PEDOT:PSS (PEDOT:PSS is not blocking electrons) and a lower energy barrier for hole injection from PVK over PEDOT to the VB edge of the SiNC. At high current densities they also have the problem of light pollution from PVK.

Gu et al. addressed the potential barrier between ITO electrode and the following PEDOT:PSS transport layer by investigating addtional interlayers in between [152]. They showed that very thin layers of either HAT-CN[3] or MoO_3 increases the work function of ITO and consequently the charge injection into the PEDOT:PSS layer. Since they us ZnO with a very high electron mobility as ETL, they indentify charge imbalance as perfomance bottleneck that can be tackeld with improved hole injection. An interlayer

---

[1] poly[2-methoxy-5-(2-ethylhexyl-oxy)1,4-phenylene-vinylene]

[2] 2,2,2"-(1,3,5-Benzinetriyl)-tris(1-phenyl-1-H-benzimidazole)

[3] dipyrazino(2,3-f:2',3'-h)quinoxaline-2,3,6,7,10,11-hexacarbonitrile

of 5 nm HAT-CN could improve the EQE by 22 %, while 3 nm of MoO_3 increased it by about 170 %. By using SiNC with diameter of 3.1 nm synthesized by nonthermal plasma and hydrosilylated with 1-Dodecyl, an optimized device with an eloborate ITO/MoO_3/PEDOT:PSS/PolyTPD/SiNC/ZnO/Ag stack could reach a peak EQE of 2.4 %.

In a similar approach from the same group and with the same particles, an all inorganic design was investigated to overcome lifetime problems associated with organic materials [154]. Using sputtered NiO (a common replacement for PEDOT:PSS) as HTL and spin coated ZnO as ETL, they showed that the introduction of a very thin Al_2O_3 layer between HTL and SiNC layer could significantly improve the device: while the turn-on voltage was reduced from 6.9 to 4.8 V, the EQE increased tenfold. THis improvement is attributed to a passivation of traps on the NiO surface that quench excitons at the interface to SiNC, which is verified by PL spectra and decay measurements. A thickness of 5.7 nm for the Al_2O_3 layer give the best restults, while thicker layers inhibit charge transport due to the insulating nature of Al_2O_3. An optimized device reached an EQE of 0.1 %.

In a study on different evaporated ETLs Cheng et al. compared Alq_3[4], TCTA[5] and CBP[6] in combiantion with PEDOT:PSS/PolyTPD as HTL [97]. All three ETL materials feature very different electron mobilities and it was shown that this seemed to have very little impact on the device performance. While the low mobility TCTA layer leads to increased turn-on voltage, quantum efficiency remains largely the same for all three materials. However, removing the ETL entirely reduces the EQE by about 50 % highlighting the importance of the blocking layer and its ability to confine charges in the emitting layer.

So far there has been only one report on an inverted device structure, injecting electrons from the bottom and holes from the top, by Yao et al. [151]. They stick to the usual ITO and aluminium electrodes, but reverse the interlayers to create the desired charge selectivity. ZnO is used as ETL, while MoO_3 primarily serves to enable whole injection from the Al electrode. An additioanl TAPC[7] layer between SiNC and MoO_3 is used for the actual electron blocking. They then show how the introduction of an ultrathin PEI layer ($\sim$2 nm) between ITO and ZnO can further improve the device by lowering the ITO work function. With PEI the charge injection is significnalty improved, lowering the turn-on voltage, significantly increasing optical power output and EQE. By using SiNC with diameter 2.6 nm, made from nonthermal plasma and the ITO/PEI/ZnO/SiNC/TAPC/MoO_3/Al stack, an EQE of 2.7 % was achieved, up from 1.1 % without PEI.

---

[4] tris-(8-hydroxyquinolinato) aluminum

[5] 4,4′,4′′-tris-(*N*-carbazolyl)-triphenlyamine

[6] *N*′-dicarbazolyl-4-4′-biphenyl

[7] 1,1-Bis[(di-4-tolylamino)phenyl]cyclohexane

Surface functionalization

As is well known, the SiNC surface and its functionalization can have a strong impact on the particles optical and electrical properties [107, 141]. Interestingly, this topic has not received much interest in the context of SiNC LEDs. So far there are two publications comparing the influence of the surface groups on the device performance.

In the work of Mastronardi et al. from the Ozin group they functionalize their SiNC with allylbenzene (AB) [101] and compare them against the study from the same group based on decyl functionalized SiNC [99]. By transmission line model (TLM) measurements they find that the dark conductivity significantly improves from 2.4×10^{-7} (decyl) to 2.1×10^{-6} S/m (AB). This increase in conductivity is attributed to the shorter chain length of the AB surface groups and the possibility of benzene-ring-induced interparticle π-π-stacking, correlating to higher packing density and improved electronic coupling between the particles. However, a comparision on a device basis is difficult as the presented device deviates significantly from the previous one. While the decyl-SiNC have a mean diameter of 3.0 nm, AB-SiNC have been specially size separated and show a mean diameter of 2.4 nm. Furthermore, the PVK HTL was replaced with PolyTPD. Eventually, the presented device features a much lower turn-on voltage associated with the improved conductivity of the AB-SiNC layer, but lower EQE of just 0.17 % compared to 0.7 % for the decyl-SiNC-LED.

In the work of Liu et al. the authors directly compare devices made from SiNC functionalized with either octyl or phenylpropyl (PhPr) [153]. The particles are synthesized by nonthermal plasma, have a diameter of 3.0 nm and are functionalized by hydrosilylation. It is reported that devices based on PhPr turn on earlier (2.2 vs 2.9 V), drive about ten times more current at the same voltage (~250 vs ~25 mA/cm^2 at 10 V) and feature almost double the optical output (0.64 vs 0.34 mW/cm^2). This tenfold increase in current for a twofold increase in output results in significantly lower EQE value: while the octyl-bassed devices go up to an impressive 6.2 %, PhPr-based devices only reach 1.1 %. The higher light output of the PhPr-SiNC is attributed to a lower surface coverage due to a larger steric hindrance of the phenylpropyl ligand containing a benzene ring compared to the chainlike octyl ligand. This lower surface coverage leads to increased surface oxidization associated with a reduction of dangling bond defects, which is supported by larger PL lifetime and PL quantum yield. By means of electron-only and hole-only devices they show that PhPr-SiNC show significantly better electron transport, but inferior hole transport compared to octyl-SiNC. As devices with ZnO ETL already exhibit a surplus of electrons, PhPr-SiNC aggravate this even further, which might explain the low efficiency of such devices.

4.5 Influence of surface functionalization on the performance of SiNC-LEDs

Surface functionalization is critical to SiNC's performance. It has to guarantee steric stabilization in solution, protect the particles from oxidation, without insulating the particles electrically (too much) and can influence their optoelectronic properties. Only few works have investigated the influence of surface functionalization on SiNC-LED performance and they focus on comparing different surface groups. In this work we compare the influence of two different functionalization *routes* – namely hydrosilylation and use of organolithium reagents – on the particles and the device performance, employing the same hexyl ligands for both routes. The details of SiNC synthesis and functionalization have been shown in section 3.3.5. The most frequently used method for the surface functionalization of hydride-terminated SiNCs is radical hydrosilylation (HS). Organic molecules are grafted to the surface through Si–C bonds formed via the reaction of surface silyl radicals with terminal alkenes or alkynes [157]. These silyl radicals can be created at elevated temperatures (T≥150 °C) [145] or using radical initiators such as azobisisobutyronitrile (AIBN) [146]. HS has some disadvantages including oligomerization of the ligands on the surface of SiNCs at elevated temperatures [145]. These surface characteristics may decrease the efficiency of SiNCs in optoelectronic devices by forming an insulating barrier and hindering charge transport [101]. Recently, an alternative method was exploited to functionalize hydride-terminated SiNCs at room temperature by using organolithium reagents (OLR) [147]. This reaction proceeds via a mechanism in which surface Si–Si bonds cleave due to an attack of the organolithium reagent (R–Li, R=alkyl), yielding Si R bonds and neighboring Si–Li surface species. Following acid workup, Si–Li groups are quenched to yield surface Si–H species [158]. Owing to its mechanism, the OLR method offers the advantage of functionalizing SiNCs under mild conditions while assuring defined monolayer coverage. The following results comparing the two methods have been published in Nanoscale [144].

4.5.1 Particle characterization

In the following we present the characterization of SiNC functionalized with hexyl groups via HS (HS-SiNCs) and OLR (OLR-SiNCs), followed by an optimiaztion of the SiNC-LED stack on the basis of HS-SiNC and eventually a comparison of optimized LEDs with HS-SiNC and OLR-SiNC.

SiNC were synthesized by thermolysis of hydrogen silsesquioxane and functionalized with 1-hexene via HS and n-hexyllithium via OLR, as described in section 3.3.5. Fig. 4.5 a) shows both kinds of particles in toluene solution. As we can see they form a very clear, yellow-ish solution without any precipitate or visible agglomerates. Fig. 4.5 b) shows how both solution exhibit orange-red photoluminescence (PL) under UV-illumination.

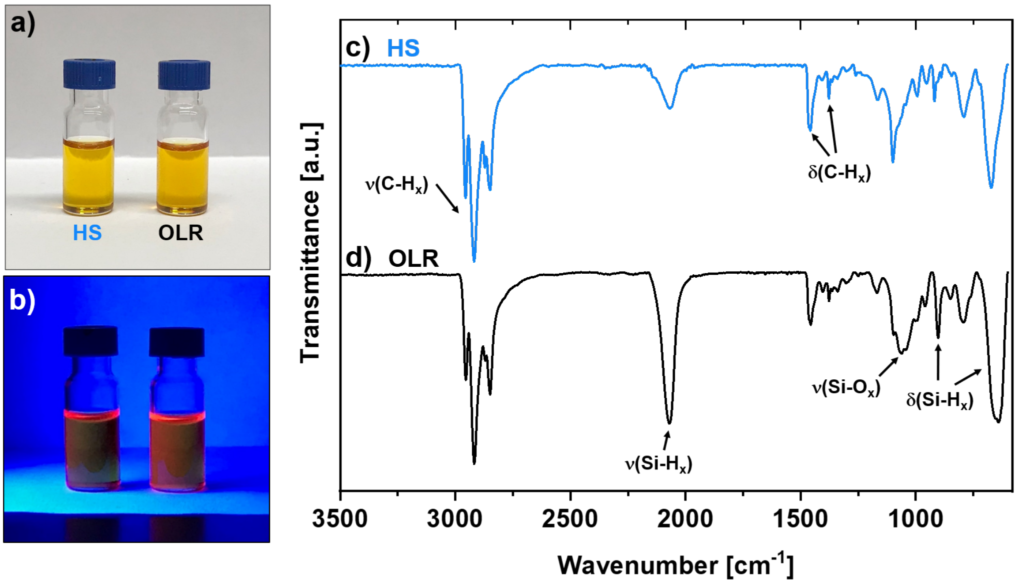

Figure 4.5: *Images of SiNC solutions in toluene: a) in normal ambient light and b) under UV light. The yellow-ish solution is clear without any precipitation for both HS and OLR functionalization. Under UV illumination the solution shows orange-red photoluminescence; c) FTIR spectra of SiNCs functionalized with 1-hexene via HS and d) with n-hexyllithium via OLR method (adapted from ref. [144] with permission from The Royal Society of Chemistry).*

Fourier transform infrared (FTIR) spectroscopy was utilized to interrogate the presence of surface groups associated with the target ligands after functionalization. For both functionalization methods, the presence of hexyl chains was indicated by strong C–H and C–C stretching bands at ca. 2980-2835 and 1450 cm^{-1}, respectively (Fig. 4.5 c) and d)). For both samples minor surface oxidation was observed as evidenced by the Si–O band at 1050 cm^{-1}. Hydride terminated SiNCs show only Si–H bands, at 2100, 906, and 660 cm^{-1} [147].

The most significant difference between the FTIR spectra of the two kinds of SiNC is the greater intensity of the Si–H band at 2100 cm^{-1} relative to the C–H signal in the case of the OLR method. This indicates that OLR-SiNC has more hydride groups on the surface than HS-SiNC. This observation is consistent with the accepted reaction mechanism, as hydride groups are not consumed, but indeed formed upon quenching of Si–Li groups during workup. In the case of HS, the intensity of Si–H band is much lower, as hydride groups are consumed during the course of the reaction.

Additionally, the lower Si–H signal relative to the alkyl chain (C–H) signal might also

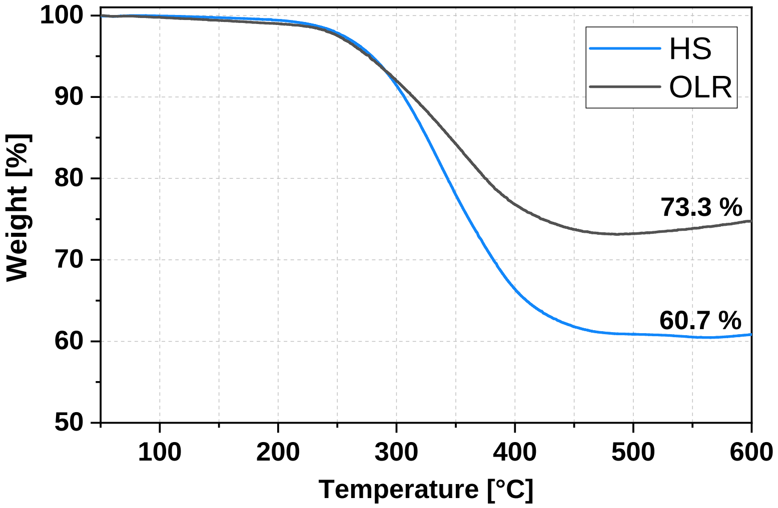

Figure 4.6: *TGA analysis of SiNCs functionalized with hexyl surface groups via OLR and HS methods after 15 hours reaction time (adapted from ref. [144] with permission from The Royal Society of Chemistry).*

indicate a higher surface coverage with hexyl chains when functionalized by HS. While such a higher C-H proportion might also be explained by oligomerization of the hexyl chains, which is possible during HS, this was excluded by Yang et al. for HS reactions initiated by AIBN as done in this work [146].

To estimate the degree of surface coverage, thermogravimetric analysis (TGA) was performed on SiNCs functionalized with both methods after 15-hour reaction time (Fig. 4.6). TGA measures the mass of a sample over a temperature range. Since organic materials burn before SiNCs evaporate, the observed weight loss can be associated with the amount of organic surface groups covering the particles. The TGA analysis revealed 39.3 % and 26.7 % weight loss for HS and OLR reactions respectively. The weight loss for HS-SiNC is 44.4 % higher than for OLR-SiNC, which indicates there is significantly more organic material on the surface of SiNC functionalized by HS. These TGA data are consistent with the FTIR data, indicating a higher surface coverage is obtained with HS in comparison to the OLR method. Transmission electron microscopy (TEM) was used to examine size and size distribution of the particles by counting at least 200 particles using the ImageJ software. The hexyl surface groups are not visible in such TEM measurements. Images of SiNCs functionalized with both methods yielded a similar size distribution centered at 3.1 ± 0.2 nm and 3.1 ± 0.1 nm, for HS and OLR methods, respectively (Fig. 4.7). These results show that both methods yield particles of same size, which suggests that the functionalization method does not influence particles size.

This is also supported by dynamic light scattering (DLS) measurements of the SiNC in toluene. An average over five different measurements, each again the average of

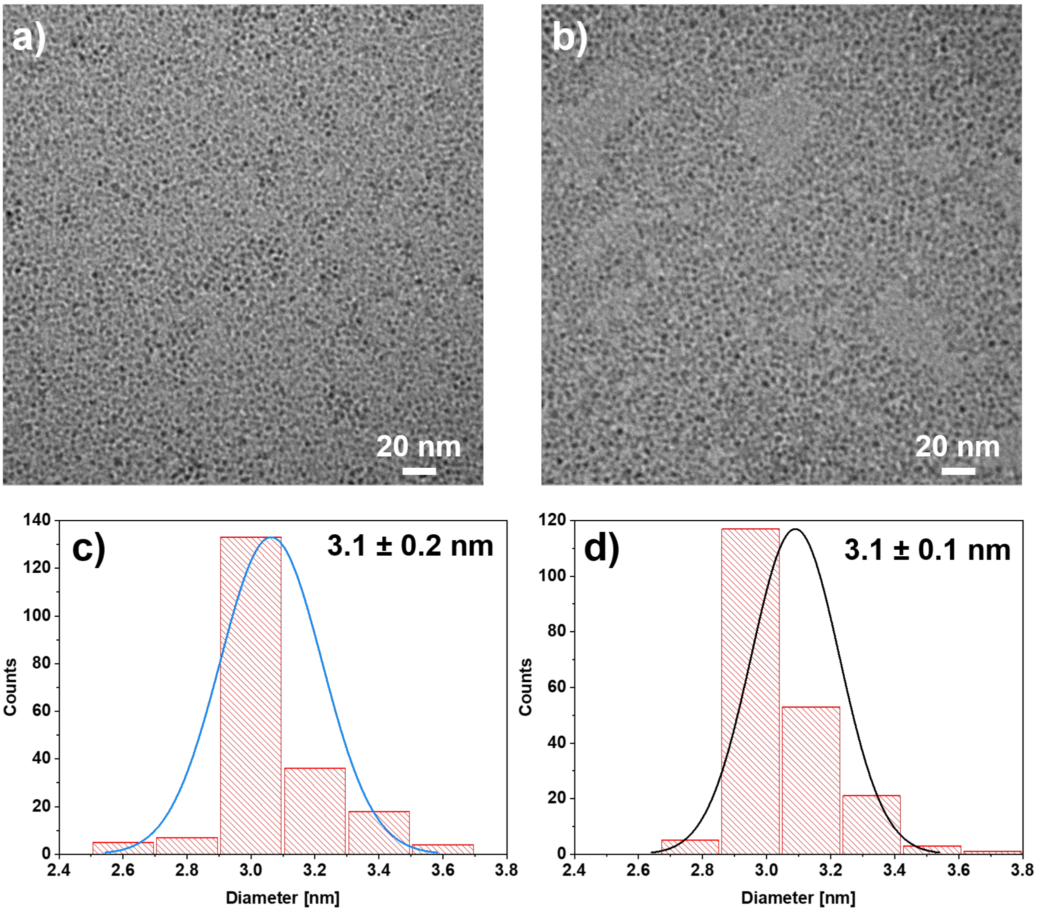

Figure 4.7: *Bright field TEM images of SiNCs functionalized with a) 1-hexene via HS method and b) n-hexyllithium via OLR, c) and d) corresponding size distributions (adapted from ref. [144] with permission from The Royal Society of Chemistry).*

ten consecutive acquisitions, yields a hydrodynamic radius of R_{Hyd} = 2.4 ± 0.2 nm and polydispersity of PD = 32.6 ± 3.1 % for OLR-SiNCs and R_{Hyd} = 2.5 ± 0.3 nm with PD = 33.8 ± 2.0 % for HS-SiNCs. This shows that the particles are freestanding in solution and also further indicates that the particles have statistically the same size.

Fig. 4.8 shows absorption and photoluminescence (PL) data of both kind of particles in toluene solution. For PL measurements the samples were excited with 365 nm UV light. Both spectra are very similar for both HS- and OLR-SiNC. Since for QDs the optical properties depend on particle size, this is another sign that both kinds of particles have identical size. The absorption spectrum shows an onset at around 550 nm and a sharply rising absorption edge into the UV. The PL spectrum shows a peak centered at 686 nm with a full width half maximum (FWHM) of 0.35 eV (0.36 eV for OLR-SiNC,

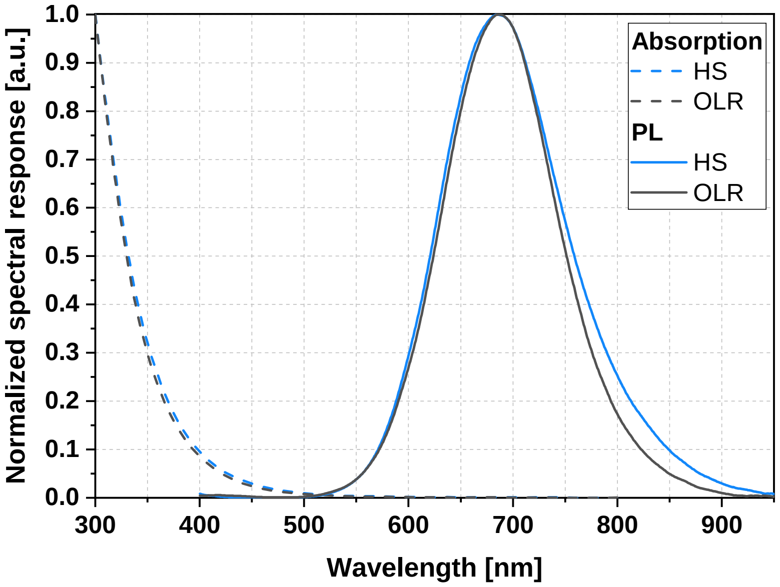

Figure 4.8: *Normalized absorption and photoluminescence spectra of SiNCs functionalized with hexyl groups via OLR and HS method in toluene (adapted from ref. [144] with permission from The Royal Society of Chemistry).*

0.34 eV for HS-SiNC). Such a large difference difference between the absorption and emission maximun (Stokes shift) is typical for QDs and frequently observed for SiNC [103, 151, 159]. Absolute quantum yield (AQY) of SiNCs in toluene (the ratio of photons emitted per photons absorbed) is 17 % for HS-SINC and 22 % for OLR-SiNC. Since the difference cannot be attributed to a size difference, it must stem from the different surface functionalization methods. A possible explanation is the removal of surface defects via surface restructuring during the course of the reaction when using organolithium reagents [141, 160].

4.5.2 Stack optimization

Introducing ZnO and PolyTPD

To assure a good comparison of SiNC-LEDs with HS- and OLR-LEDs, we investigated the LED architecture on basis of OLR-SiNC. Starting point is a barebone non-inverted architecture: ITO as transparent, high work function anode (∼120 nm) PEDOT:PSS as hole injection layer (HIL) to smooth out the ITO surface and the energetic transition between ITO and the following layer (∼20 nm), a compact layer of OLR-SiNC as emitting layer (∼30 nm), and a thin layer of Ca as low work function cathode (20 nm), followed by a capping layer of Al to protect the highly reactive Ca (100 nm). We then add first a layer

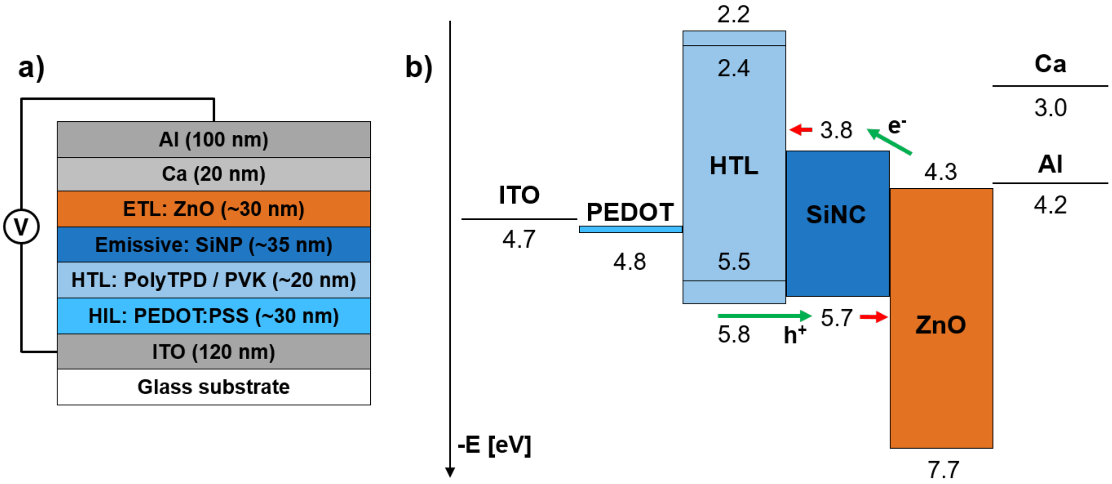

Figure 4.9: *Device architecture of SiNC-LEDs: a) schematic representation of the layer stack and b) the corresponding proposed energy level diagram; the two HTL materials are PolyTPD (smaller band gap) and PVK. The blocking layers confine charges in the light emitting layer, which prevents leakage and increases the chance for radiative recombination.*

of ZnO (~30 nm) on top of the SiNC layer as ETL and secondly a layer of PolyTPD as HTL between the PEDOT:PSS and the SiNC layer. Proper alignment of the energy levels of all layers is critical for efficient charge transport. Fig. 4.9 b) shows a proposed energy diagram of this stack and illustrates how blocking layer help to confine charges in the SiNC layer and thus facilitate radiative recombination and avoid charge leakage. The energy levels of transport layers were taken as average values from different literature reports [97, 100, 150]. Since the specific samples in this work have not been measured and the values reported in literature have a certain spread, these values can only serve as approximation. Valence band (VB) and conduction band (CB) of SiNCs were estimated with the following formula [161] which describes the broadening of the band gap as a function of the particle diameter d in crystalline semiconductors, due to the quantum confinement effect:

$$\Delta E_{\mathrm{G}}(d) = \frac{3.74}{(d/\mathrm{nm})^{1.39}}\,\mathrm{eV}. \tag{4.6}$$

With $d = 3.1$ nm, this results in a band gap widening of $\Delta E_{\mathrm{G}} = 0.77$ eV compared to bulk Si. As described by Buuren et al. [162], this band gap widening does not distribute evenly between VB and CB of SiNC, but in a ratio of $\Delta\mathrm{VB}/\Delta\mathrm{CB} = 2/1$. Using $E_{\mathrm{CB}} = -5.17$ eV and $E_{\mathrm{VB}} = -4.05$ eV of bulk Si yields CB and VB levels of SiNCs as $E_{\mathrm{CB}} = -5.68$ eV and $E_{\mathrm{VB}} = -3.79$ eV. X-ray photoelectron spectroscopy (XPS) measurements have shown VB levels of -5.5 eV for SiNC with $d = 3.2$ nm [99], -6.0 eV for SiNC with $d = 2.4$ nm [101], and -5.7 eV for SiNC with $d = 1.8$ nm [150]. These results suggest that band gap widening for SiNC with $d = 3.1$ nm is actually slightly lower than predicted by eq. 4.6, but it also shows

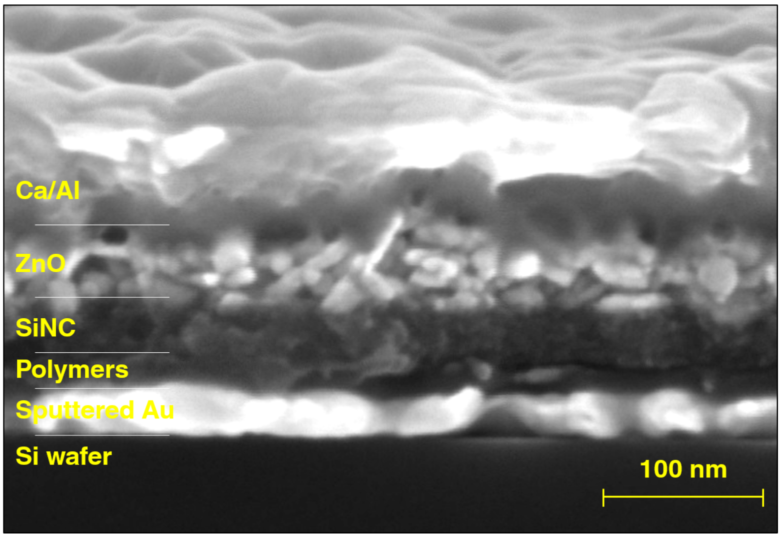

Figure 4.10: *Cross-sectional SEM image of the device stack with ZnO and PolyTPD blocking layers. The glass substrate with ITO electrode was replaced by an Au-coated Si wafer to have a more conductive substrate for SEM imaging. The two polymer layers are indistinguishable since polymers give low contrast in SEM (reproduced from ref. [144] with permission from The Royal Society of Chemistry).*

results are not consistent between different research groups (for example 2.4nm-SiNC showing more widening than 1.8nm-SiNC). Nonetheless we use the computed values in the band diagram, keeping in mind they only serve as an approximation and also neglect potential influence of the surface functionalization [141].

During operation under forward bias, electrons are injected from the low work function cathode and holes from the high work function anode. We can now see that ZnO as well as PolyTPD have favorable energy levels for blocking charges leaving the SiNC layer, while posing only very small barriers for injection into SiNC: electrons entering the SiNC layer from the ZnO see a potential barrier of about 0.5 eV, while electrons trying to leave the SiNC layer see a barrier of about 1.4 eV. Similarly, holes entering the emitting layer from PolyTPD barely see any potential barrier, holes trying to leave the SiNC layer face about 2 eV potential barrier.

Fig. 4.10 shows a cross-sectional scanning electron microscope (SEM) image of the device stack. For the SEM measurement the ITO/glass-substrate was replaced by a Si wafer substrate covered with a thin sputter coated Au layer. The image shows that all layers are spatially well-defined and in good agreement with the nominal layer structure (Fig. 4.9 a)). A common problem with spin coating stacks with many layers is the possibility of resolving an underlying layer, when two materials are soluble in the same solvent. Although PolyTPD and SiNCs were both spin coated from toluene, the SiNC layer can be clearly distinguished from the underlying polymer layers with no visible intermixing.

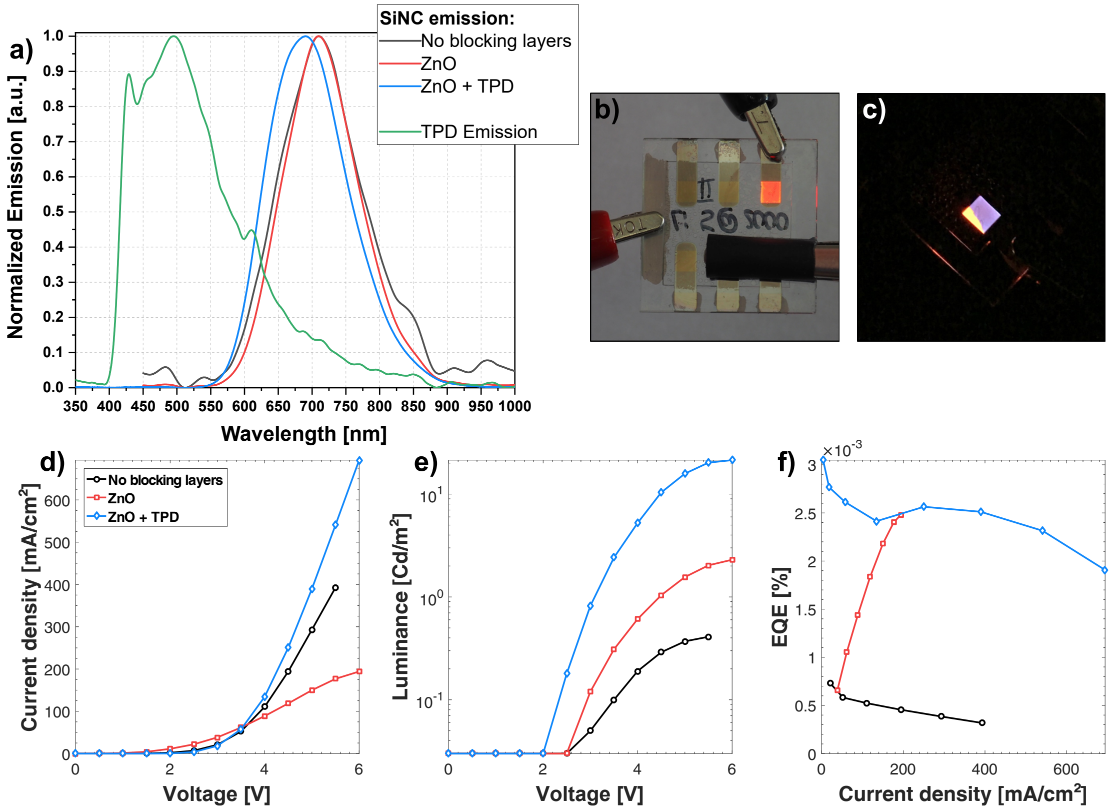

Figure 4.11: *Influence of ZnO and PolyTPD blocking layers on SiNC-LED performance: a) normalized emission spectra of SiNC-LEDs and a PolyTPD-only reference LED. While addition of ZnO does not change the emission spectrum, the PolyTPD HTL results in a slight blue shift. There are no traces of the blue TPD emission in the red emission of the SiNC-LED with PolyTPD HTL. b) Pictures of a SiNC-LED with PolyTPD HTL emitting bright red light and c) emitting blue light due to a large defect in the SiNC layer. Corresponding J-L-V characterization: d) current density vs. voltage, e) luminance vs. voltage and f) calculated EQE vs. current density. Both blocking layers significantly improve the device.*

This is also confirmed by the complete lack of PolyTPD emission from the devices. Fig. 4.11 a) shows the electroluminescence (EL) spectrum of SiNC-LED without blocking layers (NBL-LED), with ZnO ETL (ZnO-LED) and with both PolyTPD and ZnO blocking layers (TPD-LED) as well as a reference device with only PolyTPD as emitting layer. The NBL-LED and the ZnO-LED both exhibit the same emission peak at 710 nm. As such, addition of ZnO has no impact on the spectral output. The device TPD-LED has its emission peak at 690 nm, slightly blue-shifted compared to the other LEDs. As can be seen PolyTPD is itself a blue emitting polymer, but there are no traces of blue emission in the SiNC spectra. This demonstrates that the SiNC form a closed film without pinholes and charge recombination is well confined within the SiNC layer, which is important to ensure that all measured light output can be attributed to SiNC emission. The red light emitted by the SiNC can be can be easily seen with the naked eye under ambient lighting conditions (Fig. 4.11 b)), the blue light of the PolyTPD can become visible when there are defects in the SiNC layer (Fig. 4.11 c)).

The positive impact of the blocking layers on LED performance can be seen in the J-L-V-characterization presented in Fig. 4.11 d) - f). All devices show the expected diode shape with exponential rise of current and luminance after reaching the turn-on threshold. We see that the introduction of ZnO as ETL lowers the driving current a bit, while adding PolyTPD increases it slightly above the initial level (Fig. 4.11 d)). All devices turn on at relatively low voltage, which can be extracted more easily from the logarithmic representation of the luminance curves (Fig. 4.11 e)): The NBL- and ZnO-LEDs turn on after 2.5 V, the PolyTPD HTL already after 2 V. The luminance differences are more significant: while the device without blocking layers does not exceed 1 cd/cm^2, with ZnO ETL it reaches a peak value of 2.3 cd/cm^2. Adding the PolyTPD HTL leads to an almost tenfold increase reaching 21.4 cd/cm^2. This large increase can only partially be attributed to improved conversion efficiency as the TPD-LED exhibits a slight blue shifted - and thus more visible - emission spectrum. Since the luminous efficiency function (spectral sensitivity of the human eye) is very steep in the red region, small differences in the emitted color can already have large impact on the photometric luminance. This is also reflected in the EQE values (Fig. 4.11 f)): while the device with PolyTPD shows the highest EQE values, the difference to the ZnO device is not as significant as might be expected from the J-L-V-curves. While the blocking layers significantly improve the device performance, we have to note that EQE values in the order of 10^{-3} % are relatively low.

Thickness and PVK

The thickness of the active layer plays a critical role in organic and hybrid devices and typically presents a trade-off: a thicker layer offers more sites for charge recombination and can generate more light, but the low charge carrier mobilities quickly result in ohmic losses if the layers get too thick. To investigate this issue for SiNC-LEDs, we made devices based on the optimized layer stack with ZnO ETL and PolyTPD HTL and with three different SiNC layer thicknesses: 9, 42 and 70 nm. For this we used differently concentrated SiNC solutions and spin speeds: 2 mg/ml at 2000 rpm, 10 mg/ml at 2000 rpm and 15 mg/ml at 1000 rpm. Additionally, a 42 nm device has been fabricated with PVK replacing PolyTPD as HTL material. PVK is a blue emitting polymer often used as HTL material for SiNC-LEDs. Its properties are similar to PolyTPD with a slightly larger band gap, which provides an even larger barrier for electrons and should be slightly more favourable for hole injection (Fig. 4.9 b)).

From the resulting emission spectra in Fig. 4.12 c) we see that neither the device thickness

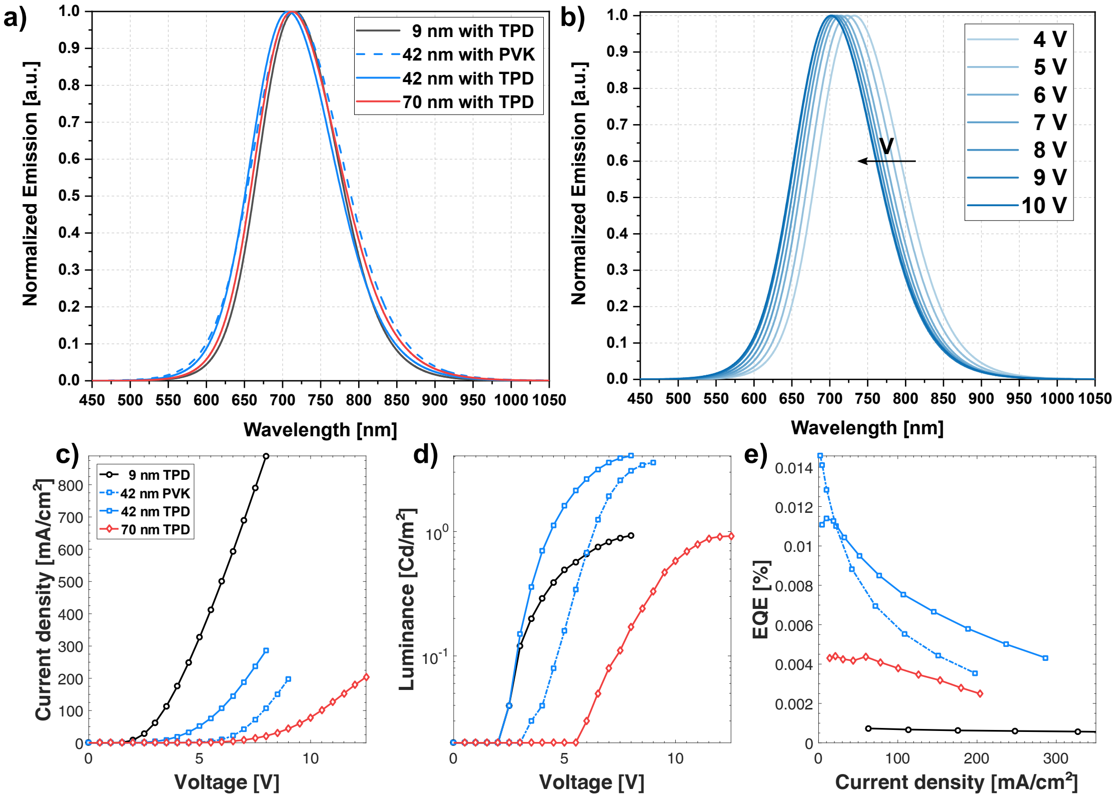

Figure 4.12: *Influence of SiNC layer thickness and PVK HTL: a) normalized emission spectra; the layer thickness has no effect on the the emitted color. b) Normalized emission spectra of 42nm-SiNC-LED with PolyTPD HTL over increasing applied voltages. Higher voltages lead to a blue shift of about 30 nm, probably due to size dispersion effects. Corresponding J-L-V-characterization: c) current density vs. voltage, d) luminance vs. voltage and e) calculated EQE vs. current density. The 42 nm device shows the highest performance.*

nor the PVK HTL have an influence on the emission spectra: all four devices have their emission peak at 711±5 nm. This value is 20 nm higher that reported in the previous experiment and reveals a larger issue with the SiNCs used in this work: we observe non-negligible batch-to-batch variations regarding the emission spectrum. This can have a strong influence on the luminance of the SiNC-LEDs. To ensure that the results are comparable we only present experiments where all devices were made from the same fabrication batch. From the J-V-curve we see a very clear trend: the thinner the device, the more current it drives at a given applied voltage. This makes sense since the layer thickness correlates with its electrical resistance. Although the 9nm-LED drives much more current than the 42nm-LED, they both turn on after passing 2 V, already a sign that the thinnest device is not as efficient in converting current into light. The thickest device only turns on much later after passing 5.5V. Looking at the luminance (Fig. 4.12 d)) we can clearly see that the middle device is significantly brighter than the other ones. It reaches a peak luminance of 4.1 cd/cm^2, while the other two only go up to 0.9 cd/cm^2. These luminance values are lower compared to the results presented in the previous experiment, because the devices in the current experiment have an emission spectrum shifted about 20 nm to the red. The 9nm- and the 70nm-LED both exhibit the same luminance, but the thinner device uses much more current. Accordingly, the EQE of the 70 nm device is significantly higher (Fig. 4.12 e)). It should be noted that EQE does only consider the injected current and not the required voltage - and thus power - to generate light. The 42 nm device is clearly the best: it shines the brightest and features much higher EQE than the other thicknesses, while not turning on later than the 9nm-LED.

The device with PVK HTL drives less current and turns on about 1 V later than the PolyTPD equivalent. This resembles the behaviour of the thicker, more resitive layer and can possibly be explained by the lower hole mobility of PVK: 2.5×10^{-6} [115] vs. 2.1×10^{-3} cm^2/Vs for PolyTPD [112]. This performance penalty is not rewarded with a higher luminance as the device only reaches a peak value of 3.6 cd/cm^2. As such PVK is not an attractive alternative to replace PolyTPD.

Fig. 4.12 e) shows EL of the 42 nm device with PolyTPD as a function of the applied voltage. We observe a ∼30 nm blue shift of the emission spectrum when the applied voltage is increased from 4 to 10 V. This behaviour is commonly observed in SiNC-LEDS [96, 97, 150–152] and typically attributed to the size distribution of the particles: larger SiNC tend to dominate EL emission, as they present a minimal energy in the potential energy landscape of the films and thus are preferentially targets for exciton transfer. Then, as driving voltage and current increase, a greater contribution also from smaller SiNC leads to a gradual blue-shift in the EL (the wider band gap of smaller particles emits higher wavelength [101]. It was shown that additional size separation of the particles could reduce this effect [150]. Others also suggest a band filling effect [151] known from bulk semiconductor LEDs [163].

4.5.3 Functionalization by hydrosilylation vs organolithium reagents

Based on the optimized LED stack, we investigate the influence of two different functionalization routes on the SiNC-LED performance comparing hydrosilylation and use of organolithium reagents. For this SiNC-LEDs were made with ZnO and PolyTPD interlayers and a medium SiNC layer thickness of about 35 nm with both HS-SiNC and OLR-SiNC (made from the same batch). The EL spectra of both LEDs are shown in Fig. 4.13 a), together with PL spectra form the particles in solution. Congruent to the PL curves, the EL spectra of HS- and OLR-SiNC-LEDs are almost identical. There is only a minor red shift between PL and EL, with the EL peaks at 694 nm compared to the PL peaks at 686 nm. The images in Fig. 4.13 b) and c) show the two LEDs in operation. They confirm that both devices emit the same color and furthermore show that both have

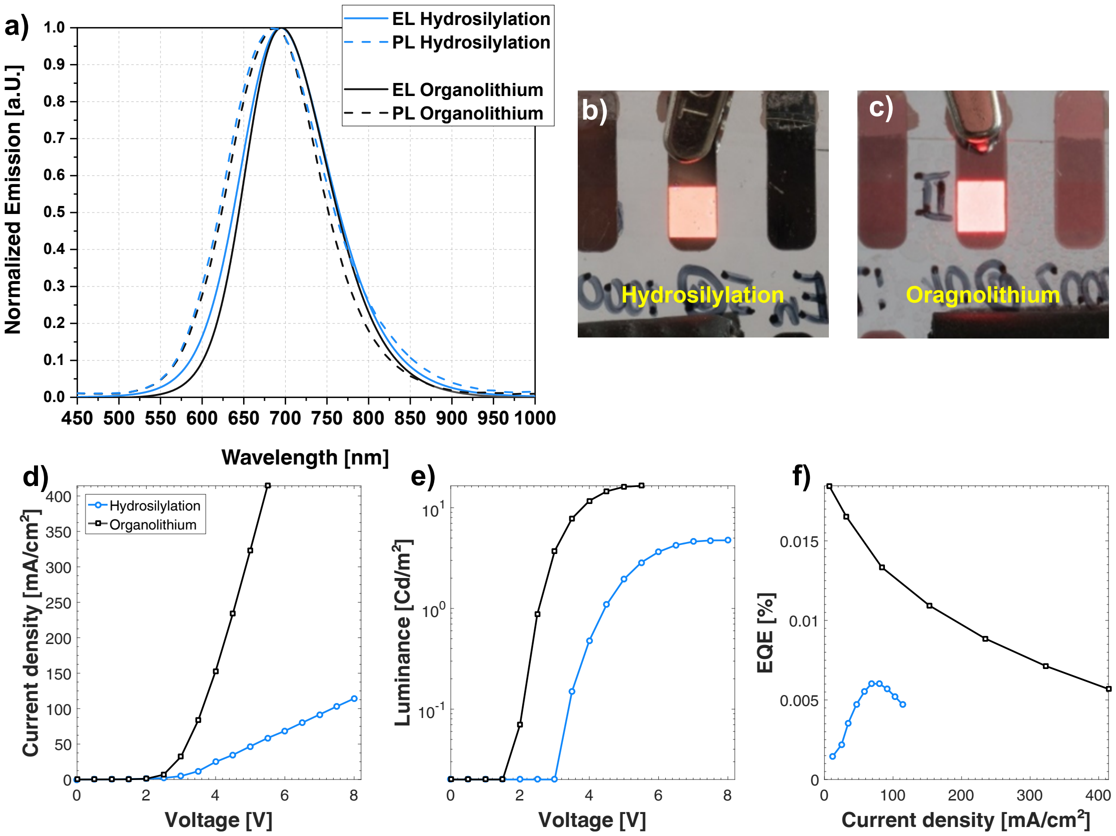

Figure 4.13: *Influence of different surface functionalization methods on SiNC-LED performance. Devices are functionalized with hexyl groups via hydrosilylation or using organolithium reagents. a) Normalized PL and EL spectra. EL is slightly red-shifted relative to PL, but both functionalizations result in identical spectra. b) Picture of HS-LED and c) OLR-LED. Corresponding J-L-V characterization: d) current density vs. voltage, e) luminance vs. voltage and f) calculated EQE vs. current density. OLR-LEDs are significantly brighter and more efficient.*

comparable SiNC film quality with very few defect. This is a critical aspect to ensure comparability of the devices as we observed that HS-SiNC have a tendency to form films with more defects and agglomerates than OLR-SiNC.

In the J-L-V characteristics in Fig. 4.13 d) and e), the OLR-SiNC device shows typical exponential current of a diode and a low turn on voltage of 2.5 V, while the HS-SiNC-LED shows a higher turn-on voltage of 3.5 V and a much lower and more linear current draw. As both device have the same SiNC layer thickness, this *J-V* behaviour reveals a higher resistance of the HS-SiNC film.

The OLR-SiNC-LED reaches a maximum luminance of 16.5 cd/cm^2 while the HS-SiNC device only goes up to 4.8 cd/cm^2. This much lower luminance of the HS-SiNC-LED cannot be compensated by its lower current draw as EQE also lower (Fig. 4.13 f)). The EQE of the OLR-SiNC-LED is higher than the HS-SiNC device's over the entire operating range, with a three times higher peak value of 1.8×10^{-2} % vs. 6.0×10^{-3} %. At the current density of 80 macm, where the HS-SiNC-LED shows the highest efficiency, luminance (7.8 vs 4.3 cd/cm^2) and EQE (1.3×10^{-2} vs. 6.0×10^{-3} %) of the OLR device are still twice as high.

Since it was assured that particle size, emission color, film thickness and film quality are identical for HS- and OLR-SiNC-LEDs and therefore not the cause for the observed performance differences, they can then be safely attributed to differences on the particle surface stemming from the different functionalization methods.

The lower electrical resistivity and the higher EQE of the OLR-SiNC-LEDs are consistent with the surface characteristics obtained via the OLR method: OLR functionalization yields a lower degree of surface coverage than HS, which decreases the amount of insulating organic material on the surface of SiNCs. This may increase the electronic coupling between SiNCs, which leads to improved charge transport and lower film resistivity. Additionally, it may facilitate charge injection into the SiNCs, so that more electrons can recombine radiatively. This and the higher QY of OLR-SiNC can account for the increased EQE of these devices.

4.5.4 Influence of different surface groups

Apart from the surface functionalization method, we also want to investigate the influence of different surface groups on the performance of SiNC-LEDs. The work of Mastronardi et al. [101] reports two factors contributing to better device performance: a) size/length of the surface group as smaller ligands enable a higher packing density of SiNC and b) the possibility of π-π-stacking in ligands containing benzene-rings leading to higher electronic coupling between the particles. In their work they are not able to discriminate between the factors and cannot determine which of them actually contributes (more) to the device performance.

To investigate this further, we tested these two factors in two separate experiments. For the influence of the chain length we prepared SiNC functionalized with alkyl chains consisting of either six (hexyl) or twelve (dodecyl) carbon atoms. The Dodecyl-SiNC are functionalized by HS and are compared to the HS-SiNC with hexyl functionalization from the previous experiment. To see if SiNC-LEDs could benefit from the introduction of a benzene-ring to the ligand, we prepared SiNCs with a phenyl surface group (Ph-SiNC) and compared them to devices with hexyl-functionalized SiNCs. Since phenyl functionalization is only possible via use of OLR, they are compared to Hexyl-SiNC also functionalized using OLR. The three different surface groups are illustrated in Fig. 4.14 b). All devices were made with the optimized stack containing PolyTPD and ZnO blocking layers.

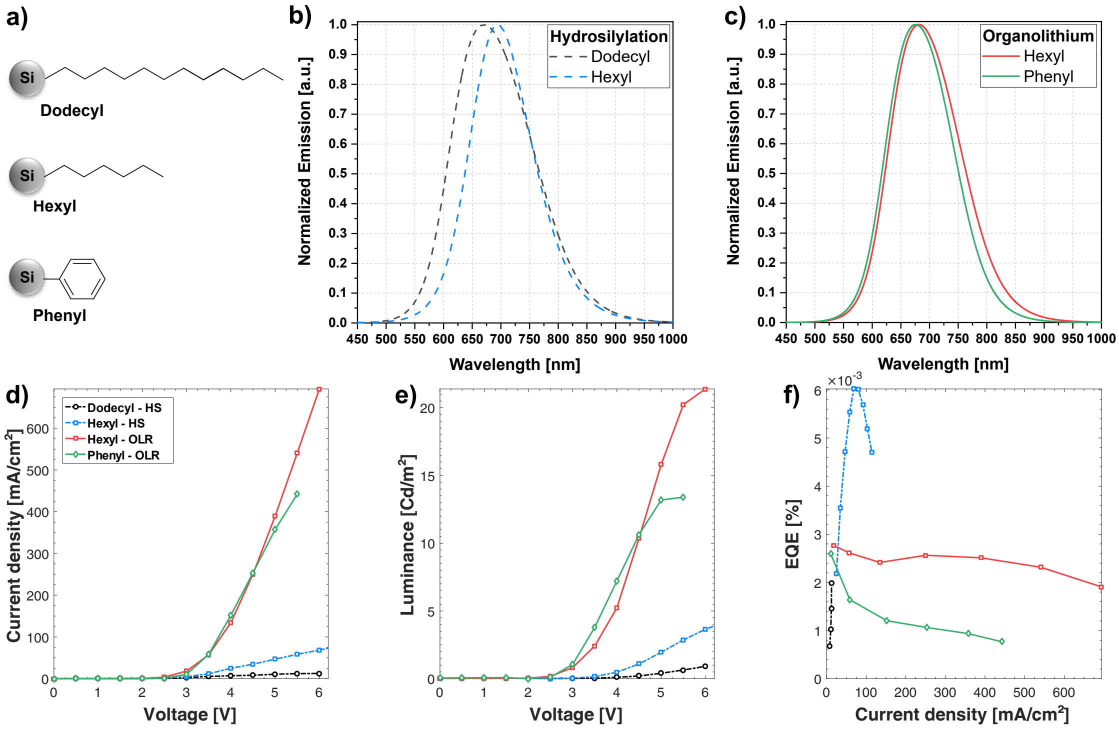

Figure 4.14: *Influence of different surface groups on SiNC-LEDs: a) schematic of SiNC with different surface groups. b) Normalized emission spectra of SiNC-LEDs functionalized by hydrosilylation with alkyl chains with either six or twelve carbon atoms and c) by OLR method with hexyl or phenyl groups. Corresponding J-L-V characterization: d) current density vs. voltage, e) luminance vs. voltage and f) calculated EQE vs. current density.*

The EL spectra of HS-Hexyl-SiNC and Dodecyl-SiNC are shown in Fig. 4.14 b). The shape of the Dodecyl-SiNC is slightly slanted towards lower wavelengths with a emission peak at 670 nm, 24 nm blue shifted compared to the HS-Hexyl-SiNC. This slanted shape might be a measurement artifact as the low signal of the device leads to a very noisy curve, which has been smoothed for a better presentation. OLR-Hexyl-SiNC and Phenyl-SiNC have very similar EL spectra (Fig. 4.14 c)) with peaks at 681 and 676 nm respectively. We conclude that the surface groups in this work do not change the emission wavelength significantly and the small differences are attributed to batch-to-batch variations and measurement inaccuracy. This is also confirmed by multiple PL studies with the same particles [147, 164, 165].

In the J-V-curves (Fig. 4.14 d)) we see, that devices based on SiNC functionalized by HS show a more resistive behaviour just as observed in the previous section. While both Dodecyl- and HS-Hexyl-SiNC-LEDs turn on at 3.5 V, the dodecyl device generates 4-5 times less current. The luminance characteristics (Fig. 4.14 e)) are quite similar: the Dodecyl-SiNC-LED reaches a maximum luminance at 0.9 cd/cm^2 before it breaks, while the HS-Hexyl-SiNC-LED goes up to 4.8 cd/cm^2. So while the current efficiency (in [Cd/A]) is very similar for both devices, the EQE is three times lower for the Dodecyl-SiNC-LED (2×10^{-3} vs. 6.0×10^{-3} %) as it emits at wavelength that are more visible to the human eye and thus should result in higher luminance values. We assume that the longer dodecyl chains result in a larger insulating layer hindering charge transport through the SiNC layer and charge injection into the SiNC similarly to effect caused by higher surface coverage as reported in the previous section; this would result in a higher film resistance, which would explain the decreased current draw and a lower charge injection would correspond to the inferior conversion efficiency.

Looking at the OLR-functionalized SiNC, we see that both devices start to turn on at 2.5 V and have very similar current draw; only at the highest operating voltages the OLR-Hexyl-SiNC-LED can generate a bit more current. This is in part owed to the fact, that the Phenyl-SiNC-LED breaks down earlier. The luminance behaviour mirrors the current characteristic: comparable emission until at the highest levels the hexyl-based device takes over reaching a maximum values of 21.4 cd/cm^{2}compared to 13.4 cd/cm^{2}for the Phenyl-SiNC-LED. Again this results in an almost identical current efficiency, but - due to a lower amount of red in the emission spectrum of the Phenyl-SiNC-LED - a lower EQE. So the phenyl-SiNC-based devices actually turn out slightly inferior to the their hexyl-based counterparts. As such we conclude that the introduction of a benzene-ring brings no improvement to the electronic coupling between SiNC or any other aspect regarding SiNC-LED performance.

4.5.5 Mixing with Super yellow

Adding QDs into a (light emitting) polymer matrix to form an organic/inorganic hybrid nanocomposite film can improve film forming properties, increase device performance, enhance long-term stability and can be used to mix emission of polymer and QD into new colors. Most of this existing work about mixing QDs into a polymer matrix has been done with the prototypical CdSe-QDs [166–171], SiNC have not been used so far.

In order to get an idea of the compatibility of SiNC with a polymer matrix, we fabricated devices with a yellow emitting, PPV-based co-polymer commonly known under its brand name *Super Yellow* (SY). The devices were made with only a PEDOT:PSS injection layer and no additional blocking layers (Fig. 4.15 a)). For the active layer we used either only SY or only OLR-Hexyl-SiNC or a mixture of the two. Interestingly, adding the solid polymer into an existing SiNC in toluene solution (3 mg/ml) would results in a very viscous, gooey liquid that was barely processable. Firstly dissolving SY in toluene and then blending it together with the SiNC solution however turned out as a normal low viscosity solution as would be expected. Therefore, the latter approach was used for fabricating the mixed layer. One has to keep in mind that this preparation lowers the concentration of solid materials in the mixed solution compared to the single solutions;

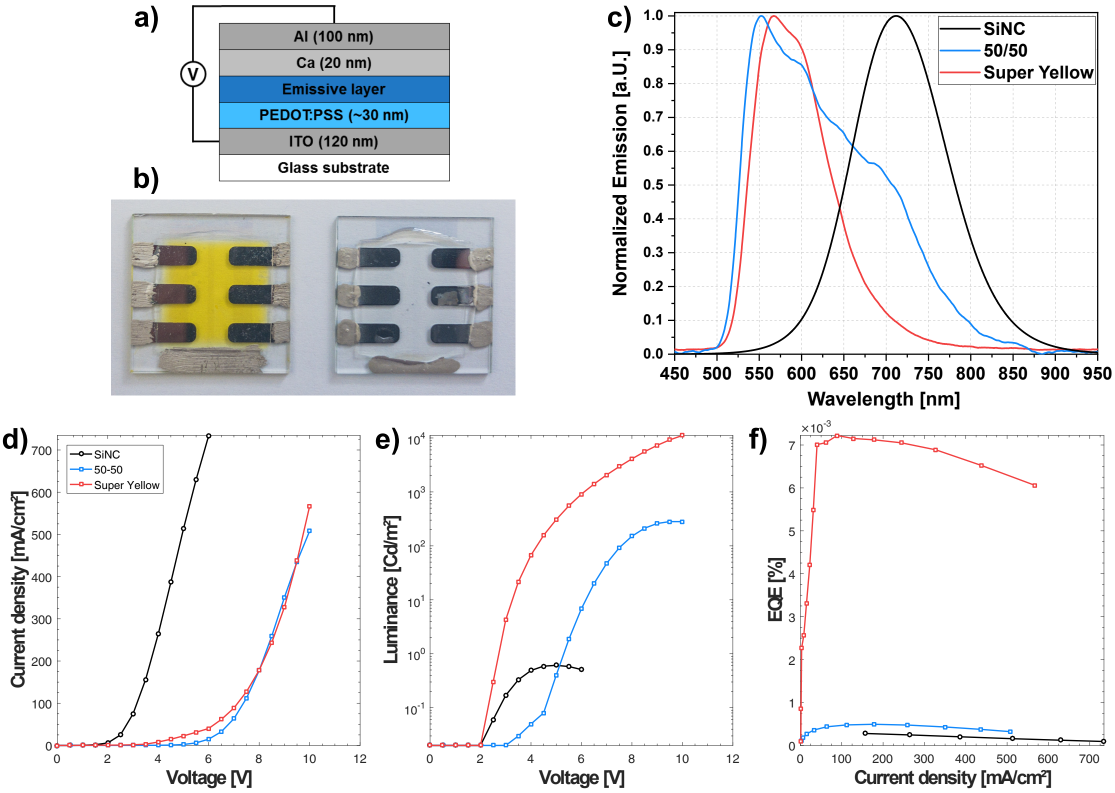

Figure 4.15: *Embedding SiNC inside a Super Yellow polymer matrix: a) LED architecture: emissive layer was either only Super Yellow, only SiNC or a blend of the two. b) Pictures of encapsulated SY- (left) and SiNC-LEDs (right). While the Super Yellow lives up to its name, the SiNC is virtually transparent. c) Normalized emission spectra. J-L-V characterization: d) current density vs. voltage, e) luminance vs. voltage and f) calculated EQE vs. current density.*

therefore, for the mixed layer the spin coating speed was lowered to achieve comparable film thicknesses.

Fig. 4.15 c) depicts a Super Yellow device (left) and a SiNC device (right). The Super Yellow film, living up to its name, has a bright yellow color, while the SiNC film is almost completely transparent. The emission spectra in Fig. 4.15 c) show the expected shapes for Super Yellow with a peak at 566 nm and a shoulder at 594 nm and for SiNC with a single peak at 711 nm. The spectrum emitted by the mixed layer clearly shows all those three features corresponding to both material components, although slightly shifted towards higher wavelength. The SiNC contribution is about half a strong as the SY part, probably a result of the mixing ratio determined by the concentration of the individual solutions before blending. Additional devices consisting of two separated emissive layer with a SiNC layer on top or underneath the SY layer would only exhibit yellow light. Since both materials are solved in toluene, such devices have to deal with severe re-solvation of the underlying layer and were not pursued further.

Looking at the J-L-V-characterization we see that the SY and the mixed device have very similar J-V curves (Fig. 4.15 d)), while the SiNC device drives much more current at the same voltages. This can mostly be attributed to the thickness of the active layers: while the SiNC film is about 30 nm thick, the SY containing layers are about three times as thick. Due to the mixing ratio of the two materials, we can assume that the electric behavior of the mixed film is dominated by the SY component.

The luminance differences are enormous (Fig. 4.15 e)): while the SiNC-LED cannot exceed 1 cd/cm^2, the SY-LED reaches a peak luminance of 11100 cd/cm^2. Again, we have to take into consideration the luminous efficiency function: the emission peak of SY EL is very close to the maximum sensitivity of the human eye, while that of the SiNC EL is at the very low end and about 500 times lower. Considering this, the SY device still emits about 22 times more light than the SiNC-LED. Correspondingly, this results in a roughly 23 times higher EQE with 7×10^{-3} vs 3×10^{-4} % (Fig. 4.15 f)) The mixed device emits yellow-orange light and has its luminance peak at 282 cd/cm^2. This is two orders of magnitude lower than the luminance of the SY-only device. Even taking into consideration that the emission spectrum now contains some red parts, this results in a low EQE of 5×10^{-4} % much closer to the SiNC-LED than to the SY-LED.

From this we suspect that the introduction of SiNC is severely quenching SY emission. One explanation might be disruption of the polymer crystal; however, that would also be visible in the J-V-curve in form of an increased series resistance in the diode. Another explanation might the formation of trap states on the SiNC-SY interface that facilitate non-radiative recombination. While the band structure of SY and SiNC is suitable for a heterojunction device, it is not ideal for hosting SiNC inside a SY matrix as holes face a potential barrier when injected from SY into SiNC. The use of a host polymer with a higher HOMO level like PVK might mitigate this issue.

4.6 Summary

In this chapter we investigated the use of surface functionalized SiNC as emitter material in solution-processable hybrid QLEDs. The devices are shining red and are clearly visible at ambient conditions. Their performance was greatly improved by introduction of PolyTPD as hole transport layer and ZnO as electron transport layer. The influence of the surface functionalization on the LED performance was analyzed along two lines: on the one had we used the same surface group but two different functionalization routes and could show that using organolithium reagents would produce better devices than the common hydrosilylation method due to a lower surface coverage and improved quantum yield of the SiNC. On the other hand different ligands were used and we found that shorter alkyl chains are better suited than longer one, while the introduction of a phenyl group containing a benzene-ring could not improve the device performance. Mixing the SiNC into a Super Yellow polymer matrix could combine the emission of both materials into a yellow-orange color, but at a large performance penalty as the SiNC seem to significantly quench SY emission.

5 Silicon nanocrystal hybrid solar cells

In this chapter we will investigate the use of surface functionalized SiNC in combination with P3HT in hybrid bulk heterojunction solar cells. Firstly, there is an introduction of the working principles in excitonic solar cells that lead to the bulk heterjunction architecture. It follows a section about how to characterize solar cells and the important performance parameters. A summary of the present state of the art will then lead over to presentation and discussion of the experimental results, which are then briefly summarized in the conclusion.

5.1 Working principle of excitonic solar cells

The fundamental working principle of organic solar cells is based on the photovoltaic effect like any conventional solar cell: incident light is absorbed and excites an electron into a higher-energy state, leaving behind a positively charged hole. These two opposite charges are then separated by a built-in potential difference to generate a photocurrent that can be used in an external circuit. The major difference of organic solar cells compared to their inorganic counterparts is their excitonic nature.

Exciton binding energy

When an electron-hole pair is generated in a semiconductor the two charges attract each other by a coulomb force. These bound electron-hole pairs can be described as quasiparticles called excitons. Excitons are chargeless and can move due to diffusion, but cannot drift and cannot be used to generate an electrical current. Therefore, to be useful for current generation these excitons have to be separated to form free charge carriers. Using the excitons similarities to the prototypic hydrogen atom, where a single electron is orbiting around the atomic core with single positive charge, their binding energy E_B can be approximated with an adapted Bohr model of the hydrogen atom, where the electron mass m_e is replaced by the adjusted effective mass m^* and the vacuum permittivity ϵ_0 is extended by the relative permittivity of the absorbing material ϵ_r:

$$E_{\mathrm{B}} = -\frac{m^* e^4}{8{\epsilon_0}^2{\epsilon_r}^2 \mathrm{h}^2}\frac{1}{n^2} \tag{5.1}$$

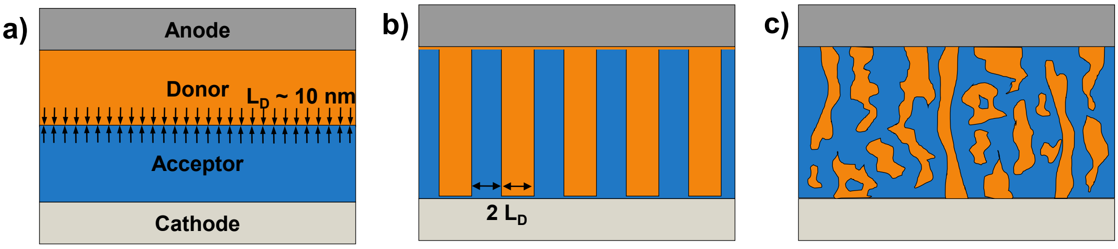

Figure 5.1: *Different heterojunction architectures that use a donor-acceptor-interface for exciton dissociation: a) the bilayer device uses two planar layers on top of each other. Exciton dissociation only occurs in a very limited area within one diffusion length from the interface. b) The ideal heterojunction makes sure that everywhere within the active layer there is an interface within one diffusion length. c) The bulk heterojunction is an easily fabricated approximation of the ideal heterojunction: donor and acceptor are deposited from one blended solution and form a random, intertwined network with a very large inner interface.*

where n is the principal quantum number of the electron. Organic materials feature lower relative permittivity ($\epsilon_{r,org} = 3.5$ compared to $\epsilon_{r,Si} = 12$), which means less electrostatic screening of the coulomb attraction between the charges and - due to their disordered crystal structure - a higher effective mass . Accodingly, excitons have significantly higher binding energies in organic materials. Inorganic semiconductors form so called Wannier-Mott excitons, which have binding energies in the order of 10 meV. Such a low energy is easily overcome by the thermal energy at room temperature ($k_BT = 26$ meV) and therefore excitons are not observed in inorganic solar cells. Organic semiconductors on the other hand mostly form so called Frenkel excitons with binding energies between 0.5 and 1 eV that cannot be dissociated by thermal energy at normal operating temperatures and an additional electrical field is required for separation [172]. The first organic solar cells used a single semiconductor material relied on the field provided by the work function difference between the two electrodes. This has proven to be a very inefficient approach and was only useful as a proof of concept with solar cell power conversion efficiencies (PCE) $\ll 1\,\%$. A much more effective way of exciton dissociation is the use of a planar heterojunction of n-type and p-type materials also called a **bilayer device** (Fig. 5.1 a)). The electron affinity (or LUMO level) of the p-type material typically is lower than of the n-type material. If this energetic difference is larger than the exciton binding energy, it becomes energetically favorable for electrons split to move to the n-type material and leave the hole behind. Vice versa a hole will move from the material with higher ionization potential (HOMO level) to the material with the lower one. Since the p-type material transfers electrons to the n-type material, they are commonly referred to as (electron) donor and acceptor. This heterojunction concept also provides the added advantage of monomolecular charge transport. After the excitons are dissociated at the material interface, the electrons travel within the n-type acceptor, and the holes travel within the p-type donor material. Those materials are optimized for the respective charge transport and the two kind of charges are separated from each other, thus greatly reducing charge recombination. These heterojunction bilayer devices were first introduced by Tang et al. in 1986 [173]. Their solar cells, based on copper phthalocyanine (CuPc) as donor and a perylene tetracarboxylic derivative (PV) as acceptor, were the first organic solar cells to reach a PCE of 1 %.

Exciton diffusion length

This was a breakthrough at the time, but the PCE is still low, which hints at another problem of organic solar cells that still needs addressing: low exciton diffusion length. The diffusion length L_D is determined by the diffusion coefficient D and the average exciton lifetime until they recombine τ:

$$L_\mathrm{D} = \sqrt{D\tau} \tag{5.2}$$

Typical excition life times are in the order of a few hundred ps [174] and the diffusion coefficient depends strongly on charge carrier mobility, which is low in organic materials. Accordingly, typical diffusion length of organic polymers lie in the order of 10 nm [175, 176], for P3HT it was shown to be between 3 - 7 nm depending on its crystalline order [177]. This means after excitation excitons can only travel 10 nm to reach an interface for dissociation, otherwise they will recombine and be lost for current generation. This explains the limitation of the bilayer device: only charges absorbed in a very small stripe around the heterojunction interface actually contribute to current generation. Such a small stripe is severely absorption limited. An ideal device would consist of an interdigitated donor-acceptor structure with a finger distance of 2 L_D as depicted in Fig. 5.1 b), so that every generated photon is always within reach of an interface for dissociation and the device thickness can be optimized for light absorption. An attempt to approximate this ideal structure is the **bulk heterojunction** (BHJ) design, firstly introduced in 1995 by Yu et al. reaching a PCE of 3 % [178]. Here, instead of fabricating two distinct layers, acceptor and donor material are put together in a single blended solution and deposited in one layer, where they form a *bicontinuous network of internal donor-acceptor heterojunctions* with an much increased interface (Fig. 5.1 c)).

Working principle

The BHJ solar cells then works in five consecutive steps, illustrated in Fig. 5.2. First, if incoming photons have sufficient energy to overcome the band gap (HOMO-LUMO difference) of the absorbing materials (E_Ph = hv ≥ E_G = E_HOMO - E_LUMO, h being Planck's constant, v the frequency of the incident light) light is absorbed in the active BHJ layer and an exciton is created (Fig. 5.2 a)). This exciton then randomly moves by a diffusion-like process and with a certain probability, depending on the network morphology, reaches a

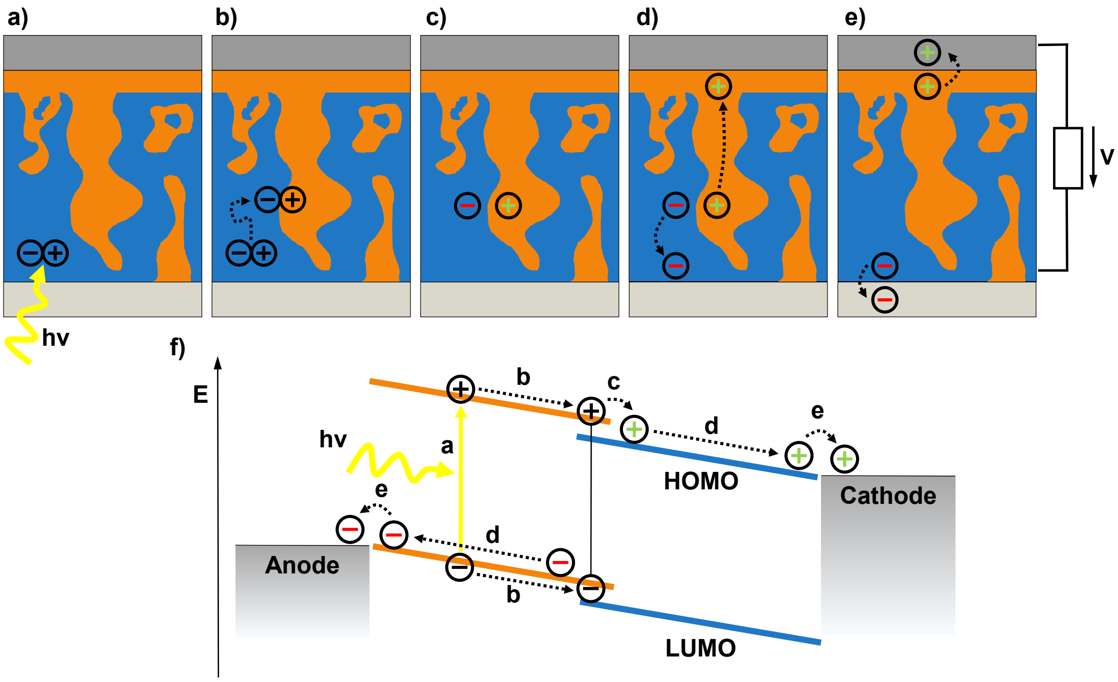

Figure 5.2: *Working principle of a bulk heterojunction solar cell (donor material in orange, acceptor in blue; anode on top, cathode at the bottom): a)* ***light absorption:*** *photons with sufficient energy to overcome the band gap of the absorbing material create an exciton (bound electron-hole pair); b)* ***exciton diffusion:*** *the exciton randomly moves around and ideally reaches a heterojunction interface within its lifetime; c)* ***exciton dissociation:*** *at the donor-acceptor interface the exciton is separated into free charge carriers; d)* ***charge transport:*** *the charge carriers drift to their respective electrodes and e)* ***charge extraction:*** *charge carriers are extracted at the metal electrodes and can be used in an external load. f) Corresponding energy diagram illustrating steps a) - e).*

donor-acceptor interface (Fig. 5.2 b)). Here it is separated into two free charge carriers. The electron will move from the donor to the acceptor phase, the hole remains in the donor phase (Fig. 5.2 c)). Then, the free charge carriers can drift to their respective electrodes (Fig. 5.2 d)). Eventually, the charges are extracted from the semiconductor layer into the electrodes (Fig. 5.2 e)). The extracted charges can then be used to do work in an external circuit.

Limitations of the bulk heterojunction

The overall efficiency of a solar cell is the product of the individual efficiencies of all the involved steps described above.

Light absorption is mainly determined by three factors: electrode transparency, active layer thickness and absorption spectra of the active materials.

For exciton diffusion it is crucial that the excitons reach a dissociation interface within their lifetime, so the morphology of the BHJ should be to have donor and acceptor domains twice the size of the exciton diffusion length. Excitons generated further away from an interface are lost for charge generation.

Efficient exciton dissociation relies on defect free interfaces and sufficient energy differences between HOMOs and LUMOs of donor and acceptor. A particular breakthrough for the charge separation was the incorporation of fullerene derivatives as acceptor material in 1992 [179, 180]. They feature strong electronegativity and high electron mobility up to $1\,\mathrm{cm^2\,V^{-1}\,s^{-1}}$ [181] and have been shown to exhibit ultrafast ($< 50\,\mathrm{fs}$) photoinduced charge transfer [182], which leads to a separation efficiency of almost 100 %.

For the charge transport there are unwanted effects stemming from the random nature of the BHJ morphology: some material phases form isolated islands that are not connected to an electrode and thus trap charges that cannot be extracted. The same goes for phases connected to the wrong electrode (donor phase to cathode or acceptor phase to anode). And some phases connect to both electrodes, where charges can also reach the wrong electrode and be lost to recombination. This recombination at the wrong electrode can be prevented by introducing blocking layers which have suitable energy bands to give small to no energy barrier for one kind of charge while providing a large one to opposite charges carriers and thus effectively blocking from reaching the wrong electrode (Fig. 5.3). Another factor for the charge transport is the layer thickness. While free charge carriers have much longer life time and higher mobility than excitons, the charge transport in disordered organic materials is still limited by polaronic effects and hopping transport as described in section 2.1.3. Therefore, there is a trade-off for the active layer thickness between maximizing light absorption and minimizing resistive losses due to charge recombination.

Eventually, the charge extraction depends on a trap free interface with the electrodes and the work functions of the electrode materials should be optimized to pose a minimal potential barrier to energy levels of the respecitve semiconductors (holes traveling in the HOMO of the donor need a high workfunction metal, electrons in the LUMO of the acceptor a low work function metal).

From this loss analysis it becomes apparent how crucial the nanomorphology of the bulk heterojunction network is to the solar cell performance. Exiction dissociation heavily depends on reaching an interface in time and charge transport on long, consecutive materials phases connected to the right electrode. As such, understanding and controlling the formation of the network morphology is a major part of the reasearch around organic photovoltaics. Some typical approaches to influence the formation involve optimizing the blend solution like solvent selection, solvent mixing and the use of processing additives others after treatments like thermal annealing or solvent annealing.

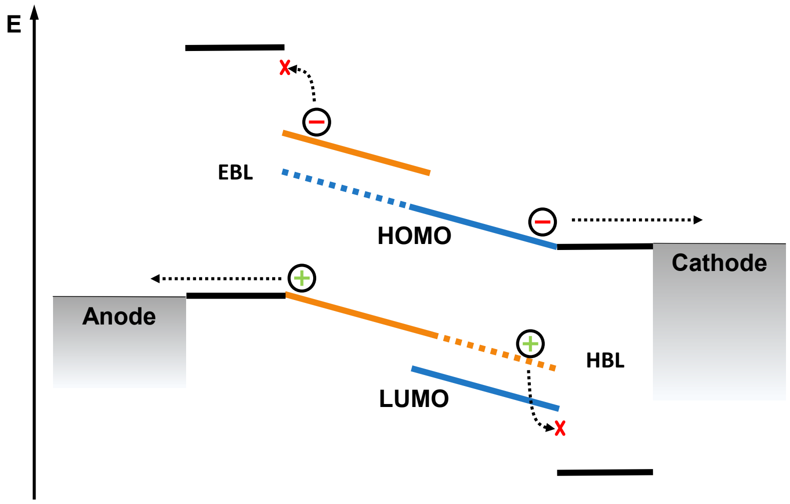

Figure 5.3: *Energy diagram of a bulk heterojunction solar cell with blocking layers on both sides (donor material in blue, acceptor in orange). Due to the random nature of the bulk heterojunction network donor and acceptor phases can touch both electrodes. Blocking layers introduced between the active layer and the electrodes prevent charges to recombine at the respective wrong electrode (electrons at anode, holes at cathode).*

Hybrid solar cells

Hybrid solar cells combine organic semiconductors with inorganic nanomaterials to choose from the best of both worlds. Inorganic materials typically offer higher thermal and morphological stability [183], broader absorption spectra and higher charge carrier mobility as os their organic counterparts. Additionally, they their properties can be tuned by changing their size (band gap), via surface functionalization and doping [184–186]. Even the generation of two or more excitons from a single high energy photon, known as multiple carrier generation (MEG), was observed, which could significantly boost power conversion efficiency [187].

The device architecture is the same as in purely organic solar cells. Bilayer devices yield very low efficiency and are only used for special investigations that require very controlled interfaces. The much more successful architecture is the bulk heterojunction as explained above. Since most polymers have significantly higher hole mobility than electron mobility, in hybrid solar cells the organic material is typically used as electron donor, while the inorganic counterpart acts as electron acceptor [183, 188]. This can help overcome a typical problem of purely organic solar cells, since the most common electron acceptor, C_{60} fullerenes, only feature very limited light absorption. In hybrid solar cells both donor and acceptor material can participate in light absorption. Furthermore, inorganic materials can generate free charge carriers at room temperature, alleviating the problem with exciton dissociation (in the inorganic phase). However, this seems not to apply to nanomaterials exhbiting quantum confinement [189–191].

As electron acceptor inorganic nanoparticles face the same requirements as their organic counter parts: to enable exciton dissociation CB needs to lie below the LUMO level of the donor polymer, the VB below the polymer HOMO level. The morphology of the bulk heterojunction network is just as important as in purely organic solar cells.

5.2 Solar cell characterization

The most important performance parameter for solar cells is their power conversion efficiency (PCE) η. It can be extracted from the current voltage (I-V) curve under illumination. To gain additional insight into the solar cell behavior different other important parameters like the open circuit voltage (V_{OC}), short circuit current (J_{SC}), fill factor (FF) and parasitic resistances can also be extracted from the I-V characterization. For information on the spectral behavior of the devices, the external quantum efficiency (EQE) is measured with monochromatic light over a range of wavelengths.

Current-Voltage (I-V) characterization

Emulating sunlight

To measure the photocurrent of a solar cell the device has to be illuminated. For measurements to be comparable all over the world there is an international standard for illuminating solar cells that defines the light intensity as well as the spectral shape of the appointed light sources. These standard test conditons (STC) specify the solar irradiation at $100\,\mathrm{mW/cm^2}$ ($1\,\mathrm{kW/m^2}$) under AM1.5 conditions. AM is the air mass coefficient, which is applied to the solar spectrum after the solar radiation has travelled through the atmosphere; it takes into account attenuation of the light by scattering and absorption by e.g. atmospheric gases.

AM0 represents the sun light before it enters the atmosphere, AM1 corresponds to sun light that traveled the shortest path through the atmosphere to sea level at ‘high noon´ when the sun’s zenith angle amounts to $z = 0°$. AM1 is only useful in equatorial regions, in most other places sunlight hits the Earth’s surface under an angle most of the time and the path length through the atmosphere is increased. AM1.5 is used as standard to account for this and approximate average conditions. It corresponds a solar zenith angle of $z = 48.19°$, where the sun light travels 1.5 times the shortest path length as under AM1 condition. This concept is illustrated in Fig. 5.4 a) and the resulting radiation spectra can be seen in Fig. 5.4 b).

In this work the light is provided by a class AAB sun simulator by Newport (Oriel

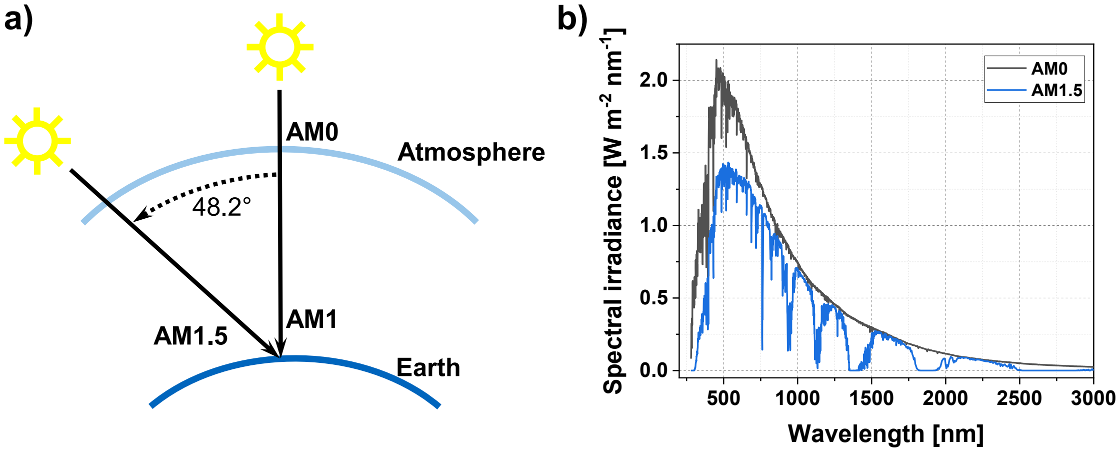

Figure 5.4: *Standard test conditions for solar cells require a light source that emulates AM1.5 conditions, which describe the spectral shape of sun light depending on how far it traveled through the atmosphere: a) schematic of the sun under different solar zenith angles z. AM0 corresponds to sun light outside Earth's atmosphere, AM1 to light that traveled the shortest path to sea level at z = 0 ° and AM1.5 to light that is incident at z = 48.19 ° and travels 1.5 times the shortest path through atmosphere. b) The corresponding solar spectral irradiance. The light is attenuated by the atmosphere due to scattering and absorption, showing charateristic absorption peaks of atmospheric gases like* O_2, O_3, CO_2 *and* H_2O *[192].*

Sol1A - 94021A) based on a xenon arc lamp and an AM1.5 filter. The irradiance is calibrated to 100 mW/cm^2 with a silicon reference solar cell (Newport 91150V). For the I-V characterization a voltage sweep is performed to the device under test with a Keithley 2602A SourceMeter. For every applied voltage, the current through the device is measured, typically in the voltage range from -0.2 V to +1 V with a step width of 0.01 V.

Equivalent circuit model

Fig. 5.5 a) shows the I-V curves of a dark and an illuminated solar cell. The dark curve shows the typical rectifying behavior of a diode with exponential current under forward bias (V > 0) and only a very small dark current (also recombination or saturation current) under reverse bias (V < 0). This diode behavior is described by the Shockley equation:

$$I_{\mathrm{D}}(V) = I_0 \left(\exp\left(\frac{qV}{n k_{\mathrm{B}} T} \right) - 1 \right) \tag{5.3}$$

where q is the electric charge, k_B the Boltzmann constant and T the temperature; n is an ideality factor, which takes the value 1 for a lossless, ideal diode and values between 1 and 2 in real diodes with recombination losses. The I-V curve of the illuminated device has the same shape as of the dark diode, but it shifted down by a photocurrent I_{Ph}. This

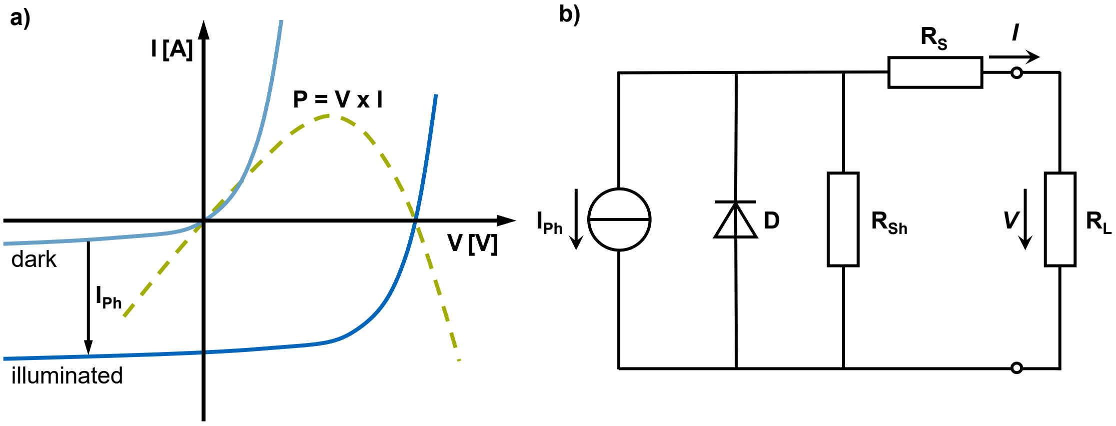

Figure 5.5: *a) I-V characteristic of a solar cell in the dark and under illumination. Both have the typical diode shape with a very low saturation current under reverse bias and an exponential current under forward bias. The curve of the illuminated solar cell is shifted down by the generated photocurrent. The power curve (dashed, green) of the illuminated device shows that power is only generated when operating in the fourth quadrant. The peak of the power curve represent the optimal operating point P_{MPP} (maximum power point). b) Equivalent circuit model of a solar cell incorporating parasitic resistances. A constant current source represents the photo-generated current, a parallel diode the rectifying nature of the device. A serial resistance stands for all ohmic losses in the device, a parallel resistance for short circuits through the device.*

photocurrent is a constant, voltage-independent current opposing the diode current.

$$\begin{aligned} I_{\mathrm{SC}}(V) &= I_{\mathrm{D}}(V) - I_{\mathrm{Ph}} \\ &= I_0 \left(\exp\left(\frac{qV}{n k_{\mathrm{B}} T} \right) - 1 \right) - I_{\mathrm{Ph}} \end{aligned} \tag{5.4}$$

While the ideality factor n accounts for some recombination losses, there are two common resistive losses that can be included more explicitly.

Fig. 5.5 b) shows the equivalent circuit model of a solar cell incorporating parasitic series and shunt resistances. A voltage-independent constant current source $\mathrm{I_{Ph}}$ represents the photocurrent, the parallel diode D represents the rectifying behavior of the device and the exponential diode current.

The parallel shunt resistance $\mathrm{R_{Sh}}$ represents alternative pathways for the current bypassing the diode, typically short circuits through the device caused by defects in the active layer directly connecting top and bottom electrode. Ideally, $\mathrm{R_{Sh}}$ should be infinite.

The series resistance $\mathrm{R_S}$ represents ohmic losses in the devices. This can be recombination losses in the semiconductor layer, depending on the quality of the organic film, network

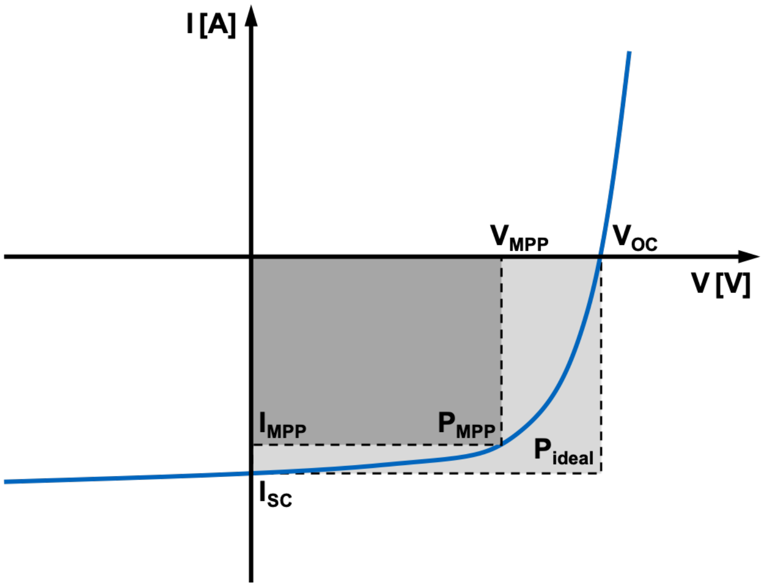

Figure 5.6: *Current-voltage-curve of an illuminated solar cell. Short circuit current* J_{SC} *and open circuit voltage* V_{OC} *are indicated. The fill factor is given by the ratio of the inner power rectangle* P_{MPP} *(maximum power generated) to the outer one* P_{ideal} *(maximum power generated by a hypothetical ideal diode).*

morphology and layer thickness, but it also includes the contact resistance between active layer and electrodes and the sheet resistance of the electrodes. Ideally, R_S should be zero.

R_L represents an external load.

Taking these parasitic resistances into account the current equation can be extended to:

$$I_{SC}(V) = I_0 \left(\exp\left(\frac{q(V - IR_S)}{n k_B T} \right) - 1 \right) - I_{Ph} + \frac{V - IR_S}{R_{Sh}} \tag{5.5}$$

The influence of the parasitic resistances on the I-V curve is discussed below (Fig. 5.7).

Performance parameters

The defining figure of merit for any solar cell is the power conversion efficiency (PCE) η. It is defined as the ratio of power generated by the device P_{out} and the input power provided by the incident light P_{in}:

$$\eta = \frac{P_{out}}{P_{in}} \tag{5.6}$$

The input power is defined by standard test conditions as $P_{in} = A \times 100\,\mathrm{mW/cm^2}$.

The electrical power generated by a solar cell is given by the product of current and voltage: $P = I \times V$. As the photocurrent is opposite to the diode current, it is typically measured as a negative current. Accordingly the power generated by the photocurrent also comes out negative. Since this is somewhat counter-intuitive the power curve is conventionally drawn inverted so that the maximum of the power curve represents It can be seen that power output is only positive when the solar cell is operated in the fourth quadrant, otherwise it is drawing power (LEDs are driven in the first quadrant, photo diodes in the third). The load resistance can be used to set the operating point of the solar cell so it always operates at maximum power point P_{mpp}, where the product of current and voltage is maximal. The respective values are called I_{mpp} and V_{mpp}.

The PCE is then easily extracted from the illuminated I-V curve:

$$\eta = \frac{P_{\text{out}}}{P_{\text{in}}} = \frac{I_{\text{MPP}} \times V_{\text{MPP}}}{A \times 100\,\text{mW}/\text{cm}^2} \tag{5.7}$$

While the PCE is an important performance parameter, by itself it gives very little insight into the behavior of the solar cell. To get further insights there are a couple more parameters that can be extracted from the I-V characterization: V_{OC}, J_{SC}, FF and parasitic resistances.

The **open circuit voltage** V_{OC} is the voltage across the device when diode current and photo current cancel out and no current is flowing: $V_{\text{OC}} = \text{V}(\text{I}=0)$ (also known as flat band condition). This is the maximum possible voltage across the solar cell. In the simplistic MIM model (introduced in section 2.3), it would constitute to the workfunction difference of the two electrode materials: $V_{\text{OC}} = 1/\text{e}\ (\Phi_{\text{Anode}} - \Phi_{\text{Cathode}})$. However, this is not true for organic solar cells. The definite description of the open circuit voltage has been under investigation for many years and is still not fully understood [193–197]. While it has been shown that the electrode workfunctions [198] and other factors like the BHJ network morphology [199] do have an impact, the main contributor is the energy difference of the donor HOMO and acceptor LUMO levels [200]:

$$V_{\text{OC}} = \frac{1}{\text{e}}(|E^{\text{D}}_{\text{HOMO}}| - |E^{\text{A}}_{\text{LUMO}}| - \Delta) \tag{5.8}$$

where the energy offset Δ has been empirically determined to lie around 0.3 - 0.6 eV. It results from interfacial recombination losses and depends on the incident light intensity [196, 197].

The **short circuit current** $\mathbf{I}_{\text{SC}}$ is the current flowing through the device when no voltage is applied (i.e., when the solar cell is short circuited). Without field there is no current contribution from the diode and all current is photo-generated (neglecting ohmic losses in the device):

$$I_{\text{SC}} = I(V = 0) = I_{\text{Ph}} \tag{5.9}$$

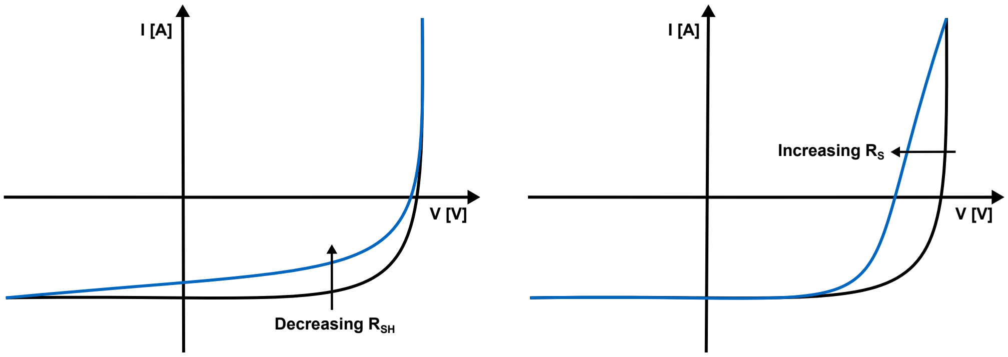

Figure 5.7: *Influence of parasitic resistances on the I-V curve: a low* R_{Sh} *decreases the voltage, a high* R_S *the current; both reduce the fill factor and thus also PCE.*

Since the generated current depends linearly on the absorption area, it is typically normalized to the area to make different devices with different areas comparable. Conventionally this current density J_{SC} is given in $\mathrm{mA/cm^2}$. It depends on how many photons are absorbed (absorption coefficient and band gap of the absorbing materials, layer thickness), but also on exciton dissociation and charge extraction and therefore the BHJ morphology, as described in section 5.1.

The **fill factor (FF)** describes how close the measured I-V curve is to the ideal, rectangular diode curve. It calculated as the ratio of the generated power $\mathrm{P_{MPP}}$ at the maximum powerpoint and the power generated by a hypothetical perfect diode with the same V_{OC} and J_{SC} as the device under test.

$$\mathrm{FF} = \frac{P_{\mathrm{MPP}}}{P_{\mathrm{ideal}}} = \frac{I_{\mathrm{MPP}} \times V_{\mathrm{MPP}}}{I_{\mathrm{SC}} \times V_{\mathrm{OC}}} \tag{5.10}$$

The closer the fill factor is to one, the more rectangular (and therefore ideal) is the I-V curve. The fill factor largely depends on the losses represented by the parasitic resistances $\mathrm{R_{Sh}}$ and $\mathrm{R_S}$ (see Fig. 5.7). These resistance values can be (approximately) extracted from the inverse slope of the I-V curve, shunt resistance at open circuit, series resistance at short circuit:

$$\frac{1}{R_{\mathrm{Sh}}} = \frac{\mathrm{d}}{\mathrm{d}V}\, I\,(V = V_{\mathrm{OC}}, I = 0) \tag{5.11}$$

$$\frac{1}{R_{\mathrm{S}}} = \frac{\mathrm{d}}{\mathrm{d}V}\, I\,(V = 0, I = I_{\mathrm{SC}}) \tag{5.12}$$

Combining the equations for FF (eq. 5.10) and PCE (eq. 5.7) then gives a description of the PCE which shows the efficiency is directly proportional of J_{SC},V_{OC} and FF:

$$\eta = \frac{I_{\mathrm{SC}} \times V_{\mathrm{OC}} \times \mathrm{FF}}{A \times 100\,\mathrm{mW/cm^2}} \tag{5.13}$$

External Quantum Efficiency (EQE)

Another efficiency measurement that can also include spectral information is the **quantum efficiency (QE)**. As the name implies it gives an efficiency not of power like the PCE but of quanta: how many photons are converted into electrons. By using monochromatic light the incoming photons can be limited to certain energies and the QE becomes a conversion efficiency per wavelength. Thus, it can give information about which wavelength contribute the most the photocurrent.

The QE is usually divided into external and internal quantum efficiency (EQE and IQE). For the EQE all incident photons are considered and therefore it is also referred to as incident photon to current efficiency (IPCE). For the IQE, reflection and transmission losses are factored out and only photons which are actually absorbed in the photoactive layer are considered (much more difficult to measure than EQE).

To measure the EQE a solar cell is illuminated with monochromatic light over a range of different wavelengths and the generated photocurrent is measured. The number of extracted electrons can then be calculated from the measured current divided by the electron charge; the number of incident photons from the power of the incident light divided by the photon energy:

$$\mathrm{EQE} = \frac{\text{number of extracted electrons}}{\text{number of incident photons}} = \frac{I_{\mathrm{Ph}}/\mathrm{e}}{P_{\mathrm{in}}/E_{\mathrm{Ph}}} \tag{5.14}$$

For this it is crucial to have a light source with calibrated intensity (irradiance) for all wavelengths.

The EQE measurement is based on comparing the photo response of the measured solar cell with the response of a calibrated reference detector with know responsivity. The EQE can then be computed from the ratio of the response of the silicon reference detector and to that of the solar cell:

$$\mathrm{EQE}_{\mathrm{SC}}(\lambda) = \frac{V_{\mathrm{SC}}(\lambda)}{V_{\mathrm{Ref}}(\lambda)} \times \frac{A_{\mathrm{SC}}}{A_{\mathrm{Ref}}} \times \mathrm{EQE}_{\mathrm{Ref}}(\lambda) \tag{5.15}$$

The details of the measurement setup are described in Chapter 3.4.5.

Since there is no load applied to the solar cell during the EQE measurement, it is operated at short circuit condition. Therefore, integrating over the EQE also gives J_{SC};

$$I_{\mathrm{SC}} = \mathrm{e} \int f_{\mathrm{Ph}}(\lambda)\ \mathrm{EQE}(\lambda)\ \mathrm{d}\lambda \tag{5.16}$$

where f_{Ph} is the photon flux of the incident light. This connection can be used to check if EQE and I-V measurement are in agreement and to identify measurement inaccuracies.

5.3 State of the art

Inorganic nano materials combine the advantageous properties of inorganic materials with low-cost solution processability typical for organic materials. Especially broad absorption spectra and high charge carrier mobility as well as tuneability by size and surface functionalization make them interesting for solar cell applications [50, 141, 184, 201, 202]. They can be used in purely inorganic devices (quantum dots solar cells) or in combination with semiconducting polymers as hybrid solar cells. Extensive reviews of purely inorganic quantum dots solar cells have been published by Prof. Sargent [201, 202].

Hybrid solar cells

The most common hybrid design is based on a bulk heterojunction of organic and inorganic materials and sometimes described as *nanocomposite* hybrid solar cells. They have been made with a variety of inorganic materials, mostly as electron acceptor together with P3HT as electron donating polymer: ZnO [203–206], TiO2 [207–210], CdSe [211], CdTe [212–214], PbS [215], PbS_xSe_{1-x} [216], $CuInS_2$ [217] and $CuInSe_2$[218]. A lot of the works only achieved modest results barely exceeding 1 % PCE. However, recently some notable works have reached PCEs exceeding 5 %: Liu et al. reached 5.5 % by optimizing a combination of $PbS_{0.4}Se_{0.6}$ nanocrystals and the low-bandgap polymer PDTPBT [216]. Jin et al. compared different device structures and optimized the mixing ratio of PPV:CdTe-NC to reach efficiencies of 5.6 % [214]. Du et al. could reach 6.4 % by constructing a porous CdTe film, which then was was infiltrated with the low bandgap polymer PTB7. This approach of separating the two materials allows to use higher annealing temperatures for the NC film without damaging the polymer and to neglect the intermiscibility of polymer and NC leading to a a record efficiency [213]. More in-depth reviews on the different hybrid solar cells can be found in the literature [12, 219].

SiNC:polymer solar cells

Wide bandgap semiconductors like TiO and ZnO cannot contribute meaningfully to light absorption and all works with noteworthy PCE are based on nanocrystals containing heavy metals like Cd and Pb.

SiNC offer an interesting alternative combining good physical properties with abundance and environmental friendliness. There is a variety of works on colloidal SiNC in hybrid solar cells in combination with a polymer [87–93, 95, 220–225]. An overview of other approaches to integrate nanoscale silion like multiple exciton generation (MEG, also photon cutting) [226, 227], light-trapping [228], reducing reflections (black silicon) [229], Si nanowires [230, 231] and photoluminescence down-shifters (solar shapers) [232–235] into solar cells can be found in the literature [236].

The first report of hybrid SiNC:polymer solar cells stems from Liu et al. in the group of Prof. Kortshagen in 2009 [88]. They used unfunctionalized, hydrogen-terminated SiNC synthesized by plasma decomposition of silane and investigated the influence of different particle sizes and SiNC:P3HT mixing ratios. The best solar cell performance was obtained for the smallest SiNC (3 - 5 nm) and 35 wt.-% SiNC in the P3HT:SiNC blend. The advantage of smaller particles is ascribed to increased interfacial area in the BHJ for exciton dissociation and improved band alignment due to quantum confinement. The optimized cells featured a PCE of 1.15 %, increasing V_{OC} from 0.6 to 0.75 V compared to P3HT-only solar cells. EQE measurements showed current contribution from both materials.

In their follow-up work the effects of annealing temperature, annealing period, and metal cathode material are studied [89]. It is shown that annealing does not change V_{OC}, but can greatly increase J_{SC} by up to 80 %. Al is shown to be the optimal cathode and that higher (Ag, Au) as well as lower (Ca, Mg) WF metals impair the device performance. The low WF materials generate less current, while the high WF metals greatly reduce V_{OC}. An optimized device made from SiNC with diameter 3 - 5 nm and 1:1 P3HT:SiNC ratio, annealed at 150 °C for 120 min could reach a PCE of 1.47 % with a V_{OC} of 0.8 V.

In their work on SiNC:MDMO-PPV devices they could show that the lower HOMO of MDMO-PPV results in an increased V_{OC} compared to P3HT (0.95 vs 0.80 V) [93]. However, due to narrower absorption spectrum and lower hole-mobility of MDMO-PVV compared to P3HT, photo current is much lower in SiNC:MDMO-PVV devices delivering only a PCE of 0.49 % for optimized devices.

Similar work was done by Niesar et al. in the group of Prof. Stutzmann. They also use unfunctionalized, hydrogen-terminated SiNC made by plasma decompostion of silane and combine them with P3HT. In their first work in 2009 they used SiNC with a diamter of 18 nm and a BHJ with material gradient to increase the number of percolation paths by spin-coating several layers from solutions with increasing SiNC:P3HT ratio [87]. They could show that both materials contribute to current generation and that a significant part of the photocurrent originates from the interface between the two materials and not from Schottky barriers at the contacts. V_{OC} increased from 0.6 to 0.76 V upon addition of SiNC to P3HT, but overall current generation was very low with a PCE of 0.01 %. In their 2011 work they investigated different particles sizes, material ratios and annealing treatments [91]. By removing the native oxide shell of unfunctionalized SiNC with an HF treatment right before processing, the current generation in their devices could be increased by two orders of magnitude. Their optimized device was made from 4 nm SiNC with 60 wt.-% SiNC and 160 °C annealing and featured a PCE of 1.1 % with a V_{OC} at 0.6 V. Similar to Kortshagen they conclude that the quantum confinement of small particles results in a bandgap widening benefical to exciton dissociation.

Svrcek et al. in the group of Prof. Kondo blended unfunctionalized SiNC made from electrochemical etching of boron-doped silicon with the low bandgap polymer PTB7 in a 1:1 ratio. The size of their SiNC is not reported and the final product after synthesis contains aggregates up to micrometer size. Replacing P3HT with PTB7 could significantly increase J_{SC} and boost V_{OC} from 0.62 to 0.95 V. A microplasma surface treatment of the SiNC and sonication of the blend could further improve the device performance and push V_{OC} to over 1 V. However, overall device performance was still low with a maximum PCE of 0.03 % [220, 221].

Ding and the group of Prof. Nozaki also used plasma synthesis, but decompose silicon tetrachloride ($SiCl_4$) which is cheaper and easier to handle than silane (SiH_4). The unfunctionalized SiNC have a diameter of 6 nm and are partially chlorine-terminated. They also investiagte the blending ratio of SiNC and P3HT and find a steady increase of J_{SC} upon SiNC addition until a ratio of 1:1 [222]. Adding more SiNC deteriorates device performance dramatically. In their first work they only reach a PCE of 0.15 % with a V_{OC} of 0.4 V. In a second publication they convert the clorinated surface into a hydrogen-terminated one by oxidization and subsequent HF vapor etching [223]. This significantly increases the current generation in their devices increasing the PCE to 0.53 % with V_{OC} of 0.44 V. When replacing the P3HT with the low bandgap polymer PTB7, performance drastically increases to a record PCE of 2.25 % with a V_{OC} of 0.58 V.

Ternary polymer:fullerene:SiNC solar cells

There are also works on ternary P3HT:PCBM:SiNC blends, where SiNC are introduced as a third component into the model system P3HT:PCBM. Kim et al. used SiNC made by laser ablation and treated with HF to remove the oxide shell with diameter of roughly 5 nm [92]. Addition of the SiNCs lead to increased current generation and an optimal ratio of 3.8 wt.-% was identified. Such devices increased the PCE from 2.8 to 3.2 %, mostly due to increased current, V_{OC} only slightly increased from 0.61 to 0.63 V. When the particles were functionalized with 1-octene, the device performance went down drastically to a PCE of 0.5 % while maintaining a V_{OC} of 0.57 V.

Similar work was done by Zhao et al. with hydrogen terminated SiNC made from plasma and diameter of 3.3 nm [225]. In contrast to adding SiNCs into the P3HT:PCBM mixture, they systematically replaced parts of either PCBM or P3HT with SiNCs. While the replacement of the polymer component significantly reduced device performance, a replacement of the fullerene could improve the device. Best results were achieved with replacing 5 wt.-% of PCBM with SiNC. While V_{OC} was slightly reduced from 0.59 to 0.51 V, J_{SC} increased from 9.1 to a very high 16.2 mA/cm^2, resulting in a PCE of 4.1 vs 2.9 % in the reference device. In an AFM study they show how higher SiNC loadings strongly disturb the film structure.

SiNC solar cells without polymer

Different efforts to use SiNC without a polymer with [95, 237] or without [90] a fullerene interlayer/heterojunction would show functional diodes with photo activity and considerable open circuit voltages, but virtually no current generation with PCEs not exceeding 0.05 %.

Summary

In summary it can be observed that in all reports small particle sizes in the order of 3 - 5 nm give the best results, presumable because the band gap widening caused by quantum confinement is beneficial for interfacing with common polymers.

The mixing ratio of SiNC and polymer is a crucial parameter in the majority of the publications. The exact value differs from group to group but typically lies between 30 - 60 % of SiNC in the blend.

Addition of SiNC mostly increases the open circuit voltage of by 0.1 - 0.2 V up from around 0.6 V for P3HT-only devices (with Al electrode). Replacing P3HT with other polymers can further increase V_{OC} towards and beyond 1 V.

Another crucial factor is the particle surface. Unfunctionalized SiNC with hydrogen termination are prone to surface oxidization and different surface treatments, typically involving HF-etching, have been shown to vastly improve device performance.

5.4 SiNC:P3HT hybrid solar cells

With one exception [92] all reports in the literature have used un-functionalized SiNC, where the Si surface atoms are terminated with hydrogen atoms. Such particles are typically prone to oxidation, which leads to formation of an insulating SiO shell, which renders them useless for electronic applications. Additionally, hydrogen-terminated particles are not very stable in solution, tend to precipitate and agglomerate. Therefore, unfunctionalized particles require HF etching and sonication immediately before usage. Functionalizaiton with suitable surface groups prevents surface oxidation and provides colloidal stability, two factors that make handling, storage and processing much easier [141]. Furthermore, the functionalization can be used to tune the optoelectronic properties of the particles [141].

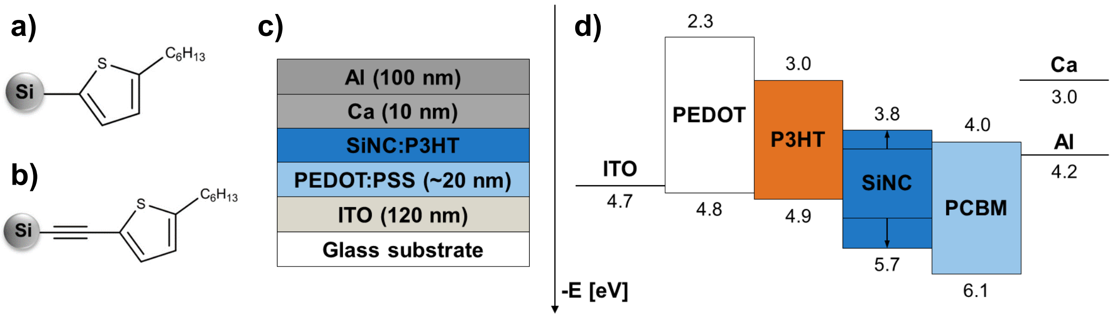

Figure 5.8: *SiNC functionalized with hexylthiophene: a) bonded on the Si surface directly (2-hexylthiophene) and b) bonded via an ethynyl group (2-ethynyl-5-hexylthiophene). c) Non-inverted device stack used for SiNC:P3HT solar cells and d) the corresponding proposed band diagram.*

5.4.1 Device architecture

Putting simple organic groups on the SiNC surface can passivate the particles and introduce energetic barriers for charge extraction. In an attempt to address this issue, the particles in this work have been functionalized with hexylthiophene groups directly bonded on the Si surface (Fig. 5.8 a)). These are the same groups that form the P3HT polymer chain that we use as donor. Therefore, the SiNC should interface well with P3HT and benzene-ring-induced π-π stacking might improve the charge transport off the SiNC. In an attempt to further improve this charge transport, we also tried a with functionalization ethynyl-hexylthiophene (Fig. 5.8 b)). The additional ethynyl group results in conjugated system right onto the Si surface. Apart from the surface groups, the SiNC are the same as used for the LEDs in the previous chapter. They have a diameter of 3.1 nm and were fabricated by Arzu Angı in the group of Prof. Rieger. The SiNC were synthesized by thermolysis of hydrogen silsesquioxane (HSQ), functionalized with organolithium reagents (OLR) and dissolved in dry toluene (described in more detail in Chapter 3.3.5).

To investigate the suitability of SiNC functionalized with hexylthiophene-groups, we made SiNC:P3HT hybrid solar cells with three different kinds of SiNC: functionalized with hexylthiophene, functionalized with ethynyl-hexylthiophene or unfunctionalized. The solar cells have been made according to the stack depicted in Fig. 5.8 c) and are fabricated as described in Chapter 3.2. The basic setup is a non-inverted device architecture with pre-structured ITO on a glass substrate as transparent electrode (anode), PEDOT:PSS as smoothing and blocking layer and evaporated calcium and/or aluminum as opaque, reflecting top electrode (cathode).

The band diagram in Fig. 5.8 d) shows the energy levels of a all involved materials. The band edges for SiNC with 3.1 nm diameter have been estimated in Chapter 4.5.2 and the corresponding band gap widening compared to bulk silicon is indicated in the figure.

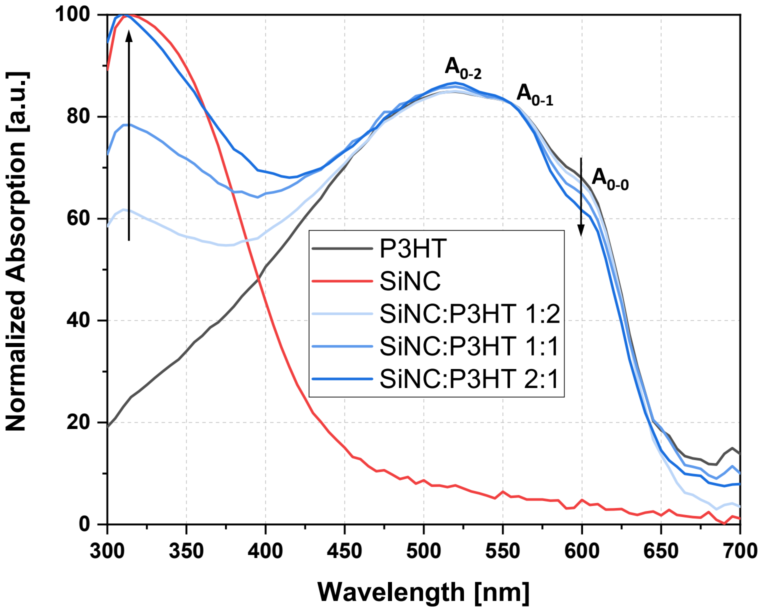

Figure 5.9: *Absorption measurements of thin films on glass. P3HT was blended with different amounts of ethynyl-hexylthiophene-SiNC in toluene and annealed at 60 °C. The two materials' spectra complement each other and in the mixed layers both materials contribute to absorption. Increasing the SiNC ratio clearly increases the respective absorption peak in the UV-region relative to the P3HT absorption peaks.*

From this estimation it can be seen that SiNC are a good match for P3HT with CB and VB about 0.8 eV below LUMO and HOMO of P3HT, providing a significant energy difference for exciton dissociation. The SiNC even provide appropriate energy differences to serve as electron donor for PCBM with a CB above the PCBM LUMO and a VB above the PCBM HOMO. Such cascading energy alignment has been shown to improve exciton separation and charge transport in ternary solar cells [225, 238–240]. This makes them suitable for integration into ternary SiNC:P3HT:PCBM devices. However, we have to keep in mind the energy differences in this case are relatively small (0.2 eV and 0.4 eV), since typically 0.3 eV is assumed as required for efficient exciton dissociation [200].

Absorption

To asses if functionalized SiNC can contribute to light absorption in combination with P3HT, transmission measurement have been done on single films. For this solutions of P3HT, SiNC and blends with 1:2, 1:1 and 2:1 ratios of P3HT:SiNC have been prepared in toluene and were spin coated on a glass substrate with subsequent annealing at 60 °C for 10 min. The results for ethynyl-hexylthiophene-SiNC are shown in Fig. 5.9.

The absorption of pure P3HT shows the well resolved, characteristic shape of regioregular, well ordered P3HT. There are two peaks at around 520 nm and 550 nm and one shoulder around 600 nm, which all correspond to π-π^* transitions with different vibrational levels. These absorption peaks are denoted as $A_{0\text{-}2}$, $A_{0\text{-}1}$, $A_{0\text{-}0}$, where the index numbers represent the vibrational band ν of ground state and excited state of the respective electron transition. Absorption cuts off at a wavelength around 650 nm, which corresponds well to the optical band gap of P3HT $E_\mathrm{G} = 1.9\,\mathrm{eV}$ as 650 nm is equal to a photon energy of $E_\mathrm{Ph} = \mathrm{hc}/\lambda \approx 1.24/0.650\,\mathrm{eV} = 1.91\,\mathrm{eV}$. The SiNC films show an absorption spectra typical for SiNC: strong absorption in the UV region, a steep decline until 450 nm and a long tail cutting off between 650 and 700 nm [88, 90, 93, 223].

The absorption of the mixed layers show clear contributions of both materials and exhibit the characteristic features of SiNC and of P3HT. The spectra of the two materials complement each other well and show little overlap. The spectra have been normalized to the main absorption peak at 520 nm and it can be clearly observed how a higher SiNC proportion increases the absorption peak in the UV region.

The absorption spectra of molecules can give a lot of information about properties like film order and chain length and P3HT has been thoroughly studied in that regard [241–244]. The spectra of P3HT with low order (e.g, in solution or films of regiorandom P3HT) are less defined and shifted to the blue [241]. The $A_{0\text{-}0}/A_{0\text{-}1}$ ratio is an indicator for the ratio of non-aggregated (amorphous) and aggregated (crystallized) P3HT molecules and thus of the film order [243]. Such a change in the $A_{0\text{-}0}/A_{0\text{-}1}$ ratio is actually observed upon addition of SiNC to P3HT and increases with larger amounts of SiNC. This indicates that SiNC are to some degree disturbing the P3HT network and lower its order.

5.4.2 Annealing

To investigate if functionalized SiNC are suitable as active material for hybrid solar cells in combination with P3HT, devices have been fabricated with either only P3HT or with a blend containing 50 % P3HT and 50 % hexylthiophene-SiNC. Both solutions were prepared with the same amount of solids and spin coated at 1000 rpm, which resulted in comparable thickness of around 55 nm for both films. The top electrode consisted of Al.

Additionally, in this experiment we wanted to see how such solar cells react to annealing treatment, as it is well know that thermal annealing can improve organic bulkhetero-junction solar cells. The heat treatment helps with crystallization of the materials, which impoves charge transport, and it drives phase separtion in the heterjunction, which can improve the morphology of the donor-acceptor network [245–247]. The beneficial effect of annealing has also been shown for hybrid devices with unfunctionalized SiNC [89, 91]. To asses if solar cells with functionalized SiNC can also profit from annealing the fabricated devices have been treated three times: firstly with relatively mild 80 °C for

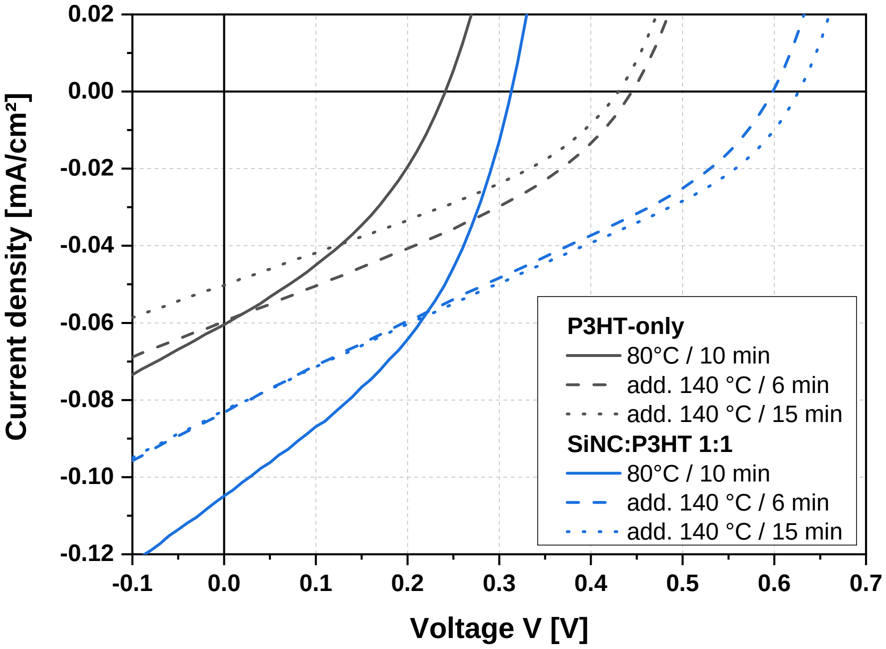

Figure 5.10: *J-V-curves of solar cells with either P3HT or P3HT:hexylthiophene-SiNC in a 1:1 ratio as active layer and with aluminum cathode. Both devices underwent three consecutive annealing treatments: firstly 80 °C for 10 min right after deposition of the active layer and then 140 °C for 6 min on the finished and encapsulated device after the first characterization, followed by another 140 °C for 10 min. Both devices profit from the higher temperature treatment, significantly increasing the open circuit voltage.*

Table 5.1: *Figures of merit of P3HT solar cells with and without 50 % hexylthiophene-SiNC after different heat treatments.*

P3HT-only	V_{OC} [V]	J_{SC} [mA/cm^2]	FF [%]	PCE [%]
80 °C / 10 min	0.24	-6.05E-02	36	0.0052
add. 140 °C / 6 min	0.44	-5.97E-02	34	0.0090
add. 140 °C / 10 min	0.43	-5.03E-02	34	0.0073
P3HT:SiNC 1:1				
80 °C / 10 min	0.31	-1.05E-01	40	0.0129
add. 140 °C / 6 min	0.60	-8.32E-02	30	0.0150
add. 140 °C / 10 min	0.63	-8.27E-02	30	0.0157

10 min right after deposition of the active layer. Then the finished and encapsulated devices were characterized and treated with 140 °C for 6 min, followed by another 10 min at 140 °C.

Table 5.2: *Performance parameters of hexylthiophene-SiNC:P3HT solar cells with different mixing ratios.*

SiNC ratio	V_{OC} [V]	J_{SC} [mA/cm^2]	FF [%]	PCE [%]
P3HT-only	0.43	-5.03E-02	34	0.0073
33 % SiNC	0.56	-6.28E-02	33	0.0115
50 % SiNC	0.63	-8.27E-02	30	0.0157
66 % SiNC	0.51	-5.09E-02	35	0.0091

The resulting J-V-curves under illumination are presented in Fig. 5.10 along with the solar cell performance parameters in Table 5.1. The presented devices are the best out of 12 with the same configuration.

It can be seen that the addition of SiNC significantly increases the performance across all annealing treatments; especially the generated photo current, but also the built-in potential. At 80 °C J_{SC} increases by 73 %, V_{OC} by 29 %. However, open circuit voltage values are lower than expected. This changes with the first 140 °C treatment, after which V_{OC} of both devices almost doubles. A V_{OC} of 0.4 V for P3HT-only and 0.6 V for a blend is similar to other reports in the literature with similar devices [91, 221]. While the generated photocurrent of P3HT-only devices barely changes upon the second annealing, there is a 20 % drop for the SiNC:P3HT device. However, the annealing still presents a net gain in efficiency. The second annealing with 140 °C has less impact: the P3HT device takes some harm and generates less current resulting in 18 % lower PCE, while the blend device slightly improves by 5 %.

Interestingly, all performance gains are driven by the gain in V_{OC} contrary to the reports of Niesar et al. [91] and Liu et al. [89]. Both groups observed efficiency gains after annealing at comparable temperatures as used here, but they are mostly driven by increasing current while V_{OC} does not change.

It can be concluded that addition of SiNC significantly improves the devices, resulting in a 74 % increase in PCE. However, the final PCE of 0.0157 % is still very low. While similar to some reports [87, 222], it is far from best reported values of over 1 % [88, 89, 91, 223] or the 3+ % that are achievable with P3HT:PCBM devices.

5.4.3 Influence of SiNC:P3HT mixing ratio

The mixing ratio of SiNC and P3HT impacts the absorption spectrum of the device (Fig. 5.9), but also film quality and morphology, with influence on the size of the donor-acceptor interface and the possibility to form percolating paths to the respective electrodes [91, 225]. To investigate this, devices have been made from solutions with 0, 33, 50 and 66 % of SiNC in the SiNC:P3HT blend with annealing at 140 °C for 15 min. All solutions

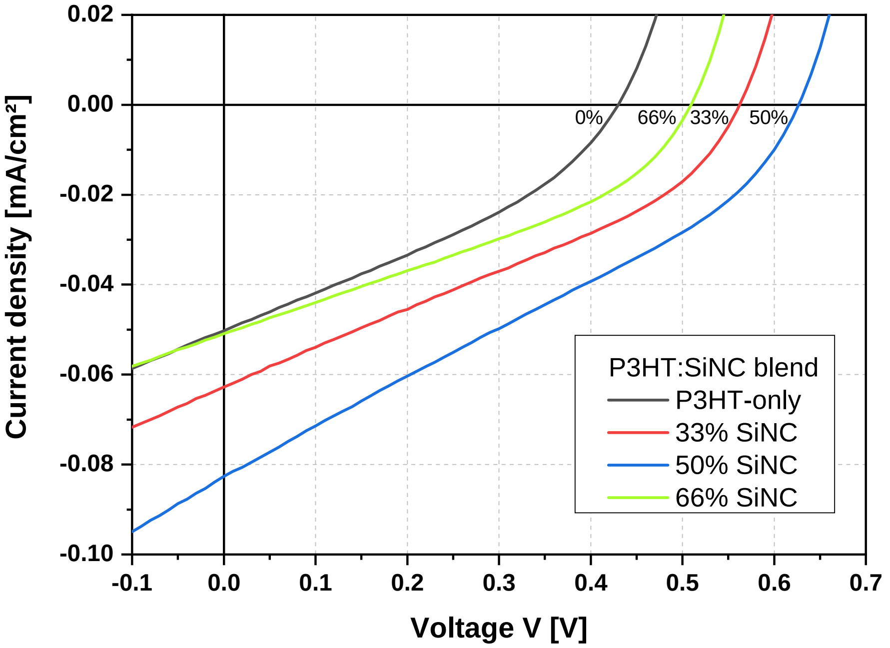

Figure 5.11: *J-V curves of solar cells with different mixing ratios of hexylthiophene-SiNC:P3HT, annealed at 140 °C and with Al cathode. Adding SiNC clearly has a positive impact as all devices with SiNC perform better than the P3HT reference. A balanced 1:1 ratio gives the best performance.*

contained the same amount of solids to ensure comparable thicknesses around 55 nm. Fig. 5.11 shows the resulting J-V-curves under illumination, the characteristic solar cell parameters are presented in Table 5.2.

As can be seen all devices with SiNC perform better than the device with only P3HT. The device with 50 % SiNC clearly best, while adding more or less particles to the blend reduces not only the photocurrent but also V_{OC}, with only minor improvements to the fill factor. The 66 % ratio performs worse than the 33 % with no current improvement over the P3HT-only device. This behavior is probably founded in the nature of the bulk heterojunction: too little SiNC in the blend leads to the formation of large P3HT domains with little interfacial area for excition dissociation and many generated exitons cannot reach an interface within their lifetime. Furthermore, if the amount of SiNC is too low, there is the risk that no or too few connect into a percolating path to the cathode. Vice-versa the same holds true if the SiNC ratio is too low.

Since the 1:1 ratio was already used in the previous experiment, the PCE of 0.0157 % could not be increased further.

5.4.4 Ca and Al electrodes

The workfunctions of the electrode materials play an important role in charge extraction of solar cells as energy mismatch between cathode and acceptor or anode and donor can introduce potential barriers. Such non-ohmic contacts lead to surface recombination. Additionally, these workfunctions also influence the open circuit voltage of the device. As discussed in section 5.2 this influence is not as strong the MIM model would suggest and V_{OC} is largely determined by the active materials. However, the electrodes have some influence and can be optimized. The most commonly used low work function cathode material is aluminum, which has a work function of $\Phi_{Al} = 4.2\,\text{eV}$. Metals with even lower work function are barium (2.6 eV), calcium (2.9 eV) and magnesium (3.7 eV). Alternatively, a thin interlayer of LiF [248, 249] or PEI [120] can be used to lower the work function of an electrode.

Low work function metals are by nature very reactive and prone to exidation, which can make them difficult to handle and can have a negative impact on the device lifetime [122]. To mitigate this to some degree the reactive metals are often covered by another less reactive metal like aluminum or silver.

For polymer:fullerene solar cells it has been shown that calcium can increase the V_{OC} by up to 0.18 eV over aluminum electrodes [250–252]. The increase comes alongside some improvements of the fill factor, but no change of J_{SC}. For polymer:SiNC solar cells reports are scarce. In the work of Liu et al. Al was found to be the optimal electrode, while metals with higher work function would quench the open circuit voltage and ones with lower work functions did not impact V_{OC}, but hampered current generation [89].

Table 5.3: *Solar cell performance parameters for P3HT devices with and without SiNC comparing Al and Ca/Al electrodes.*

Sample	V_{OC} [V]	J_{SC} [mA/cm^2]	FF [%]	PCE [%]
P3HT-only - Al	0.44	-5.97E-02	34	0.0090
P3HT-only - Ca/Al	1.18	-5.67E-02	29	0.0193
SiNP:P3HT 1:1 - Al	0.57	-9.28E-02	35	0.0186
SiNP:P3HT 1:1 - Ca/Al	0.90	-1.09E-01	29	0.0286

To investigate the difference between aluminum and calcium cathode, we made devices with either 100 nm of aluminum or 10 nm calcium and 100 nm of aluminum as capping layer. The active layer was made with the previously optimized parameters: 50 % SiNC ratio, 55 nm and annealing at 140 °C for 15 min. P3HT-only devices were made for reference.

Fig. 5.12 shows the resulting J-V-curves under illumination, the characteristic solar cell parameters are presented in Table 5.3. As can be seen the Ca electrode brings a significant

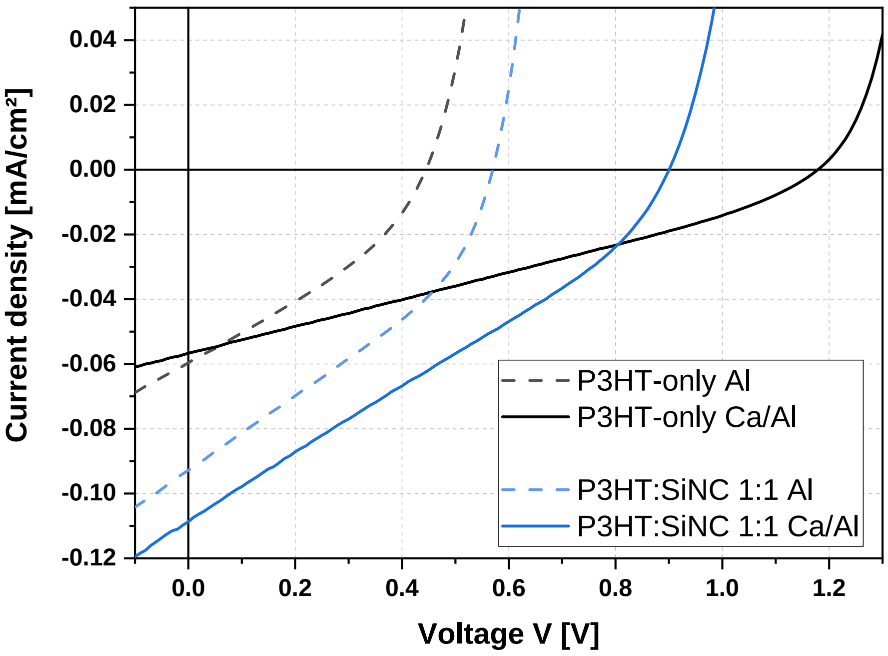

Figure 5.12: *J-V-curves of solar cells with either only P3HT or a P3HT:hexylthiophene-SiNC blend with 1:1 ratio as active layer and either Al or Ca/Al cathode. Both material systems clearly profit from the lower work function calcium electrode.*

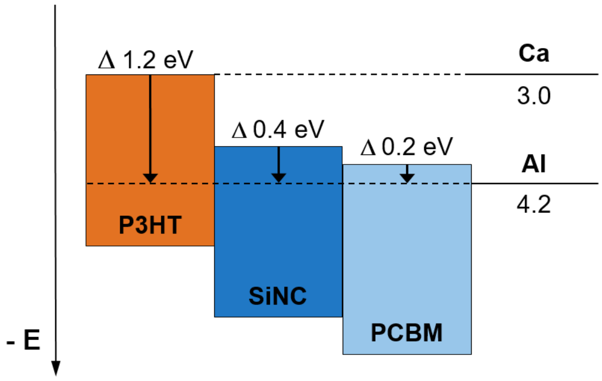

Figure 5.13: *Band diagram illustrating the potential difference between the work function of Al and the LUMO/CB of the active materials in our solar cells. Al quenches the HOMO$_D$-CB$_A$-difference of all three materials while Ca does not.*

improvement to reference devices as well as to the hybrid devices. While for the reference the current generation does not change significantly, V_{OC} increases by 170 % from 0.44 V to 1.18 V. For the SiNC:P3HT system both parameters show significant improvement. The V_{OC} increases by 50 % from 0.57 V to 0.90 V, J_{SC} goes up 17 %.

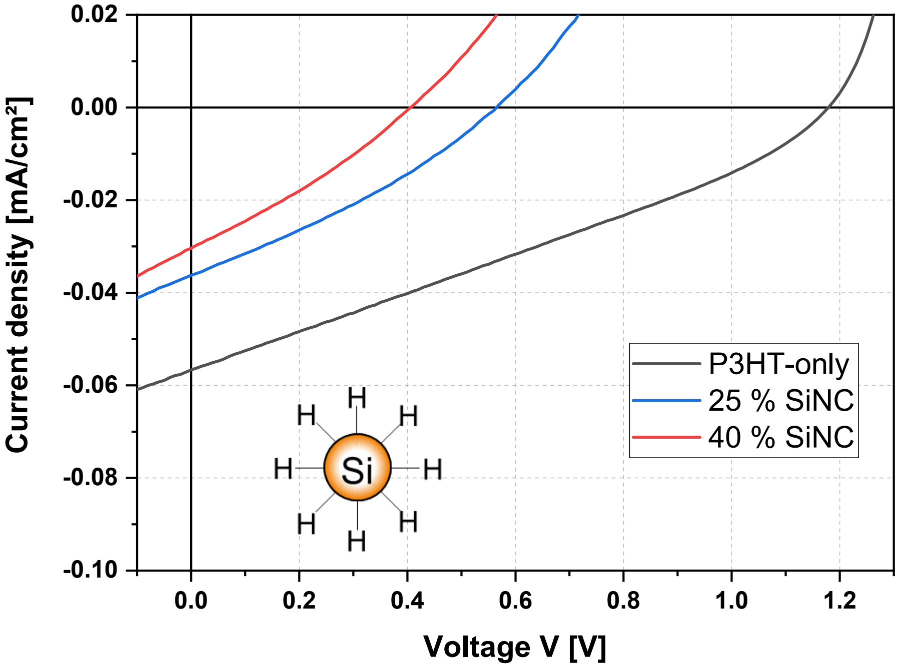

Figure 5.14: *J-V-curves of solar cells made from P3HT with and without unfunctionalized SiNC. Adding SiNC does not improve the device, but significantly deteriorates the performance.*

Concerning the open circuit voltage these results are in good agreement with the theory that V_{OC} is determined by difference between donor HOMO/VB level and acceptor LUMO/CB level, but can be quenched if the electrode work function difference is smaller. From the (approximated) band diagram (Fig. 5.8) we can extract that the Al work function lies about 1.2 eV above the P3HT LUMO, 0.4 eV above the SiNC CB and 0.2 eV above the PCBM LUMO (illustrated in Fig. 5.13) and as such quenches the potential difference created by the $HOMO_D$-LUMO/CB_A-gap of all three systems (P3HT-only, P3HT:SiNC and P3HT:PCBM). The Ca work function on the other hand is smaller or equal to the the respective LUMO/CB and should not quench any of those systems. This correlates well with with the reported V_{OC} gains associated with replacing Al with Ca of 0.74, 0.33 (from this experiment) and 0.18 V (from literature [251]) and explains why the P3HT-only system profits so much more than the blended systems.

In the work of Liu et al. the calcium electrode did not increase V_{OC}. Since they used particles with slightly larger radius (3 - 5 nm), they might have a higher CB level due to decreased band gap widening and as such experience less quenching from Al. Such a reduced CB edge would also be in agreement with the 0.1 V lower V_{OC} (0.8 V) compared to presented in this work (0.9 V) as the $HOMO_D$-CB_A-gap is reduced. Optimization of mixing ratio, annealing treatment and cathode material could significantly improve SiNC:P3HT devices. However, the best presented device exhibits a PCE of 0.03 % which

Table 5.4: *Figures of merit for solar cells with different amount of unfunctionalized SiNC.*

SiNC-ratio	V_{OC} [V]	J_{SC} [mA/cm^2]	FF [%]	PCE [%]
40 % SiNC	0.41	-3.04E-02	29	3.65E-03
25 % SiNC	0.57	-3.62E-02	31	6.31E-03
P3HT-only	1.18	-5.67E-02	29	1.93E-02

is still magnitudes below the best devices with unfunctionalized particles with PCEs in the order of 1-2 % [88, 89, 91, 223]. In order to reproduce this work, we used SiNCs from the same synthesis as above, but without the functionalization step. These hydrogen-terminated SiNC were dispersed in DCB (more suitable for bare SiNC than toluene [88]) and form a cloudy dispersion, typical for unfunctionalized particles [88, 90, 93, 153]. We then added P3HT to prepare two solutions with 25 wt.-% and with 40 wt.-% of SiNC. These were spin coated at 1000 rpm to form layers with 60 nm thickness, followed by an annealing with 140 °C for 10 min and evaporation of a 10 nm Ca and 100 nm Al.

As can be seen from Fig. 5.14 and Table 5.4 the resulting devices perform much worse than a P3HT-only reference without SiNC. Both V_{OC} and J_{SC} drop significantly. So instead of improving the devices, adding SiNC actually diminishes their performance. This leads to the assumption that these particles have formed an insulating surface oxide and are electrically not accessible. In that case they would not contribute in light absorption or exciton dissociation and have to be considered dead weight. On the one hand this effectively reduces the light absorption of the active layer, on the other the particles can lower the order of the P3HT domains and inhibit charge transport there.

The particles have been treated with highly concentrated hydrofluoric acid and thus should be oxide-free and hydrogen-terminated. Great care was taken to avoid any oxidation: the particles were dispersed in dry solvents under argon atmosphere and the vials containing the dispersion were put in another bottle under argon atmosphere for transport. However, the particles were synthesized in a lab in Garching and had to be transported to another lab in Munich 20 km away. Also particles were typically not processed on the day of synthesis, but one or two days after. These results underline the importance of surface functionalization to enable facile handling of SiNC.

5.4.5 Ternary SiNC:P3HT:PCBM devices

While adding SiNC to polymers like P3HT has shown to improve solar cell performance compared to polymer-only devices, all results from this work and even the best literature devices [88, 89, 91, 223] significantly lag behind their polymer:fullerene counter parts. Typical P3HT:PC$_{60}$BM cells reach PCEs up to 3-4 % [253], PTB7:PC$_{70}$BM cells can go up to 9 % [254]. While polymer:SiNC devices cannot surpass this so far, it has been reported

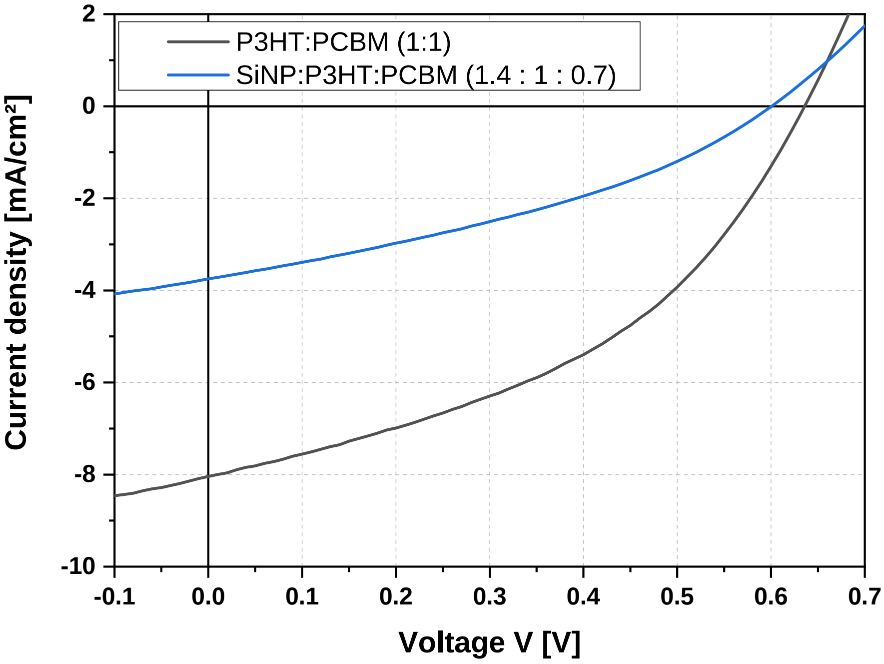

Figure 5.15: *J-V-curves of P3HT:PCBM solar cells with and without hexylthiophene-SiNC, annealed at 140 °C for 10 min and with Ca/Al cathode. Addition of SiNC does not improve the device but significantly reduces the generated photo current.*

that adding SiNC to P3HT:PCBM in ternary blends can improve device performance, especially by generating more current [92, 225]. As with all ternary devices optimization of the material ratio can become complex for three materials. In Kim's work a large amount of SiNC - between 2 and 6 times the amount of P3HT - was added to the P3HT:PCBM blend. In Zhao's work only a few tenth of the P3HT weight was added at the expense of some PCBM. For this experiment some middle ground was chosen: the reference solution was prepared with P3HT:PCBM in a 1:1 ratio. Since in the ternary solution both PCBM and SiNC serve as electron acceptor, here the PCBM ratio was slighty reduced to 1:0.65 while another 1.4 parts of functionalized SiNC were added. Both solutions were spin coated from toluene at 1000 rpm resulting in an active layer thickness between 180 and 190 nm, which is in the optimal range for P3HT:PCBM devices. The samples were annealed at 140 °C for 10 min before evaporation of 10 nm Ca and 100 nm Al.

From the resulting J-V-curves in Fig. 5.15 we see a typical P3HT:PCBM cell with V_{OC} = 0.64 V, J_{SC}= -8.0 mA/cm^2, FF = 42 % and a resulting PCE of 2.2 %. The ternary device performs significantly worse. While V_{OC} (0.60 V) and FF (35 %) only decrease slightly, the generated current drops by more then 50 % to J_{SC} = -3.7 mA/cm^2.

Unfortunately, these results resemble those from Kim's work when using SiNC funtionalized with 1-octene instead of unfunctionalized particles: slight reduction of V_{OC} and

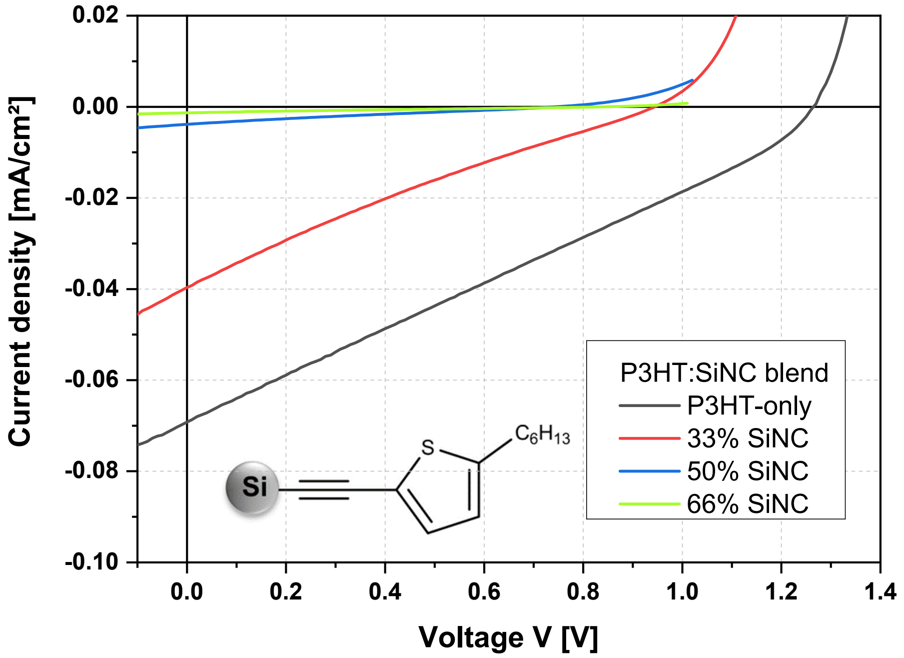

Figure 5.16: *J-V-curves of solar cells made with P3HT and different amounts of ethynyl-hexylthiophene-SiNC. Addition of SiNC clearly deteriorates the performance.*

loss of about half of the generated current.

While there is still room for optimizing the ternary material ratios, in Kim's work any addition of unfuntionalized SiNC would improve the device and it seems apparent that functionalization with hexylthiophene cannot overcome the problems associated with the insulating nature of organic surface groups. The improvements that hexylthiophene-SiNC have brought as electron acceptor in combiantion with P3HT are minor compared to results with PCBM. As such it seems that any advantage that hexylthiophene-SiNC can bring to ternary devices is outweighed by for example morphological changes that disturb the balance of an optimized P3HT:PCBM network.

5.4.6 Ethynyl-functionalized particles

From the previous experiments it seems surface functionalization of SiNC with hexylthiophene is by itself not sufficient to overcome the problems associated with organic surface groups. In an attempt to increase charge transport across the ligand molecule the hexylthiophene molecule was extended with an ethynyl group (depicted as inset in Fig. 5.16). This results in direct covalent bonding of a π-conjugated molecule to the silicon surface. Such ethynyl-hexylthiophene-SiNC were used the same way as the hexylthiophene-SiNC. To assess their performance in a solar cell, device were made from blends with P3HT

Table 5.5: *Performance parameters of solar cells made with P3HT and different amounts of ethynyl-hexylthiophene-SiNC.*

Cell	V_{OC} [V]	J_{SC} [mA/cm^2]	FF [%]	PCE [%]
P3HT-only	1.26	-6.92E-02	27	2.36E-02
33 % SiNC	0.94	-3.97E-02	22	8.13E-03
50 % SiNC	0.74	-3.86E-03	23	6.54E-04
66 % SiNC	0.84	-1.33E-03	23	2.58E-04

and 0, 33, 50 and 66 % SiNC. The solutions were spin coated from toluene to form film thicknesses of 60 nm, which were then annealed 80 °C right after layer deposition. The evaporated electrodes consisted of 10 nm Ca and 100 nm Al.

By looking at the resulting J-V-curves (Fig. 5.16) and solar cell parameters (Table 5.5) we see that SiNC with the new functionalization perform not only worse than their counterpart with simpler functionalization, but also worse than the P3HT-only reference device and such actually harm the device. While V_{OC} values are comparable to the previous experiments, we observe a drastic loss in generated photocurrent that clearly correlates with increasing amount of SiNC in the blend. It seems that these particles disturb the P3HT, maybe by reducing the ordering of the film, without adding anything to it. It is unclear why this surface functionalization performs so badly, but at this point does not warrant further investigation.

5.5 Summary

In this chapter we have investigated the use of functionalized SiNC as electron acceptor in hybrid solar cells together with P3HT as electron donor. Typically, functionalized particles are electrically insulated by the organic surface groups. We tried to address this by grafting hexylthiophene monomers on the SiNC surface to enable good contact with the hexylthiophene polymer P3HT.

We show that addition of such hexylthiophene-SiNC can indeed improve the performance of P3HT solar cells. A SiNC:P3HT mixing ratio of 1:1 was found to be superior to blends with higher or lower SiNC ratios and thermal annealing at 140 °C for 15 min could significantly improve device performance compared to a 80 °C treatment. Replacing the Al cathode with the lower work function Ca could significantly increase the open circuit voltage, presumably because the CB of the SiNC was lowered by bad gap widening (caused by quantum confinement in nanoparticles) and lies below the Al work function, which therefore quenches the generated potential in the cell. Such an optimized cell reached a PCE of 0.03 % with V_{OC} of 0.9 V compared to a P3HT-only reference device with PCE of 0.019 %.

When we put the hexylthiophene-SiNC in ternary SiNC:P3HT:PCBM devices, the addition of SiNC severly decreased the device performance compared to a P3HT:PCBM reference device.

Moreover, we tried to improve charge transfer on and of the SiNC by adding an ethynyl group to the hexylthiophen ligand, creating a conjugated system right onto the SiNC surface. However, such particles seem actually less conducting and would show lower performance than the reference without particles.

6 Optoelectronic devices with metal nanowire transparent electrodes

6.1 Introduction

The go-to material for transparent conductive electrodes (TCOs) in optoelectronic thin-film devices is indium tin oxide (ITO). ITO is well established, commercial available in large quantities and combines excellent conductivity with high transparency in the visible range. In 2013 it constituted 93 % of the entire market for transparent conductors [255]. However, ITO has three major drawbacks: i) indium is rare and resources are dwindling, therefore it is costly (~600 USD/kg in 2014) and not future proof; ii) ITO is fabricated by sputter coating, which is slow, wasteful and requires vacuum; iii) ITO is brittle and requires high temperature annealing at around 400 °C, which renders it unusable for flexible applications and on lot of foil substrates. There are many different contenders to replace ITO with cheaper and solution-processable materials that are compatible with flexible foil substrates like carbon nanotubes [256], graphene[257], graphene oxide [258] and conductive polymers like PEDOT:PSS [259]. The most promising alternative however are metal nanowires as they offer the highest electrooptical performance. Here we present spray coated films of either silver (AgNW) or copper nanowires (CuNW). The film thickness is optimized to find an optimal balance between transparency and conductivity. Their performance can be further improved with different treatments to remove insulating surfactants that are necessary to grow and disperse the nanowires. This films are then implemented as TCO into different solar cells and LEDs.

Most of the presented experimental work on AgNW has been done by Konstantions Falidas, that on CuNW by Kamyar Baghvand, as part of their master's thesis.

6.2 Nanowire inks

AgNW

The solution-based synthesis of AgNW has been extensively studied in our group [260]. However, well dispersed, high-quality AgNW are commercially available at reasonable prices. Therefore, the AgNW used in this work were bought from RAS materials

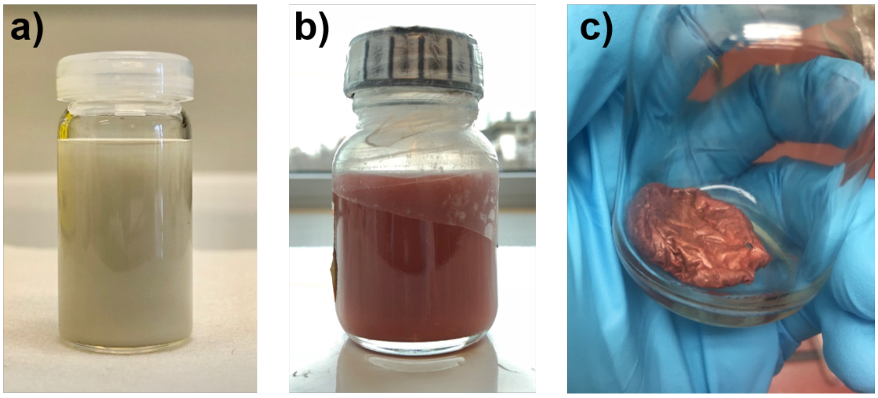

Figure 6.1: *Photos of a) AgNW solution, b) CuNW solution and c) CuNW agglomerate right after growth phase.*

(ECD0X3). They have a mean length of 25 µm and mean diameter of 40 nm. The solution contains 1 wt.-% AgNW in IPA and some polyvinylpyrrolidone (PVP). The PVP serves as capping agent during AgNW growth and some is intentionally left in the solution to serve as surfactant that prevents agglomeration. The AgNW solution is stored at 5 °C and has a shelf life of 12 month according to the supplier. For spray coating the ink is further diluted with 14 parts IPA and 5 parts DI-water and shaken for 5 min with a Heidolph vortex shaker to achieve a well dispersed solution.

CuNW

CuNW are not yet commercially available in acceptable quality and were therefore synthesized inhouse. The synthesis of CuNW requires three components: a copper precursor, a reducing agent and a capping agent. The first successful solution-based CuNW synthesis was reported by Chang et al. in 2005 [261] based on copper(II) nitrate ($Cu(NO_3)_2$), hydrazine (N_2H_2) and ethylenediamine. The CuNW in this work were fabricated by aqueous synthesis, firstly reported by Huang in 2006 [262] and recently extended by co-workers in our group [263]. It forgoes the use of hazardous hydrazine and requires only mild process temperatures.

We used copper(II) chloride dihydrate ($CuCl_2 \cdot 2H_2O$, ≥ 97 %) as copper-containing precursor, L-ascorbic acid (AA, $C_6H_8O_6$, 99 %) as reducing agent and oleylamine (OM, $C_{18}H_{37}N$, 70 %) as capping agent. The AA oxidizes to dehydroascorbic acid and in the process provides two electrons that reduce Cu^{2+} ions to neutral Cu^0-atoms, which then can contribute to wire growth. The OM selectively passivates the (100)-crystal-plane of copper and thus leaves only the (111)-plane open for growth, resulting in the uniaxial wire growth.

In a first step two separate solutions are prepared and put in an ultrasonic bath for 5 min: 300 mg $CuCl_2 \cdot 2H_2O$ are dissolved in 25 g of DI water and 300 mg of AA are dissolved in 5 g of DI-water. When the solutions are well dispersed, 900 mg OM are added to the cooper-containing solution. Due to the low solubility of OM in water, the solution is horn sonicated three times for 30 s at 200 W in a Branson Sonifier S-450D. Then, both solutions are combined and homogenized once more for 2 min on a vortex shaker. In the next step the solution goes into a silicon oil bath for 12 h to grow the particles. The bath is heated with a calibrated hotplate, which is set to 130 °C resulting in a process temperature of about 80 °C inside the copper solution. The bottle containing the solution has to be carefully sealed with PTFE (polytetrafluoroethylene) tape at the thread, to avoid evaporation of the water part. To ensure homogeneous heating it is critical to make sure that all of the solution is underneath the silicon oil level.

Once the AA is added to the chopper chloride, reduction begins and the blue solution quickly turns towards green. Once the nanowire growth sets in, it turns more towards brown and becomes darker over time. After 12 h of growth the solution is decanted to get rid of OM and other residuals and a large, bundled CuNW agglomerate remains, which is redispersed in 30 g of IPA. To wash out remaining OM, the solution is shaken and the nanowires are allowed to sediment at least one night. To minimize oxidation during this process, the solution is stored in a fridge at 5 °C. A longer duration in IPA and/or repetition of this washing step can improve the results.

After the washing, CuNW are decanted and redispersed in 30 g IPA and 5 wt.-% propionic acid is added. The acid removes residual OM and etches away any copper oxide that has formed on the CuNW surface during washing. Subsequently, remaining visible agglomerates are manually separated by pippeting the well dispersed CuNW into a second bottle. After 5 min in ultrasonic bath, the solution is centrifuged for 5 min at a speed of 1750 rpm. The heavy CuNW sediment to the bottom and smaller nanospheres and nanorods remain in the supernatant together with propionic acid and residual OM. This supernatant is decanted and the CuNWs are redispersed in 30 g IPA. If necessary this centrifugation in propionic acid can be repeated. Afterwards, the solution is put in a sonication bath once more for 25 min right before spray deposition.

CuNW length and diameter are determined by SEM measurements. With the described parameters the synthesized CuNW have a mean diameter of 100 nm and mean length of 40 µm [263].

6.3 Spray deposition

Spray coating is low-cost, vacuum-free and high throughput deposition technique that is industrially well established, e.g., in the painting industry. In this work we used a

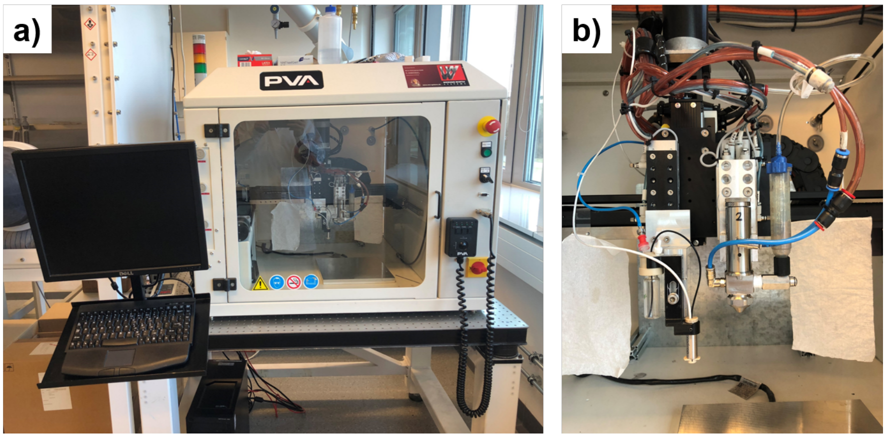

Figure 6.2: *Photos of a) automated spray robot and b) close up of the spray gun.*

automated spray robot for spraying of well dispersed inks and a hand held airbrush for less well-dispersed inks that would clogg the robot's spray gun.

Spray Robot

For the spray-deposition of the AgNWs, a fully automated bench top spray robot (PVA350 from Precision Valve & Automation, Inc.) equipped with an EFD 781S general purpose spray valve from Nordson is used. The robot can move in x, y and z direction and also has a rotational axis. To be able to cover larger areas, during deposition the spray head is scanning in lines across the sample.

The spray nozzle has an orifice of 150 µm. The processe parameters for spraying AgNW are atomizing pressure of 0.05 MPa, material pressure of 0.02 MPa, scanning speed of 250 mm/s, (scanning) line distance 3 mm and nozzle-to-sample distance of 5 cm.

Airbrush

The as-prepared CuNW dispersion is not as well dispersed as the AgNW solution and still contains a certain amount of agglomerates, they are not suitable for the spray robot as they clog the 150 µm orifice of the spray gun. To mitigate this issue the CuNW are sprayed with the help of a handhold Triplex II airbrush (Gabbert, Germany), which features a spray nozzle with 350 µm orifice. The airbrush is driven with 2.5 bar of nitrogen.

For the spray deposition a glass substrate is put on a hot plate (Thermo ScientificTM RT2 advanced), which is set to 70 °C. This temperature is enough to assure spraying in dry regime so that not wet IPA flows across the sample, but still low enough to avoid oxidation of the CuNW. A shadow mask is used to structure the CuNW film into electrode stripes.

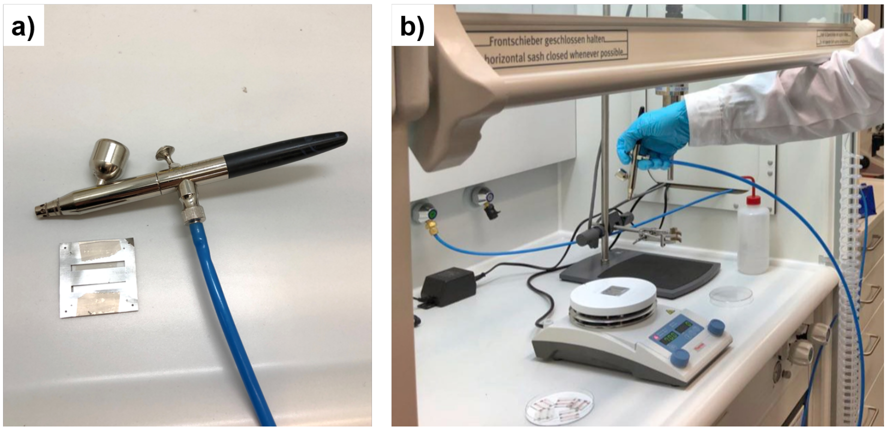

Figure 6.3: *Photos of a) airbrush and a shadow mask for two electrode stripes and b) the spray setup with substrate and mask fixed to a hotplate.*

Both the sample and the mask are fixed to the hot plate with scotch tape to make sure they are not blown away. Spray distance is set to ∼12 cm; the fumehood's door serves as stabilizer for the arm and as reproducible set point for the spraying distance. In order to avoid the spray-deposition of a material gradient, the airbrush should be hold as vertical as possible. For one layer of CuNW film 1 g of solution is sprayed.

6.4 Film characterization

Transparent conducting electrodes (TCOs) need to combine high optical transparency and high electrical conductivity. These two properties present a trade off mostly determined by the electrode thickness. Typically, both absorption and conductance of a layer are directly proportional to its thickness. For nanowire films a definite thickness is difficult to determine due to the random and rough nature of the network of wires. Unlike with spin coating the film thickness is not set by changing the solution's concentration, but the concentration is optimized once for the spraying process and typically very low. Therefore, the desired film thickness is set by the number of consecutively sprayed layers. Spraying multiple times also helps to average out inhomogeneities during a spray run.

A typical issue for metal nanowire networks are the surfactants that are required to keep the NWs well dispersed in solution, but are unwanted in the final film. Surfactants like PVP and OM are not conducting, but cover the nanowire surface and therefore prevent good contact at the nanowire junctions. To deal with them they have to be removed right before spray deposition at the risk of impairing spraying properties or they can be removed after deposition for example by washing or burning them out. However, any after-treatment of the film has to be compatible with the nanowires (i.e., not wash them off or oxidize them) and the substrate, which become important when working on foils (which can melt). Such after-treatments are also an issue when the NWs are used as top electrode deposited on top of sensitive polymers that can take damage.

Are the NW used as a bottom electrode and the device it built up on top of them, there is another issue to be dealt with: film roughness. Due to the nature of the film wires can stick out and depending on the quality of the used solution some agglomerates can be inside the film. Both can pierce through the device stack, which is typically only a few hundred nm thick. When bottom and top electrode connect, they form a short circuit bypassing the diode device. These issues will be discussed for AgNW and CuNW films in the following sections.

6.4.1 Spray-coated AgNW films

AgNW films have been fabricated by spray deposition with a spray robot as described above. A series of films with different number of sprayed layers (3, 5, 7 and 10) has been fabricated to analyze the impact of the film thickness/density on transmission and sheet resistance. Fig. 6.4 a) shows the resulting transmission curves and Fig. 6.4 b) the corresponding sheet resistance. All films exhibit a very characteristic shape with prominent features between 300 and 450 nm, which are due so surface plasmon resonance (SPR). The more pronounced peak at around 400 nm corresponds to the transverse plasmon resonance of nanowires, the smaller one at around 355 nm to the longitudinal (quadrupole) resonance excitation of nanowires [264–266].

We can clearly see how an increased film density results in decreased transmission and increased sheet resistance. While the transmission is directly proportional to the amount of sprayed layers, the sheet resistance makes a large improvement from 3 to 5 layers, but then seems to saturate. The performance of TCEs is commonly compared by their transmission at a wavelength of 550 nm: $T(550\,\text{nm})$. Here, the untreated films exhibit values of 89, 79, 69 and 63 % for 3, 5, 7 and 10 layers respectively. Only the three layer AgNW film has a comparable transmission to the 120 nm ITO film, which features $T(550\,\text{nm}) = 90\,\%$. However, the ITO film has a 4.5 times lower sheet resistance.

There is a variety of different post-treatments for AgNW films that can increase film transmission and reduce sheet resistance such as thermal [267, 268] and photonic sintering [269, 270], selective growth of silver nanoparticles at the AgNW junctions [271] and mechanical pressure (cold welding) [272, 273]. All methods are based on either remove remaining surfactant from the film and on improving the junction-junction resistance. A convenient method that yields good results is washing the AgNW film with distilled water. For this the glass substrate with AgNW film is simply immersed in a water bath for 15 min. Great care has to be taken to not delaminate the film in the process; the sample has to be slowly immersed into the water under a shallow angle and should

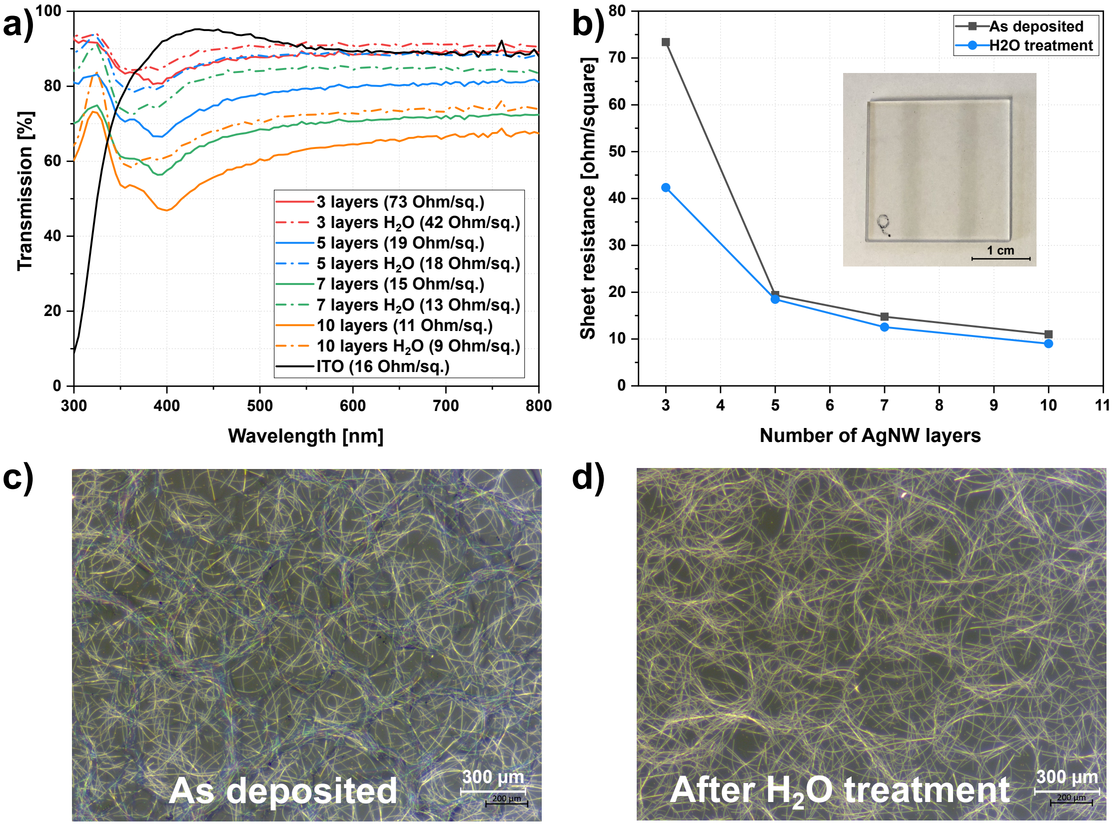

Figure 6.4: *a) Transmission of AgNW films with increasing film thickness and b) corresponding sheet resistance values before and after water treatment. The inset shows a photograph of two AgNW stripes structured with a spray mask. Microscope images of c) seven layer AgNW film without after-treatment and d) after 15 minutes immersion in water. It can be seen how residual PVP is washed out.*

not be agitated too much while in the bath. Fig. 6.4 c) shows an optical microscope image of an AgNW film consisting of 7 layers on a glass substrate. The AgNW network can be clearly seen and is partially covered by a blue veil. This is the remaining PVP that completely disappears after the water treatment as seen in Fig. 6.4 d). The PVP absorbs light and insulates the AgNW, reducing the networks conductivity. As such, its removal results in significant transmission gains and slightly improved sheet resistance. Transmission increases by roughly 10 percentage points in average resulting in $T(550\,\text{nm}) = 92, 89, 85$ and $72\,\%$ for 3, 5, 7 and 10 layers respectively. For the thinnest AgNW film there is also a significant improvement in sheet resistance from $R_{\text{Sh}} = 73$ to $42\,\Omega/\text{sq.}$, for the other layers it improves only by few Ω/sq.

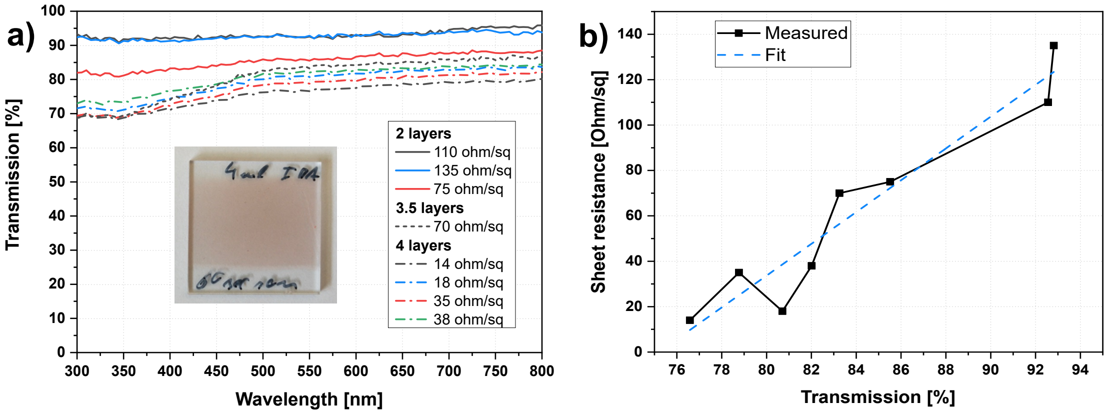

Figure 6.5: *a) Transmission of CuNW films sprayed with an airbrush and different number of layers, the inset shows a picture of such a film. b) Sheet resistance vs. transmission of the corresponding films. While the repeatability of the film thickness suffers from the handheld deposition, the ratio of resistance and transmission is relatively linear.*

6.4.2 Spray-coated CuNW films

The influence of the NW density on transmission and sheet resistance was also analyzed for CuNW films. There also exists a variety of after-treatments like acid treatments[263], thermal [263, 274] and photonic sintering [275] or different hydrogen treatments [205, 276]. For the purpose of this work we settled on a thorough washing with IPA of the CuNW solution and subsequent treatment with propionic acid right before film deposition. This yields good performance values and simplifies the process by omitting any post-deposition treatments. The resulting transmission and resistance values are presented in Fig. 6.5 a). The CuNW are much less well dispersed as the AgNW in this work. This and the use of the simple and handheld air brush set certain limits to the repeatability concerning the film density. Looking at the 2-layer films we see that two are virtually identical (black and blue line) a third film much less transparent (red line). The presented 4-layer films (dash-dotted lines) show a spread of $T(550\,\mathrm{nm})$ between 76 and 83 %. Those denser films also show some features related to surface plasmon resonance in the UV region, but much less pronounced what we observed for AgNW films. However, when we look at the sheet resistance vs. transmission (Fig. 6.5 b)) we find a relatively linear relationship. So even when the film density undergoes a certain variability, the inherent performance of the film seems reproducible. CuNW films that feature a sheet resistance comparable to ITO (16 Ω/sq.) have a $T(550\,\mathrm{nm})$ between 76 and 80 %. So while they are not as transparent as ITO (90 %), this presents a very viable performance for use in optoelectronic devices.

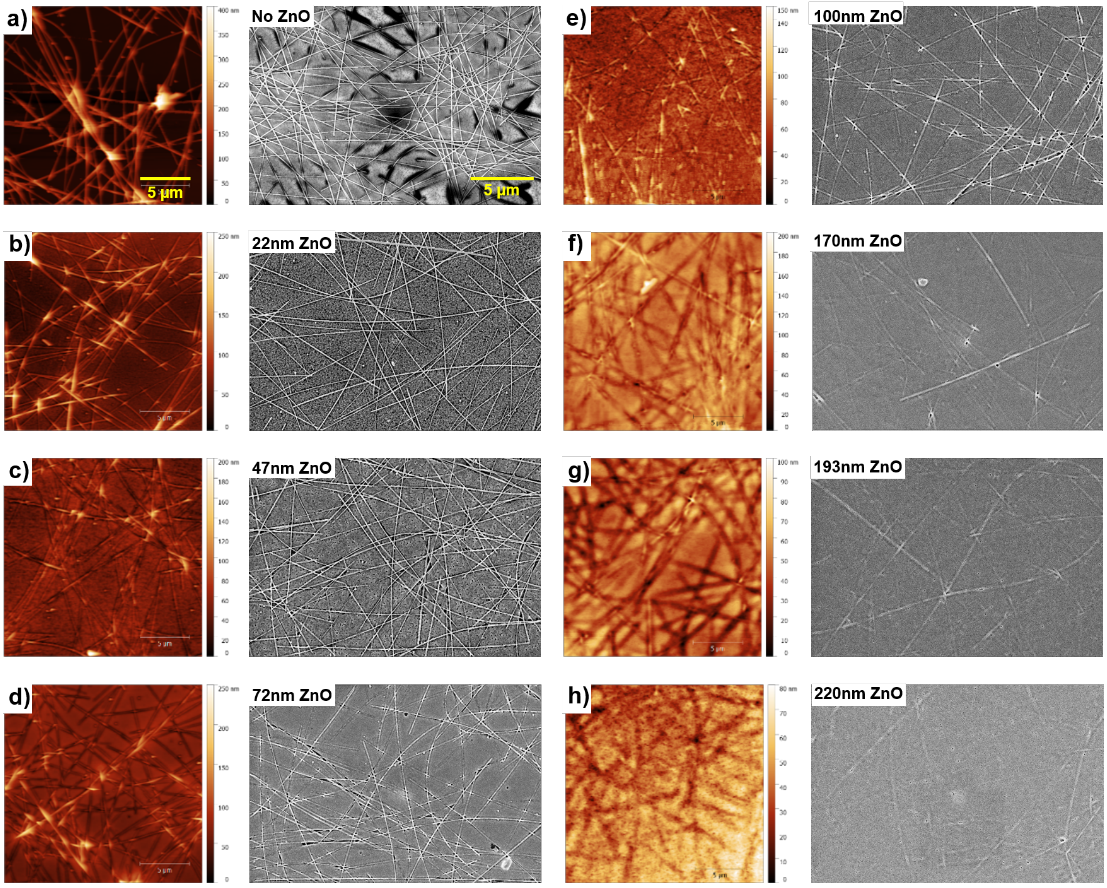

Figure 6.6: *AFM (left) and SEM (right) images of AgNW films (7 layers) covered by ZnO films with different thicknesses from 0 to 220 nm.*

6.5 AgNW bottom electrodes for organic solar cells

Planarization

AgNW networks on a flat substrate are intrinsically rough as their transparency is based on empty space between the wires and their conduction on stacking of at least two wires. As such the peak-to-peak distance can be more than double the diameter of the wires ($d \sim 40$ nm). Another issue are occasional agglomerates of several bundled NWs that could not get fully dispersed. The optimal active layer for P3HT:PCBM solar cells lies around 200 nm, therefore rough surfaces can easily connect to the top electrode of a device and create a short circuit. There are several approaches to address this issue, the two most prominent being mechanically pressure to flatten the film and covering the network with planarization layers. Since our trials with a knee lever press did not yield tangible improvements in surface roughness, but would often delaminate or damage the AgNW film, here we concentrate on planarization with an interlayer. Typical candidates for this are PEDOT:PSS as HTL or ZnO as ETL. Since thicker layers are not very transparent anymore and to absorb a lot of light, we settled on ZnO. To investigate the surface roughness we prepared spray coated AgNW films on glass consisting of seven spray layers and covered them with spin-coated ZnO layers of different thickness. The ZnO thickness was set by changing the spin speed and diluting the ZnO solution with IPA as shown in Table 6.1. It should be noted that ZnO layer spincoated at speeds below 1000 rpm decrease in film quality. We then took AFM (left) and SEM (right) measurements of all samples as shown in Fig. 6.6. There we nicely see how the AgNW are clearly visible at first and then slowly become less contoured as they are increasingly covered in ZnO. At 72 nm some wires start to be fully covered under the ZnO, at 170 nm most wires are mostly covered and at 220 nm we can only faintly make out some AgNW contours. The root mean square roughness R_q (RMS) values were extracted from the AFM images and are shown in the last column of Table 6.1. With the exception of one outlier at 47 nm we see a steady decline of R_q The biggest improvements come with the first thickness increases and additional increases deliver diminishing returns. In order to assess a possible optical penalty of a thick ZnO layer, we measured the transmission of several ZnO layers (Fig. 6.7). It can be seen that in the relevant spectrum covered by P3HT asborption (~370 nm and upwards) there is very little difference between the different layers and even the thickest one features a T(550 nm) of over 95 %. Since ZnO has a very high electron mobility and the optical losses seem negligible, no major performance loss is to be expected from introducing thicker ZnO interlayers into a solar cell.

Table 6.1: *Spin parameters for ZnO layers with different thickness and the measured root mean square roughness R_q when deposited on a 7 layer AgNW film.*

ZnO:IPA	Spin speed [rpm]	Thickness [nm]	R_q [nm]
0	0	0	56.0 nm
1:2	6000	22	27.1 nm
1:2	800	47	14.1 nm
1:0	5000	72	18.3 nm
1:0	3000	100	16.7 nm
1:0	1000	170	14.7 nm
1:0	800	193	11.3 nm
1:0	600	220	10.9 nm

Solar cells

We then prepared solar cells with either ITO or an AgNW network (7 layers, water treated) as transparent bottom electrode. Since ZnO was to be used as first interlayer, the

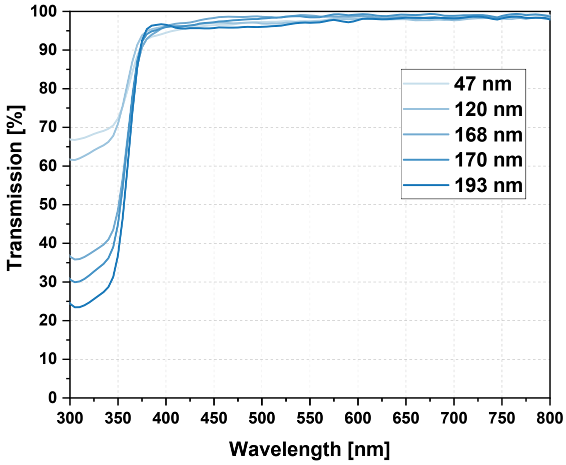

Figure 6.7: *Transmission of ZnO layers with different thickness. Even the thickest layer is highly transparent in the relevant region from 370 nm upwards.*

devices were made in inverted architecture with MoO_3 as HTL as shown in Fig. 6.8 a) with the corresponding band diagram in Fig. 6.8 b). The ZnO thickness was set as 47, 72, 130 or 170 nm. Additionally the thickness of the evaporated MoO_3 was varied between 5, 10 and 20 nm to investigate if this has an influence on the device performance and to increase the number of samples with AgNW electrode, which allows to gather more reliable statistics.

The figures of merit of the respective best devices (out of six on one sample) are presented in Table 6.2 and in Fig. 6.8 c) we collected the J-V-curves of the best devices with ITO or AgNW electrode per ZnO thickness. All devices are fully functional solar cells and apart from some outliers all devices feature a V_{OC} between 0.60 and 0.65 V as expected for this materials system. We find that neither ZnO nor MoO thickness seem to have an impact on the device performance. While there are some variations, there is no trend for either thickness and variations are within typical process deviations. It can be seen that the spread is larger for AgNW based devices, while most ITO devices have very similar parameters. This reveals the larger process variations inherent in the spray coating of nanowire networks. This also manifests itself in device yield: on ITO its very rare to have defect devices with yields of 94, 100, 94 and 89 % for 47, 72, 130 and 170 nm respectively. Although, AgNW electrodes yield functional devices on all samples, on almost all of them are a couple of shorted diodes leading to device yields of 72, 39, 39 and 67 %. Somewhat surprisingly, the ZnO thickness has no impact on the yield.

Looking at the performance we can see that on average the device with AgNW electrode outperform their ITO counterparts. While the best ITO device features a PCE of 2.6 %, AgNW devices can reach up to 3.2 %. From Fig. 6.8 c) we can clearly see that ITO device have slightly higher V_{OC} and FF, but the AgNW electrode leads to higher photo currents,

Table 6.2: *Figures of merit for solar cells with either ITO or AgNW (7 layers, water treated) as transparent bottom electrode and varying HTL and ETL thickness.* V_{OC} *is given in V,* J_{SC} *in mA/cm*^{2}*, FF and PCE in %. The traffic light color code ranks the PCE values within one ZnO thickness batch.*

Thickness [nm]		AgNW				ITO			
ZnO	MoO_3	V_{OC}	J_{SC}	FF	PCE	V_{OC}	J_{SC}	FF	PCE
47	5	0.63	-11.3	43	3.0	0.66	-7.5	52	2.6
	10	0.62	-8.9	46	2.6	0.60	-8.0	44	2.1
	20	0.64	-9.3	45	2.7	0.65	-8.3	45	2.4
72	5	0.55	-10.8	40	2.4	0.66	-7.7	49	2.5
	10	0.60	-9.7	42	2.4	0.64	-8.1	47	2.5
	20	0.63	-9.7	44	2.7	0.62	-7.6	47	2.2
130	5	0.63	-9.8	44	2.8	0.66	-7.7	48	2.4
	10	0.55	-9.7	38	2.0	0.63	-7.8	45	2.2
	20	0.59	-10.3	41	2.5	0.66	-7.7	47	2.4
170	5	0.65	-10.5	46	3.2	0.62	-9.1	44	2.5
	10	0.61	-10.2	44	2.7	0.65	-8.1	48	2.5
	20	0.62	-9.2	44	2.5	0.65	-7.5	48	2.3

which outweighs the other factors.

The water treated AgNW film with seven layers features slightly improved sheet resistance over the ITO film (13 vs 16 Ω/sq.), but not enough to overcome the roughly 5 percentage points lower transmission. A possible explanation of the higher current generation lies in the haziness of AgNW films. The diameter of AgNW in the same order as the wavelengths of visible light and as such causes a non-negligible amount of light scattering. This is highly undesirable for display applications as it decreases sharpness and contrast, but can actually result in increased light absorption. AgNW films with a T(550 nm) = 85 % - as used for the presented solar cells - have shown haze values (amount of light that is scattered at an angle greater than 2.5° from normal (ASTM D1003 [277])) of almost 15 % [278]. That is light that is passing the AgNW film but not picked up from the sensor during transmission measurement. This is in agreement with, e.g., the work of Hu et al. [279] who report a difference of about 10 percentage points between specular transmission (only parallel light is measured, normal UV-Vis scan) and diffusive transmission (light is measured under all angles in an integrating sphere). We therefore assume that the significant haziness of AgNW films reduces their specular transmission below that of the ITO film, which leads to increased light absorption and thus explains the higher photo current in the respective solar cells.

One phenomenon that bears mentioning can be seen in Fig. 6.8 d). As shown, occasionally

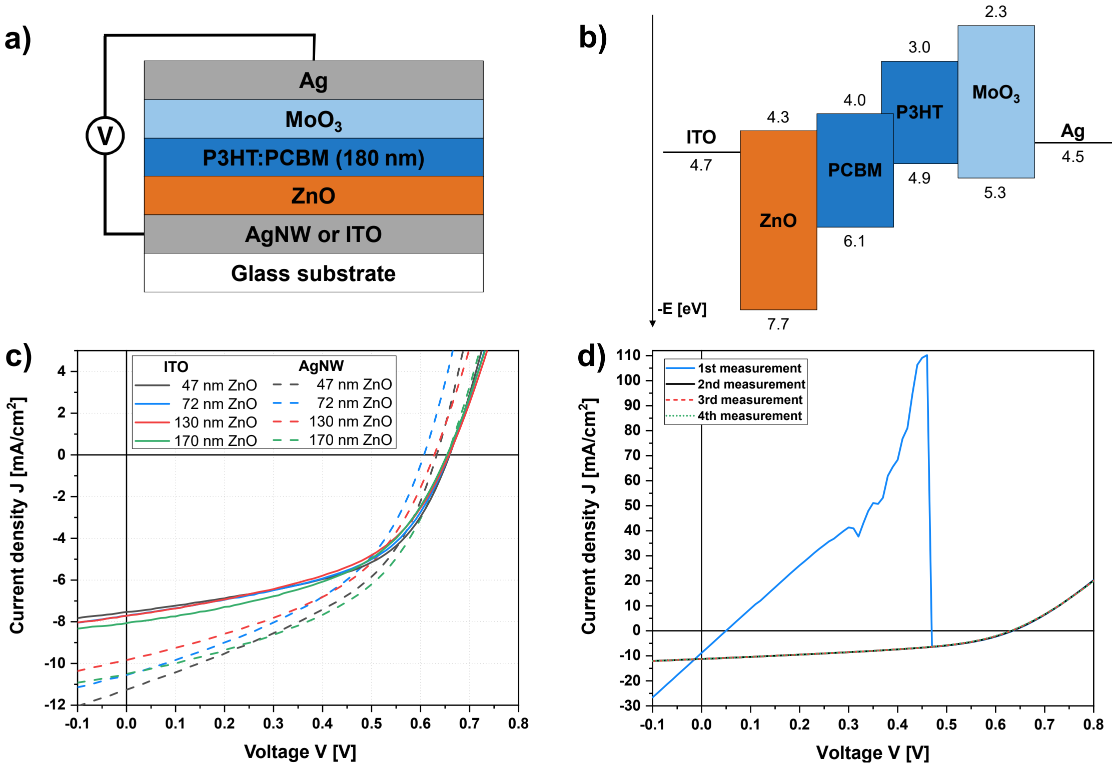

Figure 6.8: *Solar cells with either ITO or AgNW (7 layers, water treated) as transparent bottom electrode and varying HTL and ETL thickness: a) layer stack with inverted architecture and b) corresponding proposed energy diagram. c) J-V-curves of best devices for each ZnO thickness and d) J-V-curves of several consecutive measurements of a AgNW device showing how a device starts as short circuit, which then burns out and results in normal solar cell behaviour.*

a AgNW device would present a short circuit at first, but then during characterization snap into normal solar cell behaviour and stay there for all following measurements. We assume that the short circuit is caused by only few shorting pathways, probably some bundled agglomerates, which then conduct all the current flowing through the devices. This then leads to very high localized current densities, which eventually lead to break down of those shorts due to burning.

6.6 CuNW top electrodes

Due to their larger dimensions and lower dispersion CuNW films are significantly rougher than AgNW films. We investigated a lot of methods to planarize them: coverage with ZnO like with AgNW, mechanical pressure with a knee lever press, coverage with a protective photoresist and subsequent etching of protruding wires via plasma or acid

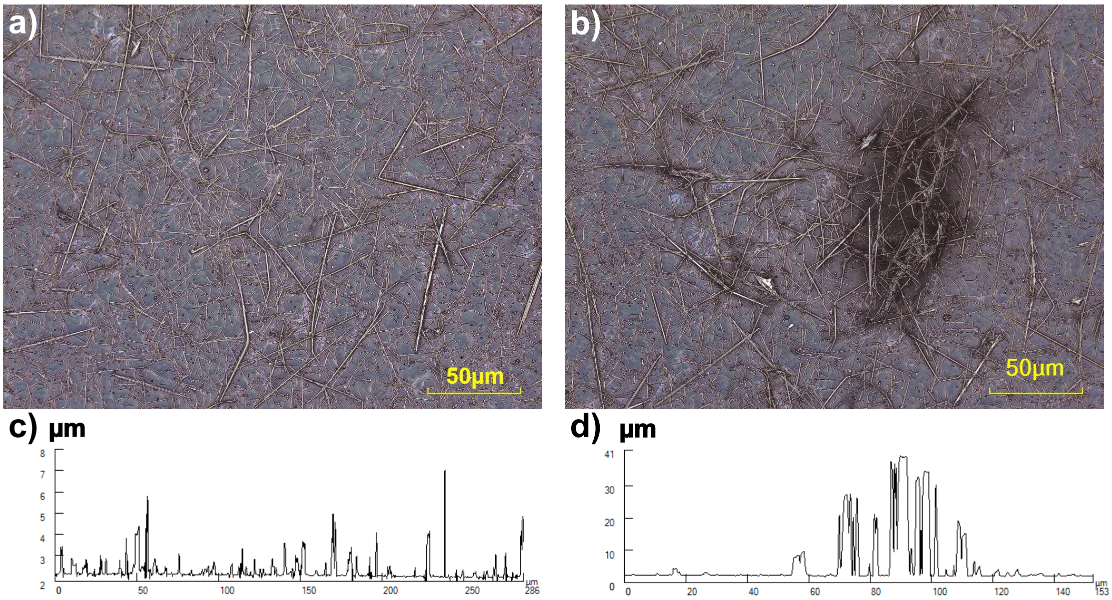

Figure 6.9: *Confocal microscope image (optical image with overlay of laser depth information) of CuNW film a) without agglomerates and b) with large CuNW cluster; c) and d) show the corresponding horizontal height profiles.*

treatment and scotch tape or PDMS (Polydimethylsiloxane) peel off. But none of these treatment would prevent the problem of short circuited devices. The dimensions of the CuNW network make an AFM study difficult as there are only few wires in the maximum scan area of $20 \times 20\,\mu m^2$ and the surface roughness can throw off the AFM cantilever. SEM imaging is Also not suitable to extract surface roughness information of such networks. Eventually a confocal microscope, which combines optical imaging with a laser scanning the surface at different focal planes to reconstruct a height profile (optical sectioning), was used to analyze the CuNW network topography. Fig. 6.9 shows two such confocal images and the associated height profile along a horizontal line across the image. On the left side (Fig. 6.9 a) and c)) we see a typical untreated CuNW film (four spray layers), which exhibits peaks with heights between 1 and 5 μm; this represents an extreme roughness for application underneath thin films in the order of a few hundred nanometers. Fig. 6.9 b) and d) present a film containing an agglomerated CuNW cluster, which reaches peaks of up to almost 40 μm. These height values have an order of magnitude that make any effort to integrate CuNW networks as bottom electrode futile.

However, since acid treatment of CuNW in solution allows to forego high after-treatments of the deposited CuNW network like further acid treatment or high temperature annealing, they can also be used as transparent top electrode, where surface roughness has no impact on the device. In the following we will present proof-of-concept applications in organic solar cells and LEDs as well as on perovskite (methylammonium lead iodide)

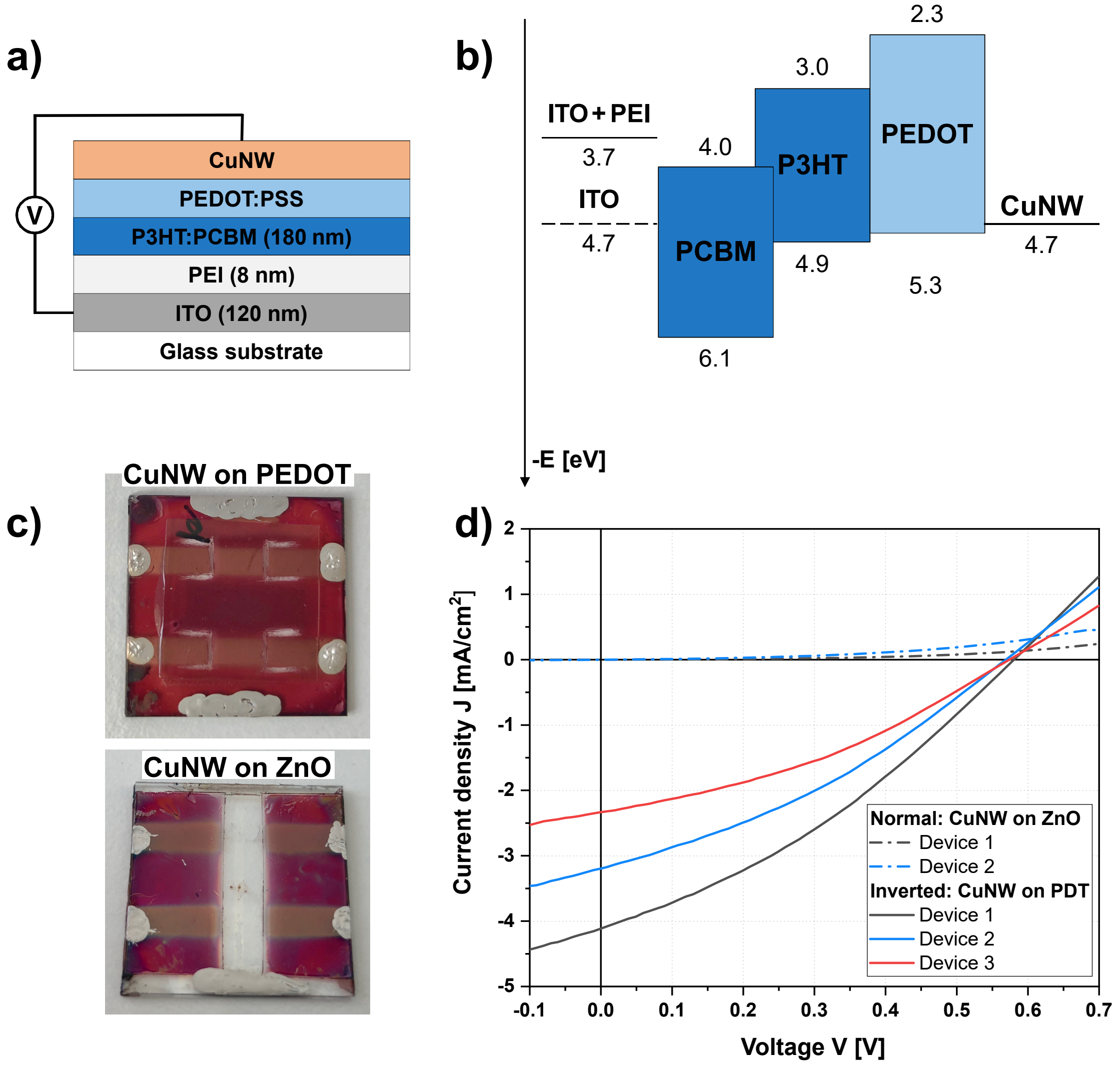

Figure 6.10: *CuNW as top electrode on organic solar cells: a) device stack with inverted architecture and b) corresponding proposed energy diagram. c) Photographs of devices with sprayed CuNW films on top of either PEDOT:PSS or ZnO and d) corresponding J-V-characterization*

solar cells. All devices have been fabricated on ITO-glass substrates with spin coating of all layers under nitrogen atmosphere followed by spray coating 4 layers of CuNW with the handheld airbrush on air.

6.6.1 OPV

Solar cells with transparent CuNW top electrode were prepared with two different architectures to investigate spraying on top of either PEDOT:PSS or ZnO. Both use

$\sim$180 nm of P3HT:PCBM as active material. Devices with normal architecture (bottom anode, top cathode) were made with PEDOT:PSS HTL underneath the active layer and ZnO ETL on top. The inverted architecture (bottom cathode, top anode) was made without explicit ETL, but with a PEI interlayer to lower the ITO work function for electron extraction and with a PEDOT:PSS HTL on top as shown in Fig. 6.10 a) along with the corresponding proposed energy diagram in Fig. 6.10 b). The CuNW electrodes were sprayed in stripes, which had to be cut to separate the two underlying devices as they already share a common bottom electrode (Fig. 6.10 c)). The resulting J-V-characteristics are shown Fig. 6.10 d). Devices with CuNW sprayed on ZnO are not photo active ($V_{OC} = 0$) and barely behave as diodes, with very little forward current. The devices with inverted architecture are functional solar cells and have a V_{OC} of almost 0.6 V as expected for this material system. However, the generated photo current is low with J_{SC} between 2 and 4 mA/cm^2, as opposed to 8 to 10 mA/cm^2 typically achieved with an evaporated metal electrode. To some degree the low current can be attributed not to electronic properties, but the lack of back reflection that typically occurs at the mirroring surface of a perfectly smooth evaporated electrode. This reflective mirror was shown to account for about one third of the generated photo current in devices with two transparent electrodes (ITO and AgNW or AgNW and AgNW) [280]. Fill factors are at around 33 % and the shape of the curve is indicative of a high series resistance. Combined, this leads to a PCE of 0.79, 0.61 and 0.47 % for the devices 1, 2 and 3 presented in Fig. 6.10 d).

6.6.2 OLED

To get further insight into the behaviour of the CuNW, we also made LEDs, which can also deliver optical information. For this devices were made in the same inverted architecture wit PEI and PEDOT:PSS as interlayers and Super Yellow polymer as light emitting material as shown in Fig. 6.11 a) with the corresponding proposed energy diagram in Fig. 6.11 b). The device is a functional LED emitting the expected yellow light (Fig. 6.11 d)). The images in Fig. 6.11 c) reveal a problem with those devices: only part of the active area are emitting light with many dark areas in between. This is not caused by defects in the polymer layer, which are pristine after spin coating. A possible explanation for these dark spots is that the spray process is damaging the underlying polymer layers. Another explanation might lie with the top deposition: NW network bottom electrodes are filled with the material deposited on top and therefore feature a very large interfacial area with the device. A top electrode however, remains porous and the interfacial area is limited to where the wires actually touch the underlying PEDOT:PSS layer. In order to address this issue, with deposited another PEDOT:PSS layer on top of the CuNW network. Three different PEDOT:PSS formulation were used: Al 4083, HTL Solar and PH 1000. AI 4083 is the standard formulation with very low conductivity, while HTL Solar is designed for wetting of hydrophobic surfaces, which might help penetrating the nanowire network, and also features very moderate conductivity. PH

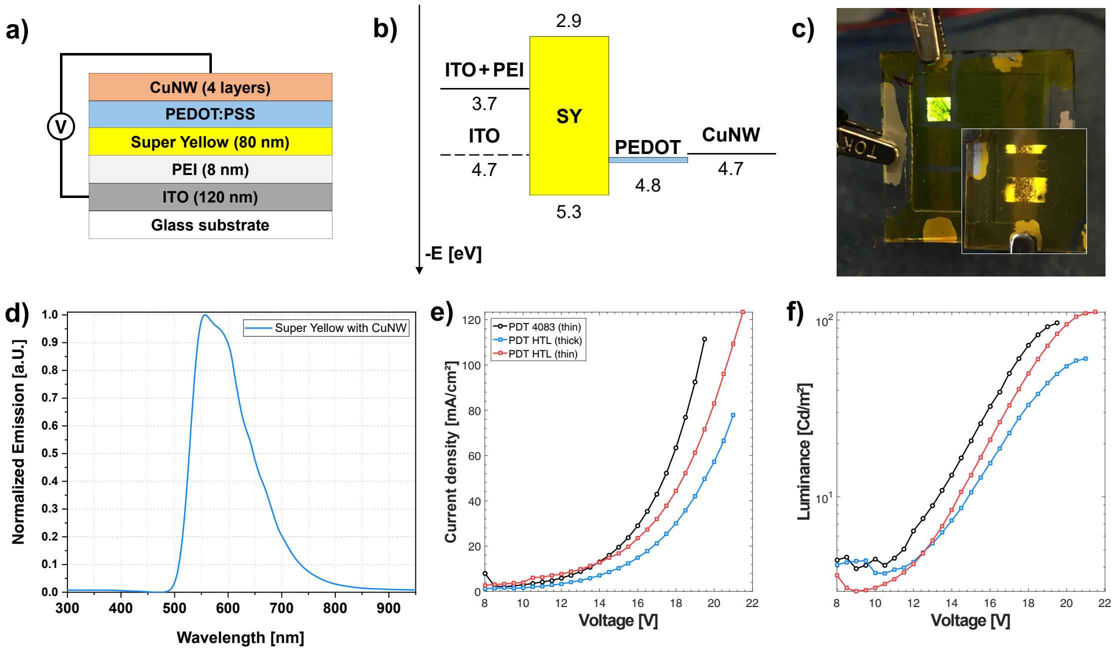

Figure 6.11: *CuNW as top electrode on organic LEDs: a) device stack with inverted architecture and b) corresponding proposed energy diagram. c) Image of LED with PEDOT:PSS Al4083 on top of CuNW, inset: LED with conductive PEDOT:PSS Ph 1000. Both devices have a lot of dark, non-emitting areas. d) Normalized emission spectrum showing the expected yellow color. Characterization of working LEDs: e) current density vs. voltage and f) luminance vs. voltage.*

1000 is highly conductive and might actually improve the sheet resistance of the nanowire network. However, none of these would solve the issue of only partially emitting area. The J-L-V-characteristics of select devices bright enough to be measurable are presented in Fig. 6.11 e) and f). All devices only turn on around 12 V and draw very little current (compare to Fig. 4.15). This is in line with the high series resistance observed in the CuNW solar cells presented above. Luminance is very low reaching about 100 cd/cm^2 as compared to a few thousand cd/cm^2 reached by a conventional Super Yellow LED at comparable current density. A low luminance however, is expected considering only a fraction of the device is emitting. Additionally, some part of the light is lost through the second transparent electrode and the absence of a reflective back electrode.

A very interesting phenomenon can be observed for the LED covered with the conductive PEDOT:PSS as shown in more detail in Fig. 6.12. Here we see that the intended active area, where ITO and CuNW electrode overlap, shows the described issue where only a very low fraction of the area whole area emits light. However, the adjacent area, which has ITO underneath, but not CuNW on top, emits largely normal. Such emission is possible because the conductive PEDOT:PSS serves as top electrode. Because the PEDOT:PSS layer is very thin (<100 nm), its conductivity is limited and therefore this additional

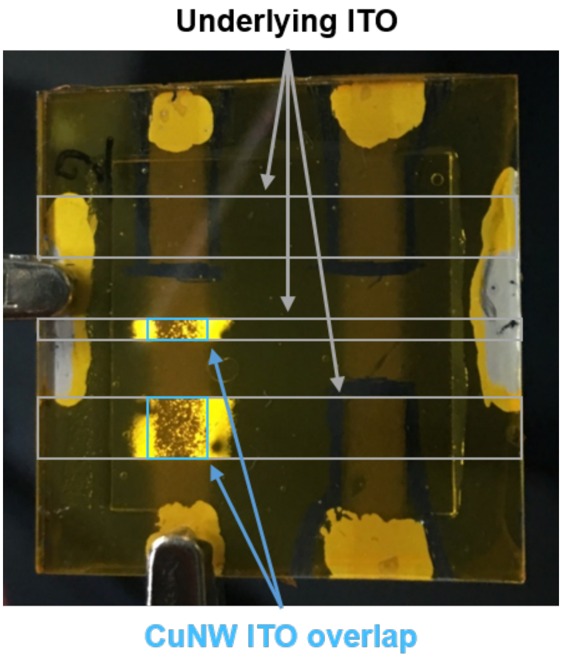

Figure 6.12: *Image of a shining Super Yellow LED with CuNW top electrode that was covered with a conductive PEDOT:PSS layer. It can be seen that the supposed active area, where ITO and CuNW overlap, shows a lot dark spots. The emission extends about 1 mm to the left and right, where there is only ITO and no CuNW electrode. This emission is almost flawless and enabled by the conductive PEDOT:PSS serving as top electrode.*

emitting area only extends roughly 1 mm beyond the ITO-CuNW-overlap area. This also means that lateral transport from the contact pad to the device area cannot stem from the PEDOT:PSS layer otherwise this extended emitting area would be much larger. As such this reveals that lateral charge transport in the CuNW film is intact and sufficient to drive the LED. So where does the dark area stem from? If it was from a lack of interface area between CuNW and the underlying device, this should be overcome by the conductive PEDOT:PSS as it is outside of the CuNW area. This makes the possibility of damage during the spray deposition likely.

6.6.3 Perovskite solar cells

Since there is the possibility that the spray process harms the active layer of organic devices, we moved to perovskite solar cells, which employs a thicker and potentially more robust active layer of the organic-inorganic hybrid material methylammonium lead iodide ($MAPbI_3$). This material system stirred great attention in the last few years due to its very rapidly increasing solar cell efficiencies, which went from around 3 %

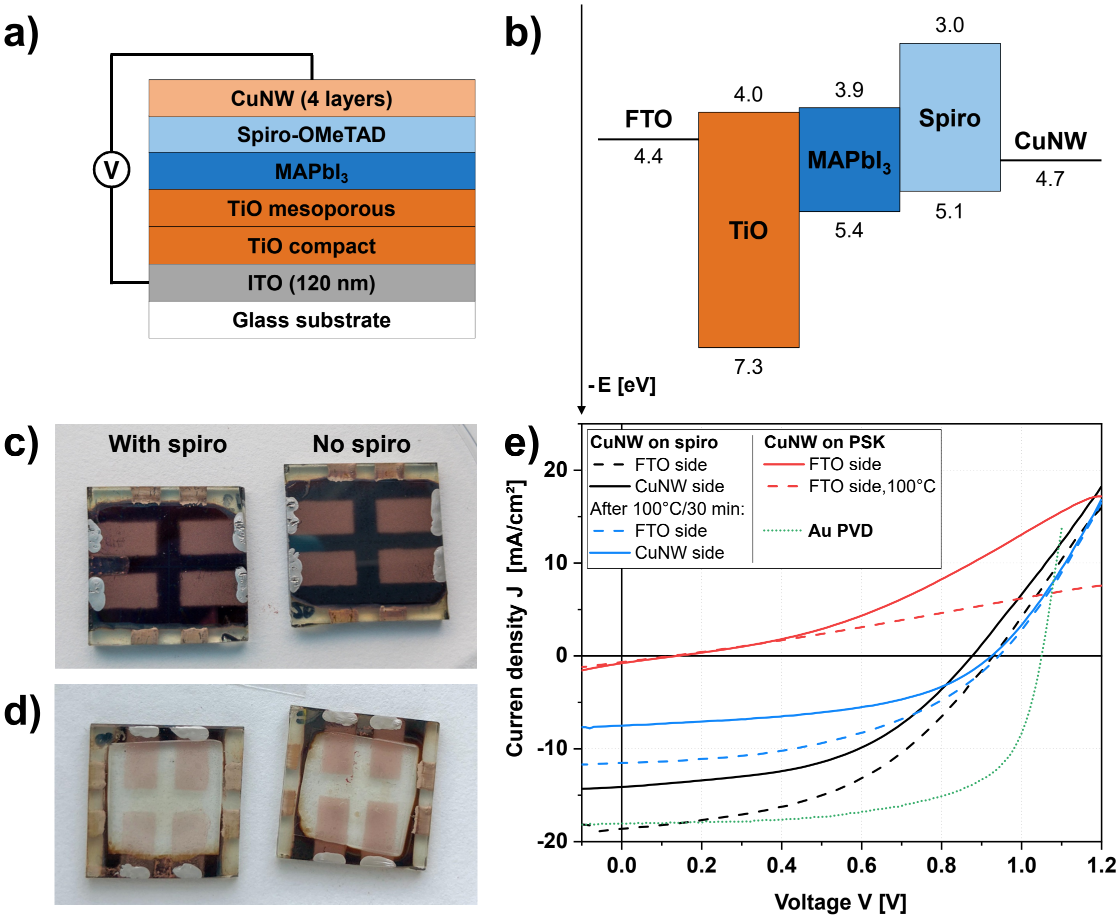

Figure 6.13: *CuNW top electrodes on perovskite solar cells: a) device stack and b) corresponding proposed energy diagram. Images of finished devices with and without Spiro-OMeTAD HTL c) before and d) after encapsulation. The perovskite seems to be dissolved by the (solvent free) encapsulation epoxy. e) J-V-curves before and after annealing at 100 °C for 30 min in nitrogen atmosphere.*

when introduced in 2009 [281] to over 20 % in 2017 [282]. The samples in this work were not made by ourselves, but were provided by Enrico Lamanna and Prof. Aldo di Carlo from the Centre for Hybrid and Organic Solar Energy (CHOSE) of the University of Rome *Tor Vergata*. The device stack consist of a FTO (fluorine tin oxide) electrode, a thin layer of compact TiO as ETL followed by about 100 nm of mesoporous TiO, which serves as scaffold which is filled with the light absorbing $MAPbI_3$ layer, which extends for another 400 nm on top of the TiO scaffold. Part of the devices were covered with a Spiro-OMeTAD (Spiro) HTL. The samples were transported from Rome to our Munich lab in a vacuum sealed container and stored inside a nitrogen filled glove box until further processing. Eventually, we spray deposited a CuNW electrode on top. A reference device was made with an evaporated Au electrode. The layer stack is illustrated in Fig. 6.13 a) with the corresponding proposed energy diagram in Fig. 6.13 b). Fig. 6.13 c) shows samples with CuNW electrodes sprayed on top of the bare $MAPbI_3$ (right) or the spiro interlayer (left). The same devices after encapsulation with a sheet of glass and epoxy glue are shown in Fig. 6.13 d). It can be seen that this material system is not compatible with our (solvent free) adhesive, as the adhesive covered area turns from dark brown to completely transparent seemingly dissolving all underlying layers. An analysis of different encapsulation methods for perovskite solar cells can be found elsewhere [283].

The resulting J-V-curves are shown in Fig. 6.13 d). The device without spiro is barely photo active ($V_{OC} = 0.13\,\mathrm{V}$) and shows little forward current, similar to the organic solar cell with PEDOT:PSS top layer shown above (sec. 6.6.1). The device with spiro HTL is a veritable solar cell with high photo current. Illuminated through the FTO side, J_{SC} reaches -18.6 mA/cm^2 - on par with the reference device with gold electrode. V_{OC} is slightly reduced for all devices with CuNW electrode from 1.05 V to an average 0.93 V. This voltage drop can be connected to a high series resistance, which is clearly visibly from the shape of the curve, but also be associated with the slightly lower work function of CuNW compared to Au. The main performance losses stem from a large drop of the fill factor from 65 to 46 %, which is caused by the large series resistance. In combination this results in a PCE of 7.9 % compared to 12.3 % of the reference device.

When the device is illuminated through the CuNW side, the J_{SC} is reduced by 24 % to 14.11 mA/cm^2. This decreased current can be attributed to a lower transmission of the CuNW network in comparison to the FTO layer and possibly additional absorption of the spiro HTL. Together with minor drops of V_{OC} and FF this results in a PCE of 4.9 %.

In an attempt to improve the sheet resistance of the CuNW network, the device was annealed at 100 °C for 30 min in nitrogen atmosphere. Unfortunately, instead of improving the performance this treatment seems to harm the devices as manifested by a significantly decreased current.

6.7 Summary

In this chapter we demonstrated spray coated metalnanowire networks from silver and copper and their integration into different optoelectronic devices as transparent electrodes.

An optimized AgNW film consisting of seven spray layers and immersed in DI-water for 15 min exhibits a (specular) transmission of 85 % at 550 nm with a sheet resistance of 13 Ω/sq. Such a film was used as transparent bottom electrode in a P3HT:PCBM solar cells with inverted architecture. Functional devices were presented, that proved independent of the thickness of the planarizing ZnO interlayer and showed better performance than the ITO reference devices.

Spray coated CuNW films were acid treated in solution and showed (specular) transmission of 80 % at 550 nm with a sheet resistance of 14 Ω/sq without post treatment. Confocal microscopy revealed extremely high roughness between a few and up to 40 µm, which makes the use of such films unsuitable as bottom electrode. Since no post treatment is necessary to achieve performant films, they were then integrated as top electrode into organic solar cells and light emitting diodes as well as perovskite solar cells. Functional organic devices could be demonstrated, when CuNW were spray coated on top of a PEDOT:PSS interlayer. However, performance was quite low and it seems that the organic active layer suffer from the spray process. Perovskite solar cells with spiro HTL handled the spray deposition better. Such a device with CuNW top electrode showed J_{SC} on par with the reference device with evaporated Au electrode when illuminated through the FTO electrode. Only the large series resistance significantly reduces the fill factor. Illumination through the CuNW electrode reduced the generated photo current by 24 %, which resulted in a PCE of 4.9 %.

7 Conclusion

In this work, we combine inorganic nanomaterials with organic polymers into optoelectronic devices that can be processed from solution. In particular, surface–functionalized silicon nanocrystals (SiNC) with a diameter of $d = 3.1\,\mathrm{nm}$ were used as light emitting layer in hybrid QLEDs and as electron acceptor in bulk heterojunction solar cells together with P3HT as electron donor.

Additionally, spray coated metal nanowire networks from copper and silver have been implemented as transparent conductive electrodes for solar cells and LEDs.

Silicon nanocrystal LEDs

We investigated photoluminescent SiNCs with different surface-functionalizations as electroluminescent emitter material in QLEDs. The SiNC form a clear solution in toluene and were spin coated into compact layers of about 30 - 40 nm. To complete the device this emitting layer was sandwiched between blocking layers and two electrodes. Such devices exhibit bright red light that is clearly visible under ambient conditions, with only little shift between photo- and electroluminescence. The device performance was significantly improved by the addition of blocking layers with appropriate band alignment. Best results were achieved with thin layers of PolyTPD for electron blocking and of ZnO for hole blocking.

We then compared SiNCs that were functionalized with the same hexyl chains, but by two different functionalization routes: the very common hydrosilylation (HS) method and the relatively new method of using of organolithium reagents (OLR). The resulting particles have identical size, absorption- and emission properties. However, SiNC functionalized with the OLR method exhibit a lower surface coverage with insulating surface groups and increased quantum yield (QY). These differences also manifest themselves in LED performance: HS-SiNCs result in device with more resistive behavior as well as lower luminance and quantum efficiency (EQE) than their OLR counterparts. These results show that properties of SiNCs can be altered by surface functionalization techniques even with identical surface groups and that usage of OLR is recommended over the widespread HS method.

Apart from different functionalization routes also different functional groups were investigated Here we investigated the influence of the chain length of alkyl chains as well as the use of an aryl group with conjugated π-system. SiNC functionalized with hexyl chains (six carbon atoms) and dodecyl chains (twelve carbon atoms) were implemented into SiNC-LEDs. The increased amount of insulating surface material of the longer dodecyl chains lead to SiNC-LEDs that drive less current and barely emit light. These results show that shorter alkyl chains are preferable over longer ones. SiNC functionalized with phenyl groups that contain a conjugated benzene ring, showed similar performance to comparable devices with hexyl functionalization. We could therefore not find any performance advantage associated with the conjugated system.

The functionalized SiNC can also be mixed into a polymer matrix. We fabricated LEDs with SiNC embedded into the light emitting polymer Super Yellow. The resulting device emission spectrum shows clearly attributable contributions from both materials. However, the polymer performance was impaired by the addition of the nanocrystals.

In conclusion, we have shown that the performance of SiNC-LEDs can be influenced by surface functionalization method and by using different surface groups. These results underline the importance of surface characteristics on the performance of SiNC optoelectronic devices and give guidelines for future research in the field.

Silicon nanocrystal hybrid solar cells

To overcome the processing hurdles that are associated with hydrogen-terminated SiNC commonly used in SiNC:polymer solar cells, we investigate the use of surface-functionalized SiNC that are stable in solution and less prone to oxidization. For this we combined SiNC as electron donor with polymer P3HT as electron acceptor into a bulk heterojunction layer. To facilitate a good interface between the poly(hexylthiophene) P3HT, the SiNC are functionalized with hexylthiophene surface groups. Those groups were either bonded directly onto the Si surface or via an additional ethynyl group that results in a conjugated system right onto the SiNC and therefore might improve charge transport off the particles.

We showed that addition of hexylthiophene-SiNC does significantly improve solar cells performance compared to a P3HT reference. There is an optimal mixing ratio of 50 wt.-% SiNC in the P3HT solution, where more or less SiNC resulted in lower photo currents. Similar to other bulk heterojunction solar cells the devices profit from a heat treatment that doubles the open circuit by likely due to a combination of beneficial morphology changes of the bulk heterojunction network and increased order in the P3HT phase. The open circuit voltage could be further lifted by replacing the Al cathode with Ca. We assume that the SiNC conduction band above the work function of Al, which then quenches the open circuit voltages. This is alleviated by the low work function of Ca. A fully optimized device reached a V_{OC} of 0.9 V and a power conversion efficiency (PCE) of 0.03 %. This leaves a lot of room for improvement to catch up with unfunctionalized SiNC that have reached PCEs over 1 % in combination with P3HT.

Extending the hexylthiophene ligand with an ethynyl group did not bring the predicted improvement. On the contrary, such SiNC actually had lower PCE than the P3HT reference.

We have to sum up, while functionalized SiNC have improved the device performance, they seem not to be a suitable replacement for unfunctionalized SiNC or fullerenes.

Transparent metal nanowire electrodes

To scale the production of printed electronics not only the active layer has to be solution processable, but also the electrodes – a factor often neglected in research devices. Printing of opaque electrodes is relatively straight forward, e.g., from silver pastes. Replacing the transparent indium tin oxide (ITO) electrode however is more critical. We addressed this issue by spray coating transparent networks of metal nanowires.

Silver nanowires (AgNW) can be dispersed well with the help of surfactants. They were spray coated on a glass substrate with an automated spray robot and the layer thickness was optimized for an optimal trade off between conductivity and transmission. With a simple water treatment remaining surfactant can be washed out and further improve transmission and sheet resistance to valuables comparable to ITO. We studied the AgNW layers roughness and showed that only a thin ZnO planarization layer of $\sim$50 nm is sufficient to fabricate functional solar cells without short circuits. The optimized solar cells based on P3HT:PCBM reach a PCE of up to 3.2 % surpassing the ITO reference devices that reached 2.6 %. This is likely due to the haziness that is inherent to nanowire networks, which further increases light absorption inside the solar cell. As such, spray coated AgNW are not only a solution-processable replacement for ITO, but even a superior alternative.

While spray coating can significantly reduce the processing cost over sputter coating of ITO, silver still has substantial material cost. A much cheaper alternative are nanowires made from copper. We spray coated CuNW solution into films with a handheld airbrush. An film with optimized thickness reaches the same sheet resistance as the ITO reference film with about 10 percentage points lower transmission. CuNW disperse not as well as AgNW, which reduces repeatability of the layer thickness and corresponding optical and electrical properties. Furthermore, the resulting agglomerates in the film lead to very rough films. This makes any planarization futile and prohibit their use as a bottom electrode in thin film devices. To enable their use as top electrode we rely on a pre-deposition acid treatment, when the CuNW are still in solution. This results in good film performance without the need for post treatments that would harm sensitive underlying polymer layers, e.g., acid or high temperature treatments are typically used. By spraying coating CuNW stripes on top of P3HT:PCBM solar cells and on Super Yellow OLEDs, we could get functional, yet low-performance devices. While charge transport through the

CuNW is working well, it seems that the spray coating process is harming the underlying polymer layers. This could partially be overcome by switching to perovskite ($MaPbI_3$) solar cells with a Spiro-OMeTAD hole transport layer on top. Such devices with CuNW top electrode showed J_{SC} on par with the reference device with evaporated Au electrode when illuminated through the FTO bottom electrode. Only an increased series resistance significantly reduces the fill factor compared to the reference. Illuminating through the CuNW top electrode decreases the photo current due to its inferior transmission, but still resulted in a respectable PCE of 4.9 %.

We can conclude that metal nanowire networks are an exciting alternative to ITO electrodes. The presented devices with AgNW electrodes already show superior performance compared to ITO reference devices. In a next step they should be brought to flexible substrates. CuNW could be implemented into functional devices, but the spraying process still needs tuning to not damage the underlying layers.

A Appendix

Process Details of SiNC fabrication

Process details for SiNC synthesis and functionalization via hydrosilylation and with organolithium reagents exemplary for functionalization with hexyl chains.

Preparation of oxide-embedded SiNCs: Polymeric hydrogen silsesquioxane (HSQ) was synthesized based on a literature known procedure [284]. HSQ (7 g) was weighed in a quartz reaction boat, heated from ambient to a peak processing temperature of 1100 °C at 18 °C/min in a Nabertherm RD 30/200/11 furnace with quartz working tube under an atmosphere consisting 5% H_2 and 95% N_2. The sample was kept at 1100 °C for 1 h. After cooling to room temperature, the resulting solid was ground into a fine brown powder using mortar and pestle. The composite was dispersed in ethanol and further ground in a shaker for 24 h with high-purity silica beads using a WAB Turbula mixer. The resulting SiNC/SiO_2 composite was dried in vacuo.

Liberation of hydride-terminated SiNCs: 300 mg of the SiNC/SiO_2 composite was transferred to an ethylene-tetrafluoroethylene (ETFE) beaker equipped with a Teflon-coated stir bar. Ethanol (3 mL) and water (3 mL) were then added, and stirred to form a brown suspension, followed by addition of 3 mL of 49% HF aqueous solution. After 30 min of etching, the color of the suspension turned to yellow. Hydride-terminated SiNCs were subsequently extracted from the aqueous layer into ca. 30 mL of toluene by multiple (i.e., 3 × 10 mL) extractions. The SiNC toluene suspension was centrifuged in an ETFE-centrifuge tube at 9000 rpm for 4 mins. Extracted particles were re-dispersed in 5 ml dry toluene and centrifuged once more to remove any residual water/ethanol.

Surface functionalization via hydrosilylation: Freshly etched hydride-terminated SiNCs (from 300 mg Si/SiO_2 composite) were dispersed in 2 mL of a dry toluene in a Schlenk flask equipped with a stir bar. 10 mg AIBN and 0.4 mL 1-hexene were added and the reaction mixture was degassed via three freeze-thaw cycles. This reaction mixture was heated at 70 °C for 15 hours. At the end of the reaction, purification was achieved by precipitating the functionalized SiNCs from a 5 mL 1:1 ethanol-methanol mixture. SiNCs were then centrifuged at 9000 rpm for 6 minutes and the sediment was re-dispersed in a minimum amount of toluene. The precipitation-centrifugation-redispersion cycle was performed two more times from toluene and ethanol-methanol. Finally, functionalized SiNCs were dispersed in toluene and filtered through a 0.45 μm PTFE syringe filter.

Surface functionalization with organolithium reagents: Freshly etched hydride- terminated SiNCs (from 300 mg Si/SiO_2 composite) were dispersed in 2 mL of a dry toluene in a Schlenk flask equipped with a stir bar. The dispersion was degassed via three freeze-thaw cycles. n-hexyllithium (0.2 mmoles from 2.3 M solution) was then added. Upon addition, the color of the reaction mixture turned dark brown. The reaction was run for 15 hours under an argon atmosphere at room temperature and terminated by precipitation of the functionalized SiNCs from a 5 mL 1:1 ethanol-methanol mixture, acidified with HCl conc. (0.2 mL). Obtained SiNCs were centrifuged at 9000 rpm for 6 minutes and the sediment was re-dispersed in minimum amount of toluene. The precipitation-centrifugation-redispersion cycle was performed two more times from toluene and ethanol-methanol. Finally, functionalized SiNCs were dispersed in toluene and filtered through a 0.45 μm PTFE syringe filter.

Bibliography

[1] A. Köhler and H. Bässler, *The Electronic Structure of Organic Semiconductors*. 2015, vol. 1, pp. 1–3, ISBN: 9788578110796. DOI: `10.1017/CBO9781107415324.004` (cit. on pp. 1, 6).

[2] T. Yokota, P. Zalar, M. Kaltenbrunner, H. Jinno, N. Matsuhisa, H. Kitanosako, Y. Tachibana, W. Yukita, M. Koizumi, and T. Someya, "Ultraflexible organic photonic skin," *Sci. Adv.*, vol. 2, no. 4, e1501856–e1501856, Apr. 2016. DOI: `10.1126/sciadv.1501856` (cit. on p. 1).

[3] A. K. Bansal, S. Hou, O. Kulyk, E. M. Bowman, and I. D. Samuel, "Wearable Organic Optoelectronic Sensors for Medicine," *Adv. Mater.*, vol. 27, no. 46, pp. 7638–7644, 2015. DOI: `10.1002/adma.201403560` (cit. on p. 1).

[4] S. El-Molla, A. Albrecht, E. Cagatay, P. Mittendorfer, G. Cheng, P. Lugli, J. F. Salmerón, and A. Rivadeneyra, "Integration of a Thin Film PDMS-Based Capacitive Sensor for Tactile Sensing in an Electronic Skin," *J. Sensors*, vol. 2016, 2016. DOI: `10.1155/2016/1736169` (cit. on p. 1).

[5] H. Ling, S. Liu, Z. Zheng, and F. Yan, "Organic Flexible Electronics," *Small Methods*, p. 1 800 070, 2018. DOI: `10.1002/smtd.201800070` (cit. on p. 1).

[6] W. Kang, C. Yan, C. Y. Foo, and P. S. Lee, "Foldable Electrochromics Enabled by Nanopaper Transfer Method," *Adv. Funct. Mater.*, vol. 25, no. 27, pp. 4203–4210, 2015. DOI: `10.1002/adfm.201500527` (cit. on p. 1).

[7] N. Espinosa, M. Hösel, M. Jørgensen, and F. C. Krebs, "Large scale deployment of polymer solar cells on land, on sea and in the air," *Energy Environ. Sci.*, vol. 7, no. 3, pp. 855–866, Feb. 2014. DOI: `10.1039/c3ee43212b` (cit. on p. 1).

[8] E. Ho, H. Lorach, G. Goetz, F. Laszlo, X. Lei, T. Kamins, J. C. Mariani, A. Sher, and D. Palanker, "Temporal structure in spiking patterns of ganglion cells defines perceptual thresholds in rodents with subretinal prosthesis," *Sci. Rep.*, vol. 8, no. 1, p. 3145, Dec. 2018. DOI: `10.1038/s41598-018-21447-1` (cit. on p. 1).

[9] N. Espinosa, M. Hösel, D. Angmo, and F. C. Krebs, "Solar cells with one-day energy payback for the factories of the future," *Energy Environ. Sci.*, vol. 5, no. 1, pp. 5117–5132, Jan. 2012. DOI: `10.1039/c1ee02728j` (cit. on p. 2).

[10] Y. Shirasaki, G. J. Supran, M. G. Bawendi, and V. Bulović, "Emergence of colloidal quantum-dot light-emitting technologies," *Nat. Photonics*, vol. 7, no. 1, pp. 13–23, 2013. DOI: `10.1038/nphoton.2012.328` (cit. on pp. 2, 13, 39).

[11] R. Wang, X. Wu, K. Xu, W. Zhou, Y. Shang, H. Tang, H. Chen, and Z. Ning, "Highly Efficient Inverted Structural Quantum Dot Solar Cells," vol. 1704882, pp. 1–5, 2018. DOI: `10.1002/adma.201704882` (cit. on pp. 2, 13).

[12] P. Müller-Buschbaum, M. Thelakkat, T. F. Fässler, and M. Stutzmann, "Hybrid Photovoltaics – from Fundamentals towards Application," *Adv. Energy Mater.*, vol. 7, no. 16, pp. 1–25, 2017. DOI: `10.1002/aenm.201700248` (cit. on pp. 2, 13, 82).

[13] B. S. Mashford, M. Stevenson, Z. Popovic, C. Hamilton, Z. Zhou, C. Breen, J. Steckel, V. Bulovic, M. Bawendi, S. Coe-Sullivan, and P. T. Kazlas, "High-efficiency quantum-dot light-emitting devices with enhanced charge injection," *Nat. Photonics*, vol. 7, no. 5, pp. 407–412, 2013. DOI: `10.1038/nphoton.2013.70` (cit. on pp. 2, 13).

[14] A. Pochettino, "Sull' effetto fotoelettrico nell' Antracene," *Atti R. Accad. Dei Lincei*, vol. 15, no. 5, p. 171, 1906 (cit. on p. 5).

[15] J. Stark and W. Steubing, "Fluoreszenz und lichtelektrische Empfindlichkeit organischer Substanzen," *Phys. Zeitschr*, vol. 15, pp. 481–495, 1908 (cit. on p. 5).

[16] J. Koenigsberger and K. Schilling, "Über Elektrizitätsleitung in festen Elementen und Verbindungen," *Ann. Phys.*, vol. 337, no. 6, pp. 179–230, 1910. DOI: `10.1002/andp.19103370608` (cit. on p. 5).

[17] W. E. Pauli, "Lichtelektrische Untersuchungen an fluoreszierenden Substanzen," *Ann. Phys.*, vol. 345, no. 4, pp. 677–700, 1913. DOI: `10.1002/andp.19133450405` (cit. on p. 5).

[18] A. Bernanose, M. Comte, and P. Vouaux, "A new method of light emission by certain organic compounds," *J. Chim. Phys.*, vol. 50, pp. 64–67, 1953 (cit. on p. 5).

[19] M. Pope, H. P. Kallmann, and P. Magnante, "Electroluminescence in Organic Crystals," *J. Chem. Phys.*, vol. 38, no. 1963, p. 2042, Apr. 1963. DOI: `10.1063/1.1733929` (cit. on p. 5).

[20] W. Helfrich and W. G. Schneider, "Recombination radiation in anthracene crystals," *Phys. Rev. Lett.*, vol. 14, no. 7, pp. 229–231, 1965. DOI: `10.1103/PhysRevLett.14.229` (cit. on p. 5).

[21] C. W. Tang and S. A. VanSlyke, "Organic electroluminescent diodes," *Appl. Phys. Lett.*, vol. 51, no. 12, pp. 913–915, Sep. 1987. DOI: `10.1063/1.98799` (cit. on p. 5).

[22] J. H. Burroughes, D. D. C. Bradley, A. R. Brown, R. N. Marks, K. Mackay, R. H. Friend, P. L. Burns, and A. B. Holmes, "Light-emitting diodes based on conjugated polymers," *Nature*, vol. 347, pp. 539–541, 1990. DOI: `10.1038/347539a0` (cit. on p. 5).

[23] H. Shirakawa, E. J. Louis, A. G. MacDiarmid, C. K. Chiang, and A. J. Heeger, "Synthesis of electrically conducting organic polymers: halogen derivatives of polyacetylene, (CH)x," *J. Chem. Soc. Chem. Commun.*, no. 16, p. 578, 1977. DOI: `10.1039/c39770000578` (cit. on p. 5).

[24] Alan Heeger, A. G. MacDiarmid, and H. Shirakawa, "The Nobel Prize in chemistry, 2000: conductive polymers," The Royal Swedish Academy of Sciences, Tech. Rep., 2000, pp. 1–16 (cit. on p. 5).

[25] J. E. Mcmurry, R. C. Fay, and J. K. Robinson, *Chemistry*, 7th. Pearson, 2015, ISBN: 9780321943170 (cit. on pp. 6, 8).

[26] E. Schrödinger, "An undulatory theory of the mechanics of atoms and molecules," *Phys. Rev.*, vol. 28, no. 6, pp. 1049–1070, 1926. DOI: `10.1103/PhysRev.28.1049` (cit. on p. 7).

[27] L. Silvestroni and R. M. Metzger, *Unimolecular and Supramolecular Electronics I*, R. M. Metzger, Ed., 2. Springer, 2012, vol. 7, p. 317, ISBN: 9783642255281. DOI: `10.1007/978-3-642-27284-4` (cit. on p. 9).

[28] A. Miller and E. Abrahams, "Impurity conduction at low concentrations," *Phys. Rev.*, vol. 120, no. 3, pp. 745–755, 1960. DOI: `10.1103/PhysRev.120.745` (cit. on p. 10).

[29] N. F. Mott, "Conduction in glasses containing transition metal ions," *J. Non. Cryst. Solids*, vol. 1, no. 1, pp. 1–17, 1968. DOI: `10.1016/0022-3093(68)90002-1` (cit. on p. 10).

[30] N. F. Mott, "Conduction in non-crystalline materials," *Philos. Mag.*, vol. 19, no. 160, p. 835, 1969. DOI: `10.1080/14786436908216338` (cit. on p. 10).

[31] H. Bässler, "Charge Transport in Disordered Organic Photoconductors a Monte Carlo Simulation Study," *Phys. status solidi*, vol. 175, no. 1, pp. 15–56, 1993. DOI: `10.1002/pssb.2221750102` (cit. on p. 11).

[32] P. Buffat and J. P. Borel, "Size effect on the melting temperature of gold particles," *Phys. Rev. A*, vol. 13, no. 6, pp. 2287–2298, 1976. DOI: `10.1103/PhysRevA.13.2287` (cit. on p. 12).

[33] J. S. Steckel, S. Coe-Sullivan, V. Bulović, and M. G. Bawendi, "1.3 μm to 1.55 μm Tunable Electroluminescence from PbSe Quantum Dots Embedded within an Organic Device," *Adv. Mater.*, vol. 15, no. 21, pp. 1862–1866, 2003. DOI: `10.1002/adma.200305449` (cit. on pp. 12, 13).

[34] A. Ekimov and A.A.Onushchenko, "Quantum size effect in three-dimensional micorscopic semiconductor crystals," *JETP Lett.*, vol. 34, pp. 345–349, 1981. DOI: `0021-3640/81/18345-05` (cit. on p. 12).

[35] A. Ekimov and A. A. Onushchenko, "Size quantization of the electron energy spectrum in a microscopic semiconductor crystal," *JETP lett*, vol. 40, no. 8, pp. 1136–1139, 1984 (cit. on p. 12).

[36] L. Brus, "A simple model for the ionization potential, electron affinity, and aqueous redox potentials of small semiconductor crystallites," *J. Chem. Phys.*, vol. 79, no. 11, pp. 5566–5571, 1983. DOI: `10.1063/1.445676` (cit. on p. 12).

[37] L. Brus, "Electron-electron and electron-hole interactions in small semiconductor crystallites: The size dependence of the lowest excited electronic state," *J. Chem. Phys.*, vol. 80, no. 9, pp. 4403–4409, May 1984. DOI: `10.1063/1.447218` (cit. on p. 12).

[38] L. Brus, "Electronic wave functions in semiconductor clusters: experiment and theory," *J. Phys. Chem.*, vol. 90, no. 12, pp. 2555–2560, 1986. DOI: `10.1021/j100403a003` (cit. on p. 12).

[39] C. B. Murray, D. J. Norris, and M. G. Bawendi, "Synthesis and Characterization of Nearly Monodisperse CdE (E = S, Se, Te) Semiconductor Nanocrystallites," *J. Am. Chem. Soc.*, vol. 115, no. 19, pp. 8706–8715, 1993. DOI: `10.1021/ja00072a025` (cit. on p. 12).

[40] R. Freeman and I. Willner, "Optical molecular sensing with semiconductor quantum dots (QDs)," *Chem. Soc. Rev.*, vol. 41, no. 10, p. 4067, 2012. DOI: `10.1039/c2cs15357b` (cit. on p. 13).

[41] Z. Yue, F. Lisdat, W. J. Parak, S. G. Hickey, L. Tu, N. Sabir, D. Dorfs, and N. C. Bigall, "Quantum-dot-based photoelectrochemical sensors for chemical and biological detection," *ACS Appl. Mater. Interfaces*, vol. 5, no. 8, pp. 2800–2814, 2013. DOI: `10.1021/am3028662` (cit. on p. 13).

[42] S. Silvi and A. Credi, "Luminescent sensors based on quantum dot–molecule conjugates," *Chem. Soc. Rev.*, vol. 44, no. 13, pp. 4275–4289, 2015. DOI: `10.1039/C4CS00400K` (cit. on p. 13).

[43] M. Bruchez, M. Moronne, P. Gin, S. Weiss, and A. P. Alivisatos, "Semiconductor nanocrystals as fluorescent biological labels," *Science*, vol. 281, no. 5385, pp. 2013–2016, 1998. DOI: `10.1126/science.281.5385.2013` (cit. on p. 13).

[44] B. Dubertret, P. Skourides, D. J. Norris, V. Noireaux, A. H. Brivanlou, and A. Libchaber, "In vivo imaging of quantum dots encapsulated in phospholipid micelles," *Science*, vol. 298, no. 5599, pp. 1759–1762, 2002. DOI: `10.1126/science.1077194` (cit. on p. 13).

[45] I. L. Medintz, H. T. Uyeda, E. R. Goldman, and H. Mattoussi, "Quantum dot bioconjugates for imaging, labelling and sensing," *Nat. Mater.*, vol. 4, no. 6, pp. 435–446, 2005. DOI: `10.1038/nmat1390` (cit. on p. 13).

[46] X. Michalet, F. F. Pinaud, L. A. Bentolila, J. M. Tsay, S. Doose, J. J. Li, G. Sundaresan, A. M. Wu, S. S. Gambhir, and S. Weiss, "Quantum dots for live cells, in vivo imaging, and diagnostics.," *Science*, vol. 307, no. 5709, pp. 538–44, 2005. DOI: `10.1126/science.1104274` (cit. on p. 13).

[47] G. Toth and C. S. Lent, "Quantum computing with quantum-dot cellular automata," *Phys. Rev. A*, vol. 63, no. 5, p. 52 315, 2001. DOI: `10.1103/PhysRevA.63.052315` (cit. on p. 13).

[48] J. M. Eizerman, R. Hanson, L. H. Van Beveren, B. Witkamp, L. M. Vandersypen, and L. P. Kouwenhoven, "Single-shot read-out of an individual electron spin in a quantum dot," *Nature*, vol. 430, no. 6998, pp. 431–435, 2004. DOI: `10.1038/nature02693` (cit. on p. 13).

[49] G. L. Snider, A. O. Orlov, V. Joshi, R. A. Joyce, H. Qi, K. K. Yadavalli, G. H. Bernstein, T. P. Fehlner, and C. S. Lent, "Electronic quantum-dot cellular automata," in *2008 9th Int. Conf. Solid-State Integr. Technol.*, 2008, pp. 549–552, ISBN: 978-1-4244-2185-5. DOI: `10.1109/ICSICT.2008.4734600` (cit. on p. 13).

[50] A. J. Nozik, "Quantum dot solar cells," in *Phys. E Low-Dimensional Syst. Nanostructures*, vol. 14, 2002, pp. 115–120, ISBN: 1386-9477. DOI: `10.1016/S1386-9477(02)00374-0` (cit. on pp. 13, 82).

[51] B. O. Dabbousi, J. Rodriguez, F. V. Mikulec, J. R. Heine, H. Mattoussi, R. Ober, K. F. Jensen, and M. G. Bawendi, "(CdSe) ZnS Core - Shell Quantum Dots : Synthesis and Characterization of a Size Series of Highly Luminescent Nanocrystallites," *J. Phys. Chem. B*, vol. 101, no. 97, pp. 9463–9475, 1997. DOI: `10.1021/jp971091y` (cit. on p. 13).

[52] D. V. Talapin, I. Mekis, S. Götzinger, A. Kornowski, O. Benson, and H. Weller, "CdSe/CdS/ZnS and CdSe/ZnSe/ZnS core-shell-shell nanocrystals," *J. Phys. Chem. B*, vol. 108, no. 49, pp. 18 826–18 831, 2004. DOI: `10.1021/jp046481g` (cit. on p. 13).

[53] J. M. Caruge, J. E. Halpert, V. Wood, V. Bulovíc, and M. G. Bawendi, "Colloidal quantum-dot light-emitting diodes with metal-oxide charge transport layers," *Nat. Photonics*, vol. 2, no. 4, pp. 247–250, 2008. DOI: `10.1038/nphoton.2008.34` (cit. on p. 13).

[54] V. I. Klimov, A. A. Mikhailovsky, S. Xu, A. Malko, J. A. Hollingsworth, C. A. Leatherdale, H.-J. Eisler, and M. G. Bawendi, "Optical Gain and Stimulated Emission in Nanocrystal Quantum Dots," *Science*, vol. 290, no. 5490, pp. 314–317, 2000. DOI: `10.1126/science.290.5490.314` (cit. on p. 13).

[55] N. N. Ledentsov, "Quantum dot laser," *Semicond. Sci. Technol.*, vol. 26, no. 1, 2011. DOI: `10.1088/0268-1242/26/1/014001` (cit. on p. 13).

[56] S. Gao, C. Zhang, Y. Liu, H. Su, L. Wei, T. Huang, N. Dellas, S. Shang, S. E. Mohney, J. Wang, and J. Xu, "Lasing from colloidal InP/ZnS quantum dots," *Opt. Express*, vol. 19, no. 6, p. 5528, 2011. DOI: `10.1364/OE.19.005528` (cit. on p. 13).

[57] C. Kirchner, T. Liedl, S. Kudera, T. Pellegrino, A. Munoz Javier, H. E. Gaub, S. Stölzle, N. Fertig, and W. J. Parak, "Cytotoxicity of colloidal CdSe and CdSe/ZnS nanoparticles," *Nano Lett.*, vol. 5, no. 2, pp. 331–338, 2005. DOI: `10.1021/nl047996m` (cit. on p. 13).

[58] G. Oberdörster, E. Oberdörster, and J. Oberdörster, "Nanotoxicology: An emerging discipline evolving from studies of ultrafine particles," *Environ. Health Perspect.*, vol. 113, no. 7, pp. 823–839, 2005. DOI: `10.1289/ehp.7339` (cit. on p. 13).

[59] A. M. Derfus, W. C. W. Chan, and S. N. Bhatia, "Probing the Cytotoxicity of Semiconductor Quantum Dots," *Nano Lett.*, vol. 4, no. 1, pp. 11–18, 2004. DOI: `10.1021/nl0347334` (cit. on p. 13).

[60] J. K. Fard, S. Jafari, and M. A. Eghbal, "A review of molecular mechanisms involved in toxicity of nanoparticles," *Adv. Pharm. Bull.*, vol. 5, no. 4, pp. 447–454, 2015. DOI: `10.15171/apb.2015.061` (cit. on p. 13).

[61] World Health Organization, *Ten chemicals of major public health concern* (cit. on p. 13).

[62] European Commission, "DIRECTIVE 2011/65/EU OF THE EUROPEAN PARLIAMENT AND OF THE COUNCIL of 8 June 2011 - ROHS," *Off. J. Eur. Union*, vol. 54, no. 1 July, pp. 88–110, 2011. DOI: `10.1017/CBO9781107415324.004` (cit. on p. 13).

[63] N. H. Alsharif, C. E. M. Berger, S. S. Varanasi, Y. Chao, B. R. Horrocks, and H. K. Datta, "Alkyl-capped silicon nanocrystals lack cytotoxicity and have enhanced intracellular accumulation in malignant cells via cholesterol-dependent endocytosis," *Small*, vol. 5, no. 2, pp. 221–228, 2009. DOI: `10.1002/smll.200800903` (cit. on p. 13).

[64] Q. Wang, Y. Bao, X. Zhang, P. R. Coxon, U. A. Jayasooriya, and Y. Chao, "Uptake and toxicity studies of poly-acrylic acid functionalized silicon nanoparticles in cultured mammalian cells," *Adv. Healthc. Mater.*, vol. 1, no. 2, pp. 189–198, 2012. DOI: `10.1002/adhm.201100010` (cit. on p. 13).

[65] S. Bhattacharjee, I. M. C. M. Rietjens, M. P. Singh, T. M. Atkins, T. K. Purkait, Z. Xu, S. Regli, A. Shukaliak, R. J. Clark, B. S. Mitchell, G. M. Alink, A. T. M. Marcelis, M. J. Fink, J. G. C. Veinot, S. M. Kauzlarich, and H. Zuilhof, "Cytotoxicity of surface-functionalized silicon and germanium nanoparticles: the dominant role of surface charges," *Nanoscale*, vol. 5, no. 11, p. 4870, 2013. DOI: `10.1039/c3nr34266b` (cit. on p. 13).

[66] X. Cheng, S. B. Lowe, P. J. Reece, and J. J. Gooding, “Colloidal silicon quantum dots: from preparation to the modification of self-assembled monolayers (SAMs) for bio-applications,” *Chem. Soc. Rev.*, vol. 43, no. 8, pp. 2680–2700, 2014. DOI: `10.1039/C3CS60353A` (cit. on pp. 13, 30).

[67] J. Liu, F. Erogbogbo, K. T. Yong, L. Ye, J. Liu, R. Hu, H. Chen, Y. Hu, Y. Yang, J. Yang, I. Roy, N. A. Karker, M. T. Swihart, and P. N. Prasad, “Assessing clinical prospects of silicon quantum dots: Studies in mice and monkeys,” *ACS Nano*, vol. 7, no. 8, pp. 7303–7310, 2013. DOI: `10.1021/nn4029234` (cit. on p. 13).

[68] B. Delley and E. Steigmeier, “Quantum confinement in Si nanocrystals,” *Phys. Rev. B*, vol. 47, no. 3, pp. 1397–1400, 1993. DOI: `10.1103/PhysRevB.47.1397` (cit. on p. 13).

[69] W. L. Wilson, P. F. Szajowski, and L. Brus, “Quantum confinement in size-selected, surface-oxidized silicon nanocrystals.,” *Science*, vol. 262, no. 5137, pp. 1242–1244, 1993. DOI: `10.1126/science.262.5137.1242` (cit. on p. 13).

[70] G. Ledoux, J. Gong, F. Huisken, O. Guillois, and C. Reynaud, “Photoluminescence of size-separated silicon nanocrystals: Confirmation of quantum confinement,” *Appl. Phys. Lett.*, vol. 80, no. 25, pp. 4834–4836, 2002. DOI: `10.1063/1.1485302` (cit. on p. 13).

[71] D. Jurbergs, E. Rogojina, L. Mangolini, and U. Kortshagen, “Silicon nanocrystals with ensemble quantum yields exceeding 60%,” *Appl. Phys. Lett.*, vol. 88, no. 23, p. 233 116, Jun. 2006. DOI: `10.1063/1.2210788` (cit. on pp. 13, 30).

[72] Q. Li, Y. He, J. Chang, L. Wang, H. Chen, Y. W. Tan, H. Wang, and Z. Shao, “Surface-modified silicon nanoparticles with ultrabright photoluminescence and single-exponential decay for nanoscale fluorescence lifetime imaging of temperature,” *J. Am. Chem. Soc.*, vol. 135, no. 40, pp. 14 924–14 927, 2013. DOI: `10.1021/ja407508v` (cit. on p. 13).

[73] L. T. Canham, “Silicon quantum wire array fabrication by electrochemical and chemical dissolution of wafers,” *Appl. Phys. Lett.*, vol. 57, no. 10, pp. 1046–1048, 1990. DOI: `10.1063/1.103561` (cit. on p. 13).

[74] Z. H. Zhang, R. Lockwood, J. G. C. Veinot, and A. Meldrum, “Detection of ethanol and water vapor with silicon quantum dots coupled to an optical fiber,” *Sensors Actuators, B Chem.*, vol. 181, pp. 523–528, 2013. DOI: `10.1016/j.snb.2013.01.070` (cit. on p. 13).

[75] Y. Yi, G. Zhu, C. Liu, Y. Huang, Y. Zhang, H. Li, J. Zhao, and S. Yao, “A label-free silicon quantum dots-based photoluminescence sensor for ultrasensitive detection of pesticides,” *Anal. Chem.*, vol. 85, no. 23, pp. 11 464–11 470, 2013. DOI: `10.1021/ac403257p` (cit. on p. 13).

[76] J. Zhang and S.-H. Yu, "Highly photoluminescent silicon nanocrystals for rapid, label-free and recyclable detection of mercuric ions," *Nanoscale*, vol. 6, no. 8, p. 4096, 2014. DOI: `10.1039/c3nr05896d` (cit. on p. 13).

[77] C. M. Gonzalez, M. Iqbal, M. Dasog, D. G. Piercey, R. Lockwood, T. M. Klapötke, and J. G. C. Veinot, "Detection of high-energy compounds using photoluminescent silicon nanocrystal paper based sensors.," *Nanoscale*, vol. 6, no. 5, pp. 2608–12, 2014. DOI: `10.1039/c3nr06271f` (cit. on p. 13).

[78] V. Svrcek, T. Yamanari, D. Mariotti, S. Mitra, T. Velusamy, and K. Matsubara, "A silicon nanocrystal/polymer nanocomposite as a down-conversion layer in organic and hybrid solar cells," *Nanoscale*, vol. 7, no. 27, pp. 11 566–11 574, 2015. DOI: `10.1039/C5NR02703A` (cit. on p. 13).

[79] F. Erogbogbo, K.-t. Yong, I. Roy, G. Xu, P. N. Prasad, and M. T. Swihart, "Biocompatible Luminescent Silicon," *ACS Nano*, vol. 2, no. 5, pp. 873–878, 2008 (cit. on p. 13).

[80] F. Erogbogbo, K.-T. Yong, I. Roy, R. Hu, W.-C. Law, W. Zhao, H. Ding, F. Wu, R. Kumar, M. T. Swihart, and P. N. Prasad, "In Vivo targeted Cancer Imaging, Sentinel Lymph Node Mapping and Multi-Channel Imaging with Biocompatible Silicon Nanocrystals," *ACS Nano*, vol. 5, no. 1, pp. 413–423, 2011. DOI: `10.1021/nn1018945` (cit. on p. 13).

[81] H. Nishimura, K. Ritchie, R. S. Kasai, M. Goto, N. Morone, H. Sugimura, K. Tanaka, I. Sase, A. Yoshimura, Y. Nakano, T. K. Fujiwara, and A. Kusumi, "Biocompatible fluorescent silicon nanocrystals for single-molecule tracking and fluorescence imaging," *J. Cell Biol.*, vol. 202, no. 6, pp. 967–983, 2013. DOI: `10.1083/jcb.201301053` (cit. on p. 13).

[82] Y. Zhong, F. Peng, F. Bao, S. Wang, X. Ji, L. Yang, Y. Su, S. T. Lee, and Y. He, "Large-scale aqueous synthesis of fluorescent and biocompatible silicon nanoparticles and their use as highly photostable biological probes," *J. Am. Chem. Soc.*, vol. 135, no. 22, pp. 8350–8356, 2013. DOI: `10.1021/ja4026227` (cit. on p. 13).

[83] E. Borsella, R. D'Amato, M. Falconieri, E. Trave, A. Panariti, and I. Rivolta, "An outlook on the potential of Si nanocrystals as luminescent probes for bioimaging," *J. Mater. Res.*, vol. 28, no. 02, pp. 193–204, 2013. DOI: `10.1557/jmr.2012.295` (cit. on p. 13).

[84] J. Graetz, C. C. Ahn, R. Yazami, and B. Fultz, "Highly Reversible Lithium Storage in Nanostructured Silicon," *Electrochem. Solid-State Lett.*, vol. 6, no. 9, A194, 2003. DOI: `10.1149/1.1596917` (cit. on p. 13).

[85] R. Teki, R. Krishnan, T. C. Parker, T. M. Lu, M. K. Datta, P. N. Kumta, and N. Koratkar, "Nanostructured silicon anodes for lithium Ion rechargeable batteries," *Small*, vol. 5, no. 20, pp. 2236–2242, 2009. DOI: `10.1002/smll.200900382` (cit. on p. 13).

[86] H. Kim, M. Seo, M. H. Park, and J. Cho, “A critical size of silicon nano-anodes for lithium rechargeable batteries,” *Angew. Chemie - Int. Ed.*, vol. 49, no. 12, pp. 2146–2149, 2010. DOI: `10.1002/anie.200906287` (cit. on p. 13).

[87] S. Niesar, R. Dietmueller, H. Nesswetter, H. Wiggers, and M. Stutzmann, “Silicon/organic semiconductor heterojunctions for solar cells,” *Phys. Status Solidi*, vol. 2781, no. 12, pp. 2775–2781, Nov. 2009. DOI: `10.1002/pssa.200925322` (cit. on pp. 13, 82, 83, 90).

[88] C.-Y. Liu, Z. C. Holman, and U. R. Kortshagen, “Hybrid solar cells from P3HT and silicon nanocrystals,” *Nano Lett.*, vol. 9, no. 1, pp. 449–52, Jan. 2009. DOI: `10.1021/nl8034338` (cit. on pp. 13, 82, 83, 88, 90, 95).

[89] C.-Y. Liu, Z. C. Holman, and U. R. Kortshagen, “Optimization of Si NC/P3HT Hybrid Solar Cells,” *Adv. Funct. Mater.*, vol. 20, no. 13, pp. 2157–2164, Jun. 2010. DOI: `10.1002/adfm.200902471` (cit. on pp. 13, 82, 83, 88, 90, 92, 95).

[90] C. Y. Liu and U. R. Kortshagen, “A Silicon nanocrystal schottky junction solar cell produced from colloidal silicon nanocrystals,” *Nanoscale Res. Lett.*, vol. 5, no. 8, pp. 1253–1256, 2010. DOI: `10.1007/s11671-010-9632-z` (cit. on pp. 13, 82, 85, 88, 95).

[91] S. Niesar, W. Fabian, N. Petermann, D. Herrmann, E. Riedle, H. Wiggers, M. S. Brandt, and M. Stutzmann, “Efficiency Enhancement in Hybrid P3HT/Silicon Nanocrystal Solar Cells,” *Green*, vol. 1, no. 4, pp. 339–350, Jan. 2011. DOI: `10.1515/GREEN.2011.034` (cit. on pp. 13, 82, 83, 88, 90, 95).

[92] S. Kim, K. Jeon, J. C. Lee, M. T. Swihart, and M. Yang, “Enhanced performance of a polymer solar cell upon addition of free-standing, freshly etched, photoluminescent silicon nanocrystals,” *Appl. Phys. Express*, vol. 5, pp. 6–9, 2012. DOI: `10.1143/APEX.5.022302` (cit. on pp. 13, 82, 84, 85, 96).

[93] C.-Y. Liu and U. R. Kortshagen, “Hybrid solar cells from MDMO-PPV and silicon nanocrystals,” *Nanoscale*, vol. 4, no. 13, p. 3963, 2012. DOI: `10.1039/c2nr30436h` (cit. on pp. 13, 82, 83, 88, 95).

[94] T. Lin, X. Liu, B. Zhou, Z. Zhan, A. N. Cartwright, and M. T. Swihart, “A solution-processed UV-sensitive photodiode produced using a new silicon nanocrystal ink,” *Adv. Funct. Mater.*, vol. 24, no. 38, pp. 6016–6022, 2014. DOI: `10.1002/adfm.201400600` (cit. on p. 13).

[95] S. Kim, J.-C. J. H. Lee, M. T. Swihart, and J. Y. Kim, “Silicon nanoparticle size-dependent open circuit voltage in an organic–inorganic hybrid solar cell,” *Curr. Appl. Phys.*, vol. 14, no. 1, pp. 127–131, 2014. DOI: `10.1016/j.cap.2013.10.006` (cit. on pp. 13, 82, 85).

[96] K.-Y. Cheng, R. Anthony, U. R. Kortshagen, and R. J. Holmes, "Hybrid silicon nanocrystal-organic light-emitting devices for infrared electroluminescence," *Nano Lett.*, vol. 10, no. 4, pp. 1154–1157, 2010. DOI: `10.1021/nl903212y` (cit. on pp. 13, 45, 47, 60).

[97] K.-Y. Cheng, R. Anthony, U. R. Kortshagen, and R. J. Holmes, "High-efficiency silicon nanocrystal light-emitting devices.," *Nano Lett.*, vol. 11, no. 5, pp. 1952–6, May 2011. DOI: `10.1021/nl2001692` (cit. on pp. 13, 45, 48, 55, 60).

[98] C.-C. C. Tu, L. Tang, J. Huang, A. Voutsas, and L. Y. Lin, "Visible electroluminescence from hybrid colloidal silicon quantum dot-organic light-emitting diodes," *Appl. Phys. Lett.*, vol. 98, no. 21, p. 213 102, 2011. DOI: `10.1063/1.3593382` (cit. on pp. 13, 45).

[99] D. P. Puzzo, E. J. Henderson, M. G. Helander, Z. Wang, G. A. Ozin, and Z. Lu, "Visible colloidal nanocrystal silicon light-emitting diode.," *Nano Lett.*, vol. 11, no. 4, pp. 1585–90, Apr. 2011. DOI: `10.1021/nl1044583` (cit. on pp. 13, 45–47, 49, 55).

[100] R. J. Anthony, K. Y. K.-Y. Cheng, Z. C. Holman, R. J. Holmes, and U. R. Kortshagen, "An All-Gas-Phase Approach for the Fabrication of Silicon Nanocrystal Light-Emitting Devices," *Nano Lett.*, vol. 12, no. 6, pp. 2822–2825, 2012. DOI: `10.1021/nl300164z` (cit. on pp. 13, 45, 55).

[101] M. L. Mastronardi, E. J. Henderson, D. P. Puzzo, Y. Chang, Z. B. Wang, M. G. Helander, J. Jeong, N. P. Kherani, Z. Lu, and G. A. Ozin, "Silicon nanocrystal OLEDs: Effect of organic capping group on performance," *Small*, vol. 8, no. 23, pp. 3647–3654, 2012. DOI: `10.1002/smll.201201242` (cit. on pp. 13, 31, 45, 49, 50, 55, 60, 62).

[102] F. Maier-Flaig, C. Kübel, J. Rinck, T. Bocksrocker, T. Scherer, R. Prang, A. K. Powell, G. A. Ozin, and U. Lemmer, "Looking inside a working SiLED," *Nano Lett.*, vol. 13, no. 8, pp. 3539–3545, 2013. DOI: `10.1021/nl400975u` (cit. on pp. 13, 45).

[103] B. Ghosh, Y. Masuda, Y. Wakayama, Y. Imanaka, J. I. Inoue, K. Hashi, K. Deguchi, H. Yamada, Y. Sakka, S. Ohki, T. Shimizu, and N. Shirahata, "Hybrid white light emitting diode based on silicon nanocrystals," *Adv. Funct. Mater.*, vol. 24, no. 45, pp. 7151–7160, 2014. DOI: `10.1002/adfm.201401795` (cit. on pp. 13, 45, 47, 54).

[104] Y. Xin, K. Nishio, and K.-i. Saitow, "White-blue electroluminescence from a Si quantum dot hybrid light-emitting diode," *Appl. Phys. Lett.*, vol. 106, no. 20, p. 201 102, 2015. DOI: `10.1063/1.4921415` (cit. on pp. 13, 45).

[105] P. Reiss, M. Protière, and L. Li, "Core/shell semiconductor nanocrystals," *Small*, vol. 5, no. 2, pp. 154–168, 2009. DOI: `10.1002/smll.200800841` (cit. on p. 13).

[106] S. Kim, B. Fisher, H. J. Eisler, and M. Bawendi, "Type-II quantum dots: CdTe/CdSe (core/shell) and CdSe/ZnTe (core/shell) heterostructures," *J. Am. Chem. Soc.*, vol. 125, no. 38, pp. 11 466–11 467, 2003. DOI: `10.1021/ja0361749` (cit. on p. 13).

[107] M. Dasog, J. Kehrle, B. Rieger, and J. G. C. Veinot, “Silicon Nanocrystals and Silicon-Polymer Hybrids: Synthesis, Surface Engineering, and Applications,” *Angew. Chemie - Int. Ed.*, vol. 55, no. 7, pp. 2322–2339, 2016. DOI: `10.1002/anie.201506065` (cit. on pp. 13, 31, 49).

[108] Milliron, I. Hill, C. Shen, A. Kahn, and J. Schwartz, “Surface oxidation activates indium tin oxide for hole injection,” *J. Appl. Phys.*, vol. 87, no. January, pp. 572–576, 2000. DOI: `10.1063/1.371901` (cit. on p. 20).

[109] D. W. Schubert and T. Dunkel, “Spin coating from a molecular point of view: Its concentration regimes, influence of molar mass and distribution,” *Mater. Res. Innov.*, vol. 7, no. 5, pp. 314–321, 2003. DOI: `10.1007/s10019-003-0270-2` (cit. on p. 21).

[110] Ossila, *Spin Coating: A Guide to Theory and Techniques* (cit. on p. 22).

[111] H. Klauk, “Organic thin-film transistors,” *Chem. Soc. Rev.*, vol. 39, no. 7, pp. 2643–66, Jul. 2010. DOI: `10.1039/b909902f` (cit. on p. 26).

[112] W. W. Zhu, S. Xiao, and I. Shih, “Field-effect mobilities of polyhedral oligomeric silsesquioxanes anchored semiconducting polymers,” *Appl. Surf. Sci.*, vol. 221, no. 1-4, pp. 358–363, 2004. DOI: `10.1016/S0169-4332(03)00939-5` (cit. on pp. 27, 60).

[113] Q. Sun, Y. A. Wang, L. S. Li, D. Wang, T. Zhu, J. Xu, C. Yang, and Y. Li, “Bright, multicoloured light-emitting diodes based on quantum dots,” *Nat. Photonics*, vol. 1, no. 12, pp. 717–722, Dec. 2007. DOI: `10.1038/nphoton.2007.226` (cit. on p. 27).

[114] O. Malinkiewicz, A. Yella, Y. H. Lee, G. M. Espallargas, M. Graetzel, M. K. Nazeeruddin, and H. J. Bolink, “Perovskite solar cells employing organic charge-transport layers,” *Nat. Photonics*, vol. 8, no. 2, pp. 128–132, 2014. DOI: `10.1038/nphoton.2013.341` (cit. on p. 27).

[115] M. W. Thesen, B. Höfer, M. Debeaux, S. Janietz, A. Wedel, K. Anna, H. H. Johannes, and H. Krueger, “Hole-transporting host-Polymer series consisting of triphenylamine basic structures for phosphorescent polymer light-Emitting diodes,” *J. Polym. Sci. Part A Polym. Chem.*, vol. 48, no. 15, pp. 3417–3430, 2010. DOI: `10.1002/pola.24127` (cit. on pp. 27, 60).

[116] L. Yang, Y. Yan, F. Cai, J. Li, and T. Wang, “Poly(9-vinylcarbazole) as a hole transport material for efficient and stable inverted planar heterojunction perovskite solar cells,” *Sol. Energy Mater. Sol. Cells*, vol. 163, no. January, pp. 210–217, 2017. DOI: `10.1016/j.solmat.2017.01.040` (cit. on p. 27).

[117] S. Tang, A. Sandström, P. Lundberg, T. Lanz, C. Larsen, S. Van Reenen, M. Kemerink, and L. Edman, "Design rules for light-emitting electrochemical cells delivering bright luminance at 27.5 percent external quantum efficiency," *Nat. Commun.*, vol. 8, no. 1, p. 1190, Dec. 2017. DOI: `10.1038/s41467-017-01339-0` (cit. on p. 27).

[118] S. Kirchmeyer and K. Reuter, "Scientific importance, properties and growing applications of poly(3,4-ethylenedioxythiophene)," *J. Mater. Chem.*, vol. 15, no. 21, pp. 2077–2088, 2005. DOI: `10.1039/b417803n` (cit. on p. 28).

[119] C. M. Palumbiny, F. Liu, T. P. Russell, A. Hexemer, C. Wang, and P. Müller-Buschbaum, "The crystallization of PEDOT:PSS polymeric electrodes probed in situ during printing," *Adv. Mater.*, vol. 27, no. 22, pp. 3391–3397, 2015. DOI: `10.1002/adma.201500315` (cit. on p. 28).

[120] Y. Zhou, C. Fuentes-Hernandez, J. Shim, J. Meyer, A. J. Giordano, H. Li, P. Winget, T. Papadopoulos, H. Cheun, J. Kim, M. Fenoll, A. Dindar, W. Haske, E. Najafabadi, T. M. Khan, H. Sojoudi, S. Barlow, S. Graham, J. L. Brédas, S. R. Marder, A. Kahn, and B. Kippelen, "A universal method to produce low-work function electrodes for organic electronics," *Science*, vol. 336, no. 6079, pp. 327–332, Apr. 2012. DOI: `10.1126/science.1218829` (cit. on pp. 28, 92).

[121] Hö, S. Fle, A. Schienle, M. Bruns, U. Lemmer, and A. Colsmann, "Enhanced electron injection into inverted polymer light-emitting diodes by combined solution-processed zinc oxide/polyethylenimine interlayers," *Adv. Mater.*, vol. 26, no. 17, pp. 2750–2754, 2014. DOI: `10.1002/adma.201304666` (cit. on p. 29).

[122] S. Stolz, M. Scherer, E. Mankel, R. Lovrinčić, J. Schinke, W. Kowalsky, W. Jaegermann, U. Lemmer, N. Mechau, and G. Hernandez-Sosa, "Investigation of solution-processed ultrathin electron injection layers for organic light-emitting diodes.," *ACS Appl. Mater. Interfaces*, vol. 6, no. 9, pp. 6616–22, May 2014. DOI: `10.1021/am500287y` (cit. on pp. 29, 92).

[123] L. Yao, T. Yu, L. Ba, H. Meng, X. Fang, Y. Wang, L. Li, X. Rong, S. Wang, X. Wang, G. Ran, X. Pi, and G. Qin, "Efficient silicon quantum dots light emitting diodes with an inverted device structure," *J. Mater. Chem. C*, vol. 4, no. 4, pp. 673–677, 2016. DOI: `10.1039/C5TC03064A` (cit. on p. 29).

[124] X. Jia, N. Wu, J. Wei, L. Zhang, Q. Luo, Z. Bao, Y. Q. Li, Y. Yang, X. Liu, and C. Q. Ma, "A low-cost and low-temperature processable zinc oxide-polyethylenimine (ZnO:PEI) nano-composite as cathode buffer layer for organic and perovskite solar cells," *Org. Electron. physics, Mater. Appl.*, vol. 38, pp. 150–157, 2016. DOI: `10.1016/j.orgel.2016.08.012` (cit. on p. 29).

[125] S. Chen, J. R. Manders, S.-W. Tsang, and F. So, "Metal oxides for interface engineering in polymer solar cells," *J. Mater. Chem.*, pp. 24 202–24 212, 2012. DOI: `10.1039/c2jm33838f` (cit. on p. 29).

[126] M. T. Greiner and Z.-H. Lu, “Thin-film metal oxides in organic semiconductor devices: their electronic structures, work functions and interfaces,” *NPG Asia Mater.*, vol. 5, no. 7, e55, 2013. DOI: `10.1038/am.2013.29` (cit. on p. 29).

[127] K. Zilberberg, J. Meyer, and T. Riedl, “Solution processed metal-oxides for organic electronic devices,” *J. Mater. Chem. C*, vol. 1, no. 32, p. 4796, 2013. DOI: `10.1039/c3tc30930d` (cit. on p. 29).

[128] J. G. C. Veinot, “Synthesis, surface functionalization, and properties of freestanding silicon nanocrystals.,” *Chem. Commun. (Camb).*, no. 40, pp. 4160–4168, 2006. DOI: `10.1039/b607476f` (cit. on p. 30).

[129] J. R. Heath, “A Liquid-Solution-Phase Synthesis of Crystalline Silicon,” *Science*, vol. 258, no. 5085, pp. 1131–1133, 1992. DOI: `10.1126/science.258.5085.1131` (cit. on p. 30).

[130] R. A. Bley and S. M. Kauzlarich, “A low-temperature solution phase route for the synthesis of silicon nanoclusters,” *J. Am. Chem. Soc.*, vol. 118, no. 49, pp. 12 461–12 462, 1996. DOI: `10.1021/ja962787s` (cit. on p. 30).

[131] M. Dasog, Z. Yang, S. Regli, T. M. Atkins, A. Faramus, M. P. Singh, E. Muthuswamy, S. M. Kauzlarich, R. D. Tilley, and J. G. C. Veinot, “Chemical Insight into the Origin of Red and Blue Photoluminescence Arising from Freestanding Silicon Nanocrystals,” *ACS Nano*, vol. 7, no. 3, pp. 2676–2685, Mar. 2013. DOI: `10.1021/nn4000644` (cit. on p. 30).

[132] J. L. Heinrich, C. L. Curtis, G. M. Credo, M. J. Sailor, and K. L. Kavanagh, “Luminescent colloidal silicon suspensions from porous silicon.,” *Science*, vol. 255, no. 5040, pp. 66–68, 1992. DOI: `10.1126/science.255.5040.66` (cit. on p. 30).

[133] Z. Kang, C. H. A. Tsang, Z. Zhang, M. Zhang, N. B. Wong, J. A. Zapien, Y. Shan, and S. T. Lee, “A polyoxometalate-assisted electrochemical method for silicon nanostructures preparation: From quantum dots to nanowires,” *J. Am. Chem. Soc.*, vol. 129, no. 17, pp. 5326–5327, 2007. DOI: `10.1021/ja068894w` (cit. on p. 30).

[134] C. M. Hessel, E. J. Henderson, and J. G. C. Veinot, “Hydrogen silsesquioxane: A molecular precursor for nanocrystalline Si-SiO2 composites and freestanding hydride-surface-terminated silicon nanoparticles,” *Chem. Mater.*, vol. 18, no. 26, pp. 6139–6146, 2006. DOI: `10.1021/cm0602803` (cit. on pp. 30, 31).

[135] S. M. Liu, Y. Yang, S. Sato, and K. Kimura, “Enhanced photoluminescence from Si nano-organosols by functionalization with alkenes and their size evolution,” *Chem. Mater.*, vol. 18, no. 3, pp. 637–642, 2006. DOI: `10.1021/cm0519636` (cit. on p. 30).

[136] J. D. Holmes, K. J. Ziegler, R. C. Doty, L. E. Pell, K. P. Johnston, and B. A. Korgel, “Highly luminescent silicon nanocrystals with discrete optical transitions,” *J. Am. Chem. Soc.*, vol. 123, no. 16, pp. 3743–3748, 2001. DOI: `10.1021/ja002956f` (cit. on p. 30).

[137] A. Gupta, M. T. Swihart, and H. Wiggers, "Luminescent colloidal dispersion of silicon quantum dots from microwave plasma synthesis: Exploring the photoluminescence behavior across the visible spectrum," *Adv. Funct. Mater.*, vol. 19, no. 5, pp. 696–703, 2009. DOI: `10.1002/adfm.200801548` (cit. on p. 30).

[138] W. R. Cannon, S. C. Danforth, J. H. Flint, J. S. Haggerty, and R. A. Marra, "Sinterable Ceramic Powders from Laser-Driven Reactions: I, Process Description and Modeling," *J. Am. Ceram. Soc.*, vol. 65, no. 7, pp. 324–330, 1982. DOI: `10.1111/j.1151-2916.1982.tb10464.x` (cit. on p. 30).

[139] X. Li, Y. He, and M. T. Swihart, "Surface functionalization of silicon nanoparticles produced by laser-driven pyrolysis of silane followed by HF-HNO 3 Etching," *Langmuir*, vol. 20, no. 11, pp. 4720–4727, 2004. DOI: `10.1021/la036219j` (cit. on p. 30).

[140] B. F. P. McVey and R. D. Tilley, "Solution Synthesis, Optical Properties, and Bioimaging Applications of Silicon Nanocrystals," *Acc. Chem. Res.*, vol. 47, no. 10, pp. 3045–3051, 2014. DOI: `10.1021/ar500215v` (cit. on p. 30).

[141] M. Dasog, G. B. De los Reyes, L. V. Titova, F. A. Hegmann, and J. G. C. Veinot, "Size vs Surface: Tuning the Photoluminescence of Freestanding Silicon Nanocrystals Across the Visible Spectrum via Surface Groups," *ACS Nano*, vol. 8, no. 9, pp. 9636–9648, 2014. DOI: `10.1021/nn504109a` (cit. on pp. 30, 31, 49, 54, 56, 82, 85).

[142] M. H. Mobarok, T. K. Purkait, and J. G. Veinot, "A Nanoscale Adventure with Silicon: Synthesis, Surface Chemistry, and other Surprises," *Solid State Phenom.*, vol. 242, no. d, pp. 383–390, 2015. DOI: `10.4028/www.scientific.net/SSP.242.383` (cit. on p. 31).

[143] R. J. Clark, M. Aghajamali, C. M. Gonzalez, L. Hadidi, M. A. Islam, M. Javadi, M. H. Mobarok, T. K. Purkait, C. J. T. Robidillo, R. Sinelnikov, A. N. Thiessen, J. Washington, H. Yu, and J. G. C. Veinot, "From Hydrogen Silsesquioxane to Functionalized Silicon Nanocrystals," *Chem. Mater.*, vol. 29, no. 1, pp. 80–89, 2017. DOI: `10.1021/acs.chemmater.6b02667` (cit. on p. 31).

[144] A. Angı, M. Loch, R. Sinelnikov, J. G. C. Veinot, M. Becherer, P. Lugli, and B. Rieger, "The influence of surface functionalization methods on the performance of silicon nanocrystal LEDs," *Nanoscale*, 2018. DOI: `10.1039/C7NR09525B` (cit. on pp. 32, 50–54, 56).

[145] Z. Yang, M. Iqbal, A. R. Dobbie, and J. G. Veinot, "Surface-induced alkene oligomerization: Does thermal hydrosilylation really lead to monolayer protected silicon nanocrystals?" *J. Am. Chem. Soc.*, vol. 135, no. 46, pp. 17 595–17 601, 2013. DOI: `10.1021/ja409657y` (cit. on pp. 32, 50).

[146] Z. Yang, C. M. Gonzalez, T. K. Purkait, M. Iqbal, A. Meldrum, and J. G. Veinot, "Radical Initiated Hydrosilylation on Silicon Nanocrystal Surfaces: An Evaluation of Functional Group Tolerance and Mechanistic Study," *Langmuir*, vol. 31, no. 38, pp. 10 540–10 548, 2015. DOI: `10.1021/acs.langmuir.5b02307` (cit. on pp. 32, 50, 52).

[147] I. M. D. Höhlein, A. Angi, R. Sinelnikov, J. G. C. Veinot, and B. Rieger, "Functionalization of hydride-terminated photoluminescent silicon nanocrystals with organolithium reagents," *Chem. - A Eur. J.*, vol. 21, no. 7, pp. 2755–2758, 2015. DOI: `10.1002/chem.201405555` (cit. on pp. 32, 50, 51, 63).

[148] L. T. Sharpe, A. Stockman, W. Jagla, and H. Jägle, "A luminous efficiency function, VD65* (λ), for daylight adaptation: A correction," *Color Res. Appl.*, vol. 36, no. 1, pp. 42–46, 2011. DOI: `10.1002/col.20602` (cit. on p. 40).

[149] Foto- und Lichtmesstechnik GmbH, *Pressebilder* (cit. on p. 41).

[150] F. Maier-Flaig, J. Rinck, M. Stephan, T. Bocksrocker, M. Bruns, C. Kübel, A. K. Powell, G. A. Ozin, and U. Lemmer, "Multicolor silicon light-emitting diodes (SiLEDs)," *Nano Lett.*, vol. 13, no. 2, pp. 475–480, Feb. 2013. DOI: `10.1021/nl3038689` (cit. on pp. 45, 46, 55, 60).

[151] L. Yao, T. Yu, L. Ba, H. Meng, X. Fang, Y. Wang, L. Li, X. Rong, S. Wang, X. Wang, G. Ran, X. Pi, and G. Qin, "Efficient silicon quantum dots light emitting diodes with an inverted device structure," *J. Mater. Chem. C*, vol. 4, no. 4, pp. 673–677, 2016. DOI: `10.1039/C5TC03064A` (cit. on pp. 45, 48, 54, 60).

[152] W. Gu, X. Liu, X. Pi, X. Dai, S. Zhao, L. Yao, D. Li, Y. Jin, M. Xu, D. Yang, and G. Qin, "Silicon-Quantum-Dot Light-Emitting Diodes with Interlayer-Enhanced Hole Transport," *IEEE Photonics J.*, vol. 9, no. 2, 2017. DOI: `10.1109/JPHOT.2017.2671023` (cit. on pp. 45, 47, 60).

[153] X. Liu, S. Zhao, W. Gu, Y. Zhang, X. Qiao, Z. Ni, X. Pi, and D. Yang, "Light-Emitting Diodes Based on Colloidal Silicon Quantum Dots with Octyl and Phenylpropyl Ligands," *ACS Appl. Mater. Interfaces*, vol. 10, no. 6, pp. 5959–5966, 2018. DOI: `10.1021/acsami.7b16980` (cit. on pp. 45, 49, 95).

[154] S. Zhao, X. Liu, W. Gu, X. Liang, Z. Ni, H. Tan, K. Huang, Y. Yan, X. Yu, M. Xu, X. Pi, and D. Yang, "Al2O3-Interlayer-Enhanced Performance of All-Inorganic Silicon-Quantum-Dot Near-Infrared Light-Emitting Diodes," *IEEE Trans. Electron Devices*, vol. 65, no. 2, pp. 577–583, 2018. DOI: `10.1109/TED.2017.2782772` (cit. on pp. 45, 48).

[155] S. Zhao, X. Liu, X. Pi, and D. Yang, "Light emitting diodes based on colloidal silicon quantum dots," vol. 39, no. 7, pp. 1–12, 2018. DOI: `10.1088/1674-4926/39/6/061008` (cit. on p. 45).

[156] M. L. Mastronardi, F. Maier-Flaig, D. Faulkner, E. J. Henderson, C. Kübel, U. Lemmer, and G. A. Ozin, "Size-dependent absolute quantum yields for size-separated colloidally-stable silicon nanocrystals," *Nano Lett.*, vol. 12, no. 1, pp. 337–342, Jan. 2012. DOI: `10.1021/nl2036194` (cit. on p. 46).

[157] J. M. Buriak, "Organometallic chemistry on silicon and germanium surfaces," *Chem. Rev.*, vol. 102, no. 5, pp. 1271–1308, 2002. DOI: `10.1021/cr000064s` (cit. on p. 50).

[158] J. H. Song and M. J. Sailor, "Functionalization of nanocrystalline porous silicon surfaces with aryllithium reagnets: Formation of silicon-carbon bonds by cleavage of silicon-silicon bonds," *J. Am. Chem. Soc.*, vol. 120, no. 10, pp. 2376–2381, 1998. DOI: `10.1021/ja9734511` (cit. on p. 50).

[159] K. Dohnalová, T. Gregorkiewicz, and K. Kůsová, *Silicon quantum dots: Surface matters*, Apr. 2014. DOI: `10.1088/0953-8984/26/17/173201` (cit. on p. 54).

[160] M. A. Islam, M. H. Mobarok, R. Sinelnikov, T. K. Purkait, and J. G. Veinot, "Phosphorus Pentachloride Initiated Functionalization of Silicon Nanocrystals," *Langmuir*, vol. 33, no. 35, pp. 8766–8773, 2017. DOI: `10.1021/acs.langmuir.7b00518` (cit. on p. 54).

[161] C. Würth, M. Grabolle, J. Pauli, M. Spieles, and U. Resch-Genger, "Relative and absolute determination of fluorescence quantum yields of transparent samples," *Nat. Protoc.*, vol. 8, no. 8, pp. 1535–1550, 2013. DOI: `10.1038/nprot.2013.087` (cit. on p. 55).

[162] T. van Buuren, L. Dinh, L. Chase, W. Siekhaus, and L. Terminello, "Changes in the Electronic Properties of Si Nanocrystals as a Function of Particle Size," *Phys. Rev. Lett.*, vol. 80, no. 17, pp. 3803–3806, 1998. DOI: `10.1103/PhysRevLett.80.3803` (cit. on p. 55).

[163] T. Mukai, M. Yamada, and S. Nakamura, "Characteristics of InGaN-Based UV/ Blue/ Green/ Amber/ Red Light-Emitting Diodes," *Jpn. J. Appl. Phys. Japanese J. Appl. Phys.*, vol. 38, no. 7A, pp. 3976–3981, 1999 (cit. on p. 60).

[164] A. Angı, R. Sinelnikov, A. Meldrum, J. G. C. Veinot, I. Balberg, D. Azulay, O. Millo, and B. Rieger, "Photoluminescence through in-gap states in phenylacetylene functionalized silicon nanocrystals," *Nanoscale*, vol. 8, no. 15, pp. 7849–7853, 2016. DOI: `10.1039/C6NR01435F` (cit. on p. 63).

[165] A. Angı, R. Sinelnikov, H. Heenen, A. Meldrum, J. Veinot, C. Scheurer, K. Reuter, O. Ashkenazi, D. Azulay, I. Balberg, O. Millo, and B. Rieger, "The influence of conjugated alkynyl(aryl) surface groups on the optical properties of silicon nanocrystals: photoluminescence through in-gap states," *Nanotechnology*, vol. 29, no. 35, p. 355 705, Aug. 2018. DOI: `10.1088/1361-6528/aac9ef` (cit. on p. 63).

[166] A. C. Balazs, V. V. Ginzburg, F. Qiu, G. W. Peng, and D. Jasnow, "Multi-scale model for binary mixtures containing nanoscopic particles," *J. Phys. Chem. B*, vol. 104, no. 15, pp. 3411–3422, 2000. DOI: `10.1021/jp993356+` (cit. on p. 64).

[167] Y. Xuan, D. Pan, N. Zhao, X. Ji, and D. Ma, "White electroluminescence from a poly(N-vinylcarbazole) layer doped with CdSe/CdS core-shell quantum dots," *Nanotechnology*, vol. 17, no. 19, pp. 4966–4969, 2006. DOI: `10.1088/0957-4484/17/19/032` (cit. on p. 64).

[168] J. Kwak, W. K. Bae, M. Zorn, H. Woo, H. Yoon, J. Lim, S. W. Kang, S. Weber, H. J. Butt, R. Zentel, S. Lee, K. Char, and C. Lee, "Characterization of quantum dot/conducting polymer hybrid films and their application in light-emitting diodes," *Adv. Mater.*, vol. 21, no. 48, pp. 5022–5026, 2009. DOI: `10.1002/adma.200902072` (cit. on p. 64).

[169] G.-H. Nam and I.-K. Park, "CdSe Quantum dot-conducting polymer hybrid structure for Phosphor-free white light-emitting diodes," *J. Korean Phys. Soc.*, vol. 66, no. 5, pp. 785–789, 2015. DOI: `10.3938/jkps.66.785` (cit. on p. 64).

[170] L. Wang, T. Chen, Q. Lin, H. Shen, A. Wang, H. Wang, C. Li, and L. S. Li, "High-performance azure blue quantum dot light-emitting diodes via doping PVK in emitting layer," *Org. Electron. physics, Mater. Appl.*, vol. 37, pp. 280–286, 2016. DOI: `10.1016/j.orgel.2016.06.032` (cit. on p. 64).

[171] F. Liang, Y. Liu, Y. Hu, Y. L. Shi, Y. Q. Liu, Z. K. Wang, X. D. Wang, B. Q. Sun, and L. S. Liao, "Polymer as an additive in the emitting layer for high-performance quantum dot light-emitting diodes," *ACS Appl. Mater. Interfaces*, vol. 9, no. 23, pp. 20 239–20 246, 2017. DOI: `10.1021/acsami.7b05629` (cit. on p. 64).

[172] M. Pope and C. E. Swenberg, *Electronic Processes in Organic Crystals and Polymers*. 1999, p. 1328, ISBN: 0195129636. DOI: `10.1063/1.327880` (cit. on p. 70).

[173] C. W. Tang, "Two-layer organic photovoltaic cell," *Appl. Phys. Lett.*, vol. 48, no. 2, pp. 183–185, Jan. 1986. DOI: `10.1063/1.96937` (cit. on p. 71).

[174] P. E. Shaw, A. Ruseckas, and I. D. W. Samuel, "Exciton diffusion measurements in poly(3-hexylthiophene)," *Adv. Mater.*, vol. 20, no. 18, pp. 3516–3520, Jul. 2008. DOI: `10.1002/adma.200800982` (cit. on p. 71).

[175] R. R. Lunt, N. C. Giebink, A. A. Belak, J. B. Benziger, and S. R. Forrest, "Exciton diffusion lengths of organic semiconductor thin films measured by spectrally resolved photoluminescence quenching," *J. Appl. Phys.*, vol. 105, no. 5, 2009. DOI: `10.1063/1.3079797` (cit. on p. 71).

[176] B. Siegmund, M. T. Sajjad, J. Widmer, D. Ray, C. Koerner, M. Riede, K. Leo, I. D. Samuel, and K. Vandewal, "Exciton Diffusion Length and Charge Extraction Yield in Organic Bilayer Solar Cells," *Adv. Mater.*, vol. 29, no. 12, p. 1 604 424, Mar. 2017. DOI: `10.1002/adma.201604424` (cit. on p. 71).

[177] M. Sim, J. Shin, C. Shim, M. Kim, S. B. Jo, J. H. Kim, and K. Cho, "Dependence of exciton diffusion length on crystalline order in conjugated polymers," *J. Phys. Chem. C*, vol. 118, no. 2, pp. 760–766, Jan. 2014. DOI: `10.1021/jp409776s` (cit. on p. 71).

[178] G. Yu, J. Gao, J. C. Hummelen, F. Wudl, and a. J. Heeger, "Polymer Photovoltaic Cells: Enhanced Efficiencies via a Network of Internal Donor-Acceptor Heterojunctions," *Science*, vol. 270, no. 5243, pp. 1789–1791, Dec. 1995. DOI: `10.1126/science.270.5243.1789` (cit. on p. 71).

[179] N. S. Sariciftci, L. Smilowitz, A. J. Heeger, and F. Wudl, "Photoinduced electron transfer from a conducting polymer to buckminsterfullerene.," *Science*, vol. 258, no. 5087, pp. 1474–6, Nov. 1992. DOI: `10.1126/science.258.5087.1474` (cit. on p. 73).

[180] S. Morita, A. A. Zakhidov, and K. Yoshino, "Doping effect of buckminsterfullerene in conducting polymer: Change of absorption spectrum and quenching of luminescene," *Solid State Commun.*, vol. 82, no. 4, pp. 249–252, Apr. 1992. DOI: `10.1016/0038-1098(92)90636-N` (cit. on p. 73).

[181] T. Singh, N. Marjanović, G. Matt, S. Günes, N. Sariciftci, a. Montaigne Ramil, a. Andreev, H. Sitter, R. Schwödiauer, and S. Bauer, "High-mobility n-channel organic field-effect transistors based on epitaxially grown C60 films," *Org. Electron.*, vol. 6, no. 3, pp. 105–110, Jun. 2005. DOI: `10.1016/j.orgel.2005.03.006` (cit. on p. 73).

[182] C. J. Brabec, G. Cerullo, G. Lanzani, S. De Silvestri, G. Zerza, N. S. Sariciftci, and J. C. Hummelen, "Direct observation of the ultrafast electron transfer process in a polymer/fullerene blend," in *Quantum Electron. Laser Sci. Conf. 2000. (QELS 2000). Tech. Dig.*, 2000, pp. 245–246 (cit. on p. 73).

[183] J. Bouclé, P. Ravirajan, and J. Nelson, "Hybrid polymer-metal oxide thin films for photovoltaic applications," *J. Mater. Chem.*, vol. 17, no. 30, pp. 3141–3153, 2007. DOI: `10.1039/b706547g` (cit. on p. 74).

[184] S. Günes and N. S. Sariciftci, *Hybrid solar cells*, 2008. DOI: `10.1016/j.ica.2007.06.042` (cit. on pp. 74, 82).

[185] H. Borchert, "Elementary processes and limiting factors in hybrid polymer/nanoparticle solar cells," *Energy Environ. Sci.*, vol. 3, no. 11, pp. 1682–1694, 2010. DOI: `10.1039/c0ee00181c` (cit. on p. 74).

[186] Y. Zhou, M. Eck, and M. Krüger, "Bulk-heterojunction hybrid solar cells based on colloidal nanocrystals and conjugated polymers," *Energy Environ. Sci.*, vol. 3, no. 12, p. 1851, 2010. DOI: `10.1039/c0ee00143k` (cit. on p. 74).

[187] R. D. Schaller and V. I. Klimov, "High efficiency carrier multiplication in PbSe nanocrystals: Implications for solar energy conversion," *Phys. Rev. Lett.*, vol. 92, no. 18, p. 186 601, May 2004. DOI: `10.1103/PhysRevLett.92.186601` (cit. on p. 74).

[188] M. Helgesen, R. Søndergaard, and F. C. Krebs, “Advanced materials and processes for polymer solar cell devices,” *J. Mater. Chem.*, vol. 20, no. 1, pp. 36–60, 2009. DOI: `10.1039/b913168j` (cit. on p. 74).

[189] A. W. Achtstein, A. Schliwa, A. Prudnikau, M. Hardzei, M. V. Artemyev, C. Thomsen, and U. Woggon, “Electronic structure and exciton-phonon interaction in two-dimensional colloidal cdse nanosheets,” *Nano Lett.*, vol. 12, no. 6, pp. 3151–3157, 2012. DOI: `10.1021/nl301071n` (cit. on p. 75).

[190] R. Benchamekh, N. A. Gippius, J. Even, M. O. Nestoklon, J. M. Jancu, S. Ithurria, B. Dubertret, A. L. Efros, and P. Voisin, “Tight-binding calculations of image-charge effects in colloidal nanoscale platelets of CdSe,” *Phys. Rev. B - Condens. Matter Mater. Phys.*, vol. 89, no. 3, p. 035 307, Jan. 2014. DOI: `10.1103/PhysRevB.89.035307` (cit. on p. 75).

[191] V. A. Hintermayr, A. F. Richter, F. Ehrat, M. Döblinger, W. Vanderlinden, J. A. Sichert, Y. Tong, L. Polavarapu, J. Feldmann, and A. S. Urban, “Tuning the Optical Properties of Perovskite Nanoplatelets through Composition and Thickness by Ligand-Assisted Exfoliation,” *Adv. Mater.*, vol. 28, no. 43, pp. 9478–9485, Nov. 2016. DOI: `10.1002/adma.201602897` (cit. on p. 75).

[192] ASTM International, “ASTM Standard Reference Spectra G173-03,” American Society for Testing and Materials, West Conshohocken, PA, Tech. Rep., 2012. DOI: `10.1520/G0173-03R12` (cit. on p. 76).

[193] K. Vandewal, K. Tvingstedt, A. Gadisa, O. Inganäs, and J. V. Manca, “On the origin of the open-circuit voltage of polymer-fullerene solar cells,” *Nat. Mater.*, vol. 8, no. 11, pp. 904–9, Nov. 2009. DOI: `10.1038/nmat2548` (cit. on p. 79).

[194] K. Vandewal, K. Tvingstedt, A. Gadisa, O. Inganäs, and J. V. Manca, “Relating the open-circuit voltage to interface molecular properties of donor:acceptor bulk heterojunction solar cells,” *Phys. Rev. B - Condens. Matter Mater. Phys.*, vol. 81, no. 12, 2010. DOI: `10.1103/PhysRevB.81.125204` (cit. on p. 79).

[195] B. Qi and J. Wang, “Open-circuit voltage in organic solar cells,” *J. Mater. Chem.*, vol. 22, no. 46, p. 24 315, 2012. DOI: `10.1039/c2jm33719c` (cit. on p. 79).

[196] T. M. Burke, S. Sweetnam, K. Vandewal, and M. D. McGehee, “Beyond Langevin recombination: How equilibrium between free carriers and charge transfer states determines the open-circuit voltage of organic solar Cells,” *Adv. Energy Mater.*, vol. 5, no. 11, 2015. DOI: `10.1002/aenm.201500123` (cit. on p. 79).

[197] N. K. Elumalai and A. Uddin, “Open circuit voltage of organic solar cells: an in-depth review,” *Energy Environ. Sci.*, vol. 9, no. 2, pp. 391–410, 2016. DOI: `10.1039/C5EE02871J` (cit. on p. 79).

[198] C. M. Ramsdale, J. A. Barker, A. C. Arias, J. D. MacKenzie, R. H. Friend, and N. C. Greenham, "The origin of the open-circuit voltage in polyfluorene-based photovoltaic devices," *J. Appl. Phys.*, vol. 92, no. 8, pp. 4266–4270, 2002. DOI: `10.1063/1.1506385` (cit. on p. 79).

[199] J. Liu, Y. Shi, and Y. Yang, "Solvation-induced morphology effects on the performance of polymer-based photovoltaic devices," *Adv. Funtional Mater.*, vol. 11, no. 6, pp. 420–424, 2001. DOI: `10.1002/1616-3028(200112)11:6<420::AID-ADFM420>3.0.CO;2-K` (cit. on p. 79).

[200] M. C. Scharber, D. Mühlbacher, M. Koppe, P. Denk, C. Waldauf, A. J. Heeger, and C. J. Brabec, "Design Rules for Donors in Bulk-Heterojunction Solar Cells—Towards 10 % Energy-Conversion Efficiency," *Adv. Mater.*, vol. 18, no. 6, pp. 789–794, Mar. 2006. DOI: `10.1002/adma.200501717` (cit. on pp. 79, 87).

[201] E. Sargent, "Colloidal quantum dot solar cells," *Nat. Photonics*, vol. 6, no. March, pp. 133–135, 2012. DOI: `10.1021/ja063166u` (cit. on p. 82).

[202] G. H. Carey, A. L. Abdelhady, Z. Ning, S. M. Thon, O. M. Bakr, and E. H. Sargent, "Colloidal Quantum Dot Solar Cells," *Chem. Rev.*, vol. 115, no. 23, pp. 12 732–12 763, 2015. DOI: `10.1021/acs.chemrev.5b00063` (cit. on p. 82).

[203] D. J. D. Moet, L. J. A. Koster, B. De Boer, and P. W. M. Blom, "Hybrid Polymer Solar Cells from Highly Reactive Diethylzinc: MDMO–PPV versus P3HT," *Chem. Mater.*, vol. 19, no. 24, pp. 5856–5861, 2007. DOI: `10.1021/cm070555u` (cit. on p. 82).

[204] S. Oosterhout, M. Wienk, S. van Bavel, R. Thiedmann, L. Koster, J. Gilot, J. Loos, V. Schmidt, and R. Janssen, "The effect of three-dimensional morphology on the efficiency of hybrid polymer solar cells," *Nat. Mater.*, vol. 8, no. 10, pp. 818–824, 2009. DOI: `10.1038/nmat2533` (cit. on p. 82).

[205] H. Wu, L. Hu, M. W. Rowell, D. Kong, J. J. Cha, J. R. McDonough, J. Zhu, Y. Yang, M. D. McGehee, and Y. Cui, "Electrospun metal nanofiber webs as high-performance transparent electrode," *Nano Lett.*, vol. 10, no. 10, pp. 4242–4248, 2010. DOI: `10.1021/nl102725k` (cit. on pp. 82, 108).

[206] S. Wu, J. Li, S. C. Lo, Q. Tai, and F. Yan, "Enhanced performance of hybrid solar cells based on ordered electrospun ZnO nanofibers modified with CdS on the surface," *Org. Electron. physics, Mater. Appl.*, vol. 13, no. 9, pp. 1569–1575, 2012. DOI: `10.1016/j.orgel.2012.04.018` (cit. on p. 82).

[207] C. Y. Kwong, A. B. Djurišić, P. C. Chui, K. W. Cheng, and W. K. Chan, "Influence of solvent on film morphology and device performance of poly(3-hexylthiophene) : TiO2 nanocomposite solar cells," *Chem. Phys. Lett.*, vol. 384, no. 4-6, pp. 372–375, 2004. DOI: `10.1016/j.cplett.2003.12.045` (cit. on p. 82).

[208] C. Y. Kwong, W. C. H. Choy, A. B. Djuri i, P. C. Chui, K. W. Cheng, and W. K. Chan, "Poly(3-hexylthiophene):TiO2 nanocomposites for solar cell applications," *Nanotechnology*, vol. 15, no. 9, pp. 1156–1161, 2004. DOI: `10.1088/0957-4484/15/9/008` (cit. on p. 82).

[209] C. Y. Kuo, W. C. Tang, C. Gau, T. F. Guo, and D. Z. Jeng, "Ordered bulk heterojunction solar cells with vertically aligned Ti O2 nanorods embedded in a conjugated polymer," *Appl. Phys. Lett.*, vol. 93, no. 3, pp. 2–5, 2008. DOI: `10.1063/1.2937472` (cit. on p. 82).

[210] G. K. Mor, S. Kim, M. Paulose, O. K. Varghese, K. Shankar, J. Basham, and C. A. Grimes, "Visible to Near-Infrared Light Harvesting in TiO 2 Nanotube Array−P3HT Based Heterojunction Solar Cells," *Nano Lett.*, vol. 9, no. 12, pp. 4250–4257, 2009. DOI: `10.1021/nl9024853` (cit. on p. 82).

[211] J. Y. Lek, G. Xing, T. C. Sum, and Y. M. Lam, "Electron transport limitation in P3HT:CdSe nanorods hybrid solar cells," *ACS Appl. Mater. Interfaces*, vol. 6, no. 2, pp. 894–902, 2014. DOI: `10.1021/am4041515` (cit. on p. 82).

[212] S. Yao, Z. Chen, F. Li, B. Xu, J. Song, L. Yan, G. Jin, S. Wen, C. Wang, B. Yang, and W. Tian, "High-efficiency aqueous-solution-processed hybrid solar cells based on P3HT Dots and CdTe nanocrystals," *ACS Appl. Mater. Interfaces*, vol. 7, no. 13, pp. 7146–7152, 2015. DOI: `10.1021/am508985q` (cit. on p. 82).

[213] X. Du, Q. Zeng, G. Jin, F. Liu, T. Ji, Y. Yue, Y. Yang, H. Zhang, and B. Yang, "Constructing Post-Permeation Method to Fabricate Polymer/Nanocrystals Hybrid Solar Cells with PCE Exceeding 6%," *Small*, vol. 13, no. 11, pp. 1–8, 2017. DOI: `10.1002/smll.201603771` (cit. on p. 82).

[214] G. Jin, H. Wei, Z. Cheng, H. Sun, H. Sun, and B. Yang, "Aqueous-Processed Polymer/Nanocrystal Hybrid Solar Cells with Efficiency of 5.64%: The Impact of Device Structure, Polymer Content, and Film Thickness," *J. Phys. Chem. C*, vol. 121, no. 4, pp. 2025–2034, 2017. DOI: `10.1021/acs.jpcc.6b07171` (cit. on p. 82).

[215] S. Günes, K. P. Fritz, H. Neugebauer, N. S. Sariciftci, S. Kumar, and G. D. Scholes, "Hybrid solar cells using PbS nanoparticles," *Sol. Energy Mater. Sol. Cells*, vol. 91, no. 5, pp. 420–423, 2007. DOI: `10.1016/j.solmat.2006.10.016` (cit. on p. 82).

[216] Z. Liu, Y. Sun, J. Yuan, H. Wei, X. Huang, L. Han, W. Wang, H. Wang, and W. Ma, "High-efficiency hybrid solar cells based on polymer/PbS(x)Se(1-x) nanocrystals benefiting from vertical phase segregation," *Adv. Mater.*, vol. 25, no. 40, pp. 5772–5778, 2013. DOI: `10.1002/adma.201302340` (cit. on p. 82).

[217] E. Arici, N. S. Sariciftci, and D. Meissner, "Hybrid solar cells based on nanoparticles of CuInS2 in organic matrices," *Adv. Funct. Mater.*, vol. 13, no. 2, pp. 165–170, 2003. DOI: `10.1002/adfm.200390024` (cit. on p. 82).

[218] E. Arici, H. Hoppe, F. Schäffler, D. Meissner, M. A. Malik, and N. S. Sariciftci, "Hybrid solar cells based on inorganic nanoclusters and conjugated polymers," *Thin Solid Films*, vol. 451-452, pp. 612–618, 2004. DOI: `10.1016/j.tsf.2003.11.026` (cit. on p. 82).

[219] W. Yue, "Organic-Inorganic Hybrid Solar Cells Based on Quantum Dots," in *Printable Sol. Cells*. Wiley-Blackwell, 2017, ch. 3, pp. 65–91, ISBN: 9781119283720. DOI: `10.1002/9781119283720.ch3` (cit. on p. 82).

[220] V. Svrcek, D. Mariotti, T. Yamanari, K. Matsubara, and M. Kondo, "Integration of surfactant-free silicon nanocrystal in hybrid solar cells," *Jpn. J. Appl. Phys.*, vol. 51, no. 10 PART 2, 2012. DOI: `10.1143/JJAP.51.10NE25` (cit. on pp. 82, 84).

[221] V. Švrček, T. Yamanari, D. Mariotti, K. Matsubara, and M. Kondo, "Enhancement of hybrid solar cell performance by polythieno [3,4-b]thiophenebenzodithiophene and microplasma-induced surface engineering of silicon nanocrystals," *Appl. Phys. Lett.*, vol. 100, no. 22, 2012. DOI: `10.1063/1.4721437` (cit. on pp. 82, 84, 90).

[222] Y. Ding, R. Gresback, R. Yamada, K. Okazaki, and T. Nozaki, "Hybrid silicon nanocrystal/poly(3-hexylthiophene-2,5-diyl) solar cells from a chlorinated silicon precursor," *Jpn. J. Appl. Phys.*, vol. 52, no. 11S, 11NM04, 2013. DOI: `10.7567/JJAP.52.11NM04` (cit. on pp. 82, 84, 90).

[223] Y. Ding, R. Gresback, Q. Liu, S. Zhou, X. Pi, and T. Nozaki, "Silicon nanocrystal conjugated polymer hybrid solar cells with improved performance," *Nano Energy*, vol. 9, pp. 25–31, 2014. DOI: `10.1016/j.nanoen.2014.06.024` (cit. on pp. 82, 84, 88, 90, 95).

[224] M. Alsari, Y. M. Omar, M. K. Panda, M. Chiesa, P. Naumov, and S. Lilliu, "Detrimental effect of silicon nanoparticles on P3HT:PCBM-Based OPV devices," *Macromol. Chem. Phys.*, vol. 216, no. 11, pp. 1155–1160, 2015. DOI: `10.1002/macp.201500051` (cit. on p. 82).

[225] S. Zhao, X. Pi, C. Mercier, Z. Yuan, B. Sun, and D. Yang, "Silicon-nanocrystal-incorporated ternary hybrid solar cells," *Nano Energy*, vol. 26, pp. 305–312, 2016. DOI: `10.1016/j.nanoen.2016.05.040` (cit. on pp. 82, 84, 87, 90, 96).

[226] M. C. Beard, K. P. Knutsen, P. Yu, J. M. Luther, Q. Song, W. K. Metzger, R. J. Ellingson, and A. J. Nozik, "Multiple exciton generation in colloidal silicon nanocrystals," *Nano Lett.*, vol. 7, pp. 2506–2512, 2007. DOI: `10.1021/nl0714861` (cit. on p. 82).

[227] M. T. Trinh, R. Limpens, W. D. A. M. De Boer, J. M. Schins, L. D. A. Siebbeles, and T. Gregorkiewicz, "Direct generation of multiple excitons in adjacent silicon nanocrystals revealed by induced absorption," *Nat. Photonics*, vol. 6, no. 5, pp. 316–321, 2012. DOI: `10.1038/nphoton.2012.36` (cit. on p. 82).

[228] P. Kowalczewski, M. Liscidini, and L. C. Andreani, "Engineering Gaussian disorder at rough interfaces for light trapping in thin-film solar cells," *Opt. Lett.*, vol. 37, no. 23, p. 4868, 2012. DOI: `10.1364/OL.37.004868` (cit. on p. 82).

[229] M.-L. Kuo, D. J. Poxson, Y. S. Kim, F. W. Mont, J. K. Kim, E. F. Schubert, and S.-Y. Lin, "Realization of a near-perfect antireflection coating for silicon solar energy utilization," *Opt. Lett.*, vol. 33, no. 21, p. 2527, 2008. DOI: `10.1364/OL.33.002527` (cit. on p. 82).

[230] M. D. Kelzenberg, S. W. Boettcher, J. A. Petykiewicz, D. B. Turner-Evans, M. C. Putnam, E. L. Warren, J. M. Spurgeon, R. M. Briggs, N. S. Lewis, and H. A. Atwater, "Enhanced absorption and carrier collection in Si wire arrays for photovoltaic applications," *Nat. Mater.*, vol. 9, no. 3, pp. 239–244, 2010. DOI: `10.1038/nmat2635` (cit. on p. 83).

[231] A. D. Mohite, D. E. Perea, S. Singh, S. A. Dayeh, I. H. Campbell, S. T. Picraux, and H. Htoon, "Highly efficient charge separation and collection across in situ doped axial VLS-grown Si nanowire p-n junctions," *Nano Lett.*, vol. 12, no. 4, pp. 1965–1971, 2012. DOI: `10.1021/nl204505p` (cit. on p. 83).

[232] M. Stupca, M. Alsalhi, T. Al Saud, A. Almuhanna, and M. H. Nayfeh, "Enhancement of polycrystalline silicon solar cells using ultrathin films of silicon nanoparticle," *Appl. Phys. Lett.*, vol. 91, no. 6, pp. 2005–2008, 2007. DOI: `10.1063/1.2766958` (cit. on p. 83).

[233] X. Pi, L. Zhang, and D. Yang, "Enhancing the efficiency of multicrystalline silicon solar cells by the inkjet printing of silicon-quantum-dot ink," *J. Phys. Chem. C*, vol. 116, no. 40, pp. 21 240–21 243, 2012. DOI: `10.1021/jp307078g` (cit. on p. 83).

[234] F. I. Chowdhury, A. Alnuaimi, K. Islam, and A. Nayfeh, "Efficiency enhancement in thin-film c-Si HIT solar cells using luminescent 2.85 nm silicon nanoparticles," in *2014 IEEE 40th Photovolt. Spec. Conf. PVSC 2014*, 2014, pp. 2209–2213, ISBN: 9781479943982. DOI: `10.1109/PVSC.2014.6925364` (cit. on p. 83).

[235] R. Lopez-Delgado, H. J. Higuera-Valenzuela, A. Zazueta-Raynaud, A. Ramos-Carrazco, J. E. Pelayo, D. Berman-Mendoza, M. E. Álvarez-Ramos, and A. Ayon, "Solar cell efficiency improvement employing down-shifting silicon quantum dots," *Microsyst. Technol.*, pp. 1–8, 2017. DOI: `10.1007/s00542-017-3405-x` (cit. on p. 83).

[236] F. Priolo, T. Gregorkiewicz, M. Galli, and T. F. Krauss, "Silicon nanostructures for photonics and photovoltaics," *Nat. Nanotechnol.*, vol. 9, no. 1, pp. 19–32, 2014. DOI: `10.1038/nnano.2013.271` (cit. on p. 83).

[237] V. Švrček, D. Mariotti, Y. Shibata, and M. Kondo, "A hybrid heterojunction based on fullerenes and surfactant-free, self-assembled, closely packed silicon nanocrystals," *J. Phys. D. Appl. Phys.*, vol. 43, no. 41, 2010. DOI: `10.1088/0022-3727/43/41/415402` (cit. on p. 85).

[238] J.-H. Huang, M. Velusamy, K.-C. Ho, J.-T. Lin, and C.-W. Chu, "A ternary cascade structure enhances the efficiency of polymer solar cells," *J. Mater. Chem.*, vol. 20, no. 14, p. 2820, Mar. 2010. DOI: `10.1039/b918362k` (cit. on p. 87).

[239] L. Yang, L. Yan, and W. You, "Organic solar cells beyond one pair of donor-acceptor: Ternary blends and more," *J. Phys. Chem. Lett.*, vol. 4, no. 11, pp. 1802–1810, 2013. DOI: `10.1021/jz400723u` (cit. on p. 87).

[240] Q. An, F. Zhang, L. Li, Z. Zhuo, J. Zhang, W. Tang, and F. Teng, "Enhanced performance of polymer solar cells by employing a ternary cascade energy structure," *Phys. Chem. Chem. Phys.*, vol. 16, no. 30, pp. 16 103–16 109, Jul. 2014. DOI: `10.1039/C4CP01411A` (cit. on p. 87).

[241] V. Shrotriya, J. Ouyang, R. J. Tseng, G. Li, and Y. Yang, "Absorption spectra modification in poly(3-hexylthiophene):methanofullerene blend thin films," *Chem. Phys. Lett.*, vol. 411, no. 1-3, pp. 138–143, 2005. DOI: `10.1016/j.cplett.2005.06.027` (cit. on p. 88).

[242] F. C. Spano, "Absorption in regio-regular poly(3-hexyl)thiophene thin films: Fermi resonances, interband coupling and disorder," *Chem. Phys.*, vol. 325, no. 1, pp. 22–35, 2006. DOI: `10.1016/j.chemphys.2005.08.019` (cit. on p. 88).

[243] J. Clark, C. Silva, R. H. Friend, and F. C. Spano, "Role of intermolecular coupling in the photophysics of disordered organic semiconductors: Aggregate emission in regioregular polythiophene," *Phys. Rev. Lett.*, vol. 98, no. 20, 2007. DOI: `10.1103/PhysRevLett.98.206406` (cit. on p. 88).

[244] P. J. Brown, D. S. Thomas, A. Köhler, J. S. Wilson, J. S. Kim, C. M. Ramsdale, H. Sirringhaus, and R. H. Friend, "Effect of interchain interactions on the absorption and emission of poly(3-hexylthiophene)," *Phys. Rev. B - Condens. Matter Mater. Phys.*, vol. 67, no. 6, 2003. DOI: `10.1103/PhysRevB.67.064203` (cit. on p. 88).

[245] Y. Kim, S. Choulis, J. Nelson, D. D. C. Bradley, S. Cook, and J. R. Durrant, "Device annealing effect in organic solar cells with blends of regioregular poly(3-hexylthiophene) and soluble fullerene," *Appl. Phys. Lett.*, vol. 86, no. 6, p. 063 502, 2005. DOI: `10.1063/1.1861123` (cit. on p. 88).

[246] L. H. Nguyen, H. Hoppe, T. Erb, S. Günes, G. Gobsch, and N. S. Sariciftci, "Effects of annealing on the nanomorphology and performance of poly(alkylthiophene):Fullerene bulk-heterojunction solar cells," *Adv. Funct. Mater.*, vol. 17, no. 7, pp. 1071–1078, 2007. DOI: `10.1002/adfm.200601038` (cit. on p. 88).

[247] F. Arca, M. Loch, and P. Lugli, "Enhancing efficiency of organic bulkheterojunction solar cells by using 1,8-diiodooctane as processing additive," *IEEE J. Photovoltaics*, vol. 4, no. 6, pp. 1560–1565, Nov. 2014. DOI: `10.1109/JPHOTOV.2014.2355042` (cit. on p. 88).

[248] F. Li, J. Zhao, K. Yao, and Y. Chen, "Origin of the efficiency improvement in pre-annealed P3HT/PCBM solar cells with LiF/Al electrodes," *Chem. Phys. Lett.*, vol. 553, pp. 36–40, Nov. 2012. DOI: `10.1016/j.cplett.2012.10.006` (cit. on p. 92).

[249] F. Cheng, G. Fang, X. Fan, H. Huang, Q. Zheng, P. Qin, H. Lei, and Y. Li, "Enhancing the performance of P3HT:ICBA based polymer solar cells using LiF as electron collecting buffer layer and UV-ozone treated MoO3as hole collecting buffer layer," *Sol. Energy Mater. Sol. Cells*, vol. 110, pp. 63–68, Mar. 2013. DOI: `10.1016/j.solmat.2012.12.006` (cit. on p. 92).

[250] C. J. Brabec, A. Cravino, D. Meissner, N. Serdar Sariciftci, T. Fromherz, M. T. Rispens, L. Sanchez, and J. C. Hummelen, "Origin of the open circuit voltage of plastic solar cells," *Adv. Funtional Mater.*, vol. 11, no. 5, pp. 374–380, 2001. DOI: `10.1002/1616-3028(200110)11:5<374::AID-ADFM374>3.0.CO;2-W` (cit. on p. 92).

[251] M. O. Reese, M. S. White, G. Rumbles, D. S. Ginley, and S. E. Shaheen, "Optimal negative electrodes for poly(3-hexylthiophene): [6,6]-phenyl C61-butyric acid methyl ester bulk heterojunction photovoltaic devices," *Appl. Phys. Lett.*, vol. 92, no. 5, pp. 2006–2009, 2008. DOI: `10.1063/1.2841067` (cit. on pp. 92, 94).

[252] W. H. Tseng, M. H. Chen, J. Y. Wang, C. T. Tseng, H. Lo, P. S. Wang, and C. I. Wu, "Investigations of efficiency improvements in poly(3-hexylthiophene) based organic solar cells using calcium cathodes," *Sol. Energy Mater. Sol. Cells*, vol. 95, no. 12, pp. 3424–3427, 2011. DOI: `10.1016/j.solmat.2011.07.036` (cit. on p. 92).

[253] D. Chi, S. Qu, Z. Wang, and J. Wang, "High efficiency P3HT:PCBM solar cells with an inserted PCBM layer," *J. Mater. Chem. C*, vol. 2, no. 22, p. 4383, May 2014. DOI: `10.1039/c4tc00003j` (cit. on p. 95).

[254] L. Lu and L. Yu, "Understanding low bandgap polymer PTB7 and optimizing polymer solar cells based on IT," *Adv. Mater.*, vol. 26, no. 26, pp. 4413–4430, Jul. 2014. DOI: `10.1002/adma.201400384` (cit. on p. 95).

[255] S. Ye, A. R. Rathmell, I. E. Stewart, Y.-C. Ha, A. R. Wilson, Z. Chen, and B. J. Wiley, "A rapid synthesis of high aspect ratio copper nanowires for high-performance transparent conducting films," *Chem. Commun.*, vol. 50, no. 20, pp. 2562–2564, 2014. DOI: `10.1039/C3CC48561G` (cit. on p. 101).

[256] A. Falco, L. Cinà, G. Scarpa, P. Lugli, and A. Abdellah, "Fully-sprayed and flexible organic photodiodes with transparent carbon nanotube electrodes," *ACS Appl. Mater. Interfaces*, vol. 6, no. 13, pp. 10 593–10 601, Jul. 2014. DOI: `10.1021/am5022123` (cit. on p. 101).

[257] X. Li, Y. Zhu, W. Cai, M. Borysiak, B. Han, D. Chen, R. D. Piner, L. Colomba, and R. S. Ruoff, "Transfer of large-area graphene films for high-performance transparent conductive electrodes," *Nano Lett.*, vol. 9, no. 12, pp. 4359–4363, Dec. 2009. DOI: `10.1021/nl902623y` (cit. on p. 101).

[258] Z. Yin, S. Sun, T. Salim, S. Wu, X. Huang, Q. He, Y. M. Lam, and H. Zhang, "Organic photovoltaic devices using highly flexible reduced graphene oxide films as transparent electrodes," *ACS Nano*, vol. 4, no. 9, pp. 5263–5268, Sep. 2010. DOI: `10.1021/nn1015874` (cit. on p. 101).

[259] M. Schmidt, A. Falco, M. Loch, P. Lugli, and G. Scarpa, "Spray coated indium-tin-oxide-free organic photodiodes with PEDOT:PSS anodes," *AIP Adv.*, vol. 4, no. 10, 2014. DOI: `10.1063/1.4899044` (cit. on p. 101).

[260] M. Bobinger, V. Dergianlis, M. Becherer, and P. Lugli, "Comprehensive Synthesis Study of Well-Dispersed and Solution-Processed Metal Nanowires for Transparent Heaters," *J. Nanomater.*, vol. 2018, 2018. DOI: `10.1155/2018/7304807` (cit. on p. 101).

[261] Y. Chang, M. L. Lye, and H. C. Zeng, "Large-scale synthesis of high-quality ultralong copper nanowires," *Langmuir*, vol. 21, no. 9, pp. 3746–3748, 2005. DOI: `10.1021/la050220w` (cit. on p. 102).

[262] C. Hwang, J. An, B. D. Choi, K. Kim, S.-W. Jung, K.-J. Baeg, M.-G. Kim, K. M. Ok, and J. Hong, "Controlled aqueous synthesis of ultra-long copper nanowires for stretchable transparent conducting electrode," *J. Mater. Chem. C*, vol. 4, no. 7, pp. 1441–1447, 2016. DOI: `10.1039/C5TC03614C` (cit. on p. 102).

[263] M. Bobinger, J. Mock, P. La Torraca, M. Becherer, P. Lugli, and L. Larcher, "Tailoring the Aqueous Synthesis and Deposition of Copper Nanowires for Transparent Electrodes and Heaters," *Adv. Mater. Interfaces*, vol. 4, no. 20, pp. 1–10, 2017. DOI: `10.1002/admi.201700568` (cit. on pp. 102, 103, 108).

[264] S. Link, M. B. Mohamed, and M. A. El-Sayed, "Simulation of the Optical Absorption Spectra of Gold Nanorods as a Function of Their Aspect Ratio and the Effect of the Medium Dielectric Constant," *J. Phys. Chem. B*, vol. 103, no. 16, pp. 3073–3077, 1999. DOI: `10.1021/jp990183f` (cit. on p. 106).

[265] C. Chang, W. Li, J. Guohua, Z. Junfeng, C. Xu, Y. Haojie, and Y. Qiang, "Study on the synthesis of silver nanowires with adjustable diameters through the polyol process," *Nanotechnology*, vol. 17, no. 15, p. 3933, 2006 (cit. on p. 106).

[266] Q. N. Luu, J. M. Doorn, M. T. Berry, C. Jiang, C. Lin, and P. S. May, "Preparation and optical properties of silver nanowires and silver-nanowire thin films," *J. Colloid Interface Sci.*, vol. 356, no. 1, pp. 151–158, 2011. DOI: `10.1016/j.jcis.2010.12.077` (cit. on p. 106).

[267] J. K. Lee, W. L. Ma, C. J. Brabec, J. Yuen, J. S. Moon, J. Y. Kim, K. Lee, G. C. Bazan, and A. J. Heeger, "Processing additives for improved efficiency from bulk heterojunction solar cells.," *J. Am. Chem. Soc.*, vol. 130, no. 11, pp. 3619–23, Mar. 2008. DOI: `10.1021/ja710079w` (cit. on p. 106).

[268] A. R. Madaria, A. Kumar, F. N. Ishikawa, and C. Zhou, “Uniform, highly conductive, and patterned transparent films of a percolating silver nanowire network on rigid and flexible substrates using a dry transfer technique,” *Nano Res.*, vol. 3, no. 8, pp. 564–573, 2010. DOI: `10.1007/s12274-010-0017-5` (cit. on p. 106).

[269] E. C. Garnett, W. Cai, J. J. Cha, F. Mahmood, S. T. Connor, M. Greyson Christoforo, Y. Cui, M. D. McGehee, and M. L. Brongersma, “Self-limited plasmonic welding of silver nanowire junctions,” *Nat. Mater.*, vol. 11, no. 3, pp. 241–249, Mar. 2012. DOI: `10.1038/nmat3238` (cit. on p. 106).

[270] C. Lee, Y. Oh, I. S. Yoon, S. H. Kim, B.-K. Ju, and J.-M. Hong, “Flash-induced nanowelding of silver nanowire networks for transparent stretchable electrochromic devices,” *Sci. Rep.*, vol. 8, no. 1, p. 2763, 2018. DOI: `10.1038/s41598-018-20368-3` (cit. on p. 106).

[271] H. Lu, D. Zhang, X. Ren, J. Liu, and W. C. Choy, “Selective growth and integration of silver nanoparticles on silver nanowires at room conditions for transparent nano-network electrode,” *ACS Nano*, vol. 8, no. 10, pp. 10 980–10 987, Oct. 2014. DOI: `10.1021/nn504969z` (cit. on p. 106).

[272] T. Tokuno, M. Nogi, M. Karakawa, J. Jiu, T. T. Nge, Y. Aso, and K. Suganuma, “Fabrication of silver nanowire transparent electrodes at room temperature,” *Nano Res.*, vol. 4, no. 12, pp. 1215–1222, 2011. DOI: `10.1007/s12274-011-0172-3` (cit. on p. 106).

[273] S. J. Lee, Y. H. Kim, J. K. Kim, H. Baik, J. H. Park, J. Lee, J. Nam, J. H. Park, T. W. Lee, G. R. Yi, and J. H. Cho, “A roll-to-roll welding process for planarized silver nanowire electrodes,” *Nanoscale*, vol. 6, no. 20, pp. 11 828–11 834, Sep. 2014. DOI: `10.1039/c4nr03771e` (cit. on p. 106).

[274] H. Guo, N. Lin, Y. Chen, Z. Wang, Q. Xie, T. Zheng, N. Gao, S. Li, J. Kang, D. Cai, and D. L. Peng, “Copper nanowires as fully transparent conductive electrodes,” *Sci. Rep.*, vol. 3, no. 1, p. 2323, Dec. 2013. DOI: `10.1038/srep02323` (cit. on p. 108).

[275] S. Ding, J. Jiu, Y. Gao, Y. Tian, T. Araki, T. Sugahara, S. Nagao, M. Nogi, H. Koga, K. Suganuma, and H. Uchida, “One-Step Fabrication of Stretchable Copper Nanowire Conductors by a Fast Photonic Sintering Technique and Its Application in Wearable Devices,” *ACS Appl. Mater. Interfaces*, vol. 8, no. 9, pp. 6190–6199, Mar. 2016. DOI: `10.1021/acsami.5b10802` (cit. on p. 108).

[276] C. Sachse, N. Weiß, N. Gaponik, L. Müller-Meskamp, A. Eychmüller, and K. Leo, “ITO-Free, small-molecule organic solar cells on spray-coated copper-nanowire-based transparent electrodes,” *Adv. Energy Mater.*, vol. 4, no. 2, pp. 1–6, 2014. DOI: `10.1002/aenm.201300737` (cit. on p. 108).

[277] “Standard Test Method for Haze and Luminous Transmittance of Transparent Plastics ASTM D1003-13,” American Society for Testing and Materials, West Conshohocken, PA, Tech. Rep., 2013. DOI: `10.1520/D1003` (cit. on p. 112).

[278] M. Bobinger, "Solution-processing of Transparent Electrodes for Novel Electronic Devices," Doctotal Thesis, Technical University of Munich, 2018 (cit. on p. 112).

[279] L. Hu, H. S. Kim, J. Y. Lee, P. Peumans, and Y. Cui, "Scalable coating and properties of transparent, flexible, silver nanowire electrodes," *ACS Nano*, vol. 4, no. 5, pp. 2955–2963, 2010. DOI: `10.1021/nn1005232` (cit. on p. 112).

[280] F. Guo, X. Zhu, K. Forberich, J. Krantz, T. Stubhan, M. Salinas, M. Halik, S. Spallek, B. Butz, E. Spiecker, T. Ameri, N. Li, P. Kubis, D. M. Guldi, G. J. Matt, and C. J. Brabec, "ITO-Free and Fully Solution-Processed Semitransparent Organic Solar Cells with High Fill Factors," *Adv. Energy Mater.*, vol. 3, no. 8, pp. 1062–1067, 2013. DOI: `10.1002/aenm.201300100` (cit. on p. 116).

[281] A. Kojima, K. Teshima, Y. Shirai, and T. Miyasaka, "Organometal halide perovskites as visible-light sensitizers for photovoltaic cells," *J. Am. Chem. Soc.*, vol. 131, no. 17, pp. 6050–6051, 2009. DOI: `10.1021/ja809598r` (cit. on p. 119).

[282] W. S. Yang, B.-W. Park, E. H. Jung, and N. J. Jeon, "Iodide management in formamidinium-lead-halide – based perovskite layers for efficient solar cells," *Science*, vol. 356, no. 6345, pp. 1376–1379, 2017. DOI: `10.1126/science.aan2301` (cit. on p. 119).

[283] F. Matteocci, L. Cinà, E. Lamanna, S. Cacovich, G. Divitini, P. A. Midgley, C. Ducati, and A. Di Carlo, "Encapsulation for long-term stability enhancement of perovskite solar cells," *Nano Energy*, vol. 30, no. July, pp. 162–172, 2016. DOI: `10.1016/j.nanoen.2016.09.041` (cit. on p. 120).

[284] H. M. Bank, M. E. Cifuentes, and T. E. Martin, *Process for the synthesis of soluble, condensed hydridosilicon resins containing low levels of silanol*, 1991 (cit. on p. 127).

Acknowledgements

No research project is done alone and I want to thank all the people that helped me on the way.

Firstly, I want to thank Prof. Paolo Lugli for giving me the opportunity do my PhD at this institute and his trust in me and my work. I will never forget how he hired me spontaneously during the lunch break of a conference.

Many thanks go to all the people who make the day-to-day work at the institute possible and are keeping it all together: Lucia Weik, Katharina Blahetek and Susanne Maier, who help us battle the bureaucracy of a big university. Thanks to Rosie Mittermaier, who is keeping all our many laboratories intact with endless endurance and patience (and teaching Bavarian to all us non-natives). And special thanks go to Markus Becherer for keeping the institute running after Prof. Lugli went to Bozen, for his contagious cheerfulness and for always having an open ear to our sorrows (and the many cookies).

I have to thank all the students that endured my supervision, especially Konstantinos and Kamyar for their work on the nanowires. Thank you for all the many hours in the lab and the endless amount of fabricated samples.
A large portion of this thesis is based on the nanoparticles provided by Arzu Angı. Thank you for the fruitful collaboration and bridging the hurdles of interdisciplinary work with me.

Thanks go to all the colleagues who so generously and patiently shared their knowledge with me: Alaa Abdellah, Almu Rivadeneyra-Torres, Bernhard Fabel, Claudio Ciceroni, Kathi Melzer, Pepe Fernández Salmerón, Simon Pfaehler and VJ Bhatt. Special thanks go to Aniello Falco, whom I still harassed with technical question long after he left the institute and to Morten Schmidt who got me on board for this journey.
Finally, I want to thank my colleagues that shared an office with me and made everyday life at work so fun: Robin, Tobi, Michi, Florin, Andi, Marco and Sepp. Sorry for all the sweets I stole from you and thank you for all the tea we shared.